SPECTRALLY-MATCHED NEUTRON DETECTORS DESIGNED USING COMPUTATIONAL ADJOINT SN FOR PLUG-IN REPLACEMENT OF HELIUM-3

A Dissertation
Presented to
The Academic Faculty

By

Scottie W. Walker

In Partial Fulfillment
Of the Requirements for the Degree
Doctor of Philosophy in Nuclear and Radiological Engineering

Georgia Institute of Technology

August 2013

SPECTRALLY-MATCHED NEUTRON DETECTORS DESIGNED USING COMPUTATIONAL ADJOINT SN FOR PLUG-IN REPLACEMENT OF HELIUM-3

Approved by:

Dr. Glenn E. Sjoden, Advisor
George W. Woodruff School
Georgia Institute of Technology

Dr. Farzad Rahnema
George W. Woodruff School
Georgia Institute of Technology

Dr. Chaitanya S. Deo
George W. Woodruff School
Georgia Institute of Technology

Dr. James C. Petrosky
Department of Engineering Physics
Air Force Institute of Technology

Dr. Adam N. Stulberg
School of International Affairs
Georgia Institute of Technology

Date Approved: [June 24, 2013]

DEDICATION

This dissertation is dedicated to my beautiful wife, Kay Diahn. I would like to thank her for the sacrifices she has made through our many years and, in some cases, for postponing her dreams so that I might pursue mine. The road toward completing my doctorate was a lot longer than I expected and it was filled with numerous unforeseen hardships; however, your love and support allowed me to overcome and to press forward toward the completion of this race. I look forward to transitioning into our post-graduate future and to the new challenges that lie ahead.

It has been my honor and privilege to be your husband for the past twenty years and now that my student days are behind me, I want to dedicate myself to being the best husband I can be for whatever remaining time God Almighty has apportioned for me on this earth. Forever my love is yours!

ACKNOWLEDGMENTS

I would first and foremost like to give glory to God for leading me to make the decision to return to graduate school and for providing the resources necessary to complete the task. I was very comfortable in my job at Sandia National Laboratories and had no intention of ever returning to a university; however, HE directed my path to the Georgia Institute of Technology for various reasons, most of which had nothing to do with education or research. The resulting journey has been exciting and a blessing beyond measure.

I could never have completed my degree without the undying love and support of my wife, Kay Diahn. She has always followed God's leading in my life without question and has joyfully managed our household while I tried to juggle work and school. There were many times during this project when she willfully accepted the lack of my presence and companionship. Her selflessness allowed me to focus solely on the tasks at hand without having to worry about whether our marriage would disintegrate. I will always be indebted to Kay Diahn and I am so thankful that God brought her into my life that day in the mountains.

Dr. Glenn Sjoden has been a constant source of inspiration and assistance since I began my Ph.D. work at the University of Florida in 2006. He is a tremendous teacher and he has an ability to explain difficult topics like reactor physics and transport theory in such a way that an average guy like me can understand it. Glenn has also been a

wonderful mentor and encourager, especially following the unraveling of my first two research efforts and after my transfer to Georgia Tech. He spent a lot of his valuable time with me to determine a new research path, he rearranged his schedule to meet with me when necessary, and he also supported me in making my measurements and in developing the computer models that were critical to this research. Throughout this whole process, we've also become good friends and I am a better engineer and man for having known him. I truly hope our careers continue to cross paths!

My mother has been a constant encouragement through the years and she always pushed me to do my best, to excel, and to never settle for mediocrity. She instilled in me the drive to begin and to extend my career in the nuclear industry, especially when things were tough in my personal life. My mom has certainly seen her share of heartaches and challenges as well, but through all of it, she has been one of my staunchest supporters.

My in-laws, Linda and Paul Bell, were a big support to my wife throughout this long journey and that, in turn, helped her to better support me. They also contributed to our cause when I transferred into the wonderful world of out-of-state tuition at Georgia Tech and without their generous support, our savings accounts would be much sparser.

Mr. Chris Edgar was a tremendous help in teaching me the basics of the PENTRAN code and for helping me understand how to setup my initial models. Chris spent many hours explaining things and answering my questions. Without his assistance, my computational modeling would have taken far longer.

I would definitely be remiss if I didn't thank Dr. Farzad Rahnema, Chair of the Nuclear and Radiological Engineering/Medical Physics Program, Dr. Wayne Whiteman, Director of the Office of Student Services in the George W. Woodruff School of Mechanical Engineering, and the other academic professionals in the Woodruff School. Their tremendous support and assistance made my transition from Florida as seamless as it could have possibly been. I really appreciate some of the special considerations afforded me because of my personal situation and I wouldn't have had the privilege of graduating from such a fine institution had it not been for these fine folks.

Finally, I would like to thank Dr. Alex Bielajew of the University of Michigan for telling me that I was wasting my time by attempting to achieve my Ph. D. so late in life and for assuring me that I would most likely not finish it (he's a Monte Carlo man). I am quite certain that Dr. Bielajew doesn't remember me or our meeting in early 2006; however, that discussion left a permanent impression upon me and I would like to thank him for being a constant inspiration whenever I felt like quitting.

TABLE OF CONTENTS

LIST OF TABLES

LIST OF FIGURES

LIST OF SYMBOLS OR ABBREVIATIONS

Adjoint angular flux ($\psi^{\dagger}$)

Advanced spectroscopic portal (ASP)

Alpha or alpha particle (α)

Atmosphere (atm)

Angular flux (ψ)

Anode wire radius (a)

Atomic number (Z)

Barn (b)

Beryllium (Be)

Boron (B)

Boron Tri-Fluoride (BF_3)

Cadmium (Cd)

Californium (Cf)

Canada deuterium-uranium (CANDU)

Carbon dioxide (CO_2)

Cathode inner radius (b)

Centimeter (cm)

Central Intelligence Agency (CIA)

Central Limit Theorem (CLT)

Compton scatter cross section (σ).....

Computed tomography (CT)

Container express (CONEX)

Counts (cts)

Curie (Ci)

Decomposition weight vector (decmpv)

Density (ρ)

Department of Defense (DOD)

Department of Energy (DOE)

Department of Homeland Security (DHS)

Department of Transportation (DOT)

Deuterium (D)

Deuterium oxide (D_2O)

Diamond zero (DZ)

Directional theta-weighted (DTW)

Discrete ordinates (S_N)

Domestic Nuclear Detection Office (DNDO)

Electron volt (eV)

Energy (E)

Equation (Eq.)

Equations (Eqs.)

Evaluated nuclear data file (ENDF)

Exponential directional-iterative (EDI)

Exponential directional-weighted (EDW)

Federal Bureau of Investigation (FBI)

Figure (Fig.)

Figures (Figs.)

Florida Institute of Nuclear Detection and Security (FINDS)

Fluorine (F)

Frequency (υ)

Gadolinium (Gd)

Graphical user interface (GUI)

Helium (He)

High-voltage power supply (HVPS)

Hydrofluoric acid (HF)

Hydrogen (H)

Improvised nuclear device (IND)

Interaction probability (μ)

International Air Transport Association (IATA)

Joule (J)

Kilo-electron volt (keV)

Kinetic energy (KE or T)

Legendre scattering moments (P_N)

Lethargy (ξ)

Linear Energy Transfer (LET)

Lithium (Li)

LND, Incorporated (LND)

Los Alamos National Laboratory (LANL)

Meter (m)

Micro-Curie (μCi)

Milli-barn (mb)

Milli-Curie (mCi)

Mixed-oxide fuel (MOX)

Mega-electron volte (MeV)

Macroscopic cross section (Σ)

Mass (m)

Message Passing Interface (MPI)

Microscopic cross section (σ)

Milli-rem (mrem)

Monte Carlo (MC)

Monte Carlo N-Particle (MCNP)

Multi-channel analyzer (MCA)

National Institute of Science and Technology (NIST)

National Nuclear Security Administration (NNSA)

Neutron (n)

Neutron scattering cross section (σ_s)

Nickel (Ni)

Number of degrees of freedom (N)

Oak Ridge National Laboratory (ORNL)

One dimensional (1-D)

Optical thickness (OT)

Oxygen (O)

Pair production cross section (κ)

Part-per-million (ppm)

Parallel-Environment Neutral Particle Transport (PENTRAN)

PENTRAN mesh generator XP (PENMSHXP)

Photoelectric effect cross section (τ)

Photon energy ($h\upsilon$)

Photon momentum ($h\upsilon/c$ or h/λ)

Planck's constant (h)

Plutonium (Pu)

Plutonium-beryllium (PuBe)

Point-of-entry (POE)

Poly-vinyl toluene (PVT)

Probability (p or P)

Probability density function (PDF)

Proton (p)

Pulse height unit (PHU)

Pulse-shape discrimination (PSD)

Q-value of a reaction (Q)

Quadrature (S)

Radiological dispersal device (RDD)

Reaction rate or detector response (R)

Russian roulette (RR)

Sandia National Laboratories (SNL)

Savannah River Site (SRS)

Scalar adjoint flux ($\phi^{\dagger}$)

Scalar flux (ϕ)

Second (s)

Single-channel analyzer (SCA)

Solid angle (Ω)

Source density (q)

Special Nuclear Material (SNM)

Speed of light (c)

Target nucleus mass (M)

Tennessee Valley Authority (TVA)

Theta-weight (TW)

Three dimensional (3-D)

Two dimensional (2-D)

Titanium (Ti)

Tritium (T or ^{3}H)

Uranium (U)

Variance (S^{2})

Voltage (V)

Volume (v or V)

Wavelength (λ)

Weapons-grade plutonium (WGPu)

Weight percentage (w)

Work function (φ)

SUMMARY

Neutron radiation detectors are an integral part of the Department of Homeland Security (DHS) efforts to detect the illicit trafficking of radioactive or special nuclear materials into the U.S. In the past decade, the DHS has deployed a vast network of radiation detection systems at various key positions to prevent or to minimize the risk associated with the malevolent use of these materials. The greatest portion of this detection burden has been borne by systems equipped with ^{3}He because of its highly desirable physical and nuclear properties. However, a dramatic increase in demand and dwindling supply, combined with a lack of oversight for the existing ^{3}He stockpile has produced a critical shortage of this gas which has virtually eliminated its viability for detector applications. And, although a number of research efforts have been undertaken to develop suitable replacements, none of these efforts are attempting to closely match a ^{3}He detector response across different neutron energy spectra, which is critical for certain non-proliferation programs and special nuclear material (SNM) assessments. Therefore, the objective of the proposed research was to produce several spectrally matched and validated equivalent neutron detectors for the direct replacement of ^{3}He in these neutron detection applications.

Prior to developing any actual designs, the fidelity of a computational approach was validated by executing radiation transport models for existing BF_3 and ^{3}He tubes and then comparing the results of these models to laboratory measurements conducted with

these exact detectors. Both tubes were 19.6 cm in height, with a 1-inch diameter, and operated at 1 and 4 atm pressure respectively. The models were processed using a combination of forward Monte Carlo and forward and adjoint 3-D discrete ordinates (S_N) transport methods. The computer codes MCNP5 and PENTRAN were used for all calculations with a nickel-filtered plutonium-beryllium (PuBe) source term that is equivalent to that of weapons-grade plutonium (WGPu). Once the computational methods were validated, six distinct plug-in models were developed that matched the neutron spectral response and reaction rate of a 1-inch diameter ^{3}He tube with a length of 10 cm and operating at 4 atm pressure. The equivalent designs consist of large singular tubes and dual tubes containing BF_3 gas, B-10 linings, and/or polyvinyl toluene (PVT).

CHAPTER 1
INTRODUCTION

1.1 The Scope of this Neutron Detection Research

Neutron detection is an integral part of our government's non-proliferation efforts, both here and abroad. These efforts have been severely hampered over the course of the past four years because of a severe shortage of the neutron detection gas ^{3}He, which had previously become the most popular neutron detection mechanism. Once the crisis was realized, the nuclear engineering research community began concerted research efforts toward developing new neutron detector materials or investigating whether existing ones could serve as an adequate replacement for the gas.

To date, all associated ^{3}He replacement research efforts have solely focused on "simple" detection cases where the overall system efficiency is the solitary concern (e.g. hand-held devices, portal monitoring systems, and backpack units). For these simple cases, the use of solid materials or the inclusion of additional alternative gas detectors can generally address the overall detection issues, because the neutron spectral response (efficiency as a function of neutron energy) is irrelevant. However, in most non-proliferation programs such safeguards and material control and accountability programs associated with fissile special nuclear material (SNM) material assessments, detection results are almost exclusively calibrated directly to a reaction rate in ^{3}He proportional

counters, and a mismatch in the neutron spectral response will result in serious mass quantification errors and potentially dire consequences.

In these instances, a “simple” material replacement or additional detector approach is neither appropriate nor possible due to influences resulting from the complex nature of neutron scattering in moderators, cross section variations, gas pressures, geometries, and surrounding structural interferences or other constraints. Instead, these more challenging detection cases require a detailed computational transport analysis be performed for each specific application. Therefore, a leveraged approach using adjoint transport computations, and validated using forward transport and Monte Carlo computations, and selected confirmatory laboratory measurements can adequately address all pertinent issues associated with ^{3}He tube replacement with spectrally-matched performance.

This dissertation begins with a historical discourse on the evolution of the ^{3}He gas crisis, discusses why this gas was highly prized as a neutron detector material and concludes with existing alternative detector materials and designs developed in this research that can serve as direct “plug-in” replacements for a 1-inch diameter, 4 atmospheres (atm), and polyethylene-moderated ^{3}He tube. The proposed replacement detectors will yield a ^{3}He spectral match while also delivering equivalent overall system efficiency for a given detection scenario.

1.2 Causal Factors of the ^{3}He Gas Crisis

Neutron detection is an integral part of our government's efforts to detect the illicit trafficking of radioactive materials across our borders. Following the events of September 11, 2001, President Bush and Congress acted swiftly to create the Department of Homeland Security (DHS) and to assign a cabinet-level position to its secretary. The objectives of this department were to: (1) prevent terrorist attacks within the United States; (2) reduce America's vulnerability to terrorism; and, (3) to minimize the damage and recover from attacks that do occur. Legislation to create the DHS was separately introduced by Senator Joe Lieberman (D-CT) in S. 1534 and Dick Armey (R-TX) in H.R. 5005 in the years 2001 and 2002 respectively. Once the separate bills were merged in committee and voted on by both houses of Congress, President Bush signed the measure into law on November 25, 2002 as the Homeland Security Act of 2002 [1].

Prior to the formal creation of the DHS, the primary focus of the country was on airline security and intelligence gathering associated with this effort. This mindset on airline security continued until March of 2002, when the terrorist Abu Zubaydah was captured in Pakistan. The interrogation of Mr. Zubaydah by the Federal Bureau of Investigation (FBI) and the Central Intelligence Agency (CIA) in May of that same year led to the discovery of a plot by Jose Padilla to deploy a radiological dispersal device (RDD) within the United States. Mr. Padilla was subsequently arrested that June [2].

Following the discovery of the RDD plot, the homeland security focus significantly shifted into the realm of nuclear terrorism and the need to be able to detect illicit trafficking of radioactive materials or nuclear devices, both domestically and internationally. Large-scale efforts such as the Second-Line of Defense and the Mega-Ports Initiative, which were borne out of the RDD threat, resulted in a significantly increased need for neutron detectors. The detectors were deployed in various locations such as airports, maritime ports, and border crossings inside portal monitors and/or cargo-screening systems. The lion share of the detection burden was borne by systems equipped with ^{3}He because of highly desirable properties that will be discussed in the next section. The dramatic increase in the use of this gas, combined with a limited supply, has led to a critical shortage that is adversely affecting not only the nuclear industry, but the medical, low-temperature physics, and the oil and gas industries as well. Gas that could be purchased for slightly more than $100 per liter in 2009 is now commanding a price in excess of $2100 per liter in 2013, if it can actually be procured at all [3].

Demand for the gas had been relatively stable at less than 25,000 liters annually for several decades prior to the formation of the DHS; however, once the department began instituting its radioactive material interdiction programs, demand for the gas soared and it is now estimated to be in the range of 75,000 – 85,000 liters per year [3 – 4]. The Department of Energy (DOE), who had been entrusted with managing the nation's supply of ^{3}He, failed to regulate the release of the gas at this critical juncture and, as a result, over two-thirds of the stockpile, which had been accumulated over a forty-year period,

disappeared in about six years. Once the extent of the shortage became apparent, the Congress removed control of the stockpile from the DOE and formed an interagency task force to regulate the dispensing of the gas. This task force suspended all distributions for 2009 and began a rationing program to release only 8,000 – 12,000 liters annually while the group actively seeks solutions to the crisis. By comparison, over 60,000 liters alone have been used for the 1300 portal monitoring systems that have been deployed for domestic border crossings, shipping ports, and airports during the short lifetime of the DHS [4].

In a separate effort, the Congressional Subcommittee on Investigations and Oversight also began holding hearings on the shortage of the ^{3}He gas in the autumn of 2009 to determine possible courses of action and the overall impacts of the gas shortage. This subcommittee has already made some short-term recommendations to the President of the United States and to the Secretary of the DHS, including the need to suspend some programs such as the Advanced Spectroscopic Portal (ASP) program [5 – 6]. This ASP program alone required over 200,000 liters of ^{3}He, but the main contractor for the program, Raytheon, was completely unaware of the ^{3}He supply problem until the congressional hearings began. Thus, the hearings demonstrated the lack of information DOE previously provided about the problem.

In April of 2010, the subcommittee held another set of hearings that were captured in the report entitled, *Caught by Surprise: Causes and Consequences of the Helium-3 Supply Crisis*. During this meeting, the subcommittee received a great deal of

testimony from two separate panels of experts regarding the large-scale effects on science and industry [7].

1.3 Neutron Detection and the Appeal of ^{3}He

Since neutrons are neutral particles, they are generally detected by nuclear reactions within the detector volume that create charged particles. The charge from these interactions can then be collected, analyzed, and quantified to provide the necessary information about the radiation field. In general, exothermic reactions are desired for slow neutron reactions, while endothermic reactions are used for faster neutrons. As a general rule, neutron energies below 0.5 eV, referred to as the cadmium-cutoff energy, are referred to as slow or thermal neutrons, while those with energies greater than this are considered fast neutrons [8]. The term thermal refers to neutron energies that are slow enough to be considered in thermal equilibrium with their surrounding materials.

There are several important factors that determine the usefulness of a material for neutron detection. First, the probability of the reaction occurring, or the cross section, should be as large as possible to ensure that a reasonable detector size can be realized. Second, excess energy created in the material due to a neutron interaction (Q-value) should be as large as possible to allow for easier discrimination between the neutrons and photons. The target material should also be available in high abundances from naturally-occurring isotopes or easily produced through artificial means such as enrichment. And finally, it is also advantageous if the material is inert and does not have any hazardous

properties such as toxicity or corrosiveness. It should be noted that no single material ever excels in all these factors, so a suitable choice must be made between the candidates for one that best meets the application-specific goals [9]. The remainder of this section will be spent discussing the useful properties of ^{3}He in order to demonstrate why this particular gas became such a popular choice for neutron monitoring applications.

The first important factor to be considered when choosing a neutron detector material is the probability or cross section for a particular reaction. The cross section for neutron interactions in all materials is heavily dependent on the incident neutron energy and, therefore, its velocity. This fact makes the magnitude of the cross section far more important for gaseous materials, such as ^{3}He because the low density of a gas nearly precludes the probability of neutron moderation within a detector volume. The mechanism of charge creation in ^{3}He results from the production of charged particles according to the following relation:

$$ {}^{3}_{2}He + {}^{1}_{0}n \rightarrow {}^{3}_{1}H + {}^{1}_{1}p + 0.764\ MeV\ . \qquad (1.1) $$

This reaction has a cross section of 5330 barns (10^{-24} cm^2) if induced by a thermal neutron and is exothermic [9].

The cross section for the ^{3}He reaction is the highest of any neutron-detection gas; however, the *Q*-value is lower by a factor of nearly four compared to another popular neutron detection gas, BF_3, which is highly enriched in ^{10}B (up to 96%). Although the

Q-value is relatively low as far as neutron detectors are concerned, this shortcoming is greatly offset by the low atomic number (*Z*) and density of the gas, which significantly reduces photon interactions within the active volume of the detector. By using a combination of activated charcoal to adsorb gas impurities in concert with the physical properties of the gas, sufficient photon discrimination can be achieved such that newer tubes can generally operate without noticeable interference up to about 2 Gy h^{-1} (200 rads h^{-1}) [10]. These reaction properties, therefore, allow for the application of a very simple photon discrimination technique based solely on pulse height as compared to more elaborate methods necessitated by the use of solid and liquid detectors.

The smaller magnitude of energy deposition resulting from photon interactions produces electrical pulses that are smaller in amplitude compared with *Q*, which allows most gas detectors, including ^{3}He, to employ a simple differential discriminator or single-channel analyzer (SCA) for photon discrimination. The SCA window is established during the equipment setup phase such that single photon pulses will fall beneath the lower-level discriminator and multiple (pileup) events result in signals that exceed the upper-level discriminator setting as depicted in Figure 1.1. An examination of this figure shows that the detector system has actually received five input pulses; however, three of the pulses do not meet the SCA energy window criteria and have, therefore, been rejected from consideration, resulting in a final tally of only two counts. In this depiction, the first event likely occurred as a result of two nearly simultaneous events that could not be resolved electronically (photon-photon or neutron-photon), while the two smaller pulses resulted from photon interactions.

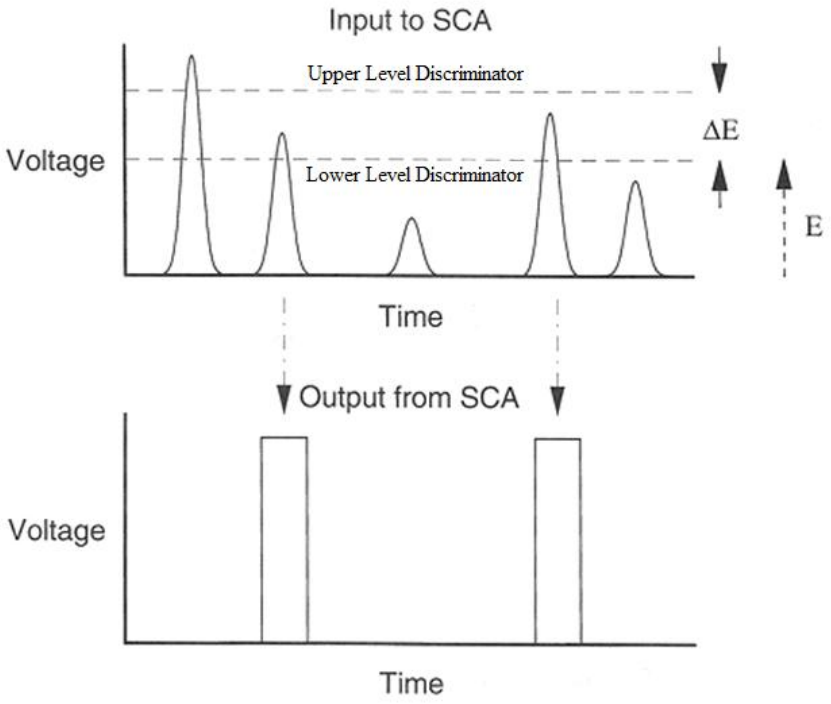

Fig. 1.1. Differential discriminator or single-channel analyzer (SCA) [9].

One final important consideration for a prospective detector material is its associated chemical properties. Here ^{3}He possesses a distinct advantage, because the gas is chemically inert and non-hazardous, which minimizes certain constraints for producers and users alike. First, the tube can be pressurized without any concern for personnel safety, which increases the neutron detection efficiency and reduces the *wall effect* in the gas. This effect occurs when the reaction products interact with the detector wall and are not fully stopped within the active volume.

1.4 The ^{3}He Economy

1.4.1 ^{3}He Supply

The single largest detractor from using ^{3}He as a detector medium is the severe lack of supply associated with the gas. Unlike other materials that are naturally abundant or that can be enriched or produced through artificial means such as neutron bombardment, or accelerators, the sole supply of ^{3}He is essentially from the decay of tritium with a 12.3 year half-life as shown by

$$ {}^{3}_{1}H \rightarrow {}^{3}_{2}He + {}^{0}_{-1}\beta + {}^{0}_{0}\bar{\nu} + 18.6\ keV\ , \tag{1.2} $$

because the natural abundance of ^{3}He in helium of 1.37 ppm makes any enrichment unattainable. The U.S. inventory, which at one time exceeded 200,000 liters due solely to gas reclamation from its nuclear weapons activities, has plunged to the neighborhood of 45,000 liters and is now being rationed to ensure a delivery of no more than 12,000 liters for 2010; moreover, the DOE currently estimates that it will have no more than 8,000 liters of gas available annually beyond 2010 [4].

Prior to 1988, the DOE produced ample quantities of tritium at its heavy-water reactor facilities of the Savannah River Site (SRS) in Aiken, South Carolina, which indirectly ensured an ample supply of ^{3}He; however, these facilities were shut down and decommissioned because of safety concerns, which eliminated the direct U.S. supply.

The lack of a direct ^{3}H-supply existed for over ten years, until the DOE contracted with the Tennessee Valley Authority (TVA) in 1999 to produce the gas at its Watts Bar and Sequoyah nuclear plants [11]. TVA is currently producing tritium using lithium aluminate ceramic absorber rods that are highly enriched with ^{6}Li (naturally-occurring lithium is only ~7.4% ^{6}Li). These rods are inserted into the reactor and removed during the 18-month refueling cycles. Tritium is produced in these rods mainly through the following reaction:

$$ {}_{3}^{6}Li \; + \; {}_{0}^{1}n \rightarrow {}_{1}^{3}H \; + \; {}_{2}^{4}He \; + 4.78 \, MeV \, . \qquad (1.3) $$

A similar reaction is also possible with ^{7}Li; however, the threshold energy for this reaction is about 4 MeV and the cross section reaches a relatively constant value of 360 *mb* at 6 MeV, making the reaction important only in the case of a thermonuclear weapon.

The irradiated rods are transferred to the Tritium Extraction Facility at the SRS where the tritium is recovered [12]. This process, although effective, provides only enough tritium to meet DOE's stockpile needs and does nothing to address the ^{3}He crisis for other applications and industries. TVA had originally offered a free and unlimited supply of tritium to the DOE if they would pay for the completion of the Browns Ferry Unit #4 nuclear plant which had been mothballed in the 1980s because of a lack of justification for the increased electrical supply; however, DOE refused the offer and decided to proceed with the current plan [13]. Had DOE chosen to accept the original TVA offer, it is possible that an adequate and cheap supply of ^{3}He would exist today;

however, attempting to increase the ^{3}He supply through similar arrangements with other commercial reactors will not ease the shortage due the 12.3 year half-life of tritium and current production costs. One estimate put the cost of the gas at approximately $20,000 per liter if produced in this manner [4]. This cost makes the commercial reactor approach cost-prohibitive for all but the defense-related applications.

Although the United States wasn't directly producing tritium following the shutdown of the SRS reactors, an indirect supply of ^{3}He continued to exist due to the dismantlement of nuclear weapons, the reconstituting of certain components within the stockpiled weapons, and the decay of the stockpiled tritium at the SRS. Since this supply alone more than accounted for the demand until around 2008, no one at the DOE took notice of the imminent crisis that was unfolding.

At the SRS, the ^{3}H/^{3}He gas mixture from weapon components is removed and passed through hydride beds to separate the two gases. The tritium must be periodically purified in this manner because approximately 5% is depleted per year due to radioactive decay, yielding the *impurity*, ^{3}He. Although ^{3}He is a valuable commodity for neutron detection, it must be periodically separated from the ^{3}H because it is a neutron absorber (poison) that will inhibit the proper function of a nuclear weapon. Until 2009, a large supply of ^{3}He (~15,000 – 25,000 liters per year) also existed from similar weapons activities in the Russian Federation; however, once the gas crisis became apparent, the Russians announced they were removing their ^{3}He supply from the worldwide market.

Although the Russians gave no reason for their recent decision, it was most likely done to ensure their own internal needs for the gas were met [4].

The only other alternative supplies of ^{3}He are from the reclamation of gas from unused detector tubes or by the removal from other tritium-containing volumes or from natural gas. It is very unclear how much gas might be retrieved from unused detectors because most people in the scientific community are aware of the gas shortage and they are not willing to part with their equipment. However, several possibilities exist to tap existing supplies of tritium that have been decaying for some time.

Heavy-water reactors such as the Canada Deuterium Uranium (CANDU) power reactors use deuterium oxide (D_2O) as a moderator. The extra neutron found in deuterium (^{2}H) makes for a substantially lower neutron absorption cross section compared with that of hydrogen (^{1}H) [14]. However, some absorption does occur in the deuterium and the reaction produces tritium according to:

$$ {}^{2}_{1}H \; + \; {}^{1}_{0}n \rightarrow {}^{3}_{1}H \; + \; {}^{0}_{0}\gamma + \; 2.23\; MeV. \qquad (1.4) $$

There are about fifteen of the CANDU reactors in operation throughout Canada, however, the units have been sold and constructed in a number of foreign countries such as Korea, Pakistan, China, India, and Romania.

The tritium produced in the Canadian reactors is routinely extracted and placed into titanium-tritide beds (Ti_3H_3). These beds have been inserted into containers that are capable of withstanding the pressures associated with the complete decay of the tritium to ^3He and they have been stored at the Ontario Power Generation facilities in Darlington, Ontario for about sixteen years. Based upon initial estimates, there is approximately 80,000 liters of ^3He available in these beds and it is likely that a continuous supply of approximately several thousand liters per year could be available if a suitable extraction facility were to be constructed [15]. Based upon the recommendation of the Chairman of the Subcommittee on Investigations and Oversight, the President of the United States began a dialogue with Canada in late 2009 to discuss the possibility of obtaining the Canadian ^3He [5]; however, since the extraction of the gas will require the construction of a facility costing at least $10 million, this option, while attractive, will not likely produce any meaningful short-term solution in the next few years. Similar deals could also be negotiated with the other owners of CANDU reactors, but these countries are far more difficult to work with bilaterally and it unlikely that any meaningful ^3He can be recovered from them.

Some recent discussions have also taken place regarding the separation of ^3He from natural gas. Natural gas contains about 7% helium and there are significant quantities that are stockpiled in various locations, such as the national reserve outside Amarillo, Texas. However, naturally-occurring helium contains only about 0.0134% (atom percent) abundance of ^3He, and a facility of the size that is being discussed would provide no more than 10,000 liters per year. Therefore, this option, as is the case with

reactor-based production, is a longer-term measure that might be possible, but will significantly increase the unit cost for ^{3}He and is also unlikely to satisfy the gas demand [16].

1.4.2 ^{3}He Demand

The current steady-state demand for ^{3}He is estimated to be between 65,000 – 75,000 liters per year; however, due to current DHS projects such as the Advanced Spectroscopic Portal monitoring program and other radiation portal monitoring projects, the demand in 2009 alone was more than 213,000 liters [7, 16]. The ASP program alone would have accounted for more than 200,000 liters of demand over the next few years [3 – 4]; however, the acting Director of the Domestic Nuclear Detection Office (DNDO) who has responsibility for the program, recently announced that ^{3}He would no longer be used in its portal monitoring systems [7]. This news was a complete shock to the prime contractor, Raytheon, who was not informed of this decision prior to the Director's announcement at the congressional hearings on the matter.

Approximately one-thousand additional ^{3}He detectors are also required for the Spallation Neutron Source at the Oak Ridge National Laboratory. The DOE has apparently already set aside 58,000 liters of ^{3}He for use in this facility; however, the facility needs another 15,000 liters prior to 2015 and DOE has also informed the other numerous neutron scattering facilities that are in various stages of development that they will have to fend for themselves [4].

The DOE and the Department of Defense (DOD) together are estimated to need between 13,200 – 22,400 liters for the next five years for additional projects [15]. The DOE's Second Line of Defense (SLD) and Mega-Ports Initiative programs had sufficient quantities of portal monitors to meet the installation needs in 2009; however, their installations beginning in 2010 have been delayed due to the gas shortage.

In summary, the current demand for ^{3}He gas is exceeding supply by at least a factor of about 6 even in the absence of the larger programs mentioned in this section and, had not these programs been halted, the disparity would likely be in the range of 20 – 30 times the supply. Even in light of conservation efforts, the gap between supply and demand will likely widen in the near future if industry visions of a *nuclear renaissance* come to fruition and as we see an increased use of mixed-oxide (MOX) fuel that is helping to reduce proliferation concerns worldwide. Since there is no imminent supply on the horizon that will offset ^{3}He demand, alternatives must clearly be sought. While it is certainly important to develop and test new alternative materials, this effort requires a substantial investment of time and capital. In the meantime, a more prudent first step should be undertaken to develop methods that will allow the adaptation of existing materials to fill the role currently being played by ^{3}He in neutron monitoring applications.

1.5 Topics of Discussion

In most dissertations, the chapter subsequent to the introduction is typically referred to as a literature search or the like. The goal of such a chapter is to evaluate and

report on the current state of affairs associated with issues that are tangential or directly related to the proposed research proposal. However, since the methodology developed in this research has never been attempted or applied toward neutron detector design, a chapter so titled would be inappropriate and vanishingly short. Therefore, Chapter 2 has been given a more appropriate title, Neutron Detection Protocols, and will provide coverage of the current state of affairs related to neutron detectors, an overview of current techniques and information related to the alternative ^{3}He materials used for this research. The latter part of Chapter 2 will also provide a statement of the research objectives.

Chapter 3 provides the reader with a detailed discussion of the radiation interactions that are applicable and important for neutron detection, including photons, since they must be accurately discriminated by the detection system in order to obtain an accurate evaluation of the neutron environment.

A detailed description of the computational methods that were used for modeling the radiation detectors and materials is given in Chapter 4. The description provides coverage of the deterministic and Monte Carlo methods and also discusses the basic aspects of the Parallel Environment Neutral Particle Transport (PENTRAN) and Monte Carlo N-Particle Version 5 (MCNP5) codes. These codes were used to apply the two unique transport methodologies for validating the computational detector design approach, thereby laying the foundation for the fidelity of the computationally-designed detector models.

Chapter 5 discusses the application of the techniques mentioned in Chapter 4 toward modeling the ^{3}He baseline detector and then developing computational models for testing. The initial models were used to validate the computational approach by directly comparing their results to physical laboratory measurements taken with ^{3}He and BF_3 tubes. The plug-in designs that follow were achieved through an iterative process of adjusting the material dimensions and gas pressures. Each design is described in detail and the information includes material listings, cross sections, and diagrams of the detector model. Several similar detectors have been tested and validated with a purely Monte Carlo approach in the past several years, but these studies were lacking the valuable insights that can be gained by an adjoint deterministic approach. Additionally, these prior tests did not have the multiple assurances of designs based on comparisons between measurements, deterministic adjoint, and forward deterministic and Monte Carlo methods [16 – 20].

Chapter 6 provides a description of the test facility, characteristics of the radioactive source that was used for the neutron measurements, and the nickel shield that was used for the source deployment. The chapter includes photographs and diagrams of the facility so the reader can gain an understanding of the conditions that existed during the detector measurements and that were folded into the computational models.

The actual neutron detector setup is described in Chapter 7 and includes the procedures that were followed to ensure the ^{3}He and BF_3 systems were setup and operating properly prior to taking any measurements. The chapter also details some of

the precautions that were taken to ensure the other experiments and equipment did not pose a problem for this experiment. The central issue associated with the use of the facility housing the container express (CONEX) was gamma and X-ray radiation coming from radioactive sources related to another detector system test and a computed tomography (CT) scanner used by medical physicists. The chapter concludes with information regarding the moderator materials and the detector setup on the CONEX.

The results associated with the operational setup of the ^{3}He and BF_3 neutron detector systems and neutron measurements are provided in Chapter 8. This chapter also describes the computational modeling results associated with the neutron measurement validation. The remainder of the material provides an in-depth analysis of each plug-in detector design, including adjoint profile, adjoint function, and reaction rate comparisons with the baseline ^{3}He model. The chapter concludes with an overall summary of the testing results.

The dissertation closes with a presentation of the overall conclusions from the research activities and recommendations for extending the effort toward evaluating existing systems, designing radiation detectors in general, and testing new neutron detector materials.

1.6 References

1. Borja, E., Brief documentary history of the Department of Homeland Security 2001 – 2008. Department of Homeland Security (DHS) Office, 2008.

2. Ripley, A., The Case of The Dirty Bomber. Time Magazine, New York, Vol. 159, No. 25, June 14, 2002.

3. Feder, T., U.S. Government Agencies Work to Minimize Damage Due to Helium-3 Shortfall. Physics Today, Vol. 62, Issue 10, pp. 21-23, October 2009.

4. Kramer, D., DOE Begins Rationing Helium-3. Physics Today, Vol. 63, Issue 6, pp. 22–25, June 2010.

5. Miller, B., Chairman of the Subcommittee on Investigations and Oversight, Letter to President Barack Obama. Washington, November 29, 2009.

6. Miller, B., Chairman of the Subcommittee on Investigations and Oversight, Letter to the Honorable Janet Napolitano. U.S. DHS, Washington, November 29, 2009.

7. U.S. House of Representatives Committee on Science and Technology, Subcommittee on Investigations and Oversight, Hearing Charter, Caught by Surprise: Causes and Consequences of the Helium-3 Supply Crisis. Washington, April 22, 2010.

8. Tsoulfanidis, N. and Landsberger, S., Measurement and Detection of Radiation – 3rd Ed. CRC Press, Boca Raton, FL, 2011.

9. Knoll, G., Radiation Detection and Measurement, 4th Ed. John Wiley & Sons, Inc., New York, 2010.

10. National Council on Radiation Protection and Measurements (NCRP). Structural Shielding Design and Evaluation for Megavoltage X- and Gamma-Ray Radiotherapy Facilities, NCRP Report No. 151. NCRP, Bethesda, MD, 2005.

11. Production of Tritium for the United States Department of Energy, Rhea and Hamilton Counties, TN., Federal Register, Vol. 65, No. 88, Friday, May 5, 2000.

12. Savannah River Tritium Enterprise Fact Sheet, Savannah River Nuclear Solutions, 11PA00218, February, 2013.

13. Kent, C., Personal communication with the former Radiological Controls Manager at the Tennessee Valley Authority's Sequoyah nuclear power plant.

14. Garland, W., How and Why Is CANDU Designed The Way It Is? Rev. 3. McMaster University, Hamilton, Ontario, CANTEACH Initiative, February, 2003.

15. Kouzes, R., The ^{3}He Supply Problem. Pacific Northwest National Laboratory (PNNL), PNNL Technical Report – 18388. PNNL, Richland, WA, April 2009.

16. Lintereur, A., Siciliano, Kouzes, R., Boron-10 Lined Proportional Counter Model Validation, Pacific Northwest National Laboratory (PNNL), PNNL Technical Report – 21501. PNNL, Richland, WA, June 2012.

17. Peerani, P., Tomanin, A., Pozzi, S., Dolan, J., Miller, E., Flaska, M., Battaglieri, M., De Vita, R., Ficini, L., Ottonello, G., Ricco, G., Dermody, G., and Giles, C., Testing on Novel Neutron Detectors as Alternatives to ^{3}He for Security Applications, Nuclear Instruments and Methods in Physics Research A, 696 (2012), pp. 110 – 120.

18. Kouzes, R., Ely, J., Erikson, L., Kernan, W., Lintereur, A., Siciliano, E., Stromswold, D., and Woodring, M., Alternative Neutron Detection Testing Summary, Pacific Northwest National Laboratory (PNNL), PNNL Technical Report – 19311. PNNL, Richland, WA, April 2010.

19. Woodring, M., Ely, J., Kouzes, R., and Stromswold, D., Boron-Lined Multichamber and Conventional Proportional Counter Tests, Pacific Northwest National Laboratory (PNNL), PNNL Technical Report – 19725. PNNL, Richland, WA, September 2010.

20. Woodring, M., Ely, J., Kouzes, R., and Stromswold, D., Boron-Lined Multitube Neutron Proportional Counter Test, Pacific Northwest National Laboratory (PNNL), PNNL Technical Report – 19726. PNNL, Richland, WA, September 2010.

CHAPTER 2
NEUTRON DETECTION PROTOCOLS

2.1 Current Protocols

The human body is not equipped to sense the presence of radiation, since no pain or other sensation occurs during an interaction. Large, and even lethal doses of radiation, could be received without a person becoming aware of the situation until weeks later. Since neutrons possess no electrical charge, their presence along a given path in a detector is analogous to the case of biological dose. Unless the particles produce some form of ionizing radiation that can be subsequently collected by the detection system electronics, their passage will occur unnoticed.

Radiation detectors are typically categorized according to their detection mechanism (gas, solid, etc.), output signal (current or pulse), and application; however, regardless of these characterizations, most detectors are based upon ionization and the collection or charge within a sensitive volume (notable exceptions are devices such fission, radio-chromic, and track detectors). For the purposes of this study, the focus will be placed on gas and solid detectors used in the pulse mode of operation for detecting neutrons. Systems of this type are vital for scanning personnel, transportation platforms (vehicles, planes, etc.), and material for use in non-proliferation applications and programs.

Since neutrons, as their name implies, are uncharged particles, their total energy must somehow be converted to produce the ionizing event we require for the production of a detector signal. Depending on the energy of the neutrons of interest, the conversion process can include scatter (recoil), absorption, or both. The absorption conversion process can also include radiative capture or fission; however, for the purposes of this study, discussion will be confined to captures resulting in the emission of heavy charged-particles. Unlike the case for reactor applications, Knoll, Tsoulfanidis, and other major authors group their discussions of neutron detectors into two broad categories, slow and fast, based upon the incident neutron energy of interest [1 – 2] and this convention will also be used in this paper.

The fast category is conventionally typified by neutron energies of > 0.5 eV, while the slow category encompasses all other energy states. The conventional value of 0.5 eV was most likely chosen because ^{109}Cd, which is a very popular neutron absorber for nuclear applications, has a very large (21,000 barns) neutron capture cross section for thermal neutrons and will absorb essentially all neutrons below energies of 0.4 eV [2]. Until recently, all neutron detectors using a slow neutron detection mechanism had housings made of specially-coated cadmium to ensure that the response was solely due to neutrons that were moderated within the detector itself. Regardless of the neutron energy, several important factors must be considered in the choice of a detector material.

First, since all detector systems are generally size-constrained, one of the primary challenges is to choose a material such that the interaction probability and conversion

mechanism is maximized for the neutron energy of interest. For example, if the aim is to field a neutron detector on the basis of a scattering reaction (fast neutrons) to reduce the response time, a material that preferentially undergoes a recoil reaction such as (n, p) should be selected over a slower-responding detector that requires an absorption reaction such as (n, α).

The choice of the reaction type must also include a consideration of whether energy information is to be obtained from measurements. Detectors employing the (n, p) or other recoil interactions typically measure only the initial interaction event, unless the detector volume is greatly increased or a capture-gating system is utilized. However, since the detection takes place without the prior thermalization of the neutrons, information regarding the incident neutron energy can be preserved. Detectors utilizing the (n, α) or other absorption interactions can benefit from the increased probability of interaction at the lower neutron energies; however, the large degree of moderation that is necessary will usually eliminate all knowledge of the incident neutron energy. For these reasons, most neutron detectors operate simply as neutron counters and not as dose rate instruments.

Next, the material should have acceptable material properties and be relatively abundant in nature or capable of being economically produced by artificial means and, finally, the material should be relatively insensitive to other radiation such as photons or it must exhibit a sufficiently large Q-value in the interaction with the neutron to ensure the resulting electronic pulse can be adequately discriminated from those created by

photon interactions. Once the appropriate material has been identified, it must also be matched with the appropriate amount and type of moderator to ensure the peripheral conditions are established such that the detector efficiency is tuned or maximized. For example, a system based on scatter reactions will generally employ far less moderator between the radiation source and the detector than will one based on slow detection methods. However, regardless of the interaction mechanism, each detector system must also have a specific amount of moderation behind the detector to ensure neutrons can be reflected into the detector through what is known as the *albedo effect*. The optimal moderator thickness or amount can be determined using radiation transport codes or by simply conducting a series of counting experiments where the detection rate is evaluated as a function of the moderator thickness.

One of the greatest advantages ^{3}He possesses over competing materials is its ability to function well in both of the broad neutron energy realms (slow and fast). It has a large absorption cross section of 5316 barns at thermal neutron energies (0.025 eV), which is significantly greater than other popular slow detector materials such as ^{6}Li (940 barns) and ^{10}B (3843 barns) [1 – 2]. And for fast neutron applications, the relatively small mass difference between ^{3}He atoms and neutrons ensures good energy transfer in elastic scatters, while the reasonable (*n, p*) cross section produces a full-energy peak at reasonable efficiencies. Furthermore, since the gas is non-toxic and doesn't experience degradation in its performance as a proportional gas at higher pressures, its absolute pressure can be increased significantly above 1.0 atm (typically 4 – 10 atm), which will vastly improve the detection efficiency.

2.1.1. Slow Methods

As far as homeland security applications go, the only important interaction between a low-energy neutron and the detector is absorption, leading to some type of heavy charged-particle as shown below:

$$targt\ nucleus + incident\ neutron \rightarrow \begin{cases} proton, or \\ alpha\ particle, or \\ fission\ fragment\ and \\ recoil\ nucleus. \end{cases}$$

One advantage of this particular reaction type is the assurance that the reaction will be exothermic, with *Q*-values in the typically ranging between 0.764 – several MeV, depending on the target. And since the kinetic energy of the incident neutron in this case is negligible when compared to the *Q*-value of the reaction, the kinetic energy of the reaction products is determined solely by *Q*.

The advantage to such an interaction as this is that if a detector could be fabricated such that the kinetic energy of the reaction products is fully stopped within the sensitive volume, the response function for the detector would appear as a relatively discrete pulse corresponding to this cumulative energy as shown in Figure 2.1 and this would result and this would greatly simplify our ability to perform neutron spectroscopy. However, the reality is that neutrons rarely deposit their full energy in a single detector because of energy losses within the detector walls (gases and solids), escape of particles due to a large range, or optical thickness, in the material (gases) and various electronics issues (solids and gases). As a result, the detector response function associated with slow

methods will have multiple features resulting from the various mechanisms at play, and its form will have the appearance of Figure 2.1, but with the superimposition of certain broad-energy continuums as shown in Figure 2.2. The regions of Figure 2.2 that are marked as *Recoil Li* and *alpha* result from the instance in which the companion reaction product collided with the detector wall thus excluding its kinetic energy from the charge collection process. This phenomenon is called a *wall effect* and can have serious consequences for gas-filled detectors. In all cases, the only instance in which a full-energy peak is produced is when all the reaction product kinetic energy is collected within the gas volume.

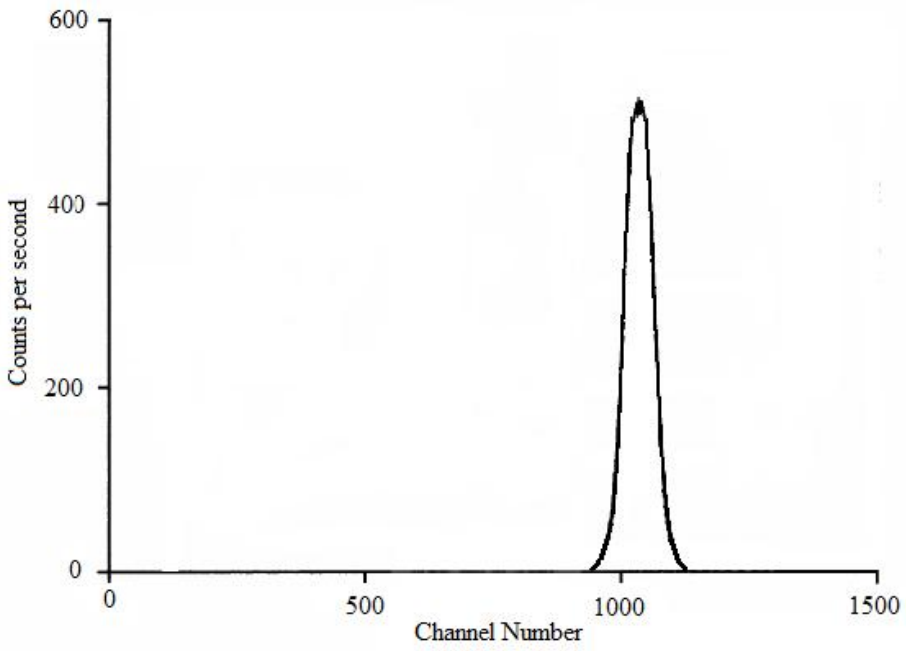

Fig. 2.1. Example of ideal neutron-induced detector pulses [adapted from [2]].

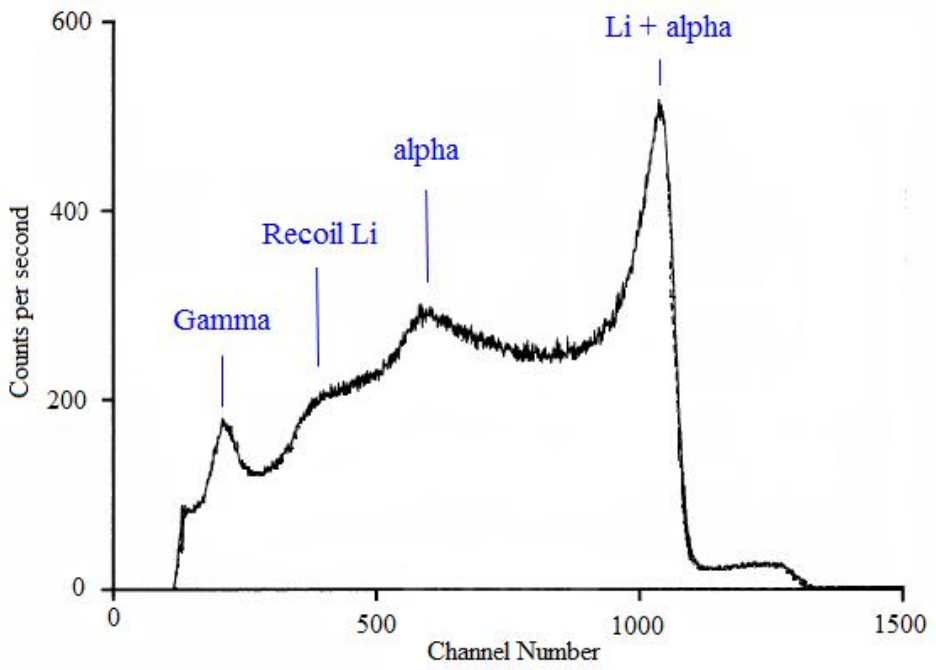

Fig. 2.2. Example of realistic neutron-induced pulses in BF_3 [adapted from [2]].

There are a number of materials that exhibit some of the important neutron detection characteristics mentioned in Section 2.1; however, the vast majority of detectors for homeland security type applications, both past and present, use the following reactions as the neutron kinetic energy conversion mechanism: ^{10}B (n, α) ^{7}Li; ^{6}Li (n, α) ^{3}H; or, ^{3}He (n, p) ^{3}H. There have been some advances in the use of materials such as the odd-numbered gadolinium (Gd) isotopes, which have capture cross sections rivaling the greatest of any material, and fission counters; however, for the purposes of this research, the focus will be placed solely on detectors employing reactions in ^{10}B or ^{3}He because they are readily available and ^{10}B can also easily be incorporated into a gas ($^{10}BF_3$) or a plastic scintillator.

2.1.2 Fast Methods

The methods mentioned in Section 2.1.1 can also be applied to fast neutrons in theory; however, since many neutrons are scattered out of the detector before slowing down to thermal (slow) energies and the absorption probability decreases rapidly with increasing neutron energy, the slow detection methods must either be significantly altered or completely replaced with a new method to produce acceptable detection results for fast neutrons. Since neutron absorption is less probable at higher energies, the most important reaction for fast neutrons is elastic scattering in the detector medium resulting in the production of a recoil proton and recoil nucleus that will give rise to an electrical pulse.

2.2 Applied Protocols and Materials

2.2.1 Research Motivation and Methodology

It has already been established that ^{3}He is an excellent and effective choice for neutron detection. However, the features that made this particular gas so attractive also led to its ultimate demise in detector applications due to the absence of a dependable and sustained supply. Given the security concerns facing our nation and that of the international community, there has never been a greater demand for radiation monitoring systems. Therefore, it is imperative that appropriate materials and methods be developed now to ensure our sustained mission success in this key area.

There have already been a number of efforts to develop such replacement technologies for ^{3}He [3 – 6]; however, as has been previously mentioned, all of these research efforts are solely targeted toward determining which detectors can be inserted into existing systems to deliver an equivalent sensitivity to a ^{3}He tube(s). These cases generally involve the results of monitoring of a single radioactive material that is typically ^{252}Cf [3 – 18]. While this approach will certainly ensure that a particular detector system meets the established sensitivity criteria (e.g. $c\ min^{-1}\ ng^{-1}$ of ^{252}Cf at 2 m) [16, 18] listed in the technical specifications for most, if not all, detector contracts, it will certainly not be able to demonstrate that the proposed replacement has an equivalent spectral response to that of ^{3}He across a wide range of neutron energies. In other words, while a replacement detector might demonstrate an equivalent sensitivity for neutron emissions from ^{252}Cf within a given geometry (e.g. an existing portal monitor), the detector spectral response could deviate significantly from ^{3}He for other neutron sources or exposure geometries.

The approach discussed in the paragraph above is adequate for the simple detection scenarios in which the only concern is achieving baseline detection sensitivity for a particular radionuclide; however, a simple approach will not do for more complex non-proliferation and safeguards detector applications. In these instances, such as fissile material quantification assessments for ^{239}Pu and ^{235}U, the detectors have almost exclusively been ^{3}He tubes of various designs and the neutron spectral response of any would-be replacement cannot be ignored and must demonstrate equivalency in both function (spectral shape) and magnitude (efficiency) [19]. Ignoring this requirement in a

misguided effort to achieve overall system sensitivity will produce serious and potentially dire consequences for material control and accountability (MCA) programs and other global non-proliferation efforts.

Possibly the most important international effort that is hampered by the lack of adequate ^{3}He supplies stems from the 2004 United Nations Security Council Resolution 1540 [20]. This particular resolution addresses the risk of non-state actors acquiring, developing, and trafficking in or using nuclear, chemical, or biological weapons and their means of delivery. The document specifically imposes obligations on member states to prevent these proliferation activities by refraining from providing any form of support to non-state actors attempting to engage in these types of efforts. The explicit portions of the resolution that are directly affected by the lack of ^{3}He supplies are those associated with maintaining effective border controls, detection capabilities used to prevent and combat the trafficking of radiological and nuclear materials, and measures to account for and secure items during production, use, storage, and transport.

With these motivations in mind, this research effort will be directed toward investigating and developing a new method for evaluating candidate ^{3}He replacement detectors and identifying detector designs that can serve as direct *plug-in equivalents* for a standard 1-inch diameter ^{3}He tube pressurized to 4 atmospheres (atm) or 3040 torr. The performance of the chosen candidates will be compared against the spectral response and efficiency achieved by the ^{3}He baseline detector monitoring neutron emissions from an engineered weapons-grade plutonium (WGPu) source described in a later chapter.

Additional measurements will also be conducted using a geometrically-equivalent BF_3 tube (dimensions and active volume). Although this tube will obviously not prove adequate as a plug-in replacement for the baseline case, it is intended to provide a second data point for an objective assessment of the computational models.

Once the initial ^3He and BF_3 measurements have been gathered, the detector responses will be calculated using 3-D adjoint and forward deterministic transport and forward Monte Carlo simulations. The deterministic calculations will be performed using the discrete-ordinates code PENTRAN[1] (Parallel Enhanced Neutral Particle Transport) and the code MCNP5[2] (Monte Carlo N-Particle Version 5), both of which will be described in detail in a later chapter. A comparison of the baseline measurements and computational results will first be used to demonstrate that a firmly established fidelity exists between the actual measurements and computational models. Once fidelity has been established between the two methods, the computational approach can then be confidently applied for evaluations of the suitability of all prospective alternative material and designs.

At this point, the design model of each candidate detector will be evaluated and adapted to mimic the baseline response as closely as possible. The suitability of a particular candidate material and design will be established by the achievement of a ^3He-equivalent neutron spectral response and overall efficiency within an acceptable

[1] HSW Technologies LLC, 2501 Porter Street NW #220, Washington, DC 20008, USA – Tel. 352-871-1099. www.hswtech.com.
[2] Los Alamos National Laboratory, P.O. Box 1663, Los Alamos, NM 87545, USA – Tel. 505-667-5061. www.lanl.gov.

uncertainty. The overall objective of the research is to yield at least one detector design (material and geometry) that delivers an equivalent performance to ^{3}He across a broad spectrum of neutron energies and that can, therefore, be used as a plug-in equivalent of the baseline design.

2.2.2 ^{3}He and Proposed Alternatives

The chosen alternative materials consisted entirely of commercially available off-the-shelf products such as BF_3 gas and ^{10}B-lined tubes because they are well-established technologies, they are readily available to the radiation detection community at a reasonable price, and they don't require expensive electronic components and/or elaborate neutron and gamma discrimination schemes (such as PVT and liquid scintillators). Materials employing the ^{6}Li(n, α)^{3}H reaction such as *LiI* were also rejected from consideration because, although the *Q*-value of 4.78 MeV is more than double that of the ^{10}B reaction and nearly seven times greater than that of the ^{3}He reaction, the solid crystalline form of this solid is far more sensitive to photon radiation, making the task of neutron and photon discrimination nearly impossible [1 – 2, 10]. Newer applications using ^{6}Li such as glass fiber detectors are becoming more in vogue, but they remain in the minority compared with the readily-available materials selected for this study.

The suitability of each of the chosen candidates will be discussed in the next section. This information will focus on the desirable properties of the specific materials as have been previously discussed and any specific photon discrimination methods that may be necessary will also be addressed. Photon discrimination for all the gas designs

can easily be handled using a single-channel analyzer (SCA) or window technique previously discussed in Chapter 1. Photon discrimination in poly-vinyl toluene (PVT) must be conducted using some form of pulse-shape discrimination (PSD), which is beyond the scope of this research effort.

2.2.2.1 ^{3}He Gas

The flexibility of ^{3}He gas, combined with its other desirable properties caused ^{3}He to become the overwhelming choice for neutron monitoring over the past two decades. However, its desirability, combined with its reasonable price and limited supply resulted in the current crisis that has necessitated the search for a suitable replacement. These advantages and disadvantages were discussed in depth in Sections 1.2 and 1.3 and will not be repeated here. However, one main disadvantage in the use of ^{3}He remains and must be addressed.

The low-Z of ^{3}He ensures a large degree of energy transfer for incoming neutrons; however, it also creates a charge collection problem because of its low stopping power for ions and electrons. A low stopping power means that the range and path length of the charged reaction products is significantly greater, producing enhanced wall effects as seen in Figure 2.2. The low stopping power also works to decrease the magnitude of the full-energy peak associated with neutron absorptions because fewer counting events are attributed to the associated energy channel.

The wall effect combined with a lower *Q*-value (Eq. 1.1) also means that there is less separation between neutron and photon events, making photon discrimination potentially more difficult. The situation is very slightly mitigated by the fact that ^{3}He has a very low probability for photon interaction; however, this mitigation is minimal because most photon interactions cause interference indirectly through interactions within the detector walls, thereby injecting recoil electrons into the detector gas. Consequently, care must be taken in the construction of ^{3}He tubes to minimize these effects. Therefore, these particular tubes are generally constructed from low-*Z* materials such as aluminum.

The most obvious technique to reduce wall effects is to simply increase the size of the detector. The increased size reduces the effects by: 1) increasing the probability that a neutron interaction occurs at a greater distance from the wall; and, 2) increasing the probability that the reaction product kinetic energy will be fully absorbed in the gas because a greater path length must be traversed to reach the wall itself. Another method involves increasing the gas pressure to elevate the stopping power for the reaction products. The increased stopping power will reduce the range of the reaction products, inhibiting their ability to interact with the wall. One final approach toward reducing the wall effect is to introduce a small amount of a heavier gas such as CO_2 to increase the stopping power. Since all detectors have size constraints, as has been previously mentioned, the most popular method for reducing the wall effects has typically been to increase the gas pressure in the detector.

2.2.2.2 BF_3 Gas

BF_3 is a popular neutron detection gas that is operated as a proportional counter and used in many different nuclear engineering applications. Unlike ^{3}He, the gas is not the product of radioactive decay and thus it is readily available from numerous manufacturers in a pressure range of 0.5 to several atm [2] and for very reasonable prices. The stopping power of BF_3 is much greater than that of ^{3}He, which helps to minimize wall effects even in the absence of a higher gas pressure. The boron in the BF_3 is enriched with ^{10}B, so the gas acts as both the proportional gas and the neutron detection mechanism according to:

$$ {}^{10}_{5}B \; + \; {}^{1}_{0}n \rightarrow \begin{cases} {}^{7}_{3}Li \; + \; {}^{4}_{2}He \; + 2.792\ MeV\ (ground\ state) \\ {}^{7}_{3}Li \; + \; {}^{4}_{2}He \; + 2.310\ MeV\ (excited\ state) \end{cases} . \qquad (2.1) $$

The ^{10}B content can easily be enhanced upwards of 96%, which improves the detection efficiency by a factor of five compared to natural boron. For thermal neutrons (0.025 eV), the ground-state reaction occurs only about 6% of the time, while the ^{7}Li is left in an excited state the remaining 94% of the time, followed by a the emission of a 0.482 MeV gamma ray. The *Q*-value energy of the reaction is shared by the recoil ^{7}Li nuclue and the alpha particle, resulting in alpha particle energy of approximately 1.47 MeV. The alpha produces a large number of ionizations in the gas near the interaction site which produces the electrical pulse necessary for counting neutron interactions.

Since the *Q*-value of the reaction in Eq. 2.1 is much larger than that of ^{3}He, the photon discrimination techniques discussed in Section 1.2 can be more easily applied to BF_3. A comparison of the interaction probabilities for thermal neutrons and 1 MeV photons in ^{3}He and BF_3 is provided in Table 2.1. The information clearly demonstrates that both gases are quite capable of photon discrimination on the basis of probability alone, which is important in homeland security and nonproliferation applications. Judging solely by the neutron/gamma ratio, one could come to the conclusion that ^{3}He has superior photon discrimination properties compared with BF_3; however, the aforementioned *Q*-value disparity between the two gases actually results in far superior qualities associated with BF_3.

Table 2.1. Comparison of neutron and photon interaction probabilities in ^{3}He and BF_3.

Thermal Detector	Probability		
	Thermal Neutrons	1 MeV Photons	Neutron/Gamma Ratio
^{3}He (2.5 cm diameter, 4 atm)	0.72	1.00E-04	7200
BF_3 (5.0 cm diameter, 1 atm)	0.29	6.00E-04	483

Although photon discrimination in BF_3 is easier than with ^{3}He, the use of this gas does present some challenges. First, the (n, α) cross section for BF_3 is significantly smaller than the (n, p) cross section of ^{3}He for all neutron energies of interest as shown in Figure 2.3 and, for thermal neutrons, it is only 72.3% that of ^{3}He, which means that the detection efficiency will suffer somewhat. This disadvantage can be overcome; however,

it will always necessitate the use of additional, denser, or larger volume detectors. Of course, if a single larger cylindrical detector of radius r is used, this choice will require, in

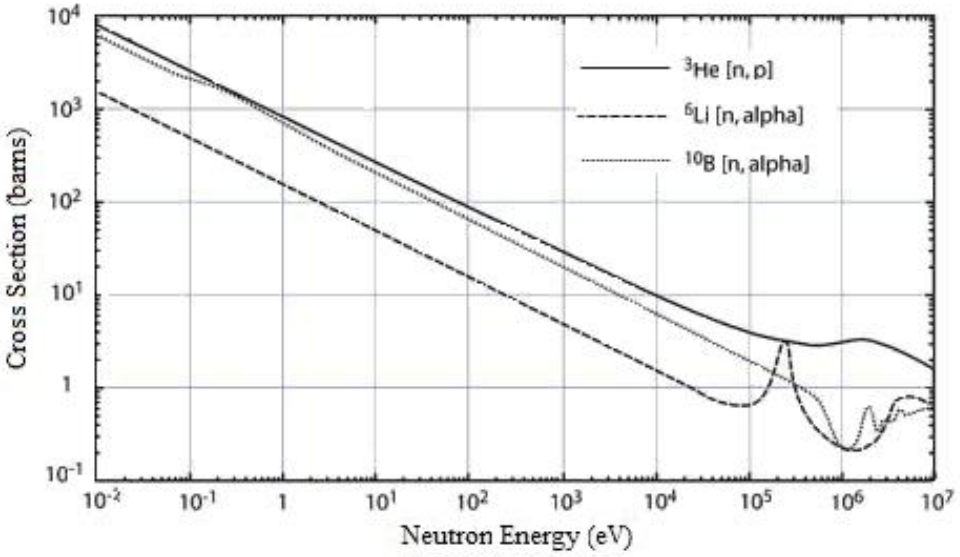

Fig. 2.3. Neutron reaction cross sections for energies of interest [adapted from [2]].

the absence of anode wire changes, a higher voltage to achieve electric field strength adequate for charge collection according to the following relation:

$$\xi(r) = \frac{V}{r \ln\left[\frac{b}{a}\right]}. \tag{2.2}$$

In Eq. 2.2, V is the applied voltage between the cathode and anode, a is the anode wire radius, and b is the cathode inner radius in consistent units of length. Care must be taken to balance the parameters of the larger detector to ensure a reasonable voltage can be achieved; otherwise, the detector will not be viable.

The need to increase the tube size in order to achieve similar sensitivities to ^3He highlights another disadvantage of BF_3 pertaining to its toxic properties [3, 5, 14, 16]. As a result of its toxicity, the shipment of BF_3 tubes is carefully controlled by the United States [19 – 20] and the International Air Transport Association (IATA). The hazardous materials transportation law in the U.S. seemed to be rather confusing; so much so, that LND, Inc., who is a major manufacturer of gas detector tubes in the U.S., recently requested a series of clarifications from the U. S. Department of Transportation (DOT). The government's clarifications on the U.S. law basically allow BF_3 tubes containing less than 1 gram of BF_3 to be shipped as non-hazardous materials, provided that the detector is not pressurized to more than 1 atm [21]. As a point of reference, non-toxic gases such as ^3He can be shipped as non-hazardous materials (due to pressure) if they are pressurized to less than 2.7 atm [22 – 23]. It is important to remember that the regulations don't prohibit the shipment of BF_3 tubes within the U.S. or abroad; however, the additional controls that are necessary in order to exceed the pressure and mass limits significantly increases the cost of such detectors.

One final disadvantage that must be considered with BF_3 detectors is the more frequent replacement frequency compared with inert gases such as ^3He. BF_3 is toxic in the sense that it is poisonous to humans, but it will also react violently with certain other compounds such as water to create hydrofluoric acid (HF) that is highly corrosive to the inner portions of the detector. The corrosion rate is also unfortunately enhanced by the detection process within BF_3 because the absorption of a neutron liberates three fluorine atoms. Although the detector tubes are filled in an inert environment, some moisture

inevitably may enter the volume with the gas fill and through leakage around electrical connections, leading to the formation of HF. These chemical phenomena inevitably lead to a reduced lifetime for these particular detectors when compared with inert-filled detectors.

2.2.2.3 ^{10}B-Lined Proportional Tubes

In gas-filled radiation detectors, the detection mechanism is generally always the gas itself; however, in this particular arrangement, the ^{10}B lining is the sensitive element and it is coupled to a suitable proportional gas that receives the charged-particles produced in the energy conversion process. An advantage of using an alternate gas to BF_3 is the elimination of its associated toxicity and corrosion problems; however, in the energy conversion process one of the reaction products will always be lost to the system because they are emitted in opposite directions. This process results in an unusual-looking response function that will appear as steps associated with the alpha particle energy (1.47 MeV) and the lithium recoil nucleus (0.84 MeV) as shown in Figure 2.4.

Since 1.47 MeV is the largest amount of energy that can be transferred to the proportional gas in this design, ^{10}B-lined detector will have photon discrimination properties that are inferior to BF_3 detectors; however, the lithium recoil nucleus energy remains greater than the *Q*-value of ^{3}He and the chosen proportional gas will likely be less dense than, so the end result is that this particular scheme should exhibit a discrimination capacity approaching that of BF_3 and that can be handled in the same

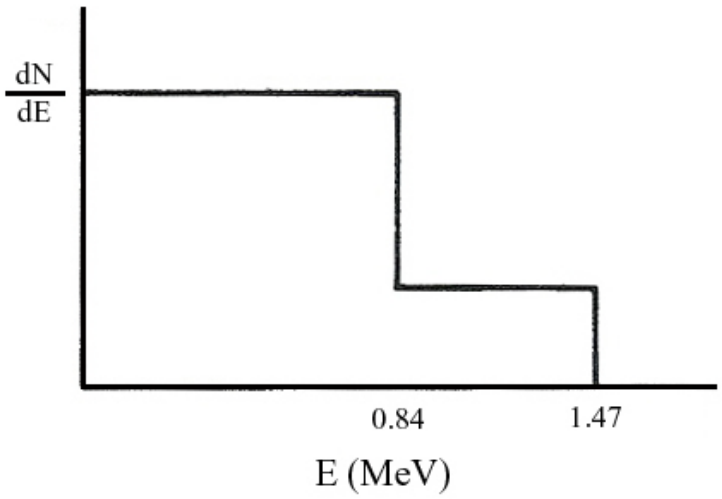

Fig. 2.4. Pulse height spectra in a ^{10}B-lined tube showing the wall effects produced by the alpha particle and ^{7}Li recoil nucleus [adapted from [2]].

manner. One other design limitation associated with this type of detector is the range of the reaction products of the ^{10}B reaction and, in particular, the range of the alpha particle.

For most radiation detectors, the adage "more is better" generally applies and increasing the active volume coincides with increased detection efficiency. However for the case of ^{10}B-lined tubes, the adage applies only to a certain extent because of the small penetrability of the reaction products. Since the alpha particle is emitted with the greatest energy of the boron reaction products, it will determine the maximum thickness of the boron layer. In gas detectors, the range of the alpha particle can be several centimeters; however, in solid ^{10}B, the maximum range of the 1.47 MeV alpha particle is only about 1 mg cm^{-2} . This corresponds to thickness of ~0.4 cm for boron at 2.3 g cm^{-3} density. Therefore, the detection efficiency of this specific design will increase only as long as the boron coating doesn't exceed ~0.4 cm and it is useless to add any additional boron

beyond this point. While the addition of more boron will indeed result in the occurrence of more reactions, the result will be a dead layer beyond ~0.4 cm where the reaction products are incapable of reaching the proportional gas and, therefore, excluded from being detected. Furthermore, the addition of extra boron will actually begin to degrade the detection efficiency because of increased neutron attenuation in the wall.

2.2.2.4 ^{10}B-Loaded Poly-Vinyl Toluene (PVT)

PVT is one of a number of organic plastic solutions that are commonly referred to as plastic scintillators. These materials have many similarities to liquid scintillators and they are readily able to detect neutrons through proton recoil interactions above 0.5 MeV in their base condition. The response of these scintillators to more moderated neutron energies can be greatly enhanced by the addition of neutron absorbers such as the ^{10}B incorporated into the previously-mentioned detectors. The detection mechanism associated with ^{10}B-loaded PVT is identical to that described for the previous ^{10}B-based detectors; however, the signal is initially transmitted via light emission from the scintillator and must later converted to an electrical pulse via a photomultiplier tube, photodiode, or another such device.

PVT is a low-*Z* material and, as such, has virtually no photo-electric cross section; however, the material is very sensitive to photon radiation. The solid nature of PVT assures that its density exceeds that of the gases by approximately three orders of magnitude or more. This property ensures a greater degree of neutron interaction;

however, the greater density guarantees that secondary electrons generated via photon interactions will likely be captured within the solid. The collection of these secondary electrons, coupled with the greater degree of sensitivity for plastics relative to electrons, produces a large Compton continuum that must be discriminated from the neutron signal via some form of PSD.

2.3 References

1. Tsoulfanidis, N. and Landsberger, S., Measurement and Detection of Radiation – 3rd Ed. CRC Press, Boca Raton, FL, 2011.

2. Knoll, G., Radiation Detection and Measurement, 4th Ed. John Wiley & Sons, Inc., New York, 2010.

3. Kouzes, R., The ^{3}He Supply Problem. Pacific Northwest National Laboratory (PNNL), PNNL Technical Report – 18388. PNNL, Richland, WA, April 2009.

4. Jones, R., FYI: The AIP bulletin of Science policy news - Science Committee Hearing Spotlights Shortage in Critical Isotope. American Institute of Physics, Number 53, May 12, 2010.

5. Kouzes, R., Ely, J., Lintereur, A., Siciliano, E., and Woodring, M., BF_3 Neutron Detector Tests, PNNL Technical Report – 19050. PNNL, Richland, WA, 2009.

6. Kouzes, R., Wright, M., Crawford, R., and Robertson, J., The ^{3}He Supply Problem and Possible Alternative Technologies. PNNL Technical Report – 18550, Pacific Northwest National Laboratory, Richland, WA, 2009.

7. Athanasiades, A., Shehad, N., Martin, C., Sun, L., and Lacy, J., Straw Detector for High Rate, High Resolution Neutron Imaging. Proceedings of the IEEE Nuclear Science Symposium Conference, San Juan, Puerto Rico, Record N14-124: 623–627.

8. Lacy, J., Boron-Coated Straw Neutron Detector, United States Patent No. US7002159 B2. Assignee Proportional Technologies, Inc. Houston, TX, USA.

9. Katagiri, M., and Matsubayashi. M., Radiation or Neutron Detector Using Fiber Optics. United States Patent No. US7214943 B2. Assignee Japan Atomic Energy Research, Kashiwa Japan.

10. Lintereur, A., Kouzes, R., Ely, J., Erikson, L., and Siciliano, E., Boron-Lined Neutron Detector Measurements, PNNL Technical Report – 18938. PNNL, Richland, WA, 2009.

11. Ely, J., Erikson, L., Kouzes, R., Lintereur, A., and Siciliano, E., Lithium-Loaded Glass Fiber Neutron Detector Tests, PNNL Technical Report – 18988. PNNL, Richland, WA, 2009.

12. Lintereur, A., Ely, J., Kouzes, R., Erikson, L., and Stromswold. D., Coated-Fiber Neutron Detector Test, PNNL Technical Report – 18919, PNNL, Richland, WA, 2009.

13. Kouzes, R., Erikson, L., and Kernan, W., Full Scale Coated-Fiber Neutron Detector Measurements, PNNL Technical Report – 19264. PNNL, Richland, WA, 2010.

14. Kouzes, R., Ely, J., Erikson, L., Kernan, W., Lintereur, A., Siciliano, E., Stephens, D., Stromswold, D., Van Ginhoven, R., and Woodring, M., Neutron Detector Alternatives to ^{3}He for National Security Applications. Nuclear Instruments and Methods in Physics Research A 623, 1035-1045 (2010).

15. Van Ginhoven, R., Kouzes, R., and Stephens, D., Alternative Neutron Detector Technologies for Homeland Security, PNNL Technical Report – 18471, PNNL, Richland, WA, 2009.

16. Kouzes, R., Ely, J., Erikson, L., Kernan, W., Lintereur, A., Siciliano, E., Stromswold, D., and Woodring, M., Alternative Neutron Detection Testing Summary, PNNL Technical Report – 19311, PNNL, Richland, WA, 2010.

17. Kouzes, R. and Ely, J., Status Summary of ^{3}He and Neutron Detection Alternatives for Homeland Security, PNNL Technical Report – 19360, PNNL, Richland, WA, 2010.

18. Stromswold, D., Ely, J., Kouzes, R., and Schweppe, J., Specifications for Radiation Portal Monitor Systems, Rev. 6.7, PNNL Technical Report – 14716, PNNL, Richland, Washington (2003).

19. Office of Nuclear Regulatory Research, Passive Nondestructive Assay of Nuclear Materials (PANDA). U. S. Nuclear Regulatory Commission, NUREG/CR-5550, Washington, March, 1991.

20. United Nations, Security Council Resolution 1540, United Nations, New York, April, 2004.

21. U.S. Government, Title 49 CFR Parts 171-180, Special Provision 238. Federal Hazardous Materials Transportation Law, Code of Federal Regulations, U.S. Department of Labor, 2012.

22. Pohanish, R., Sittig's Handbook of Toxic and Hazardous Chemicals and Carcinogens, 6th ed., Elsevier, Inc., Oxford, 2012.

23. U.S. Government, Title 49 CFR Parts 171-180. Federal Hazardous Materials Transportation Law, Code of Federal Regulations, U.S. Department of Labor, 2012.

CHAPTER 3
RADIATION INTERACTIONS IN MATERIALS

It is important to discuss the mechanisms by which radiation interacts with materials prior to discussing the actual detectors and electronics that comprise an effective neutron detection system. While it would seem logical that this chapter should focus solely on the radiation physics associated with neutrons, this approach would be short-sighted and lacking. In order to fully understand how to effectively employ a neutron detector, one must not only understand the mechanisms that produce the electrical pulses being sought, but also those events that serve to hamper our efforts of reliably evaluating the neutron environment, such as photon interactions.

Discussions of photon radiation within the confines of neutron detector research may seem misplaced to some; however, photons are always present to a certain degree in all neutron environments, whether due to neutron scattering in surrounding materials or as a result of the process that gave rise to the neutrons themselves (e.g. neutrons arising from (α, n) reactions in PuBe). Although neutron detector materials are chosen such that the probability of neutron interaction is maximized, photons will inevitably collide with these materials to a certain degree and produce electrical pulses that must be discriminated from neutron-related events. While it is true that any single photon interaction will not produce an electrical pulse magnitude comparable to that of a neutron interaction, numerous photon events at a certain rate will create coincidence or summed

pulses that can easily be confused with neutron interactions. Therefore, all neutron detector research must include some treatment of photon interference or *cross talk*.

3.1 Photons

The term photon is used as a general categorization for electromagnetic radiation, which under various conditions can display a duality of both waves and particles. Photons have an energy $h\upsilon$ (or hc/λ) and momentum $h\upsilon/c$ (or h/λ), where h is Planck's constant (6.626×10^{-34} *J s*), c is the speed of light (3.00×10^{8} m s^{-1}), υ is the frequency of the radiation and λ is the wavelength ($\lambda = \upsilon/c$). The exact classification of photons is generally specified according to the process of origination without regard to energy. For example, gamma rays originate from nuclear transitions; *X*-rays originate from the acceleration of charged particles (Bremsstrahlung) or from transitions within the electron orbitals (characteristic), and annihilation radiation results from the combination of an electron and positron. Photons always travel at the speed of light, possess wave and particle properties, and have no physical mass, so they are highly penetrating and require dense materials for shielding purposes.

Since photons are uncharged, they do not experience the Coulomb forces that cause continuous energy dissipation in charged particles. Rather, photons travel with a specified probability of interaction per unit distance of having some type of interaction. This probability is referred to as the linear attenuation coefficient and is typically denoted by the symbol μ.

The principle modes by which photons interact with matter are Compton scattering, the photoelectric effect, and pair production, with the first two modes being dominant in all cases except when the incident photon energy greatly exceeds 1.022 MeV. Although it is not extremely probable event within radiation detectors, pair production is briefly discussed for completeness.

3.1.1 Photoelectric Effect

The photoelectric effect is a mechanism by which the entire incident photon energy is absorbed by an atom. During the absorption process, the photon disappears and the atom ejects an orbital electron with a kinetic energy (T) equal to

$$T = h\upsilon - \varphi\,, \tag{3.1}$$

Where $h\upsilon$ is the incident photon energy and φ is the work function or the amount of energy necessary to free the electron from its state within one of the atomic orbitals (K, L, etc.). The binding of the electron and interaction with the atom are necessary conditions for the photoelectric effect to occur because total energy and momentum cannot be conserved in the interaction between a photon and a free electron. The ejected electron is referred to as a photoelectron and will dissipate its energy in the surrounding materials via charged-particle interactions that lead to the rise of an electrical pulse in the detector.

The photoelectric effect is dominant at low photon energies of several tens to a few hundreds of keV, depending on the atomic number of the target, and the interaction cross section (τ) is roughly described by the relation

$$\tau \propto \frac{Z^4}{(h\upsilon)^3}, \tag{3.2}$$

where Z is the atomic number [1]. For non-monatomic detector materials such as BF_3 or PVT, Z is replaced by the effective atomic number (Z_{eff})

$$Z_{eff} = \sum_{i=1}^{N} w_i Z_i , \tag{3.3}$$

with the weight percentage (w_i) determined by

$$w_i = \frac{M_i}{M_m}, \tag{3.4}$$

where M_i is the atomic mass of the i^{th} element and M_m is the molecular mass of the detector material.

Although the numerator of Eq. 3.2 is of a higher power than the denominator, the cross section decreases with increasing photon energy. Figure 3.1 demonstrates the large

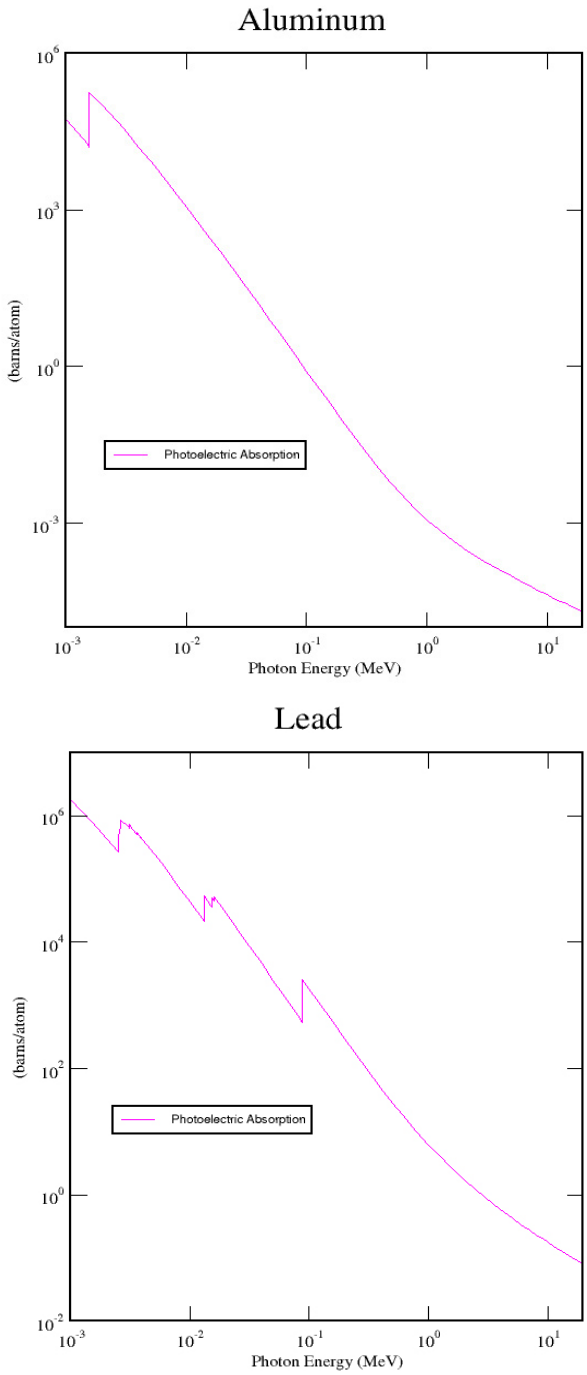

Fig. 3.1. Photoelectric cross sections in aluminum (Z=13) and lead (Z=82) [2].

dependence on atomic number and also shows the cross section becoming insignificant above the 1.022 MeV threshold where pair production begins to take place [1]. The

figure also illustrates that the photoelectric cross section for lead is substantially greater than that of aluminum for all photon energies and the disparity rises with increasing energy, ranging from about 19 at 1 keV to over 5300 at 1.02 MeV, after which both cross sections begin to significantly decline [3 – 5]. The strong dependence on atomic number is the primary reason that lead and other dense materials such as lead excel as low to mid-energy photon shields.

The complete absorption of the photon is highly desirable in solid-state systems because the electrical pulse resulting from the interaction is nearly equivalent to the incident photon's energy (within a few eV) and, in the absence of substantial scatter, can be used to identify the radiation source. However, an inspection of Eq. 3.2 demonstrates that, for neutron detectors using gas or PVT, this cross section will be extremely small due to a small effective atomic number. Therefore, the photoelectric effect is a small contributor to photon interference within neutron detection systems.

3.1.2 Compton Scattering

A Compton scattering event occurs when a photon interacts with an atomic electron and is scattered at a reduced energy and at an angle from its prior trajectory. The energy which is transferred to the electron serves both to overcome the work function discussed in Section 3.1.1 and to accelerate the ejected electron. Compton scattering is the principle means of energy dissipation for photon energies between several hundred keV to several MeV, depending on the atomic number of the absorbing material [1].

Following the interaction, the scattered photon can either escape the detector or undergo further Compton scatters that produce streaming losses or eventual photoelectric absorptions. The Compton scattering cross section (σ) increases rapidly in conjunction with the declining photoelectric cross section and can be described by the relation [1]

$$\sigma \propto \frac{Z}{h\upsilon} . \tag{3.5}$$

Compton scattering is the dominant mechanism of photon interactions between energies of a few hundred keV to about 5 MeV. The cross section for aluminum and lead is shown in Figure 3.2 to demonstrate that, unlike the photoelectric effect, there is a much smaller dependence on the atomic number as Eq. 3.5 indicates. In fact, the ratio of the lead to aluminum cross section varies only between 1.93 at 1 keV to a value of about 6.30 above 14 MeV [2].

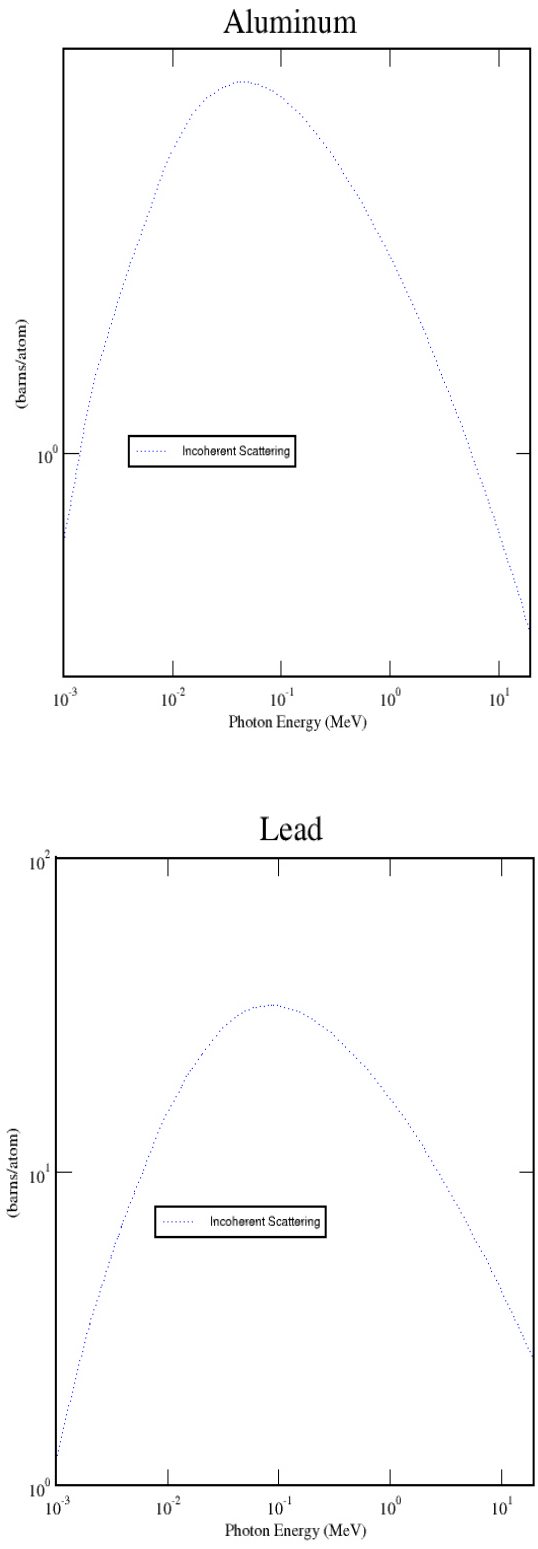

Fig. 3.2. Compton scattering cross sections in aluminum (Z=13) and lead (Z=82) [2].

The Compton scattering process is depicted in Figure 3.3 where an incoming photon of energy (E) is scattered through an angle (θ_s), producing a Compton electron of kinetic energy (T) which is scattered through angle (θ_c), with all angles measured relative to the original direction of the incident photon. Although the speed of the photon does not change in an interaction, the

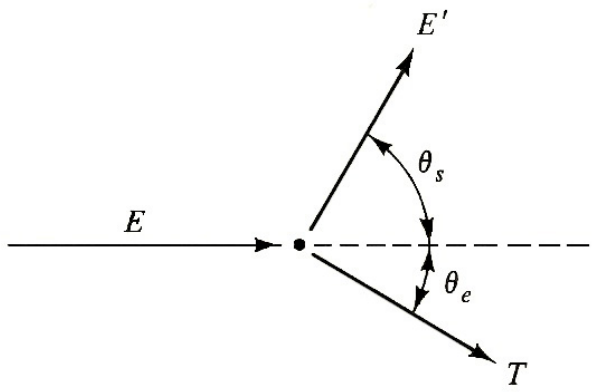

Fig. 3.3. Diagram illustrating a Compton scattering event.

wavelength of the photon must of necessity increase to account for the energy loss. The change in wavelength can be determined by evaluating the conservation of energy and momentum of the reactants to arrive at the relation

$$\Delta\lambda = \lambda' - \lambda = \frac{h}{m_o c}(1 - \cos\theta_s)\,, \tag{3.6}$$

where m_o is the rest mass of an electron (see derivation in Appendix A). It is interesting to note that the wavelength change is dependent solely on the angle through which the photon is scattered and is completely independent of the incident photon energy.

The energy of the scattered photon ($h\upsilon'$) can also be expressed as a function of the scattering angle by performing algebraic manipulations on Eq. 3.6. Begin by using an alternate relation for the photon wavelengths according to

$$\Delta\lambda = \lambda' - \lambda = \left(\frac{c}{\upsilon'} - \frac{c}{\upsilon}\right) = c\left(\frac{1}{\upsilon'} - \frac{1}{\upsilon}\right). \tag{3.7}$$

Next, set Eqs. 3.6 and 3.7 equal to one another and divide both sides by *hc* to arrive at

$$\left(\frac{1}{h\upsilon'} - \frac{1}{h\upsilon}\right) = \frac{1}{m_o c^2}(1 - \cos\theta_s). \tag{3.8}$$

Since we want to solve for $h\upsilon'$, we move the $h\upsilon$ term to the right side of Eq. 3.8 and manipulate the terms to reach a common denominator

$$\frac{1}{h\upsilon'} = \frac{m_o c^2 + h\upsilon(1 - \cos\theta)}{h\upsilon m_o c^2}. \tag{3.9}$$

We then take the inverse of both sides of this result to arrive at

$$h\upsilon' = \frac{h\upsilon m_o c^2}{m_o c^2 + h\upsilon(1-\cos\theta)}. \tag{3.10}$$

The desired relationship is finally achieved by multiplying the right-side of Eq. 3.10 by a magnitude of one associated with the electron rest mass energy

$$h\upsilon' = \left[\frac{h\upsilon m_o c^2}{m_o c^2 + h\upsilon(1-\cos\theta)}\right] \cdot \left[\frac{\frac{1}{m_o c^2}}{\frac{1}{m_o c^2}}\right], \tag{3.11}$$

to arrive at the desired relation shown in Eq. 3.12

$$h\upsilon' = \frac{h\upsilon}{1 + \frac{h\upsilon}{m_o c^2}(1-\cos\theta)}. \tag{3.12}$$

This equation specifies the scattered photon energy in terms of the incident energy and scattering angle. The scattered photon continues at the speed of light in its new direction until it either escapes the detector or undergoes further Compton scatterings or a photoelectric absorption. Each interaction results in the creation of some amount of charged-particle kinetic energy that is imparted to the detector and that can possibly be mistaken for a neutron interaction because of pulse summing or coincidence, which is referred to as pulse pileup or cross talk.

The kinetic energy imparted to the recoil electron is given simply by

$$T = h\upsilon - h\upsilon' , \tag{3.13}$$

and by substituting the $h\upsilon'$ term from Eq. 3.12, the following relation can be obtained

$$T = \frac{h\upsilon\,(1 - \cos\theta_s)}{\frac{m_o c^2}{h\upsilon} + (1 - \cos\theta_s)} . \tag{3.14}$$

By inspection of Eq. 3.12, it can be seen that $h\upsilon'$ will be at a minimum when θ_s is 180º or π radians, because the cosine of this angle is equal to -1. In this case, Eq. 3.14 dictates that T will reach a maximum value of

$$T_{max} = \frac{2h\upsilon}{\frac{m_o c^2}{h\upsilon} + 2} . \tag{3.15}$$

From a neutron detection standpoint, large values of T represent a worst-case scenario because this energy can potentially interfere with the determination of the true neutron interaction rate. The bounding values of T in this case can be determined by considering the limiting cases for $h\upsilon$ and T in Eqs. 3.12 and 3.15. The limiting minimum value attained by $h\upsilon'$ is

$$h\upsilon'_{min} = \lim_{h\upsilon \to \infty} \left[\frac{h\upsilon}{1 + \frac{h\upsilon}{m_o c^2}(1 - \cos\theta_s)} \right] \approx \frac{m_o c^2}{2} \approx 0.256\ MeV\ . \qquad (3.16)$$

By substitution of these results into Eq. 3.13, the worst-case T (θ_s equal to 180° or π radians and T > 255.5 keV) can be bounded as

$$0 \leq T \leq (h\upsilon - 0.256\ MeV), \qquad (3.17)$$

where the lower limit represents the case of Thomson scatter. From Figure 3.2, it can be seen that the Compton scattering cross section exhibits a severe decrease with increasing photon energy at higher photon energies making this interaction less probable. At these higher energies, pair production, which will be discussed in the next section, becomes the dominant interaction.

Of the various photon interaction mechanisms, Compton scattering is considered the most undesirable for neutron detection applications. The first reason for the undesirability is because the cross sections for the other interactions is vanishingly small for the low-Z materials typically found in neutron detectors, rendering them as insignificant. However, the chief reason this particular interaction is unwanted is because the coincidence pulses that can arise from multiple recoil electrons can produce signals that are indistinguishable from those arising via neutron interactions. If the detector volume is sufficiently small compared with the path length of the recoil electrons in the

media, such as is the case for gas-filled detectors, then the magnitude of the Compton pulse will be minimal. However, for PVT and other solid or liquid detectors, a sufficient volume of material is typically present to allow incident photons to undergo additional scatterings and possibly even a final photoelectric event. In this case, simple neutron/photon discrimination techniques are ineffective and more elaborate electronics and pulse-shape discrimination (PSD) methods must be employed to effectively separate the photon and neutron events.

3.1.3 Pair Production

At higher photon energies, an interaction can occur between the photon and the intense electric field surrounding the nucleus of an atom causing the photon to disappear and be replaced by an electron-positron pair that is emitted in opposite directions, equally sharing the energy of the incident photon. Since an electron and positron both possess rest mass energies of 511 keV or 0.511 MeV apiece, it is apparent that in order to conserve energy and mass, the threshold photon energy is $2m_oc^2$ or 1.022 MeV as shown in Figure 3.4.

After the electron-positron pair is created, the particles will exhaust its kinetic energy through charged particle interactions in the detector which can potentially produce interference in a neutron detector. Meanwhile, the positron will eventually slow and combine with an electron, causing annihilation photons to be emitted in opposite directions. Since annihilation photons are the result of a mass-to-energy conversion, they

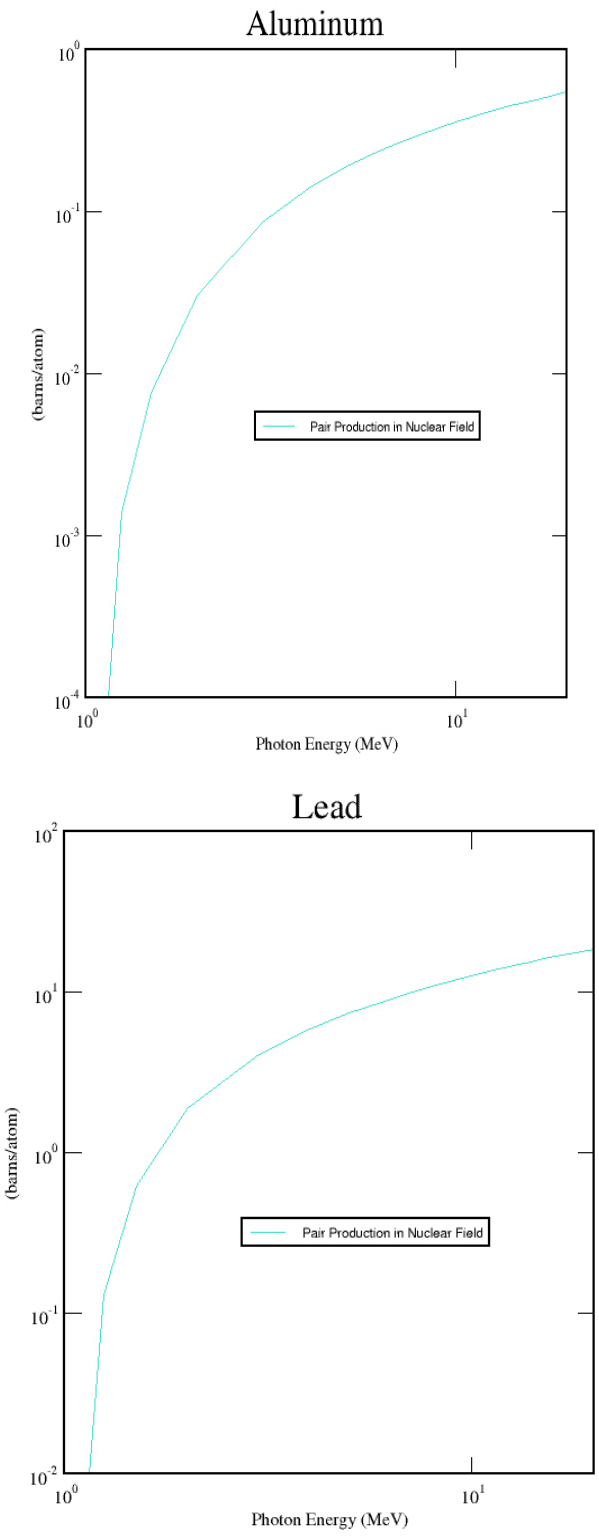

Fig. 3.4. Pair production cross sections in aluminum (Z=13) and lead (Z=82) [2].

will each have a minimum energy of 511 keV, depending on the kinetic energy of the positron at the time of annihilation. Once produced, these photons can subsequently cause Compton scatter or photoelectric effects within the detector that creates additional interference.

The pair production cross section (κ) is calculated using one of three screening models depending on the magnitude of

$$\alpha \propto \frac{137}{Z^{0.5}}\,, \tag{3.18}$$

where α is equal to $h\upsilon/m_o c^2$ [1]. Regardless of the screening model used, the following approximation holds true for all cases [1]:

$$\kappa \propto Z^2\,. \tag{3.19}$$

The effect of the atomic number is by far most pronounced in the region of 1.022 – 5 MeV as seen in Figure 3.4, after which the behavior appears asymptotic in nature. The ratio of the pair production cross sections for lead and aluminum varies between 92.7 at 1.25 Mev to a slowly decreasing value of 34.1 at 20 MeV [2].

As with Compton scattering, the amount of the pair production energy deposited in the detector depends on the size and composition of the detector. However, given that

most neutron detectors have a relatively low-Z or Z_{eff} as discussed in the previous two sections and they are operated in areas where the photon energies rarely exceed the 1.022 MeV pair production threshold, this interaction mechanism will normally be considered negligible. Notwithstanding the previous statement, pair production must be adequately evaluated in situations where neutron detectors are operated in the vicinity of active interrogation systems because photon beams with energies greater than 5 MeV are generally employed in these devices. Detectors utilizing the conversion reactions of ^{155}Gd or ^{157}Gd isotopes also bear further evaluation because neutron absorption in these isotopes will produce in excess of 8 MeV of total energy, with some of the individual photon energies exceeding 6 MeV.

3.1.4 Total Interaction Cross Section for Photons

The total linear photon interaction probability is the sum of probabilities for all reactions of importance. For the energy region of interest associated with this research, only the reactions discussed in this section are applicable and thus, the total interaction probability, μ, is simply

$$\mu = \tau + \sigma + \kappa . \tag{3.20}$$

The μ for lead is displayed Figure 3.5, while Figure 3.6 demonstrates the regions where the various photon interaction processes are dominant.

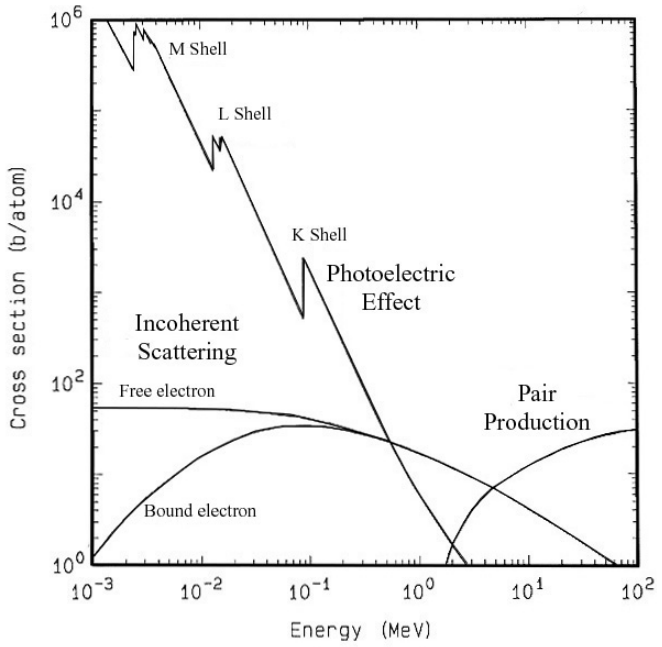

Fig. 3.5. Interaction cross sections for photons in lead [adapted from [1]].

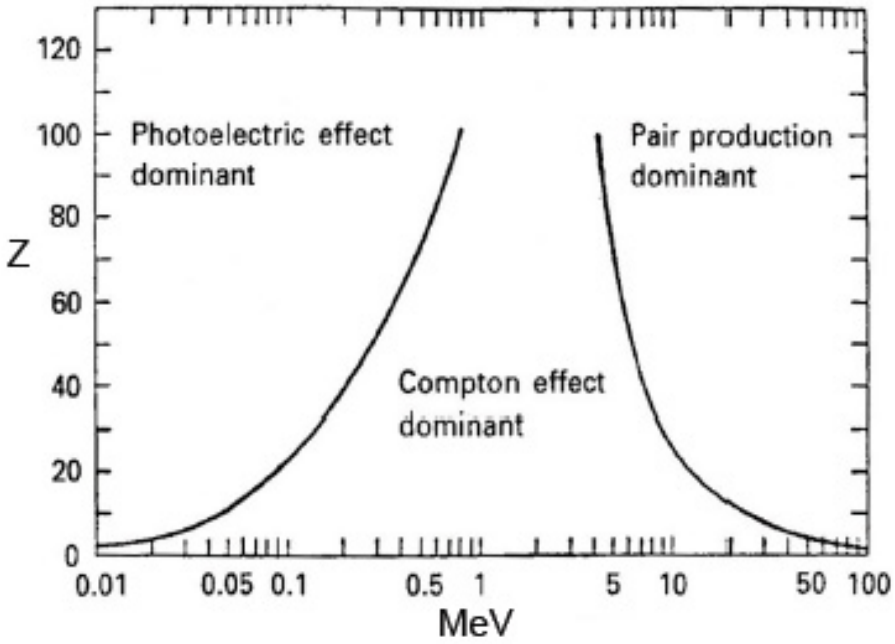

Fig. 3.6. Dominance of photon interaction cross sections for materials of atomic number Z as a function of energy [adapted from [1]].

3.1.5 Photon Interaction Probability

Since photons, unlike charged particles, are absorbed or scattered in singular events, the uncollided flux of a collimated beam will exhibit a truly exponential decrease per unit thickness of material as the photons pass through. The interaction process follows first-order kinetics and can be described by the differential relation

$$d\phi = -\mu\phi\, dx\,, \tag{3.21}$$

where ϕ is the flux, *dx* is a differential thickness of shielding material and the negative sign implies the function is decreasing with the absorber thickness. The solution to this differential equation is

$$\phi(x) = \phi_0 e^{-\mu x}\,, \tag{3.22}$$

where ϕ_0 is the initial flux. The ratio of the positional flux and the initial flux tells us the percentage of photons that do not interact within a thickness (*x*)

$$\frac{\phi(x)}{\phi_0} = e^{-\mu x}\,. \tag{3.23}$$

Therefore, the probability of having an interaction occur within a thickness *x* can be simply calculated by

$$p(x) = 1 - e^{-\mu x}\,. \tag{3.24}$$

It is also useful to calculate a quantity known as the mean-free path which describes the mean distance travelled by a photon between interactions. This quantity can be calculated by applying the laws of probability toward the scenario in which a photon travels a certain distance without interaction and then experiences an interaction within a differential thickness (*dx*). The probability that a photon will not interact in distance (*x*) is given by Eq. 3.23, while the probability of interaction per unit path length from Section 3.1.4 is just μ; therefore, the probability of having an interaction in *dx* is μ *dx*. By combining these probabilities, we can calculate the mean free path by integrating the equation for calculating averages by parts to obtain

$$\overline{x} = \int_0^\infty x\, p(x) dx = \mu \int_0^\infty x\, e^{-\mu x} dx = \frac{1}{\mu}. \tag{3.25}$$

By considering this equation in the context of Figure 3.5, it can be seen that $\overline{x}$ will vary with energy and composition of the material being traversed. This quantity is extremely important for statistically-based Monte Carlo transport codes because it can be used to determine, on average, when photon interactions will occur.

3.2 Neutrons

Neutrons are neutral particles with a comparable size and mass to protons and are constituents of the nucleus of all atomic nuclei with the exception of ^{1}H. However, neutrons, unlike protons, do not have to overcome the repulsive Coulomb barrier before entering the nucleus. Since this particle is also electrically neutral, it is highly penetrating and only interacts by means of the strong nuclear force which is within a range on the order of 10^{-15} m. Regardless of the production mechanism (fission, D-T reactions, etc.) neutrons have a fast energy at birth and, with the exception of cosmic ray interactions in our atmosphere, there are no natural neutron emitters in our environment. Therefore, in non-proliferation applications, all neutron signals must be investigated.

Neutrons are generally categorized according to energy regions (e.g. thermal, epithermal, or fast) when consideration is given to issues of transport or fuel analysis. Although these terms are brandished about with regularity by scientists and engineers alike, no exact convention exists and one must take care to quantify the terms. For example, fast neutrons are generally considered to be those with kinetic energies exceeding 0.1 MeV and thermal neutrons are considered to be those below 0.1 eV; however, numerous contrary examples exist in textbooks and journal articles because authors sometimes choose to vary the energy thresholds for a particular purpose.

Because neutrons are large, neutral particles traveling within a velocity distribution, the manner in which they interact with their surrounding matter is vastly

different from that of photons. Whereas photons of energies less than the pair production threshold interact primarily with the atomic electrons, neutrons interact almost exclusively with the atomic nucleus and have a vanishingly small cross section for electron interactions. Photons also travel at the speed of light independent of their material interaction history; however, a neutron's velocity is generally only a small fraction of the speed of light and has a highly variable magnitude that is directly dependent on the history. For these reasons, neutron cross sections vary widely as a function of the neutron velocity (kinetic energy), element, and even isotopes of the same element, while photon cross sections vary within only a few percent between neighboring elements of the periodic chart and across a wide-energy range for a given element.

Although the interaction possibilities for neutrons greatly outnumber those of photons, the most important considerations for detector applications will be the probability of the interaction and the amount of energy that is transferred to the detector media. Despite the large number of interaction possibilities, neutron interactions can be broadly grouped into the categories of scatter, absorption, or radiative capture. Which mechanism is paramount depends on the detector material being used for the neutron energy conversion.

3.2.1 Scatter

High-energy neutrons generally lose energy by colliding with the surrounding atoms in the medium they are traversing. These collisions can either be elastic or

inelastic in nature, depending on the target material and the incident neutron energy. Elastic collisions are those in which both kinetic energy and momentum are conserved in the interaction. This type of interaction, unlike the inelastic variety, leaves the nucleus of the atom unchanged in isotopic composition and internal energy. Apart from elastic scatter, all other neutron interactions are inelastic in nature.

Both of scatter mechanisms can be efficient at moderating or slowing the neutron velocity; however, their effectiveness is dictated by the target material and the incident neutron energy (velocity). Because of physical relationships that will be described later in this section, it will become evident that elastic scatter will be the most important reaction for ^{3}He, while this same mechanism will be essentially irrelevant for BF_3 where the capture reaction will be predominant.

3.2.1.1 Inelastic Scatter

Inelastic collisions are best described by a compound nucleus model in which an incident neutron is considered to be captured and then reemitted at a lower energy. In this case, the momentum and energy exchange that led to the excited state is dissipated through the emission of a gamma photon. The cross section for inelastic scatter exhibits a threshold phenomenon where the probability of the interaction is zero until an incident neutron has enough energy to stimulate the nucleus into its first excited state. The reaction isn't possible for hydrogen, since the nucleus consists of a single proton, but in general, the threshold increases to a maximum of about 6 MeV for ^{16}O and then gradually

decreases with atomic number to only about 44 keV for ^{238}U [2]. The magnitude of the cross section is generally on the order of only a barn or less for neutron energies around 0.1 MeV, but it increases with increasing neutron energies and approaches a maximum corresponding to the geometric cross section of the target nucleus.

Photons emitted in inelastic collisions tend to be of a higher energy, so they will typically escape the detector; however, interactions within the detector will obviously serve to obscure the true neutron counting rate unless discriminated. Because the detector materials used in this research contain materials with low atomic numbers, the incident neutrons energies will typically be much less than the inelastic scatter threshold and the reaction will be negligible compared with elastic scattering.

3.2.1.2 Elastic Scatter

An elastic scatter is generally described as a billiard-ball type interaction in which kinetic energy and momentum of the products are conserved. Since elastic scatter with neutrons is much more prevalent in low-*Z* materials such as ^{3}He, the energy transfer will generally produce recoil protons that deliver the detection signal. In this reaction, the neutron transfers some of its kinetic energy to the target nucleus and is directed into some new solid angle at a lower energy. Since the neutron experiences both a change in direction and energy in this transition, the probability for the interaction is typically characterized through what is known as a double differential cross section which characterizes the probability of the neutron scattering from one energy (E) into a final

energy (dE') about E and from an initial direction (Ω) into a final direction ($d\Omega'$) about Ω [6]

$$\sigma_s(E \to E', \Omega \to \Omega')dE'\,d\Omega'. \tag{3.26}$$

The double differential scattering cross section can be reduced to a differential scattering cross section or to the scattering cross section by integrating over energy or angle as shown below:

$$\sigma_s(E \to E') = \int_{4\pi} \sigma_s(E \to E', \Omega \to \Omega')\, d\Omega' \,, \tag{3.27}$$

$$\sigma_s(\Omega \to \Omega') = \int_0^{\infty} \sigma_s(E \to E', \Omega \to \Omega')\, dE' \,, \tag{3.28}$$

or,

$$\sigma_s(E) = \int_{4\pi} \int_0^{\infty} \sigma_s(E \to E', \Omega \to \Omega')dE'\,d\Omega'. \tag{3.29}$$

The calculation of differential scattering cross sections is generally an enormous task; however, in situations where elastic scattering from stationary nuclei occurs, the laws of conservation of energy and momentum can be used to calculate these quantities in a relatively straightforward manner. In the case of radiation detection applications, the differential energy scattering cross section (Eq. 3.27) is usually the quantity of interest, because this term quantifies the magnitude of the energy deposition and, therefore, the

pulse amplitude. The first step in the process is to specify the probability that a scatter reaction changes the incident neutron energy (E) to a value between E' and $E' + dE'$ according to

$$\sigma_s(E \rightarrow E')dE' \ . \tag{3.30}$$

The next step is to decompose Eq. 3.30 into separate scalar and differential probability components by

$$\sigma_s(E \rightarrow E'')dE' = \ \sigma_s(E)\ P(E \rightarrow E')dE', \tag{3.31}$$

where $P(E \rightarrow E')\ dE'$ describes the energy probability distribution. Since a significant compilation of scalar terms $\sigma_s(E)$ already exist for most isotopes [63], the challenge of solving Eq. 3.31 lies in calculating

$$P(E \rightarrow E')dE'.$$

Thankfully, this term can be explicitly evaluated for instances in which neutrons of moderate energy (< 1 MeV) undergo elastic scatter in stationary nuclei with a small mass number (A). This situation is applicable to most neutron detection scenarios, including those within the confines of this study. Scalar quantities such as $\sigma_s(E)$ are measured in what is known as a laboratory frame-of-reference that realistically represents the

scattering relationship between an incident neutron and the target nucleus; however, this system is computationally cumbersome. To ease this burden, it is helpful to choose a frame of reference in which the center-of-mass remains stationary after the collision between the two bodies. This new frame of reference is known as the center-of-mass system and its comparison to the laboratory system is shown in Figure 3.7.

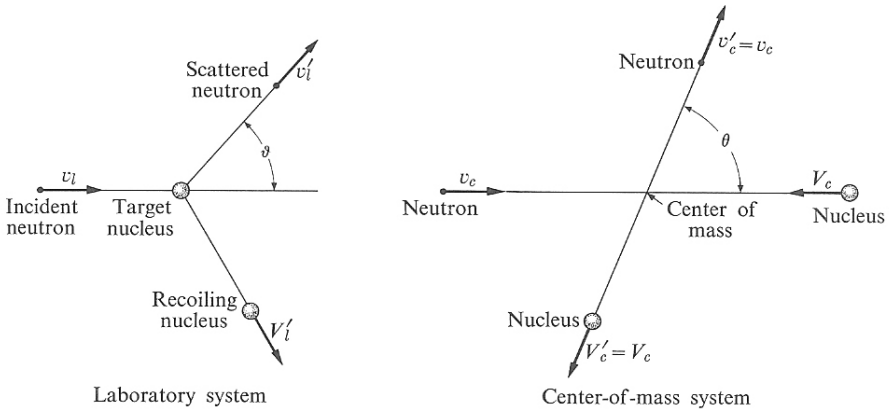

Fig. 3.7. Comparison of the laboratory and center-of-mass systems for scattering reactions [adapted from [6]].

The relationship between the different velocities and the center of mass at some arbitrary reference point in the laboratory system (scattering point) can be described graphically as shown in Figure 3.8, where $\boldsymbol{r}_l$ and $\boldsymbol{R}_l$ are position vectors describing the location of the neutron and nucleus following a scatter interaction, $\boldsymbol{r}_c$ and $\boldsymbol{R}_c$ are position vectors showing the center of mass coordinates, and $\boldsymbol{\rho}$ is the position vector displaying the location of the center of mass with respect to the scattering site.

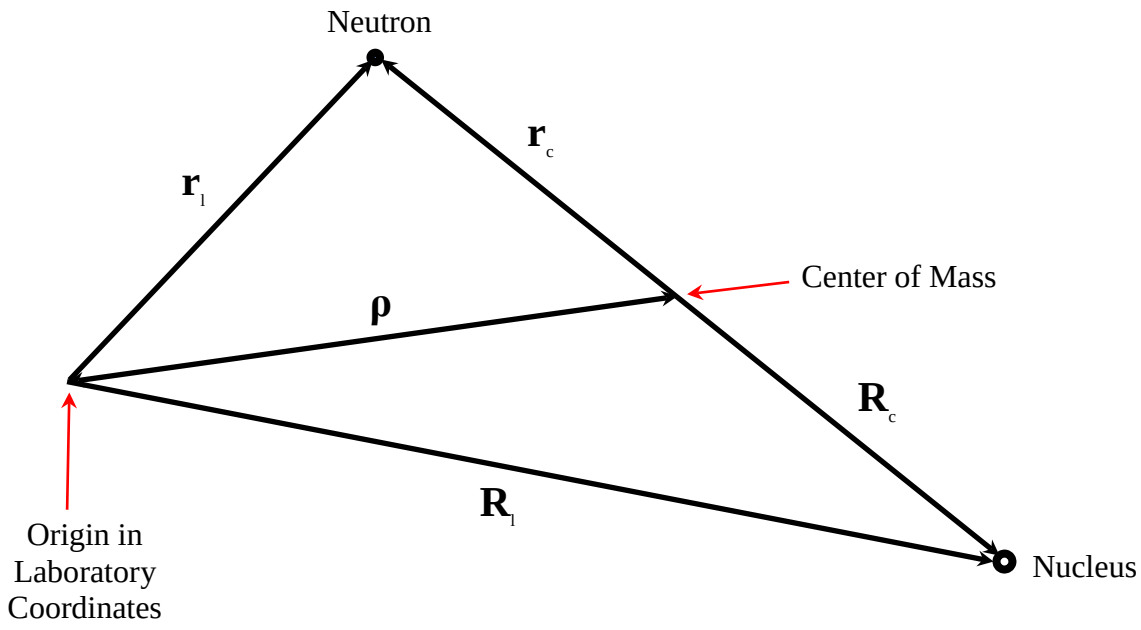

Fig. 3.8. Positional relationships of the scattering products in the laboratory and center-of-mass coordinate systems.

The equation for the center of mass ($\boldsymbol{\rho}$) of the system shown above can be adapted from the formal definition provided in college-level calculus and physics texts [64]

$$\boldsymbol{\rho} = \frac{m\boldsymbol{r}_l + M\boldsymbol{R}_l}{m + M}, \tag{3.32}$$

where and m and M are the masses of the neutron and the target nucleus, respectively. By inspection of Figure 3.8, the center of mass coordinates of the neutron and nucleus are given by

$$\boldsymbol{r}_c = \boldsymbol{r}_l - \rho \ \ and \tag{3.33}$$

$$\boldsymbol{R}_c = \boldsymbol{R}_l - \rho \ . \tag{3.34}$$

Because the particles described in Eqs. 3.33 and 3.34 are in motion, these vectors are functions of time and their respective velocities can be determined by taking their derivatives to obtain

$$\frac{\mathrm{d}\mathbf{r_c}}{dt} = \boldsymbol{v}_c = \boldsymbol{v}_l - \boldsymbol{V}_{CM} \ , \tag{3.35}$$

$$\frac{\mathrm{d}\mathbf{R_c}}{dt} = \boldsymbol{V}_c = \boldsymbol{V}_l - \boldsymbol{V}_{CM} \ , \tag{3.36}$$

where $\boldsymbol{v}_c$ and $\boldsymbol{V}_c$ are the velocities of the neutron and nucleus with respect to the center of mass, $\boldsymbol{v}_l$ and $\boldsymbol{V}_l$ are the velocities in the laboratory coordinate system, and $\boldsymbol{V}_{CM}$ is the velocity of the center of mass that is can be obtained by differentiating Eq. 3.32

$$\frac{d\boldsymbol{\rho}}{dt} = \boldsymbol{V}_{CM} = \frac{m\boldsymbol{v}_l + M\boldsymbol{V}_l}{m + M}. \tag{3.37}$$

Now, since the neutron velocity is significantly greater than the molecular motion of the target nucleus ($\boldsymbol{V}_l$) in the laboratory system, $\boldsymbol{V}_l$ is considered to be zero and Eq. 3.37 reduces to

$$\boldsymbol{V}_{CM} = \frac{m\boldsymbol{v}_l}{m+M}. \tag{3.38}$$

It can be seen from this equation and Figure 3.8 that in cases where M is very large, $\boldsymbol{V}_{CM}$ approaches zero and the two coordinate systems become identical. By substituting Eq. 3.38 into Eqs. 3.35 and 3.36 and equating $\boldsymbol{V}_l$ to zero, the velocities of the neutron and nucleus in the center-of-mass system become

$$\boldsymbol{v}_c = \boldsymbol{v}_l - \boldsymbol{V}_{CM} = \frac{M\boldsymbol{v}_l}{m+M} \tag{3.39}$$

$$\boldsymbol{V}_c = -\boldsymbol{V}_{CM} = -\frac{m\boldsymbol{v}_l}{m+M}\ . \tag{3.40}$$

The total momentum ($\boldsymbol{p}_{CM}$) of the center-of-mass system can then be described by

$$\boldsymbol{p}_{CM} = \boldsymbol{m}\boldsymbol{v}_c + \boldsymbol{M}\boldsymbol{V}_{CM} = \frac{mM\boldsymbol{v}_l}{m+M} - \frac{mM\boldsymbol{v}_l}{m+M} = 0\,, \tag{3.41}$$

which means that the total momentum in the center-of-mass system is exactly zero. It is this outcome that affords the simplicity of calculation mentioned previously.

The simplicity can be divulged by first correlating the total energy in both coordinate systems and then substituting a relative speed for the particles that exists

before any collision occurs. Remember that $\boldsymbol{V}_L = 0$, the initial energy in the laboratory system is

$$E_l = \frac{1}{2} m \, \boldsymbol{v_l^2} \, , \tag{3.42}$$

and the energy in the center-of-mass system, using Eqs. 3.39 and 3.40 is

$$E_C = \frac{1}{2}\left(\frac{mM}{m+M}\right)\boldsymbol{v}_l{}^2 \, . \tag{3.43}$$

Through the comparison of Eqs. 3.42 and 3.43, it is evident that the energy of the two coordinate systems can be correlated by the relation

$$E_C = \frac{1}{2}\left(\frac{M}{m+M}\right) m \boldsymbol{v}_l{}^2 = \left(\frac{M}{m+M}\right) E_l \, . \tag{3.44}$$

Now that an energy correlation for the two systems has been established, consider that the relative speed of the particles before a collision is

$$v_l = v_c + V_C \, . \tag{3.45}$$

Substituting Eq. 3.39 into Eq. 3.44 yields

$$E_C = \frac{1}{2}\left(\frac{mM}{m+M}\right)(v_c + V_C)^2, \tag{3.46}$$

or,

$$E_C = \frac{1}{2}\mu(v_c + V_C)^2, \tag{3.47}$$

where μ is referred to as the reduced mass of the two-particle system

$$\mu = \left(\frac{mM}{m+M}\right). \tag{3.48}$$

Following the collision, the total energy is unchanged because the interaction was elastic, therefore,

$$E_C = \frac{1}{2}\mu(v_c' + V_C')^2. \tag{3.49}$$

By equating Eqs. 3.47 and 3.49, it follows that

$$v_c + V_C = v_c' + V_C'. \tag{3.50}$$

Since we know that the total momentum in the center-of-mass system remains zero before and after a collision, it is evident that

$$mv_c = MV_C \,, \tag{3.51}$$

and

$$mv_c' = MV_C' \,. \tag{3.52}$$

Using these two equations to eliminate terms in Eq. 3.50 yields

$$\left(1 + \frac{m}{M}\right) v_c = \left(1 + \frac{m}{M}\right) v_c' \,, \tag{3.53}$$

which demonstrates that the neutron speed does not change following a collision in the center-of-mass system. Coupling Eq. 3.53 with Eq. 3.50 also shows that the speed of the target nucleus remains unchanged in the interaction as well. The important relationship between the scattering angles shown in Figure 3.9 can also be divulged by using Eq. 3.39. This equation is a general result that is valid before and after a scattering reaction, so we can write

$$\boldsymbol{v}_c' = \boldsymbol{v}_l' - \boldsymbol{V}_{CM} \,, \tag{3.54}$$

which can be depicted in the following vector diagram.

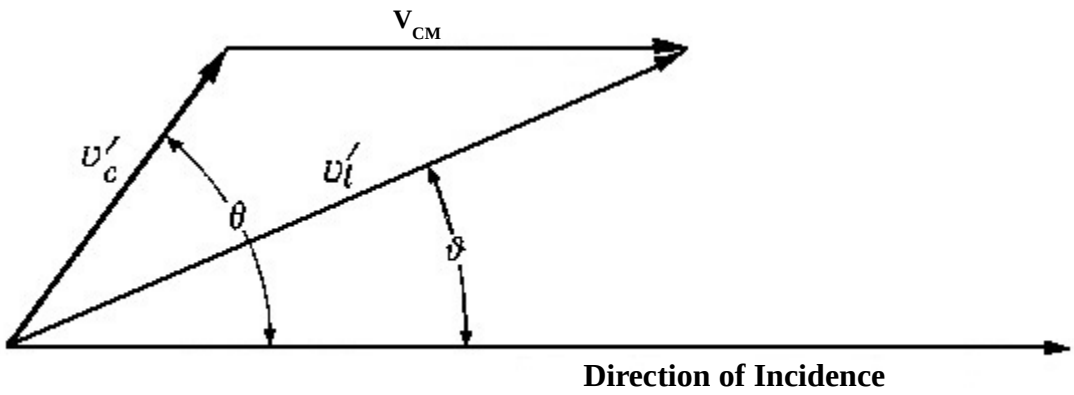

Fig. 3.9. Relationship of the scattering angles in the laboratory and center-of-mass coordinate systems [adapted from [1]].

From Figure 3.9, the relationships between the scattering angles are

$$\boldsymbol{v}_l' \sin\vartheta = \boldsymbol{v}_c' \sin\theta \ , \tag{3.55}$$

$$\boldsymbol{v}_l' \cos\vartheta = \boldsymbol{V_{CM}} + \boldsymbol{v}_c' \cos\theta \ . \tag{3.56}$$

Dividing Eq. 3.55 by Eq. 3.56 and remembering that $\boldsymbol{v}_c = \boldsymbol{v}_c'$ provides the following direct correlation between the two scattering angles

$$\tan\vartheta = \frac{\sin\theta}{\frac{m}{M} + \cos\theta} \, . \tag{3.57}$$

One additional and perhaps more useful relationship can also be extracted by rewriting Eq. 3.56 as

$$\cos\vartheta = \frac{\boldsymbol{V_{CM}} + \boldsymbol{v}_c' \cos\theta}{\boldsymbol{v}_l'}. \tag{3.58}$$

The denominator can then be expanded using the law of cosines to yield

$$\boldsymbol{v}_l' = \sqrt{(\boldsymbol{v}_c')^2 + (\boldsymbol{V}_{CM})^2 + 2\boldsymbol{v}_c'\boldsymbol{V}_{CM}\cos\theta}\,. \tag{3.59}$$

Now by using the relations $\boldsymbol{v}_c = \boldsymbol{v}_c'$ and Eqs. 3.40 and 3.51, we arrive at

$$\cos\vartheta = \frac{1 + \left(\frac{M}{m}\right)\cos\theta}{\sqrt{\left(\frac{M}{m}\right)^2 + 1 + 2\left(\frac{M}{m}\right)\cos\theta}}. \tag{3.60}$$

Since the whole point of this mathematical exercise was to determine the probability of a neutron scattering from $E \rightarrow E'$, the next step will be to use Eq. 3.59 and the other velocity relations to determine the energy transfer and scatter probability terms. When these steps are taken, the following important relations result, including the probability term we were originally seeking (see Appendix B for the derivation)

$$\frac{E'}{E} = \begin{cases} \dfrac{(1+\alpha) + (1-\alpha)\cos\theta}{2} & \alpha E \le E' \le E \\ 0 & \text{otherwise} \end{cases} \tag{3.61}$$

and,

$$P(E \rightarrow E') = \begin{cases} \dfrac{1}{E(1-\alpha)} & \alpha E \leq E' \leq E \\ 0 & \text{otherwise} \end{cases} \tag{3.62}$$

where the scattering parameter (α) is defined as

$$\alpha \equiv \left(\frac{M-1}{M+1}\right)^2. \tag{3.63}$$

Eq. 3.63 can now be combined with the scalar term in Eq. 3.31 to arrive at the differential scatter cross section we were seeking

$$\sigma_s(E \rightarrow E')dE' = \left[\frac{\sigma_s(E)}{E(1-\alpha)}\right]dE'. \tag{3.64}$$

By integrating this relation over the neutron energy range of interest, one can determine the scatter cross section. Eqs. 3.61 and 3.62 are very interesting results because they show that the energy transfer to the detector medium and the probability of achieving any final neutron energy is only dependent on the incident neutron energy and the scattering material itself. Furthermore, for the maximum energy transfer to take place ($\theta = \pi$), Eq. 3.61 yields

$$\frac{E'}{E} = \frac{2\alpha}{2} = \alpha \tag{3.65}$$

or,

$$E' = E\alpha\ . \tag{3.66}$$

By interpreting Eq. 3.66 with the aid of Eq. 3.63, it can readily be seen why a material of low mass number is so vital in a neutron detector utilizing the scattering reaction to produce an electrical signal. For elastic scattering in hydrogen (A=1), these equations demonstrate that it is possible for a neutron to lose its entire kinetic energy in a single collision. However, since no detector can be comprised entirely of hydrogen, these results explain one of the reasons why ^{3}He is very popular for neutron monitoring. For example, in ^{3}He, the neutron can potentially lose up to 75% of its initial energy in a single elastic collision. Figure 3.10 provides an overall view of the values $\sigma_s(E)$ for the materials being evaluated in this research and shows that the cross section increases significantly at lower neutron energies [63]. This behavior will be discussed further in Section 3.2.3.

As a fast neutron slows, the number of collisions it experiences increases. For this reason, it is convenient to introduce an independent variable other than energy to

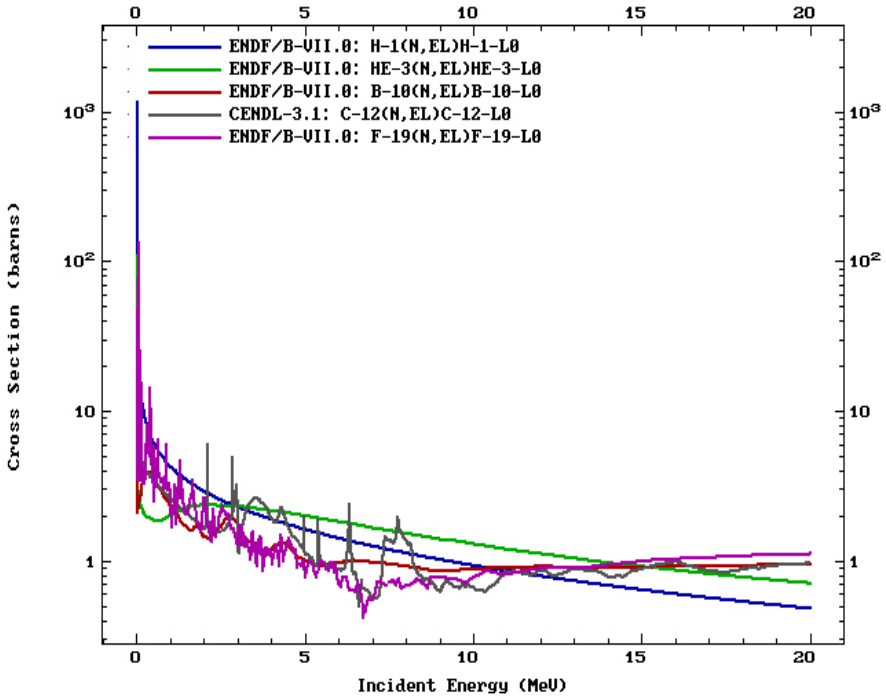

Fig. 3.10. Elastic scattering cross sections for various detector elements [7].

describe the collision density. This variable is call lethargy and is usually denoted by the symbol u. Lethargy is specifically defined by

$$u \equiv \ln \frac{E_0}{E}, \tag{3.67}$$

where E_0 is an arbitrary energy that is generally chosen based on the most energetic neutrons for the case being considered because this choice will ensure that the lethargy value will always be positive. If u is chosen in this fashion, the lethargy is zero for neutrons of this energy and will increase with a decreasing energy. In other words, the neutrons become more lethargic as their energy level decreases.

The lethargy term can be also be used to develop an important parameter denoted as ξ, which is called the average increase in lethargy per collision. This parameter is important, because it can be used to determine the average number of collisions necessary to reduce the incident neutron energy from E_0 to some final E. The change in lethargy resulting from a single collision can be calculated using the equation of the mean from calculus as

$$\overline{\Delta u} = \xi = \frac{\int_{\alpha E}^{E} \ln\left(\frac{E}{E'}\right)\, P(E \rightarrow E') dE'}{\int_{\alpha E}^{E} P(E \rightarrow E')\, dE'} \ , \tag{3.68}$$

where the probability of distribution across all energies in the denominator is equal to one. Eq. 3.68 must be numerically evaluated except for the case of isotropic scattering in the center-of-mass system. In this case, one can substitute Eq. 3.62 into Eq. 3.68, thereby reducing the integral to the following expression

$$\xi = \frac{1}{E(1-\alpha)} \int_{\alpha E}^{E} \ln\left(\frac{E}{E'}\right)\, dE' \ , \tag{3.69}$$

which can evaluated analytically by making the substitution $x = E' / E$ and inserting the appropriate new limits

$$\xi = \frac{1}{(1-\alpha)} \int_{1}^{\alpha} \ln(x)\ dx\ , \tag{3.70}$$

which leads to the final result

$$\xi = 1 + \left(\frac{\alpha}{1-\alpha}\right) \ln \alpha\ . \tag{3.71}$$

Eq. 3.71 can also be correlated to mass number (*M*) by substituting Eq. 3.63

$$\xi = 1 + \frac{(M-1)^2}{2M} \ln\left(\frac{M-1}{M+1}\right)\ . \tag{3.72}$$

The fractional term in the natural logarithm term can be inverted to obtain the following relation

$$\xi = 1 - \frac{(M-1)^2}{2M} \ln\left(\frac{M+1}{M-1}\right)\ , \tag{3.73}$$

which allows for an easier expansion as the power series of 1 / (1 – *M*). When this expansion is performed, Eq. 3.73 reduces to the following simple expression

$$\xi = \frac{2}{M + \frac{2}{3}} \, . \tag{3.74}$$

When the moderating medium contains more than one isotope, the average lethargy of the material can be calculated using the discrete form of the average by writing

$$\xi = \frac{\sum_{i=0}^{n} \xi_i \Sigma_s^i}{\sum_{i=0}^{n} \Sigma_s^i} \, , \tag{3.75}$$

where Σ_s is the macroscopic scattering cross section at the lower energy of interest (e.g. 0.0253 eV for thermal) calculated using the microscopic scatter cross section and the number of atoms per cm^3 according to

$$\Sigma_s = \sigma_s N \, . \tag{3.76}$$

We can determine what fractional energy escapes the detector following an elastic scatter by evaluating Eq. 3.67 for average energies and rearranging the terms to get

$$-\xi = \ln \frac{\overline{E}}{E_0} \, . \tag{3.77}$$

and then solving for the energy relation

$$\frac{\overline{E}}{E_0} = e^{-\xi} . \tag{3.78}$$

The fractional amount of energy (*f*) that is transferred to the target during an elastic collision is

$$f = 1 - \frac{\overline{E}}{E_0} = 1 - e^{-\xi} . \tag{3.79}$$

An estimation of the number (*N*) of scatterings that are necessary to moderate a neutron to a lower energy is given by

$$N = \frac{u}{\xi} . \tag{3.80}$$

It is interesting to calculate *N* for the case of 2 MeV neutrons that are moderated to 1 eV because these are roughly the parameters associated with the lifecycle of a neutron from birth to fission in ^{235}U. When these energy parameters are inserted into Eq. 3.77, we get the following result

$$N = \frac{14.5}{\xi} . \tag{3.81}$$

Various quantities related to elastic scattering and moderation have been calculated and provided in Table 3.1 for general comparison. An evaluation of the data demonstrates the large dependency on the mass number of the scattering medium, including the severe decrease in the fractional energy transfer beyond a mass number of four. The values of ξ and f can also be seen to approach one another as the atomic mass increases, differing only by the 3rd decimal place beyond a mass number of 16 (oxygen). And, on average, it takes 119 times more scattering to moderate fission neutrons to 1 eV in uranium compared with hydrogen. This highlights one of the main design differences between thermal and fast reactors, where the latter employs a coolant with a higher mass number such as liquid sodium to minimize the energy lost during collisions.

Table 3.1. Elastic scattering and moderation parameters for select nuclides.

Nuclide	Mass No.	α	ξ	f	N
Hydrogen	1	0.000	1.000	0.632	14.500
Deuterium	2	0.111	0.725	0.516	19.990
Water	--	--	0.945	0.611	23.700
Helium	3	0.250	0.538	0.416	26.957
Helium	4	0.360	0.425	0.346	34.092
D_2O	--	--	0.535	0.414	34.999
PVT (EJ-200)[3]	--	--	0.403	0.332	43.694
BF_3	--	--	0.354	0.298	48.655
Beryllium	9	0.640	0.207	0.187	70.184
Carbon	12	0.716	0.158	0.146	91.907
Oxygen	16	0.779	0.120	0.113	120.887
Sodium	23	0.840	0.084	0.081	171.620
Iron	56	0.931	0.035	0.035	410.848
Uranium	238	0.983	0.008	0.008	1730.337

[3] Eljen Technology, 1300 W. Broadway, Sweetwater, TX 79556, (325) 235-4276.

For neutron detectors designed on the basis of elastic scattering or absorption, the premium choices will be made from materials having lower values of α and higher values of ξ and f. The data show that ^{3}He and PVT both have very respectable properties in this sense, requiring an average of only 3 and 10 additional collisions to achieve the moderation of water. Although PVT is a solid with substantial hydrogen content, the ^{3}He gas performs better as a moderator because of the large carbon content in the PVT [8]. In fact, the data also show that BF_3 performs nearly as well as the PVT in terms of moderation despite the fact that it operates on the principle of neutron absorption.

3.2.2 Absorption

In the same sense that the term scattering was a higher-order expression encompassing both inelastic and elastic processes, the term absorption incorporates a number of different reactions that are possible when an incident neutron is *absorbed* into the nucleus of the atom. The various reactions that are probable include the emission of charged particles, additional neutrons, or photons and even fission, depending on the target and the energy level within its nucleus. Of these processes, only the radiative capture and charged-particle reactions are of importance for the detectors being considered. Normally, radiative capture is the most important reaction of this kind; however, the materials under evaluation here are either enriched with materials that enhance an absorption reaction (i.e. ^{10}B (n, α) ^{7}Li) or that have a large elastic scattering probability (i.e. ^{3}He (n, p) ^{3}H).

3.2.2.1 Radiative Capture

This particular interaction can occur at all neutron energies; however, it becomes more probable at low energies. In radiative capture reactions, the excited compound nucleus reaches the ground-state by emitting gamma radiation, so this reaction is usually referred at as an (n, γ) reaction. This process is represented symbolically by

$$ {}^{A}_{Z}X \; + \; {}^{1}_{0}n \; \rightarrow \; ({}^{A+1}_{Z}X)^{*} \; \rightarrow \; {}^{A+1}_{1}X + \; \gamma + E \; . \tag{3.82} $$

Since the atomic number does not change in this reaction, the resultant product is an isotope of the original element that can be stable or radioactive. If a radioactive isotope results, it will likely be a beta-emitter because this decay is prevalent in isotopes having an elevated neutron/proton ratio. In most cases, the excess energy is carried away by several photons, although in a few cases, such as ^{1}H, a single energetic photon is emitted

$$ {}^{1}_{1}H \; + \; {}^{1}_{0}n \; \rightarrow \; ({}^{2}_{1}H)^{*} \; \rightarrow \; {}^{2}_{1}H + \; \gamma + 2.2 \; MeV \; . \tag{3.83} $$

Although the cross section for this reaction is only 1 – 10 barns at thermal energies as seen in Figure 3.11, the reaction is important in PVT because of its large hydrogen content. These photons can potentially skew the neutron detection rate if they are not discriminated in some fashion [39]. All the detector materials considered in this research have (n, γ) cross sections at or below that of ^{1}H for all neutron energies. The

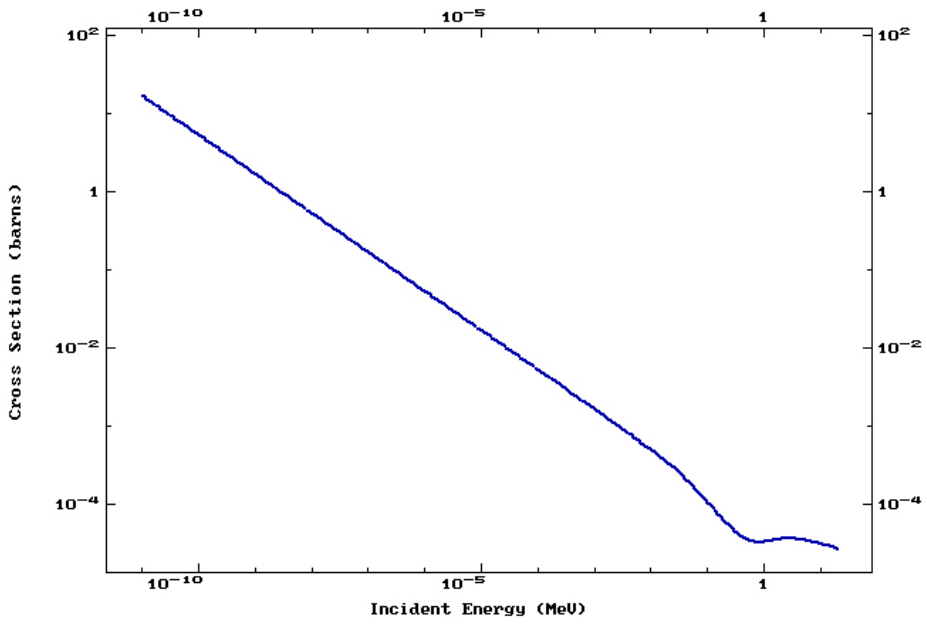

Fig. 3.11. Radiative capture cross section in ^{1}H [7].

behavior of the ^{1}H (n, γ) cross section below 0.1 eV is interesting because it varies as a line with slope of the reciprocal of velocity or as the square-root of energy. This phenomenon is generally referred to as the *1/v* behavior and, unlike other regions of the cross section plot, it allows one to easily calculate the cross section value at another neutron energy as long as the new data point is still within the *1/v* behavior range. The relationship below shows how to perform the calculation behavior region if the cross section is known at a particular energy (velocity)

$$\frac{\sigma}{\sigma_o} = \frac{v_o}{v} = \sqrt{\frac{E_o}{E}}\ , \tag{3.84}$$

where σ_o is the known cross section value at the initial velocity (v_o) or energy (E_o) and σ is the cross section to be determined at a new velocity (v) or energy (E).

The *1/v* region can sometimes extend to energies of up to 1 keV, depending on the target nucleus. The reason for this behavior, which is witnessed in all elements below a varying endpoint, will be discussed further in Section 3.2.3.

3.2.2.2 Charged-Particle Reactions

The charged-particle absorption reactions of interest in this study are the ^{3}He (n p) ^{3}H and the ^{10}B (n, α) ^{7}Li, which were described in detail in Chapter 1. It should be noted that the (n, p) reaction is a scatter reaction caused by a direct collision with a proton and not an absorption reaction in which the neutron interacts within the quantum framework of the nucleus. The absorption of a fast neutron is not very probable because the cross section is very small for all nuclei at higher energies; however, as a neutron is moderated through the scattering processes discussed in the previous section, the absorption cross section increases for all nuclei. Eventually, a point is reached where this cross section also begins to vary inversely with the velocity of the neutron. Once the neutron has reached a point when it is at thermal equilibrium with the surrounding media, it can no longer impart kinetic energy and can either be lost by absorption (capture) or leakage from the system.

As can be seen from Figure 3.12, the elastic scattering cross section in ^{3}He (n, p) is larger than the (n, α) reaction in ^{10}B below ~ 0.1 MeV, after which the two cross sections follow the 1/v behavior discussed in the preceding section [7]. At the thermal energy of 0.025 eV, the cross sections for the two reactions are 5330 and 3840 barns respectively. Both these cross sections are reasonably large in magnitude and the excess energy resultant in the absorption produces a charged particle that can be sensed by the detection medium and attributed to a neutron interaction. In ^{3}He and BF_3 detectors, the resulting pulse height is significantly higher than that produced by even a high-energy photon, so photon discrimination is straightforward and requires only a simple pulse-height discriminator.

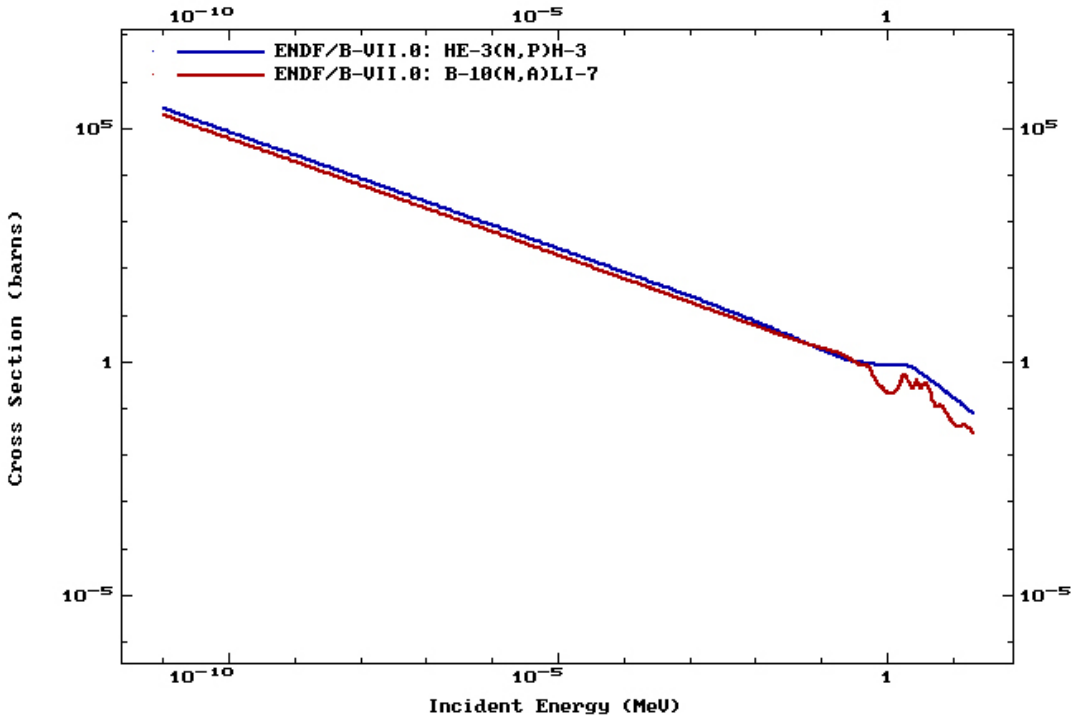

Fig. 3.12. Cross section comparison for ^{3}He and BF_3 [7].

3.2.3 Total Interaction Cross Section for Neutrons

The total interaction probability for neutrons is the sum of probabilities for the reactions of importance, as was the case for photon interactions. Only the reactions discussed in this section are applicable for this study; therefore, the total interaction probability is

$$\sigma_t = \sigma_s + \sigma_a \,, \tag{3.85}$$

and the total macroscopic cross section (expectation of the interaction probability) is then

$$\Sigma_t = \Sigma_s + \Sigma_a \,, \tag{3.86}$$

where Σ_s is the elastic scattering cross section and Σ_a is the absorption cross section of interest (either *n,p* or *n,α*). The macroscopic cross section for a material (*x*) is related to σ_x by the relation

$$\Sigma_x = N_x \sigma_x \,, \tag{3.87}$$

and is considered an *expectation* value because of the variability associated with *N*, which is the number density or number of atoms per unit volume (cm^3) for a particular the

element. The total cross sections (microscopic) for all the elements present in the detector materials being considered are collectively provided in Figure 3.13 [7].

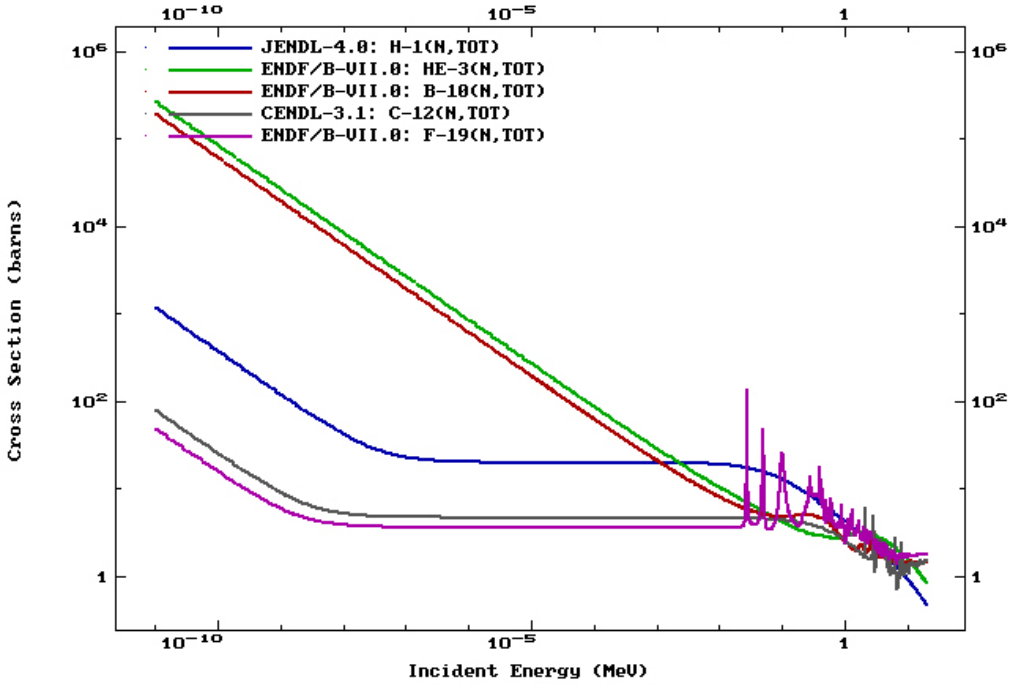

Fig. 3.13. Total cross sections for applicable detector elements [7].

The energy dependence that exists for neutron cross sections can be discussed in terms of the reactions we have previously discussed. In the lower energy range, where the neutron energy is less than the chemical binding energy of the atoms in a material, the neutron does not interact with an individual nucleus, but rather the total of the bound nuclei. The thermal motion in this range is characterized by a thermal energy of (3/2) kT where $k = 8.6173 \times 10^{-5}$ eV/° K. Since the neutron is no longer moving with a velocity much different from the nuclei, the motion of the neutron ($\boldsymbol{v}$) relative to that of the nuclei ($\boldsymbol{V}$) or $|\boldsymbol{v} - \boldsymbol{V}|$ becomes extremely important and the cross section behaves as 1/v when an average cross section is calculated [9].

The irregular behavior exhibited by the cross sections between 0.025 – 10 MeV are related to the wavelength of the neutron. These rapid oscillations result from situations in which the neutron wavelength is approximately the same as the atomic spacing between the nuclei, causing the neutron to interact with the material as a whole and resulting in the neutron being diffracted in a similar manner as *X*-rays passing through a crystal lattice. The large energy dependencies are caused by wavelengths that are comparable to several of these interstitial lattice distances. However, once the neutron energy decreases to a point, the wavelength becomes large relative to the lattice spacing and diffraction is no longer possible, causing the cross section behavior to become smooth again. The patterns of irregular behavior will become apparent again at higher neutron energy levels; however, these patterns are referred to as resonance reactions and they occur when the incident neutron energy is comparable to the lowest energy levels of a compound nucleus. In these instances, the reaction probability increases and decreases abruptly according to the energy state within the compound nucleus [1, 3 – 4].

3.2.4 Neutron Interaction Probability

Neutron interactions in materials of small thicknesses, can be described using the same process described for photons in Section 3.1.5 where the percentage of neutron that do not interact within a thickness (x) is given by

$$\frac{\phi(x)}{\phi_0} = e^{-\Sigma_t x}, \tag{3.88}$$

and the probability of having an interaction occur within a thickness (x) is simply

$$p(0) = 1 - e^{-\Sigma_t x}. \tag{3.89}$$

where is the total macroscopic cross section defined in Section 3.2.3. Likewise, the neutron mean-free path ($\overline{x}$) can be determined using the same logic applied to photons according to

$$\overline{x} = \int_0^\infty x\, p(x)dx = \Sigma_t \int_0^\infty x\, e^{-\Sigma_t x} dx = \frac{1}{\Sigma_t}. \tag{3.90}$$

This quantity is similarly used by Monte Carlo codes to determine the average flight distance of a neutron before an interaction.

3.3 Cosmic Muons

Cosmic muons have the charge of an electron, but carry approximately 209 times greater mass. Like electrons, these particles mainly undergo interactions with the atomic electrons; however, since they are *massive* compared to an electron, their path is not tortuous, but relatively linear in fashion and they experience a more gradual energy loss.

Muons have energies from a few eV to 10^{10} GeV; however, the average muon energy reaching the earth's surface is approximately 3 GeV due to interactions within the atmosphere.

These particles can interact with solid neutron detector materials resulting in pulses that are characterized as photons and/or neutrons; however, the muon flux at the earth's surface is fairly constant (varies slightly with latitude) and, therefore, the rate of false coincidences should also be relatively constant. Regardless, muon interactions can be easily correctable by the pulse processing system [3] and are of no consequence for gas-filled detectors due to the small magnitude of their density.

3.4 References

1. Evans, R., The Atomic Nucleus, Krieger Publishing, Co., Malabar, FL, 1985.

2. Walker, S., Photon Cross Section Evaluation, data retrieved from XCOM: Photon Cross Sections Database, available at www.nist.gov/pml/data/xcom/index.cfm , accessed during 2012 – 2013.

3. Knoll, G., Radiation Detection and Measurement, 4th ed. John Wiley & Sons, Inc., New York, 2010.

4. Turner, J., Atoms, Radiation, and Radiation Protection, 2nd ed. John Wiley & Sons, Inc., New York, 2000.

5. Tsoulfanidis, N. and Landsberger, S., Measurement and Detection of Radiation – 3rd Ed. CRC Press, Boca Raton, FL, 2011.

6. Duderstadt, J. and Hamilton, L., Nuclear Reactor Analysis. John Wiley & Sons, Inc., New York, 1976.

7. Walker, S., ENDF/B-VII Evaluation, data retrieved from the ENDF database, available at www.nndc.bnl.gov, accessed during 2012 – 2013.

8. Birks, J., The Theory and Practice of Scintillation Counting. Pergamon Press, Oxford, 1964.

9. Bell, G. and Glasstone, S., Nuclear Reactor Theory. Krieger Publishing Co., Malabar, FL, 1985.

CHAPTER 4
COMPUTATIONAL METHODS OF THREE-DIMENSIONAL RADIATION TRANSPORT

This chapter describes the computational methods that will be applied to determine whether a suitable replacement for ^{3}He exists among the materials being considered in this research. The intent of the modeling effort is to draw a correlation between the modeling results for 1-inch diameter ^{3}He (4 atm) and BF_3 (1 atm) tubes and direct laboratory measurements made using the same devices to ensure fidelity exists between the two. Once an excellent statistical correlation has been established for the case of the gases, the modeling effort can then be confidently extended to other tube designs and materials.

The goal of any computational radiation detection effort is to provide a solution of the linear Boltzmann transport equation (*LBE*), which describes neutral-particle behavior as a function of spatial, angular, and energy. Since detector materials represent a non-multiplying environment for neutral particles, we will concern ourselves with the forward, non-multiplying, steady-state form of the *LBE* shown in Eq. 4.1. The left-hand side of Eq. 4.1 represents losses associated with streaming and collisions, while the right-hand side details any gains produced by scattering and fixed source terms. The solution to the angular flux term in is computationally expensive because the equation contains seven independent variables. Therefore, regardless of the method employed to solve Eq. 4.1, some technique must be applied in order to reduce the problem space to one that is

$$\hat{\Omega} \cdot \nabla\psi(\vec{r}, \hat{\Omega}, E) + \sigma(\vec{r}, E)\psi(\vec{r}, \hat{\Omega}, E)$$

$$= \int_{\forall E} \int_{4\pi} dE'\, d\Omega'\, \sigma_s(\vec{r}, \hat{\Omega}' \cdot \hat{\Omega}, E' \rightarrow E)\psi(\vec{r}, \hat{\Omega}', E') + q(\vec{r}, \hat{\Omega}, E)\,. \qquad (4.1)$$

where:

$\hat{\Omega}$ = solid angle (particle direction);

$\vec{r}$ = spatial coordinate (particle position);

E = energy;

$\psi(\vec{r}, \hat{\Omega}, E)$ = angular flux;

$\sigma(\vec{r}, E)$ = total macroscopic cross section;

$\sigma_s(\vec{r}, \hat{\Omega}' \cdot \hat{\Omega}, E' \rightarrow E)$ = macroscopic differential scatter cross section; and,

$q(\vec{r}, \hat{\Omega}, E)$ = fixed source term.

calculable through the use of a high-performance computer system. Deterministic codes that attempt to solve the *LBE* directly generally use some type of spatial, energy, and angular discretization technique such as discrete ordinates, while statistical approaches such as Monte Carlo require variance reduction techniques.

4.1 Deterministic Transport

4.1.1 Deterministic Basis

The direct solution of the *LBE* offers an attractive alternative to other methods such as Monte Carlo because it can be significantly faster and more accurate, it provides universal information which can directly support fluxes and other applications such as

burnup calculations, and the solution is without statistical uncertainty, yet is limited to the accuracy of the cross sections and truncation error of the applied numerical discretization schemes [38]. Problems must be broken or decomposed into discrete algebraic expressions to use this method, since digital computers cannot directly perform calculus operations. One popular method for decomposition of the phase space (dimension, angle, energy, and time) is the discrete ordinates (S_N) method [1 – 2].

4.1.2 The Discrete Ordinates (S_N) Method

Rather than solving the *LBE* across the entire spatial domain, this technique solves the *LBE* for only a discrete set of directions (ordinates), energy bins, and spatial meshes. Although 1-D and 2-D problems can be well-managed on a conventional laptop computer, a 3-D problem typically requires a robust parallel algorithm for efficiency, combined with a high-performance computer system.

As is the case with any computational method, the advantages also come with a set of disadvantages that must be understood and accounted for during the modeling phase. As noted, each and every radiation transport application is only as effective as the cross section data used for determining particle reactions such as absorption, scatter, fission, etc. One challenge associated with the deterministic method is that using something akin to point-wise or continuous-energy cross sections is prohibitive from a time and computer memory perspective. Therefore, the user must choose the proper subset of a fine-group data collection to apply in a model, and he or she must somehow collapse this information into something that is representative of the actual overall

physical behavior (broad-group). The choice of a proper broad-group set will ensure that a problem is computationally manageable, while accounting for all the important physical characteristics associated with a particular model, such as the source term and scattering moments that will be discussed in a later section.

Possibly the most deleterious condition associated with the most popular deterministic method, discrete ordinates, is the existence of *ray effects* that can render analytical solutions that are unphysical or inaccurate. These effects are actually an artifact of the approach itself, which uses only a discrete number of ordinates (directions) in order to minimize the computational expense. In cases where the transport media presents little scattering or a high optical thickness (i.e. highly absorbing or sparse materials), angular flux values along the chosen ordinates will be satisfactory; however, areas of the media between the ordinates may contain few if any source particles and this will yield angular fluxes that are small to non-existent. The term optical thickness refers to the number of mean-free paths a photon or particle will travel in a certain medium; however, in radiation transport applications where the radiation is being projected along an ordinate, it is customary to keep track of this quantity according to its directional cosine along a particular axis to help determine whether a particular differencing scheme (discussed later) is becoming ineffective. Therefore, for deterministic transport applications, the optical thickness (*OT*) is generally referred to by the following relationship

$$OT = \left(\frac{\sigma \Delta x}{\mu}\right), \tag{4.2}$$

where σ is the macroscopic cross section for the medium, Δx is the distance along x traveled by the radiation in the medium, and μ represents the direction cosine along the x-axis in this example.

The ray effects can generally be minimized by increasing the quadrature (e.g. S_8 versus S_2), but this action will significantly increase the computation time and must be applied judiciously. Another approach that one can take is to couple the deterministic transport with a Monte Carlo routine that can be called upon to handle particle transport in regions of optical thickness where the effects are noticeable [3]. One additional technique that can be employed, and the one applied to the deterministic models of this research, is to displace the actual source from a region of large optical thickness to a region adjacent to the detector by determining the equivalent surrogate source strength for this volume. This method will be discussed further in a later section of this chapter.

Earlier in this section, mention was made of the need to separate or discretize the entire phase space of the problem for using a deterministic method. The processing of 3-D models places a heavy burden on storage capacity and processor memory. An effective differencing scheme must also be employed to ensure the problem converges to a good solution and the problem must absolutely be run on a parallel processing system that will adequately produce an effective discretization. The latter element was primarily to blame for the slow progress toward applying the deterministic method.

Prior to 1990, the computer resources necessary to handle large problems did not exist and would-be S_N users had to employ lower-order approximations or significant simplifications to apply the method. However, since that time, a number of effective decomposition algorithms have been successfully tested that have provided for a greatly improved memory partitioning and computational acceleration [4]. By coupling these algorithms with improved input/output (I/O), such as the message passing interface (MPI), problems that were previously impossible to handle, can now be efficiently and quickly processed on distributed computing environments that are widely available.

The first step in doing so is to address the energy variable by separating the entire energy spectrum into a discrete number of energy groups ($g = 1, G$) representing the entire interval from ψ_{min} to ψ_{max}. When this is done, Eq. 4.1 takes the following form

$$\hat{\Omega} \cdot \nabla\psi_g(\vec{r},\hat{\Omega}) + \sigma_g(\vec{r})\psi_g(\vec{r},\hat{\Omega}) = \sum_{g'=1}^{G} \int_{4\pi} d\Omega' \; \sigma_{s\; g'\to g}(\vec{r}, \hat{\Omega}' \cdot \hat{\Omega}) \; \psi_g(\vec{r},\hat{\Omega}') + q_g(\vec{r},\hat{\Omega}), \qquad (4.3)$$

which is referred to as the multi-group form of the *LBE*, operating on the forward group angular flux ψ_g and all terms are as previously defined [1]. The scattering term is then replaced by an expression which accounts for higher-order or anisotropic scattering. This expansion is typically done with Legendre polynomials as highlighted in Appendix C and combining this with spherical harmonics, results in [2]

$$\hat{\Omega} \cdot \nabla\psi_g(\vec{r},\hat{\Omega}) + \sigma_g(\vec{r})\psi_g(\vec{r},\hat{\Omega})$$

$$= \sum_{g'=1}^{G}\sum_{l=0}^{L}(2l+1)\sigma_{s,g'\to g,l}(\vec{r})\left\{P_l(\mu)\phi_{g',l}(\vec{r}) + 2\sum_{k=1}^{l}\frac{(l-k)!}{(l+k)!}P_l^k(\mu)\right.$$

$$\left.\cdot\left[\phi^k_{C\,g',l}(\vec{r})\cos(k\vartheta) + \phi^k_{S\,g',l}(\vec{r})\sin(k\varphi)\right]\right\} + q_g(\vec{r},\hat{\Omega}), \qquad (4.4)$$

where old terms are as previously defined and the new terms are:

ϑ = azimuthal angle constructed from arctan(ξ/η), with proper phase shift

l = Legendre expansion index

$\sigma_{s\,g'\to g,\,l}$ = l^{th} Legendre moment of the macroscopic differential scattering cross section from group g′ to g

P_l = l^{th} Legendre polynomial (P_N)

$\phi_{g',l}$ = l^{th} Legendre scalar flux moment for group g

$P_l^k(\mu)$ = l^{th} , k^{th} associated Legendre polynomial

$\phi^k_{C\,g',l}$ = l^{th} , k^{th} cosine associated Legendre scalar flux moment for group g

$\phi^k_{S\,g',l}$ = l^{th} , k^{th} sine associated Legendre scalar flux moment for group g .

And where the flux moments, $\phi_{g',l}$, , $\phi^k_{C\,g',l}$, and $\phi^k_{S\,g',l}$ are defined in terms of μ' and ϕ' as:

$$\phi_{g',l}(x,y,z) = \int_{-1}^{1}\frac{d\mu'}{2}\,P_l(\mu')\int_{0}^{2\pi}\frac{d\phi'}{2\pi}\,\psi_{g'}(x,y,z,\mu',\phi') \qquad (4.5)$$

$$\phi^{k}_{C\,g',l}(x,y,z) \;=\; \int_{-1}^{1} \frac{d\mu'}{2}\, P_l^k(\mu') \int_{0}^{2\pi} \frac{d\phi'}{2\pi}\, \cos(k\phi')\, \psi_{g'}(x,y,z,\mu',\phi') \tag{4.6}$$

$$\phi^{k}_{S\,g',l}(x,y,z) \;=\; \int_{-1}^{1} \frac{d\mu'}{2}\, P_l^k(\mu') \int_{0}^{2\pi} \frac{d\phi'}{2\pi}\, \sin(k\phi')\, \psi_{g'}(x,y,z,\mu',\phi') \tag{4.7}$$

If the streaming term in Eq. 4.3 is expanded in 3-D Cartesian coordinates, it becomes

$$\hat{\Omega}\cdot\nabla = \mu\frac{\partial}{\partial x} + \eta\frac{\partial}{\partial y} + \xi\frac{\partial}{\partial z} \tag{4.8}$$

And this result can be substituted into Eq. 4.4 to produce the final form of the non-multiplying Legendre-expanded multi-group form of the LBE in 3-D Cartesian geometry, where μ, η, and ξ refer to the direction cosines along the *x*, *y*, and *z* axes [2]. This new expression represents a coupled set of sub-interval equations that can be solved for the total flux in each energy group.

$$\begin{aligned}\left(\mu\frac{\partial}{\partial x} + \eta\frac{\partial}{\partial y} + \xi\frac{\partial}{\partial z}\right)\psi_g(\vec{r},\hat{\Omega}) + \;\sigma_g(\vec{r})\psi_g(\vec{r},\hat{\Omega}) \\ = \sum_{g'=1}^{G}\sum_{l=0}^{L}(2l+1)\sigma_{s,g'\to g,l}(\vec{r})\left\{P_l(\mu)\phi_{g',l}(\vec{r}) + 2\sum_{k=1}^{l}\frac{(l-k)!}{(l+k)!}P_l^k(\mu)\right. \\ \left.\cdot\left[\phi^{k}_{C\,g',l}(\vec{r})\cos(k\phi) + \phi^{k}_{S\,g',l}(\vec{r})\sin(k\phi)\right]\right\} + \;q_g(\vec{r},\hat{\Omega})\end{aligned} \tag{4.9}$$

We begin by integrating Eq. 4.9 according to spatial variables over the *x*, *y*, and *z* coordinates of a parallel-piped mesh cell. This produces an expression that describes the LBE in terms of an averaged angular flux across these cells. By combining this information with the choice of a set of discrete set of directions and collapsing the right-side of Eq. 4.9 into a single term (q) which accounts for scattering, fission (if applicable) and external sources, we reach the following non-multiplying discrete ordinates form of Eq. 4.1 in Cartesian coordinates which is the recursive zeroeth spatial moment balance equation [5]

$$\frac{|\mu_x|}{\Delta x}\left(\psi^x_{out,g} - \psi^x_{in,g}\right) + \frac{|\eta_y|}{\Delta y}\left(\psi^y_{left,g} - \psi^y_{right,g}\right) + \frac{|\xi_z|}{\Delta z}\left(\psi^z_{top,g} - \psi^z_{bottom,g}\right) + \sigma_{ave,g}\psi_{ave} = q_{ave,g}\,. \tag{4.10}$$

The terms *g* and *m* in Eq. 4.10 refer to the energy group and direction, *ave* is an average, and all other indices refer to the position of the angular flux along a cell defined by its Cartesian coordinates (*x*, *y*, and *z*). The absolute value of the direction cosines is used in Eq. 4.10 to ensure a positive sense in the equations, which will exist in the direction of particle motion. The average angular flux used for the collision term ($\psi^m_{ave,g}$) in each direction (*x*, *y*, and *z*) is calculated by considering the angular flux at the cell boundaries according to the Eqs. 4.11 – 4.13 [5]:

$$\psi^x_{out,g} = \left(\frac{1}{a^x_{xyz,g}}\right)\left(\psi_{ave} + \psi^x_{in,g}(a-1)\right) \tag{4.11}$$

$$\psi^{y}_{out,g} = \left(\frac{1}{a^{y}_{xyz,g}}\right)\left(\psi_{ave} + \psi^{y}_{in,g}(a-1)\right) \tag{4.12}$$

$$\psi^{z}_{out,g} = \left(\frac{1}{a^{z}_{xyz,g}}\right)\left(\psi_{ave} + \psi^{z}_{in,g}(a-1)\right) . \tag{4.13}$$

Eq. 4.10 contains seven variables and the $\psi^{m}_{ave,g}$ and $\psi^{m}_{out,g}$ terms are unknowns; therefore, the normal approach is to solve for $\psi^{m}_{ave,g}$ and use this value to calculate $\psi^{m}_{out,g}$ in Eqs. 4.11 – 4.13. To do this, first begin with the formula for $\psi^{m}_{ave,g}$ and solve for the $\psi^{m}_{out,g}$ expressions in each direction according to the following [5]:

$$\psi^{m}_{avg,g} = \left(\frac{\psi^{m}_{out,g} + \psi^{m}_{in,g}}{2}\right) , \tag{4.14}$$

and

$$\psi^{m}_{out,g} = 2\psi^{m}_{ave,g} - \psi^{m}_{in,g} . \tag{4.15}$$

Substituting Eq. 4.15 into Eq. 4.10 and performing some algebra results in an expression for one of the unknowns we are seeking:

$$\psi_{ave} = \frac{\frac{|2\mu_m|}{\Delta x}\left(\psi^{x}_{in,g}\right) + \frac{|2\eta_m|}{\Delta y}\left(\psi^{y}_{right,g}\right) + \frac{|2\xi_m|}{\Delta z}\left(\psi^{z}_{bottom,g}\right) + q_{ave,g}}{\sigma_{ave,g} + \frac{|2\mu_m|}{\Delta x} + \frac{|2\eta_m|}{\Delta y} + \frac{|2\xi_m|}{\Delta z}} . \tag{4.16}$$

Now ψ_{ave} is substituted into Eq. 4.15 to solve for $\psi^m_{out,g}$, since the $\psi^m_{in,g}$ and $\sigma_{ave,g}$ terms in Eq. 4.10 are already known [5].

Eqs. 4.11 – 4.13 represent what are known as low-order *differencing* equations or *differencing* schemes, and in the current form, they are referred to as a diamond differencing scheme (*DD*). In normal practices, the coefficient *a*, *b,* and *c* are solved via an iterative technique such as Gauss – Seidel; however, a simplified form known as the linear diamond differencing scheme (*LDD*) can be reached by simply equating each coefficient to ½. The benefit of using a low-order scheme such as the *DD* or *LDD* is that the calculations are very fast; however, if a negative flux solution results or irregular oscillations are observed during the convergence process, a more effective scheme must be substituted.

Some of the additional differencing equations that are now available are the diamond zero (*DZ*) [5], theta-weighted (*TW*) [5], directional Θ-weighted (*DTW*) [6], exponential directional weighted (*EDW*) [7], and the exponential directional iterative (*EDI*) [8]. The various schemes are described in depth in the respective references; however, a brief mention of their important feature(s) is in order here. The *TW* scheme ensured that fluxes always remains positive to eliminate the negative fluxes that occasionally happened with use of the *DZ* differencing equations, although the use of *TW* continued to produce undesirable oscillations during the convergence period. The *DTW* scheme was introduced in 1996 to simultaneously eliminate both the flux and the oscillation problems of previous schemes [6]. *DTW* used a theta-weighting parameter

that forces positivity on the fluxes; however, it did not prove to be highly accurate in all situations.

Rather than focusing solely on developing new differencing equations, some of the newer schemes such as *EDW* and *EDI* were also created to review or predict the behavior of some baseline scheme such as *DTW*, and then perform some form of exponential correction to yield a more stable and accurate solution than the baseline scheme alone. This technique is commonly referred to as a predictor-corrector scheme. The *EDW* operates on the baseline *DTW* performance, while the *EDI* uses the same exponential basis as the *EDW*, but with the addition of an iterative refinement for the exponential constants.

Most discrete ordinates codes begin with the *LDD* and then another scheme has to be substituted after-the-fact if *LDD* proves unreliable. However, more advanced S_N codes, such as PENTRAN[4], have an adaptive differencing strategy that allows the code to automatically select the most appropriate scheme on a coarse-mesh-by-coarse-mesh basis [9]. The selection strategy for this adaptive method will be discussed in a subsequent section.

4.1.3 Parallel Environment Neutral Particle Transport (PENTRAN) Code System

PENTRAN is a multi-group, anisotropic S_N code for Cartesian geometries that was specifically designed for distributed memory and scalable parallel computing using

[4] HSW Technologies LLC, 2501 Porter Street NW #220, Washington, DC 20008, (352) 871-1099.

the F90 MPI library [10]. This code optimizes parallel decomposition and also automatically optimizes the memory allocation. The code has demonstrated an excellent agreement with various standard deterministic transport codes such as DORT, TORT[5], TWODANT and THREEDANT and PARTISN[6] as well as the current reference Monte Carlo code MCNP5. PENTRAN has also performed quite well in comparisons against experimental measurements that have been conducted for a variety of problems in reactor physics, radiation detection, and medical physics applications [11].

PENTRAN is actually a family of codes that allows one to readily generate discrete mesh geometries and macroscopic cross sections, to solve up to 3-D transport models, and to collate the resulting parallel data. The program utilizes a Taylor Projection Mesh Coupling (TPMC) to interpolate between coarse and fine-mesh grids in order to minimize the loss of angular flux information that can occur between materials of differing density [12].

PENTRAN solves problems such as multi-group, isotropic/anisotropic scatter, fixed-source and criticality in Cartesian geometry. The code accepts directions through a FIDO input file, which is very common among applications such as PENTRAN that were written in the FORTRAN language. The code can operate in either the forward or adjoint transport modes, which allows for maximum flexibility in detector design. These modes will be discussed in subsequent sections.

[5] DORT and TORT were developed by the Oak Ridge National Laboratory, P.O. Box 2008, Oak Ridge, TN 37831.
[6] TWODANT, THREEDANT, PARTISN and MCNP5 were developed by the Los Alamos National Laboratory, Los Alamos, NM 87545.

In addition to specifying important parameters associated with a particular problem, the input file directs how PENTRAN distributes the processors and memory associated with the phase-space decomposition discussed previously. The decomposition is conducted through a line in the input file referred to as the decomposition weight vector (*decmpv*) which instructs the code to project the angular, energy, and spatial information according to a specified number of processors. Once the problem is initiated, PENTRAN functions to allow the various processors to communicate effectively and proceeds toward a parallel iterative solution of Eq. 4.4. During processing, PENTRAN produces a large amount of individual processor data associated with the *decmpv* settings.

4.1.3.1 PENTRAN Differencing Strategies

All the differencing strategies discussed in Section 4.1.2 are fully implemented in PENTRAN. The schemes can be individually selected in the PENTRAN input file, or alternatively, the code will automatically select the best method to apply for a particular problem using its built-in adaptive differencing strategy. The adaptive strategy works by gradually elevating the differencing scheme based on established *upgrade criteria* that are resident within the code. For example, if the *DZ* scheme is being used for a certain energy group and, during the convergence process a negative flux occurs inside any coarse mesh, the code will automatically switch to the *DTW* scheme. The convergence process then continues using the *DTW* method until the code switches to the next energy group, after which it returns to the *DZ* scheme. However, if at any point, the upgrade criterion for the *DTW* scheme is reached, the code will switch to the *EDI* and so forth.

All the PENTRAN output files contain coarse mesh information associated with each energy group of a model and list the differencing scheme that was used in each coarse mesh. By subsequently inspecting this information following the job processing, one can make an objective assessment regarding the mesh sizes used in the model. An example of the coarse cell differencing mapping table from a PENTRAN job is provided in Appendix D and shows the differencing decisions made by the code for various coarse meshes. This is valuable information for cases in which one or more energy groups did not reach full convergence. The various differencing schemes and upgrade criteria are displayed in Table 4.1. The final column also indicates how one can automatically choose (lock-in) a particular scheme within the PENTRAN input file.

Table 4.1. Adaptive PENTRAN differencing schemes and upgrade criteria.

Number	Method	Average Metric Description	Upgrade Criteria	Lock-In Method
0	DD	Not Used	None	0
1	DZ	Flux Fixup / Sweep	Fixup	-1
2	DTW	Maximum Weight / Sweep	W = 0.9500	-2
3	EDI	Iterations / Sweep	$\sigma\Delta h_{max}$ [7] = 0.02	-3
4	EDW	DTW Use / Sweep	$\sigma\Delta h_{max}$ = 0.02	-4

The *W* value in Table 4.1, which can be varied by the user, refers to the *DTW* weighting factors for the *xyz* axes. When *W* reaches a high weight, this condition indicates that the *DTW* scheme is having difficulty maintaining positivity as is typically the case with significantly streaming environments. In this case, a shift to the *EDI*

[7] This criterion is actually an exception to the upgrade between DTW and EDI due to a small optical thickness.

scheme will allow for an exponential treatment of the optically-thick cells (see Eq. 4.2) that best handles this situation.

The other term in Table 4.1 that requires explanation is $\sigma\Delta h_{max}$, which refers to the maximum case of the optical thickness value and $\Delta h_{max} = maximum\ (\Delta x, \Delta y, \Delta z)$. Unlike the other criteria, this value actually provides an exception to the upgrade criteria. The default setting is 0.02 and indicates that a particular coarse mesh has a very small optical thickness. In this instance, even if *W* exceeds the *DTW* upgrade criterion, the switch to *EDI* will not occur because the *DTW* scheme should be able to accurately resolve the angular flux for this situation.

4.1.3.2 Developing the PENTRAN Input File

The utility code, PENMSHXP[8] [13], was used to generate the PENTRAN input files for each model. The utility comes resident with a graphical user interface (*GUI*) that allows new users to build the input file by answering a series of geometry questions regarding the model; however, more advanced users are allowed to build the input file directly using any word processor.

The code strictly requires the two input files *penmsh.inp* that details the meshing parameters and a *prbname.inp* file for each z-level that lists all other parameters that are necessary for the PENTRAN input file. The optional files *prbname.spc* and *prbname.mba* were also supplied to the utility so that the source spectrum would be

[8]HSW Technologies LLC, 2501 Porter Street NW #220, Washington, DC 20008, (352) 871-1099.

inserted correctly into the PENTRAN input file and to allow for the production of a material balance file for each model. The material balance output is a very handy tool for verifying that the geometry and volumes of the model are as expected and it also lists a detailed accounting of *xyz* meshes so that users can determine if the geometry settings require updating prior to executing PENTRAN.

PENMSHXP also delivers very useful 2-D or 3-D model plots for each z-level through the commercially available TECPLOT[9] software. These pre-computation plots enable users to visually verify that the coarse and fine meshes are properly aligned within the model and that there are no overlapping shapes (spheres, pipeds, etc.) within the model. After a PENTRAN job has fully executed, PENMSHXP can also be used to produce plots of quantities such as the energy group flux, which not only displays the flux profile for that particular model, but also the existence of any harmful ray effects that would necessitate a revamping of the original model.

4.1.3.3 Cross Section Processing

The multi-group cross section library, BUGLE-96 [14], was used to calculate the broad-group neutron cross sections for the PENTRAN calculations. The library consists of 47-neutron groups and 20 gamma-ray groups that were produced and tested for light-water reactor shielding and pressure-vessel dosimetry applications and the library has been used extensively in detector applications as well [4, 15 – 17]. The forward energy group structure of the BUGLE-96 library is provided in Table 4.2.

[9] Tecplot, Inc., P.O. Box 52708, Bellevue, WA 98015, (425) 653-1200.

Table 4.2. Forward energy group structure of the BUGLE-96 broad-group library.[10]

Group	Energy (MeV)	Group	Energy (MeV)	Group	Energy (MeV)	Group	Energy (MeV)
1	1.73E+01	13	2.37E+00	25	2.97E-01	37	1.58E-03
2	1.42E+01	14	2.35E+00	26	1.83E-01	38	4.54E-04
3	1.22E+01	15	2.23E+00	27	1.11E-01	39	2.14E-04
4	1.00E+01	16	1.92E+00	28	6.74E-02	40	1.01E-04
5	8.61E+00	17	1.65E+00	29	4.09E-02	41	3.73E-05
6	7.41E+00	18	1.35E+00	30	3.18E-02	42	1.07E-05
7	6.07E+00	19	1.00E+00	31	2.61E-02	43	5.04E-06
8	4.97E+00	20	8.23E-01	32	2.42E-02	44	1.86E-06
9	3.68E+00	21	7.43E-01	33	2.19E-02	45	8.76E-07
10	3.01E+00	22	6.08E-01	34	1.50E-02	46	4.14E-07
11	2.73E+00	23	4.98E-01	35	7.10E-03	47	1.00E-07
12	2.47E+00	24	3.69E-01	36	3.35E-03		

4.1.3.4 Post-Processing Software

The GMIX[11] code was used to create the actual macroscopic cross section data file for use in the PENTRAN calculations. The code requires an input file that contains all the items that are necessary for the production of the cross section file that is needed, such as all the materials used within a model as weight percent or atom fractions, the number of energy groups, and the P_N order. GMIX accesses this input file upon execution, takes note of the associated material information, then accesses the applicable elemental data in the BUGLE-96 broad-group cross section library and produces the cross section file (*problemname.xs*) that PENTRAN requires for the deterministic transport calculations.

[10] Forward Group 1 (fast) is Adjoint Group 47 and vice versa.
[11] HSW Technologies LLC, 2501 Porter Street NW #220, Washington, DC 20008, (352) 871-1099.

The PENTRAN code possesses a resident post-processing utility that is called from the command line using the syntax < *ppen-post prbname pen n m* >, where *prbname* is the name of the PENTRAN input file *prbname.pen* minus the extension, *n* is the number of computer cores used for the job, and *m* is the number of processors used per core. This routine will remove the excess processing information that was created during the PENTRAN run and produce the output files that can be accessed through the PENDATA[12] utility or a computer program that was written to obtain specific information from the PENTRAN output files.

The PENDATA utility program gathers the parallel results from multiple files and produces group-specific flux files in the ASCII format that can then be used for additional applications such as plotting or in calculating an important quantity such as the reaction rate for a detector.

4.1.4 Deterministic Forward Transport

In the typical forward circumstance, the *LBE* is solved to yield the scalar flux (ϕ) for a specific neutron source term (q). If more than one source exists, separate computations must be completed for each of them, which is one disadvantage of the forward method. Once all the flux computations are complete, the reaction rate for a detector can be calculated using the following equation (see discussion of the flux terms given in 4.1.5)

[12] HSW Technologies LLC, 2501 Porter Street NW #220, Washington, DC 20008, (352) 871-1099.

$$R = \int_E dE \int_{V_d} \sigma_d\,(x,y,z,E)\ \phi(x,y,z,E)\,dx\,dy\,dz \approx \sum_{\substack{\Delta V_i \in V_d \\ g=1,G}} \phi_{g,i}\ \sigma_{d\,g,i}\,\Delta V_i\,, \qquad (4.17)$$

where:

R	= detector response (s^{-1})
V_d	= detector volume (cm^3)
(x, y, z)	= spatial location of detector
$\phi(x, y, z, E)$	= spatial, energy dependent scalar flux ($n\ cm^{-2}\ s^{-1}$) from quadrature of ψ
$\sigma_d(x, y, z, E)$	= spatial, energy dependent detector cross section (cm^{-1})
$\phi_{g,i}$	= i^{th} cell scalar flux for group g ($n\ cm^{-2}\ s^{-1}$), from quadrature of $\psi_{g,i}$
$\sigma_{d,g,i}$	= i^{th} cell detector cross section for group g ($n\ cm^{-2}\ s^{-1}$)
ΔV_i	= i^{th} cell volume (cm^3)

4.1.5 Deterministic Adjoint Transport and the Adjoint Importance Function

In the design of a radiation detector, it is essential to account for particle importance, which reveals the specific spatial and corresponding energies where neutrons will contribute the most to the detector response. The adjoint solution to the adjoint form of the *LBE* provides such information and insight, which is not available through forward deterministic or Monte Carlo methods. The adjoint form of the *LBE* can be derived using the adjoint identify for real-valued functions,

$$\langle \psi_g^{\dagger} H \psi_g \rangle = \langle \psi_g H^{\dagger} \psi_g^{\dagger} \rangle\,, \qquad (4.18)$$

where the Dirac brackets ‹ › represent integration over all independent variables and

$$H = \hat{\Omega} \cdot \nabla + \sigma_g(\vec{r}) - \sum_{g'=1}^{G} \int_{4\pi} d\Omega' \ \sigma_{s\ g'\to g}\left(\vec{r}, \hat{\Omega}' \cdot \hat{\Omega}\right). \tag{4.19}$$

In Eqs. 4.18 and 4.19, $\psi_g^{\dagger}$ is the angular adjoint (importance) function and *H* is the forward transport operator. We develop the adjoint transport operator ($H^{\dagger}$) by applying the boundary condition that particles leaving the system have a zero importance for all groups and by requiring that a continuous importance function exists to arrive at

$$H^{\dagger} = -\hat{\Omega} \cdot \nabla + \sigma_g(\vec{r}) - \sum_{g'=1}^{G} \int_{4\pi} d\Omega' \ \sigma_{s\ g\to g'}\left(\vec{r}, \hat{\Omega} \cdot \hat{\Omega}'\right). \tag{4.20}$$

The minus sign on the streaming term reflects that, in the adjoint condition, particles travel in a reversed direction, where particles scatter from group g to other groups g' (groups formerly contributing to group g in the forward equation) [1 – 2]. For the case of a fixed forward detector problem, the neutron flux must satisfy the following relation:

$$H\psi_g = q_g\,, \tag{4.21}$$

because the source term is purposely omitted from the forward operator (*H*) relation. Likewise, the inhomogeneous adjoint equation must be satisfied with an adjoint source that is aliased to the group detector response cross section ($\sigma_{d,g}$) by

$$H^{\dagger}\psi_g^{\dagger} = \sigma_{d,g} \,. \tag{4.22}$$

Now, by substituting Eqs. 4.21 and 4.22 into Eq. 4.18 and simplifying, the following important result is obtained:

$$R = \langle \psi_g \sigma_{d,g} \rangle = \langle \psi_g^{\dagger} q_g \rangle \,, \tag{4.23}$$

where R is the detector response or reaction rate. This relation demonstrates that the detector response can be computed directly from several forward transport computations for each source or a single adjoint transport computation as

$$R = \int_E dE \int_{V_q} \sigma_d^{\dagger}(x', y', z', E)\; q(x', y', z', E)\, dx', dy', dz' \approx \sum_{\substack{\Delta V_i \in V_d \\ g=1,G}} \phi_{d\,g,i}^{\dagger}\; q_{g,i}\, \Delta V_i \,, \tag{4.24}$$

where:

R	= detector response (s^{-1})
V_q	= source volume (cm^3)
(x', y', z')	= spatial location of non-zero source cells (adjoint)
$\phi_d^{\dagger}(x', y', z', E)$	= spatial, energy dependent scalar adjoint function for detector d
$q(x', y', z', E)$	= spatial, energy dependent source ($n\ cm^{-3}\ s^{-1}$)
$\phi^{\dagger}_{d,g,i}$	= i^{th} cell scalar adjoint function for detector d and group g.
$q_{g,I}$	= i^{th} cell source density for group g ($n\ cm^{-3}\ s^{-1}$)
ΔV_i	= i^{th} cell volume (cm^3).

Although PENTRAN provides the capability to calculate reaction rate using angular flux as shown in Equation 4.23, the scalar flux can be substituted in cases where it is deemed appropriate as shown in Equations 4.17 and 4.24. This simplification significantly reduces the output file size and speeds computations. Regardless of the flux term that is used, the ability to determine the detector response for an arbitrary source distribution, weighted by the computed adjoint function, shows the incredible power of the adjoint technique and its obvious application toward problems of detector design.

A forward transport code can actually be used to solve for the adjoint function by replacing the source term with transposed group cross sections and by also transposing the cross section scattering matrix to progress from *G* to 1. This is the exact method by which PENTRAN handles adjoint problems, although the code performs the cross section transposition internally. If the numerical truncation errors are negligible, the forward and adjoint results should be directly comparable, which will provide further proof, along with the forward Monte Carlo method, that the detector model is valid.

4.2 Monte Carlo Transport

4.2.1 History of the Technique

The basic tenant of this computational radiation transport method was developed out of the boredom of a solitaire session in 1946 by Stanislaw Ulam, who was one of the

most prominent mathematicians of the 20th century. During a convalescent period, Ulam, who was participating in the Manhattan Project, began to wonder what his chances were of successfully laying out a hand of solitaire with a deck of 52 cards. After unsuccessfully attempting to estimate the probability of this occurrence through various combinatorial schemes, he wondered if a better approach might be to just lay out the cards and count the number of successful attempts. And, after having this revelation, Ulam's next thought was to envision the application of this new idea to neutron diffusion and other physical problems. Later that same year, Ulam described his idea to John von Neumann, who quickly became enamored with the idea of applying this technique to the developing technique of electronic computing. Von Neumann eventually outlined a statistical approach to solving neutron diffusion and multiplication problems in a letter to the Theoretical Division Leader, Dr. Robert Richtmyer, at Los Alamos in early 1947. This outline detailed the computational flow of the process, including its application through an electronic computer for the first time [18].

The technique found broad application in the field of nuclear engineering, because the macroscopic cross section for a neutron interaction can be interpreted as the probability of interaction per unit distance traveled by the particle. On the basis of this important premise, a collection of neutrons could now be individually tracked from origin (e.g. in-scatter, fission or emission) to conclusion (e.g. scatter, capture, or escape) by determining the interaction locations and types, directional changes, and the subsequent neutron energies through probability sampling. Each neutron history in the set is analogous to an individual game of solitaire in von Neumann's original formulation, with

the digital computer *drawing* (generating) the *probabilities* (random numbers) that dictate the events and the ultimate outcome of the game. The use of probability sampling along with the card game that originally inspired Ulam led von Neumann to nickname the process *Monte Carlo* [18]. In the decades that have passed since World War II, this elegant method has been significantly enhanced and has become one of the most useful numerical methods in all of nuclear engineering.

4.2.2 Monte Carlo Basis

Monte Carlo is a statistical method that is used to solve physical problems which occur due to random processes and that can be mathematically modeled. The objective of such a simulation is to recreate only those processes in which the basic physics is understood (i.e. radiation transport). The method uses the laws of probability and random number generation to obtain an average or expectation of a particular random variable (e.g. x) that corresponds to a certain random process with $p(x)$ [19]. The inference is that x is related to a random number (ξ). The random variable used in the Monte Carlo simulation can be either discrete or continuous; however, in radiation transport problems, continuous random variables are the norm.

All basic physical processes give the appearance of randomness in the sense that one cannot predict the outcome of every individual progression. What the Monte Carlo process attempts to accomplish is to effectively characterize these random (stochastic) processes by observing and estimating the average behavior of many elements (e.g.

particles or photons for radiation transport). Requiring a large number of elements for the estimation means that this computational technique is far more computationally "expensive" when compared with deterministic methods, although the advent of faster and parallel computers have eased this limitation in the past decade. And, since the result that is produced is an estimate, it will also have an uncertainty associated with it and the estimate should never be mentioned in the absence of this uncertainty, unlike deterministic results which are exact solutions of the LBE. A basic step-by-step Monte Carlo process is included in Appendix E that describes how particle transport progresses through the use of the technique.

4.2.3 Monte Carlo Tally Variance

Prior to discussing techniques to reduce the Monte Carlo variance, it is prudent to discuss what the term means in relation to the calculations, so we can understand exactly what we're trying to reduce or minimize. Since this computational technique necessitates the production of many histories, we can take advantage of the Central Limit Theorem (*CLM*) to describe what is meant by the estimate (mean) and variance. The *CLM* states that if we repeat a model a great many times and with numerous histories, the average of the means ($\bar{x}$) from each model will be distributed normally about the true mean (x) and with a variance ($S_{\bar{x}}^2$), even if the set of true means are not normally distributed. The variance or the uncertainty is the value that we'd like to minimize or even optimize as the case may be. Each of these terms is specified in mathematical terms by the following set of equations:

$$x \equiv \int_0^\infty x\, p(x) dx \ , \tag{4.25}$$

$$\bar{x} \equiv \frac{1}{N} \sum_{i=1}^{N} x_i \ \ , and \tag{4.26}$$

$$S^2 \equiv \frac{1}{N-1} \sum_{0}^{\infty} (x_i - \bar{x})^2 \ \cong \overline{x^2} - \bar{x}^2 \ , \tag{4.27}$$

where

$$\overline{x^2} \equiv \frac{1}{N} \sum_{i=1}^{N} {x_i}^2 \ . \tag{4.28}$$

In Eq. 4.26, the Law of Large Numbers specifies that the average of the various means will approach the true mean as $N \rightarrow \infty$. Eq. 4.27 represents the standard deviation of the population histories, which tells us how far each history varies from the average history; however, the actual variance we're seeking to reduce or optimize is called the variance of the average and is calculated by

$$S_{\bar{x}}^2 \equiv \frac{1}{N} \sum_{0}^{\infty} S^2 \ . \tag{4.29}$$

Since Monte Carlo results are estimates of the transport behavior, they should never be quoted in literature without the estimate of the variance (error).

4.2.4 Variance Reduction

The real goal of any Monte Carlo calculation is to produce a result with an acceptable relative error as has just been stated. In most current problems, the newer computing abilities can ensure we achieve the stated goal above; however, one area where Monte Carlo struggles is in transporting particles thick radiation shields. In the absence of some technique (non-analog) to increase the number of particles penetrating the shield, the problem would require far too many histories (elements) and computer time to yield an estimate with an acceptable relative error. Two basic approaches can be applied to reduce both the calculation expense and the relative error and these are to simplify the model and/or use non-analog techniques [20]. Since these techniques have been exhaustively described in the MCNP5 manual [21], they will only be described briefly here.

4.2.4.1 Model Simplification Techniques

Model simplification techniques are those that typically reduce the variance by simplifying or truncating the geometry and/or the physics associated with a problem in an effort to eliminate particles or histories that have little or no bearing on the outcome of the simulation, thereby reducing the necessary computation time. The application of these techniques is probably as much about art or intuition as it is about science and care must be taken such that accuracy is not sacrificed in the name of precision (i.e. low variance) because each choice will introduce some degree of bias.

Examples of model simplifications are those associated with the physics treatment, particle energy, and time or history. Physics simplifications include such things as disallowing the production of Bremsstrahlung during transport, allowing only non-coherent scattering, and ignoring neutron energies beyond some maximum. One can also set cutoffs (minima or maxima) associated with tracking of particle energy or the maximum number of particle histories or computational time that is allowed.

4.2.4.2 Non-Analog Techniques

Unlike model simplification techniques, the goal of non-analog methods is to increase the number of particles that reach some tally point such as a detector or surface in order to speed the solution, thereby allowing one to reduce the computation time. The basic tenant of this technique is to track particle weight rather than the sheer number of the particles themselves. A particle is assigned an initial weight upon emission from the source and when it is artificially forced toward the tally point, the weight is decreased in a manner that ensures the average weights reaching the tally point are the same as what would occur in the normal analog situation. In other words, we must maintain a *fair game* or the tally outcome will be unavoidably altered.

Non-analog techniques are extremely important in the Monte Carlo method because of the very nature and rate of radioactive source emissions. While it might seem to some that running a complex transport problem using 10^{10} total neutron histories is overkill, this magnitude must be considered in the context of the source strength of the

radioactive material, which can easily emit this many particles every second depending on its activity! Due to the angular nature of every source emission in the analog case, many source particles are not directed toward the tally point, in which case they are considered *lost*. In a real-world case, a sufficient number of particles might reach our detector over the course of even one minute that would constitute an accurate source assessment due to the source emission strength; however, the Monte Carlo case of 10^{10} total histories might only represent the number of particles emitted in one or two seconds from the actual source. Non-analog methods are therefore used to increase the number of particles arriving at our detector by directing more source particles with a varied weight toward the tally point, thereby significantly reducing the number of *lost* particles. The main techniques of this type that are used include source biasing, particle splitting, Russian roulette, and implicit capture.

In source biasing, we emit *m* times more particles toward the source with initial weights of only *1/m*, thus maintaining a fair game compared with the analog case. We can play a similar game using splitting, where a particle is split into *m* number of particles with a reduced weight of *1/m* as was the case with source biasing. In the case of most Monte Carlo programs, the actual splitting process is controlled by assigning an *importance* factor for specific spaces within a model. When a particle crosses a boundary into a space of greater importance, the splitting process occurs and an increased number of particles continue to be tracked, but at a reduced weight.

Russian roulette (*RR*), on the other hand, is played in the converse case of a particle exiting a region of higher importance into one of lower importance. In this instance, the particle is *eliminated* or *killed* (i.e. shot by a bullet) with a probability equal to

$$p(RR) = \frac{Imp_{new\ cell}}{Imp_{previous\ cell}}\ , \tag{4.30}$$

where *Imp* is an abbreviation for importance. For example, if the particle exits a region of *Imp=2* and crosses into a space with *Imp=1,* the particle is killed with a probability of 0.5. If the particle is killed during the *RR* process, its weight is eliminated and the particle is no longer tracked; however, if the particle survives the encounter, its importance is increased by a factor of *1/p (RR)* and it continues to be tracked, thus maintaining a fair game as before. The *RR* process is basically used to prevent the continued tracking of particles that are moving away from the tally point and that are unlikely to contribute to the tally.

4.2.5 MCNP-5 Code Description

MCNP-5 is a general-purpose, continuous-energy, Monte Carlo transport codes that is capable of handling coupled neutron, photon, and electron transport [21]. The code has thousands of person-years of development behind it and is the global standard by which all Monte Carlo codes are judged. MCNP-5 can be used in singular transport

modes for neutron/photon/electron or in various combinations of these three modes. The continuous-energy cross sections used by the code cover the neutron energy range of 10^{-11} MeV to 20 MeV and continue up to 150 MeV for some isotopes. The code can be obtained from the Radiation Safety Information Computational Center (RSICC) which is operated by the Oak Ridge National Laboratory (ORNL). The code package provided by RSICC includes a setup program to install all the necessary accessories used by MCNP-5. The end user can choose to copy one of the applicable executable programs (MCNP.EXE) that are provided for several computer platforms or to create a new executable by compiling one from the setup disks. The program also automatically runs a substantial number of sample problems that should yield specified results upon the successful installation of the code. The verification of the sample problem results is left as an exercise to the user; however, it is extremely important that this task be accomplished, because it provides the final quality assurance that the code installed all the associated files properly.

All the necessary physics (and much more) discussed in the previous section are provided within the installed code package. The user must formally implement the code by calling the executable file at the command prompt (Windows-based systems) while also listing the name of an input file that will direct the code toward some calculation goal. This input file, which must be written by the user, contains information such as: 1) geometry (mathematical description) of the problem; 2) material descriptions; 3) cross sections to apply; 4) location and type of source (neutron, photon, electron); the type of information (tally) that is desired; and, any variance reduction techniques that are to be

employed to improve the efficiency of the calculation and its associated uncertainty (error). The MCNP5 and PENTRAN models for the computational experiments will be shown in the following chapter.

4.3 References

1. Bell, G. and Glasstone, S., Nuclear Reactor Theory. Krieger Publishing Co., Malabar, FL, 1985.

2. Lewis, E. and Miller, W., Computational Methods of Neutron Transport. American Nuclear Society, LaGrange, IL, 1993.

3. Yi, C. and A. Haghighat, A 3-D Block-Oriented Hybrid Discrete Ordinates and Characteristics Method. Nuclear Science and Engineering, 2010.

4. Sjoden, G., Deterministic Adjoint Transport Applications for He-3 Neutron Detector Design. Annals of Nuclear Energy, 29, 1055-1071, 2002.

5. Sjoden, G. and Haghighat, A., PENTRAN code system – PENTRAN Users Guide to Version 9.4X.5 series. HSW Technologies, LLC, Washington, November, 2011.

6. Petrovic, B. and Haghighat, A., New Directional Theta-Weighted S_N Differencing Scheme. Transactions of the American Nuclear Society, 73: 195-197 (1995b).

7. Sjoden, G. and Haghighat, A., The Exponential Directional Weighted (EDW) Differencing Scheme in 3-D Cartesian Geometry. Proceedings of the Joint International Conference on Mathematics and Supercomputing for Nuclear Applications, Saratoga Springs, NY, Vol. II, pp. 1267 – 1276, October, 1997.

8. Sjoden, G., An Efficient Exponential Directional Iterative Differencing Scheme for 3-D S_N Computations in XYZ Geometry. Nuclear Science and Engineering, Vol. 155, pp. 179 – 189, 2007.

9. Sjoden, G., "PENTRAN": A parallel 3-D S_N Transport Code with Complete Phase Space Decomposition, Adaptive Differencing, and Iterative Solution Methods. Ph. D. Thesis in Nuclear Engineering, The Pennsylvania State University, May, 1997.

10. Sjoden, G. and Haghighat, A., A New Adaptive Differencing Strategy in the PENTRAN 3-D Parallel S_N Code. Transactions of the American Nuclear Society, 75, 1996.

11. Haghighat, A., Sjoden, G., and Kucukboyaci, V., Effectiveness of PENTRAN's Unique Numeric for Simulation of the Kobayashi Benchmarks. Progress in Nuclear Energy Journal, 3-D Radiation Transport Benchmarks for Simple Geometries with Void Region, Santa Fe, NM, 39, No. 2., pp. 191 – 206, 2001.

12. Sjoden, G. and Haghighat, A., Taylor Projection Mesh Coupling Between 3-D Discontinuous Grids for S_N. Transactions of the American Nuclear Society, Vol. 74, pp. 178 – 179, 1996.

13. Yi, C. and Haghighat, A., PENMSHXP: A 3-D Mesh Generator for PENTRAN, Version 2.6b, University of Florida, 2008.

14. White, J., Ingersoll, D., Slater, C., and Roussin, R., BUGLE-96: A Revised Multi-Group Cross Section Library for LWR Applications Based on ENDF/B-VI Release 3. ORNL, DLC-185, 1996.

15. Ghita, G., Sjoden, G, and Baciak, J., On Neutron Spectroscopy using Gas Proportional Detectors Optimized by Transport Theory. Nuclear Technology, Vol. 168, pp. 620 – 628, Dec. 2009.

16. Ghita, G., and Sjoden, G., Design of a Neutron Detector Array for SNM Optimized by Radiation Transport Methods. American Nuclear Society, International Conference on Mathematics, Computational Methods, and Reactor Physics, Saratoga Springs, NY, 2009.

17. Al-Basheer, A., Sjoden, G., and Ghita, M., Critical Discretization Issues in 3-D S_N Simulations Relevant to Dosimetry and Medical Physics. Nuclear Technology, Vol. 169, pp. 252 – 262, March, 2010.

18. Eckhardt, R., Stan Ulam, John Von Neumann, and the Monte Carlo Method. Los Alamos Science, Los Alamos National Laboratory, Los Alamos, NM, Special Issue, 1987.

19. Warnock, T., Random-Number Generators. Los Alamos Science, Los Alamos National Laboratory, Los Alamos, NM, Special Issue, 1987.

20. Shultis, J. and Faw, R., An MCNP Primer. Kansas State University, Manhattan, KS, Revised December, 2011.

21. Briesmeister, J., ed., MCNP – A General Purpose Monte Carlo N-Particle Transport Code, Version 5, LA-UR-03-1987. Los Alamos National Laboratory, Los Alamos, NM, April, 2003.

CHAPTER 5
COMPUTATIONAL MODELING EXPERIMENTS

Now that the scientific foundation has been laid for the computational design approach, we must consider how to apply this approach toward identifying detector designs that are ^{3}He-equivalent. The identification process was carried forward in two distinct phases.

5.1 Models for Comparisons to Neutron Measurements (Phase 1)

The first step taken during the experimental phase was to create models for the ^{3}He baseline and a singular BF_3 design (length of 19.6 cm and 1-inch diameter) that matched the two actual detector assemblies that were going to be used for the laboratory measurements of the PuBe source. Although the computational models for all PENTRAN and MCNP5 designs in the second phase were identical, save for the detection material, the source configuration for the PENTRAN model was altered in the initial phase to allow for the use of a lower-order quadrature (S_8) and Legendre moment (P_2) for the PENTRAN calculations while precluding any ray effects. Specifically, a baseline surrogate source box strength of 15623 ± 63 $n\ cm^{-3}\ s^{-1}$ (1.96σ)was determined by using MCNP5 to calculate the source necessary to produce the same surface current (J_-) across the outer detector surface as the true source configuration used in the MCNP5 detector models.

The combination of the surrogate source and the lower-order quadrature and Legendre moment (S_8 / P_2) produced excellent convergence (< 8.0E-04) for both the forward and adjoint cases in all models, while requiring calculation times of less than 4 hours. For computational expense comparisons, a test case using the true source location and an S_{20} / P_3 combination produced equivalent results, but required over 24 hours to fully converge.

Since the only difference between the two comparative computational models was the type of gas within the detector, the plots appear identical; therefore, only one figure is provided for each of the respective computer codes and detectors. The surrogate box source for the PENTRAN model is shown in red in Figure 5.1 and Figure 5.2 displays the MCNP5 model geometry, although the actual figure was produced using the PENMSHXP utility. Figure 5.2 also highlights the significant number of meshes initially

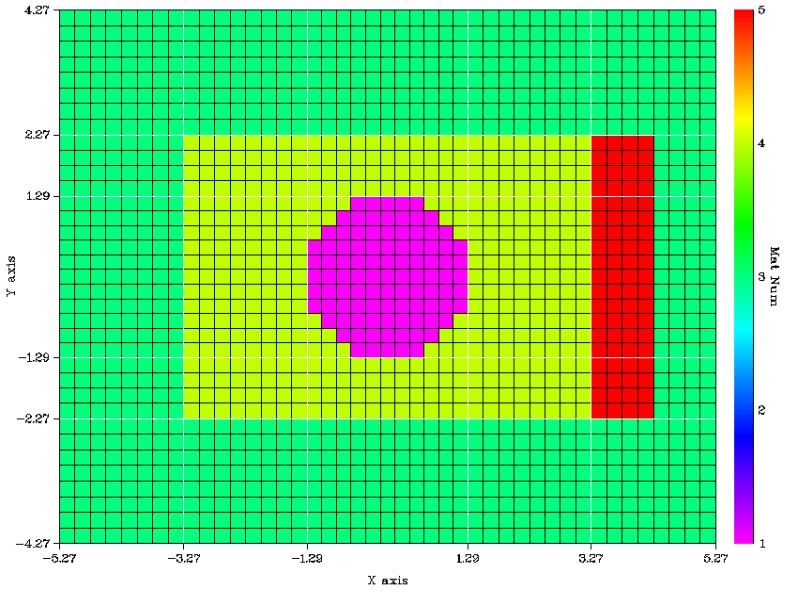

Fig. 5.1. PENTRAN model for ^{3}He and BF_3 tubes with a 1.27 cm radius.

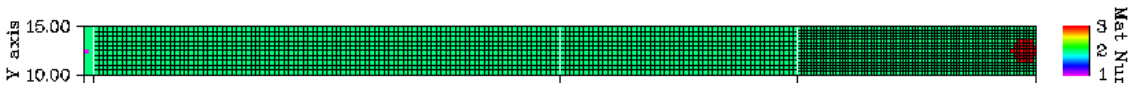

Fig. 5.2. Equivalent MCNP5 model used for comparisons to the PENTRAN results and actual neutron measurements.

required for the S_{20} / P_3 combination when the source was placed at its actual location of 100 cm away from the detector. The material data associated with the two models is also given in Table 5.1.

Table 5.1. ^{3}He / BF_3 material data.

Number	Material	Density (g cm^{-3})
1	Detector (^{3}He / BF_3)	5.39E-04 / 2.73E-03
3	Air	1.20E-03
4	Polyethylene	9.40E-01
5	Air Source	1.20E-03

The final task of the first phase was to compare the computational calculations to the neutron measurements to determine if the models reflected the actual conditions inside the room with an acceptable fidelity. Additional information about the source configuration, shielding and the overall experimental facility setup is provided in Chapter 6, while the actual neutron detector system setup and testing is discussed in Chapter 7. Chapter 7 will also show the neutron tubes and demonstrate how they were fitted with the moderator material and positioned during the measurements. The results associated with the modeling and measurements mentioned herein will be given in Chapter 8 and grouped according to the type of detector design (i.e. BF_3, ^{10}B lining, or PVT).

5.2 Models for Comparisons to the Baseline Detector (Phase 2)

The second phase of the process consisted of developing PENTRAN and MCNP5 models for the reference ^{3}He detector, and then executing the problem for a global neutron source of 1000 $n\ s^{-1}$ surrounding the detector assembly and having the emission probabilities listed in Table 5.2. Each of these probabilities coincides with the energy group structure detailed in Table 4.2 of the previous chapter. The reaction rate and adjoint function that stemmed from this job provided the baseline quantities that would determine the suitability of the potential replacement designs.

Table 5.2. PuBe emission probability associated with the BUGLE-96 broad-group library structure.[13,14]

Group	Emission Probability	Group	Emission Probability	Group	Emission Probability	Group	Emission Probability[15]
1	1.17E-04	13	3.39E-03	25	4.67E-02	37	1.32E-05
2	3.15E-04	14	2.07E-02	26	2.48E-02	38	1.78E-06
3	1.50E-03	15	5.95E-02	27	1.21E-02	39	6.04E-07
4	3.10E-03	16	6.15E-02	28	5.64E-03	40	4.31E-07
5	6.16E-03	17	7.84E-02	29	9.82E-04	41	3.75E-08
6	1.62E-02	18	1.11E-01	30	1.30E-03	42	5.01E-09
7	2.91E-02	19	6.49E-02	31	2.73E-04	43	3.62E-09
8	7.15E-02	20	2.99E-02	32	3.06E-04	44	1.34E-09
9	6.50E-02	21	5.67E-02	33	7.54E-04	45	2.79E-10
10	3.49E-02	22	4.79E-02	34	5.62E-04	46	2.83E-10
11	3.75E-02	23	5.82E-02	35	1.74E-04	47	0.00E+00
12	1.69E-02	24	3.16E-02	36	5.26E-05		

[13] Forward Group 1 (fast) is Adjoint Group 47 and vice versa.
[14] Data from [1].
[15] Emission probabilities for Forward Groups 41 – 47 are set equal to zero for computations because they significantly increase the computational expense, but contribute nothing to the detector reaction rate.

After the baseline results were established, alternative models were executed, processed, and adjusted in an iterative fashion using PENTRAN and MCNP5 to obtain designs that matched the baseline ^{3}He reaction rate and adjoint function. MCNP5 was used to more quickly establish the iterative starting point for each plug-in design by inserting estimates of the detector dimensions and then evaluating the resultant reaction rate. During this phase, one additional wrinkle was added to the computational mix by using tube lengths that were only half that (10 cm) of the actual tubes used for the final phase of the research (19.6 cm). The intent of this action was to ensure that the results of the research would be valid for more than a singular case, thereby demonstrating additional fidelity for the computational approach used herein. The overall flow for the development effort is shown in Figure 5.3.

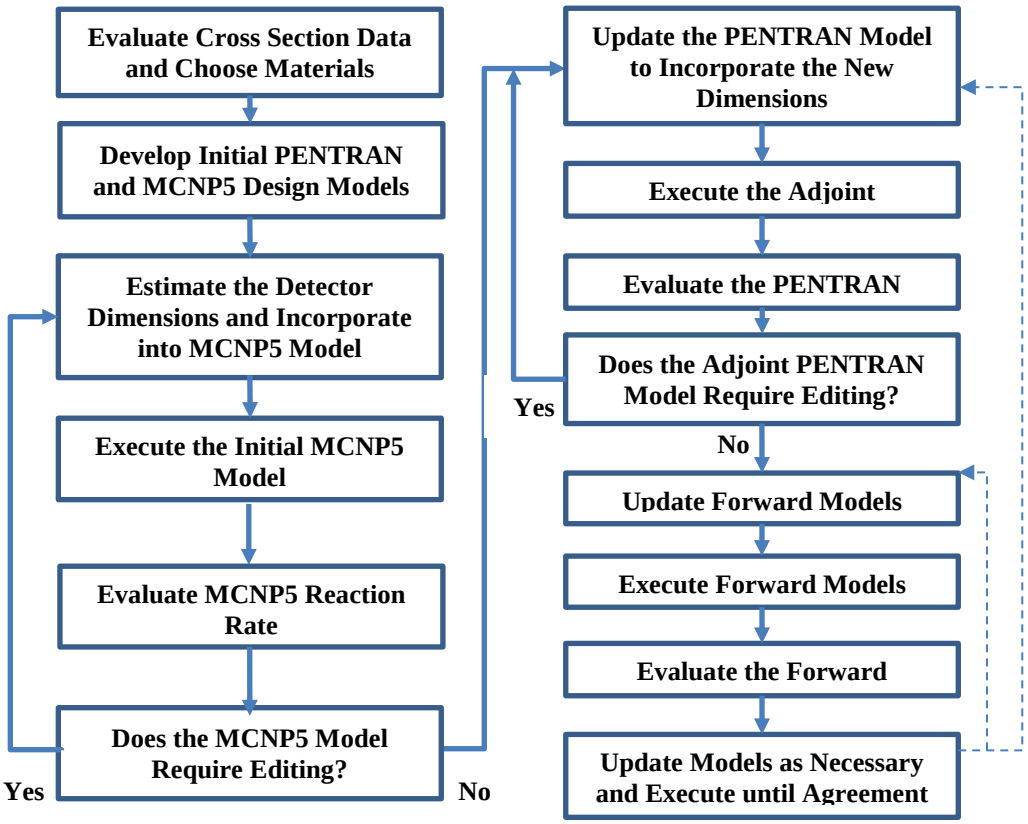

Fig. 5.3. Design Flow Path for Plug-In Detector Development .

The PENTRAN calculations utilized cross sections derived from the BUGLE-96 library by the GMIX utility. The Evaluated Nuclear Data Files Version 7 (ENDF/B-VII) continuous-energy neutron cross sections were used for the MCNP5 calculations [2].

5.3 General Detector Design Parameters

Although the detectors consisted of various materials and configurations, there were several design features that were common to all. For example, each detector used in the study was outfitted with 2 cm of polyethylene at the rear of the detector (away from the source) based on research done by Ghita et al. [1, 3 – 4]. The stipulation for the rear moderator thickness was based on achieving the highest-degree for the *albedo* response, which results from neutrons that are scattered backwards into the detector.

Another common feature was that each detector included 2 cm of polyethylene on the front-side of the detector (toward the source), 1 cm thick walls on either side, and a common height of either 10 cm or 19.6 cm as was discussed in the previous section (see Figure 5.1.). The sidewall thickness was simply a procurement result; however, the forward moderator thickness was based upon on measurements taken of the PuBe source during the equipment setup, using a varying thickness of polyethylene (0 – 6 cm) which will be discussed in Chapter 7. The only variance in the sidewall thickness occurred in the multi-detector designs with dissimilar radii. In this case, the sidewall thickness was kept at 1 cm from the outside radius of the larger tube. The 2 cm forward moderator

proved to be the optimal choice, because it provided the highest detector count rate during the source measurements.

Each model also utilized a global source that surrounded the entire detector assembly (see Figure 5.3) with vacuum boundary conditions, because an initial MCNP5 investigation of neutron reflection along the borders indicated there was < 2% albedo condition for any surface. The boundary having the greatest albedo was also a few feet from the detector, which rendered any potential albedo contribution insignificant.

Although no firm constraint exists regarding the physical size of any replacement design, serious consideration was only given for detectors that would not present any undue installation issues associated with existing detection systems. As a general rule, the width of a detector assembly presents the greatest challenge regarding plug-in potential and, since this potential is the primary research focus, an arbitrary width constraint of 7.62 cm (3 inches) was chosen to limit the detector possibilities. The choice of this constraint eliminated single-tube BF_3 detectors operating at 1-atm pressure from consideration, although it is certainly possible to create a detector with this fill pressure that mirrors the characteristics of the ^{3}He baseline detector selected for this study.

5.4 ^{3}He Detector Baseline

The baseline detector used for comparison purposes was a 1-inch diameter ^{3}He tube pressurized to 4 atm. This particular tube is discussed in detail in Chapter 7 and is a

common design that is found in various nuclear-related applications. The PENTRAN model for this baseline design is shown in Figure 5.4., with a ubiquitous source that was previously mentioned. For the initial experiments, the MCNP5 and PENTRAN models were identical, employing the materials provided in Table 5.3 and with the absorption cross sections given in Table 5.4.

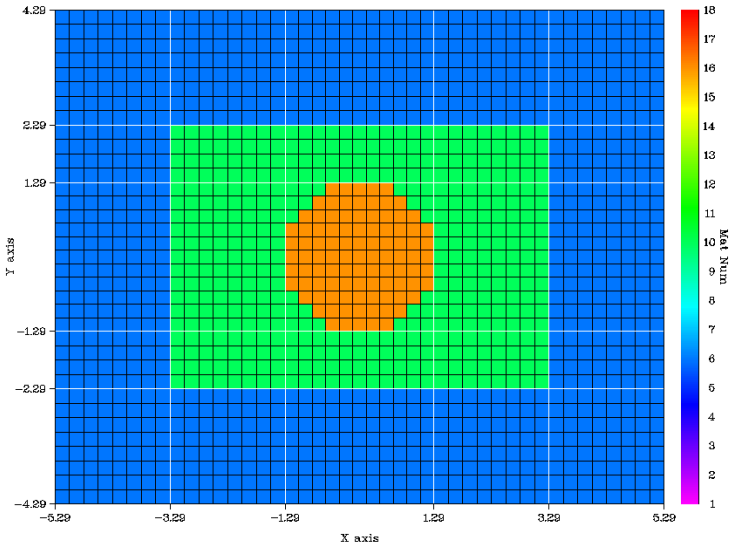

Fig. 5.4 ^{3}He baseline design.

Table 5.3. Baseline ^{3}He material data.

Number	Material	Density (g cm^{-3})	Volume (cm^{3})
1	Air Source	1.20E-03	603.20
2	Polyethylene	9.40E-01	246.25
3	^{3}He	5.39E-04	50.67

Table 5.4. Four atmosphere ^{3}He tube absorption cross sections derived from the BUGLE-96 library.[16]

Group	Σ_a (cm^{-1})	Group	Σ_a (cm^{-1})	Group	Σ_a (cm^{-1})	Group	Σ_a(cm^{-1})
1	1.88E-05	13	7.60E-05	25	1.15E-04	37	2.84E-03
2	2.11E-05	14	7.74E-05	26	1.48E-04	38	4.71E-03
3	2.39E-05	15	8.19E-05	27	2.00E-04	39	6.91E-03
4	2.67E-05	16	8.71E-05	28	2.75E-04	40	1.08E-02
5	2.93E-05	17	8.85E-05	29	3.46E-04	41	1.92E-02
6	3.27E-05	18	8.59E-05	30	3.96E-04	42	3.14E-02
7	3.70E-05	19	8.43E-05	31	4.31E-04	43	4.90E-02
8	4.45E-05	20	8.58E-05	32	4.54E-04	44	7.56E-02
9	5.74E-05	21	8.91E-05	33	5.23E-04	45	1.10E-01
10	6.52E-05	22	9.34E-05	34	7.28E-04	46	2.10E-01
11	7.08E-05	23	9.77E-05	35	1.10E-03	47	4.86E-01
12	7.47E-05	24	1.03E-04	36	1.68E-03		

Since BF_3 at 1 atm is far less efficient at neutron detection when compared to ^{3}He at 4 atm, the only possible way to get an efficiency match between the two gases is to somehow increase the amount of BF_3 gas in a system. In all simple detection cases where only the gross neutron count rate matters (e.g. portal monitors, backpack units, etc.) designers can simply increase the detector size, increase the amount of moderator, and/or add additional detectors in order to improve the efficiency without regard for shifts in the adjoint function; however, for the more difficult detection cases, the challenge of increasing the efficiency must be balanced with the requirement to maintain the overall neutron spectral response. In other words, one cannot simply insert a larger detector, obtain an acceptable cumulative count from a ^{252}Cf source at 1 m, and assume the detector will respond in equivalent fashion to the ^{3}He spectral response.

[16] Forward Group 1 (fast) is Adjoint Group 47 and vice versa.

5.5 ^{3}He-Equivalent Tube Designs Based on BF_3 Gas

The approach taken in this research was to investigate a single-tube design (Design 1) with an increased gas pressure (2 atm) and two different two-tube designs at 1 atm pressure (Designs 4 and 5) with moderation consistent with the approach discussed in Section 5.3.1. These three designs are shown in Figs. 5.5 – 5.7 below and their associated material properties and cross sections are also provided in Tables 5.5 – 5.8. As a point of convention, when two-tube designs are discussed, the rear tube is toward the left and the forward tube is toward the right as you look at the *XY* design plots.

The housings for radiation detection systems such as portal monitors generally prohibit the inclusion of additional items in horizontal directions because of electrical boards and other related items that are in close quarters with the detectors. The vertical nature of the dual-tube designs in this research was borne out of space considerations where the use of a larger or additional tube would be impossible. Aside from the increased footprint, larger tubes require a higher operating tube voltage to maintain an electrical field sufficiently large enough for efficient charge collection and to reduce recombination effects that occur in some gases at higher pressure. The magnitude of the voltage increase can be minimized by adjusting the radius of the anode wire (a) in relation to the cathode inner radius (b) as seen in Eq. 2.2. However, one advantage of a larger tube radius is that it reduces wall effects that were discussed in Chapter 2.

5.5.1 Design 1 – Large Single Tube Operating at 2 Atmospheres Pressure

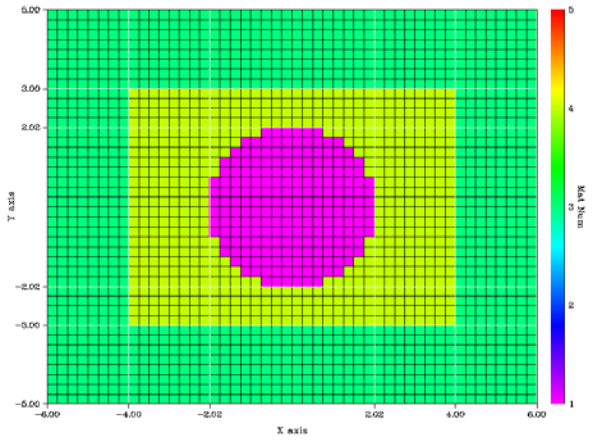

Fig. 5.5. Single BF_3 tube with 2 cm radius.

Table 5.5. BF_3 tube material data (2 atm – Design 1).

Number	Material	Density (g cm^{-3})	Volume (cm^3)
1	Air Source	1.20E-03	720.00
2	Polyethylene	9.40E-01	354.34
3	BF_3	5.45E-03	125.66

Table 5.6. Two atmosphere BF_3 absorption cross sections derived from the BUGLE-96 library (Design 1).[17]

Group	Σ_a (cm^{-1})	Group	Σ_a (cm^{-1})	Group	Σ_a (cm^{-1})	Group	Σ_a(cm^{-1})
1	2.11E-05	13	1.65E-05	25	6.01E-05	37	9.94E-04
2	2.32E-05	14	1.73E-05	26	8.09E-05	38	1.63E-03
3	2.66E-05	15	2.27E-05	27	9.98E-05	39	2.38E-03
4	3.10E-05	16	2.61E-05	28	1.25E-04	40	3.70E-03
5	3.58E-05	17	1.52E-05	29	1.48E-04	41	6.54E-03
6	4.29E-05	18	1.04E-05	30	1.75E-04	42	1.07E-02
7	4.27E-05	19	1.24E-05	31	1.77E-04	43	1.67E-02
8	3.34E-05	20	1.52E-05	32	1.84E-04	44	2.57E-02
9	1.96E-05	21	2.08E-05	33	2.07E-04	45	3.75E-02
10	2.08E-05	22	3.17E-05	34	2.77E-04	46	7.13E-02
11	1.79E-05	23	3.98E-05	35	4.04E-04	47	1.65E-01
12	1.61E-05	24	4.53E-05	36	6.01E-04		

5.5.2 Design 4 – Two Dissimilar Tubes Operating at 1 Atmosphere Pressure

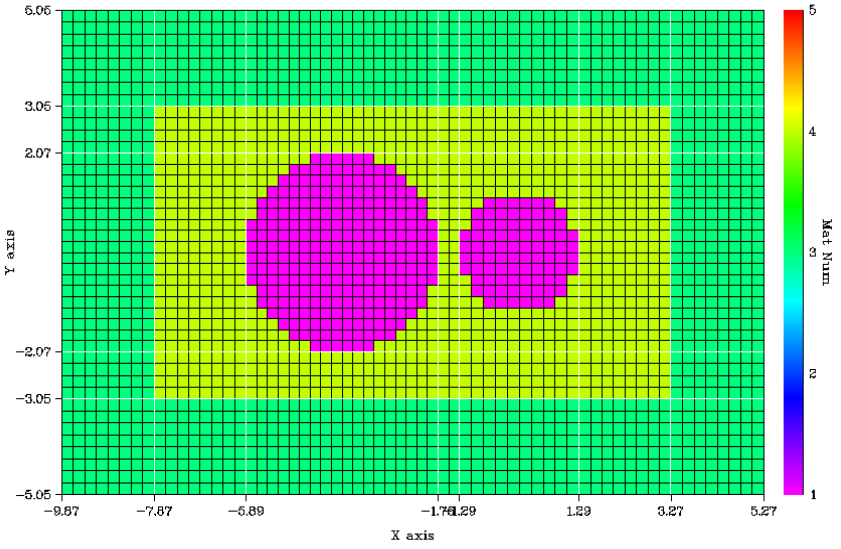

Fig. 5.6. Dual BF_3 tubes with dissimilar radii (2.05 cm rear / 1.27 cm forward).

[17] Forward Group 1 (fast) is Adjoint Group 47 and vice versa.

Table 5.7. BF_3 tube material data (1 atm – Designs 4 and 5).

Number	Material	Density (g cm^{-3})	Volume (cm^3)[18]
1	Air Source	1.20E-03	849.60 / 948.00
2	Polyethylene	9.40E-01	496.84 / 547.09
3	BF_3	2.73E-03	182.70* / 304.11†

*There is 50.67 cm^3 of BF_3 in the forward tube and 132.03 cm^3 in the rear tube.
†There is 152.06 cm^3 of BF_3 in each tube.

Table 5.8. One atmosphere BF_3 absorption cross sections derived from the BUGLE-96 library (Designs 4 and 5).[19]

Group	Σ_a (cm^{-1})	Group	Σ_a (cm^{-1})	Group	Σ_a (cm^{-1})	Group	Σ_a (cm^{-1})
1	1.06E-05	13	8.25E-06	25	3.00E-05	37	4.97E-04
2	1.16E-05	14	8.66E-06	26	4.05E-05	38	8.15E-04
3	1.33E-05	15	1.14E-05	27	4.99E-05	39	1.19E-03
4	1.55E-05	16	1.30E-05	28	6.23E-05	40	1.85E-03
5	1.79E-05	17	7.58E-06	29	7.39E-05	41	3.27E-03
6	2.15E-05	18	5.21E-06	30	8.77E-05	42	5.35E-03
7	2.13E-05	19	6.18E-06	31	8.86E-05	43	8.33E-03
8	1.67E-05	20	7.62E-06	32	9.19E-05	44	1.29E-02
9	9.82E-06	21	1.04E-05	33	1.04E-04	45	1.87E-02
10	1.04E-05	22	1.59E-05	34	1.38E-04	46	3.57E-02
11	8.94E-06	23	1.99E-05	35	2.02E-04	47	8.25E-02
12	8.07E-05	24	2.26E-05	36	3.00E-04		

[18] Volumes are listed as Design 4 / Design 5.
[19] Forward Group 1 (fast) is Adjoint Group 47 and vice versa.

5.5.3 Design 5 – Two Identical Tubes Operating at 1 Atmosphere

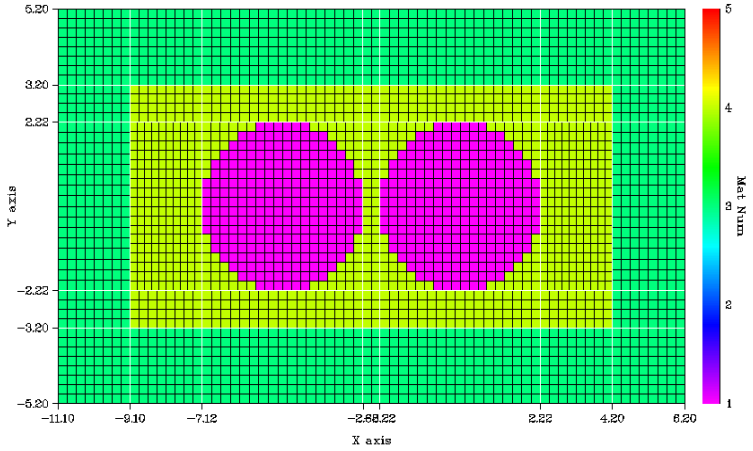

Fig. 5.7. Dual BF_3 tubes with the same radii (2.20 cm).

5.6 ^{3}He-Equivalent Tube Designs Based on a ^{10}B-Lining

Although the ^{10}B lining in these designs undergoes the same reaction as the material incorporated into BF_3 gas, there are some differences between the approaches. Whereas the BF_3 gas provides for both interaction and charge collection, the sole purpose of the solid ^{10}B lining is to introduce one of the two reaction products to a separate proportional gas. Although BF_3 performs adequately as a proportional gas, it suffers from deterioration of its counting and resolution properties with time, and especially in high neutron counting-rate and higher temperature environments [5 – 6] due to the increased release rate of fluorine free-radicals.

There are a number of commercially-available gases with superior gas amplification and resolution properties and BF_3 is typically utilized only for its photon

discrimination properties [7 – 9]. Detectors using a ^{10}B lining suffer from none of the aforementioned BF_3 drawbacks and they can be designed to have a similar efficiency as their BF_3 counterparts. And since the lining only serves as a neutron detection mechanism, the detector can be fitted with one of the more suitable proportional gases that do not suffer from the BF_3 dissociation problems [7 – 9].

One important design limitation that is unique to the ^{10}B lining is that the thickness should not exceed a density thickness of about 1 mg cm^{-2} because of the limited range of the alpha particle reaction products in the boron [6, 8 – 9]. In theory, the photon discrimination properties of boron-lined detectors are inferior to BF_3 gas because of the smaller magnitude of energy transferred to the proportional gas; however, the use of superior proportional gases such as ^4He significantly reduce the total photon interaction cross section and allows for the use of a lower high voltage. The net result is that boron-lined detectors can operate in the same intense gamma fields as that of BF_3.

Knoll mentions that the lining thickness is based on the alpha particle range in boron [8]; however, both particles contribute to the detector signal and establishing the wall thickness to achieve the highest efficiency is an art of balancing the greater reaction rate associated with a thicker lining with the higher efficiency of reaction product charge collection associated with a thinner lining. The fact that the alpha particle range is greater than that of the lithium nuclei can be shown by evaluating the stopping power of both particles in the boron lining.

The full stopping power calculation is a complex relation, but according to Evans [10], the following description is a very reasonable approximation for particles that are massive in relation to an atomic electron

$$S(E) = -\frac{dE}{dx} = \frac{4\pi z^2 e^4 NZ}{m_o V^2 A} \ln\left(\frac{Z m_o V^2}{I}\right), \tag{5.1}$$

where

S(E) is the stopping power of a specific particle as a function of energy (g or mg cm^{-2});

z is the particle atomic number (amu);

Z is the absorber atomic number (amu);

e is the electronic charge (esu);

m_o is the rest mass of an electron (MeV);

A is the atomic mass number of the absorber (amu);

V is the particle velocity (cm s-1);

N is Avagadro's Number; and,

I is the ionization potential of the absorber (eV).

By inspection of Eq. 5.1, one can determine that the maximum energy transfer possible is equal to $2m_oV^2$; therefore, Eq. 5.1 can be further reduced to

$$-\frac{dE}{dx} = \frac{144 Z z^2}{EA} \ln\left(\frac{2195E}{I}\right), \tag{5.2}$$

where E is the particle energy (MeV) and all other terms are as previously defined in Eq. 5.1. The actual ionization potential can be used in Eq. 5.2; however, if the quantity is unknown, it can also be estimated by [11]

$$I(Z) = \begin{cases} 13Z, & Z \leq 13 \\ 9.76Z + 58.8Z^{-0.019}, & Z > 0 \end{cases} . \tag{5.3}$$

Since the range of the alpha particle was previously given as 1 mg cm^{-2}, one can estimate the range of the lithium ion by substituting the appropriate values into Eq. 5.2 for each case and then evaluating the associated ratio according to

$$\frac{-\frac{dE}{dx}_{Li}}{-\frac{dE}{dx}_{\alpha}} = \frac{(9)(1.47\ MeV)\ \ln\left(\frac{(2195)(0.84\ MeV)}{(13)(5)}\right)}{(4)(0.84\ MeV)\ \ln\left(\frac{(2195)(1.47\ MeV)}{(13)(5)}\right)} , \tag{5.4}$$

which reduces to the following result:

$$\frac{dE}{dx}_{Li} = (3.37)\frac{dE}{dx}_{\alpha} . \tag{5.5}$$

Now that we have an estimate of the lithium nuclei stopping power, the range of this particle can now be estimated by remembering that the range of a particle is associated with the integral of the reciprocal stopping power per energy interval. By

substituting the known quantities into Eq. 5.6 below, an estimate of the lithium nuclei range in boron is

$$R_{Li} = \int_{0}^{E_{max}} \frac{1}{(3.37)\, S(E)}\, dE \approx 0.297\ mg\ cm^{-2}\ . \tag{5.6}$$

Although the lithium nuclei have a greater magnitude of charge (+4) compared with the alpha particles (+2), the latter are more important from a detection standpoint. This is due to the fact that the alpha particles are traveling at a velocity nearly twice that of the lithium nuclei and this produces collisions with the proportional gas molecules at dispersed intervals, thus causing ionizations further within the gas. These ionizations are more efficiently collected because electric field magnitude increases as you approach the center of a detector. The ^{10}B-lined tube designs presented in this section all utilize the 1 mg cm^{-2} wall thickness because no lined tubes were available for measurements during this research effort. The absence of these tubes precluded any efforts to draw a balance between the neutron absorption rate and the collection efficiency; however, it is clear from the literature that each of these particular designs needs to be individually evaluated in order to optimize this balance [12 – 13]. Consequently, the final plug-in designs stipulated in this section likely represent the minimum diameter case and the actual designs will need to be adjusted for the use of a 0.28 mg cm^{-2} thickness to allow for a more efficient collection of the lithium nuclei [12].

The normal density of ^{10}B is 2.34 g cm^{-3}, which means that a 1 mg cm^{-2} density thickness of ^{10}B is only 4.27E-04 cm thick (or 1.20E-04 cm for a density thickness of 0.28 mg cm^{-2})! Such a vanishingly small section of material would make it virtually impossible to establish a useable mesh size in any discrete ordinates code; therefore, in the computational models, the ^{10}B thickness was increased to 0.5 cm by using the following material balance relation and then solving for the reduced density (ρ_2)

$$\rho_1 \, dx_1 = \rho_2 \, dx_2 \, . \tag{5.7}$$

The resulting ^{10}B density of 1.998E-03 g cm^{-3} (or 5.60E-04 g cm^{-3} for a density thickness of 0.28 mg cm^{-2}) allowed for at least two meshes of 0.25 cm thickness to be used in the boron portion of the PENTRAN models. This ensured that an adequate number of interactions would occur within the sensitive volume of this particular detector and that convergence of the angular flux would proceed in an acceptable fashion. The validity of the material balance shown in Eq. 5.7 will be demonstrated in Chapter 8.

The lined detector models have also been equipped with a ^{4}He fill gas operating at 10 atm to provide an increased stopping power for the reaction products, while also presenting moderation properties that are very similar to that of ^{3}He. And while the ^{10}B lining thickness cannot be increased beyond the stipulated limitation, the detection efficiency can be improved in a manner similar to the BF_3 tubes by increasing the tube size or by adding additional tubes. These two designs are shown in Figs. 5.8 and 5.9 and their associated material data and cross sections are given in Tables 5.9 and 5.10.

5.6.1 Design 2 – Large Tube with ^{4}He Operating at 10 Atmospheres

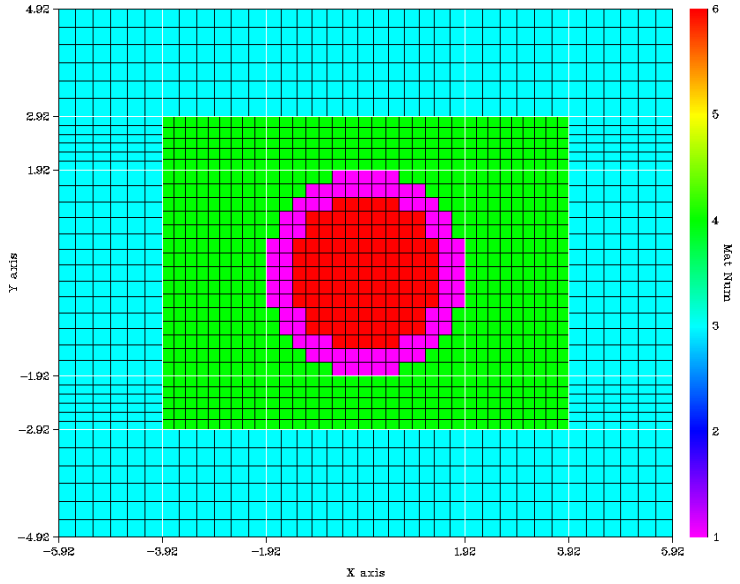

Fig. 5.8. Single ^{10}B-lined tube with a 1.90 cm radius for a ^{10}B density thickness of 1.00 mg cm^{-2} (2.37 cm radius required for 0.28 mg cm^{-2}).

Table 5.9. ^{10}B-lined tube material data (10 atm – Designs 2 and 3).

Number	Material	Density (g cm^{-3})	Volume (cm^{3})[20]
1	^{10}B Lining	2.00E-03	51.84 / 64.09*
3	Air Source	1.20E-03	707.20 / 708.00
4	Polyethylene	9.40E-01	344.26 / 182.38
6	^{4}He	1.23E-03	61.76 / 37.25

*There is 32.05 cm^{3} of ^{10}B per tube at the reduced density

[20] Volumes are listed as Design 2 / Design 3 with a reduced ^{10}B density.

Table 5.10. ^{10}B-lined tube absorption cross sections derived from the BUGLE-96 library.[21]

Group	Σ_a (cm^{-1})	Group	Σ_a (cm^{-1})	Group	Σ_a (cm^{-1})	Group	Σ_a(cm^{-1})
1	2.20E-05	13	4.03E-05	25	1.47E-04	37	2.43E-03
2	2.49E-05	14	4.23E-05	26	1.98E-04	38	3.99E-03
3	2.79E-05	15	5.55E-05	27	2.43E-04	39	5.81E-03
4	3.16E-05	16	6.38E-05	28	3.03E-04	40	9.05E-03
5	3.58E-05	17	3.70E-05	29	3.61E-04	41	1.60E-02
6	4.15E-05	18	2.54E-05	30	4.02E-04	42	2.62E-02
7	4.34E-05	19	3.02E-05	31	4.30E-04	43	4.08E-02
8	5.14E-05	20	3.72E-05	32	4.49E-04	44	6.29E-02
9	4.53E-05	21	5.09E-05	33	5.07E-04	45	9.16E-01
10	5.06E-05	22	7.74E-05	34	6.76E-04	46	1.74E-01
11	4.37E-05	23	9.73E-05	35	9.89E-04	47	4.04E-01
12	3.94E-05	24	1.11E-04	36	1.47E-03		

5.6.2 Design 3 – Twin Tubes with ^{4}He Operating at 10 Atmospheres

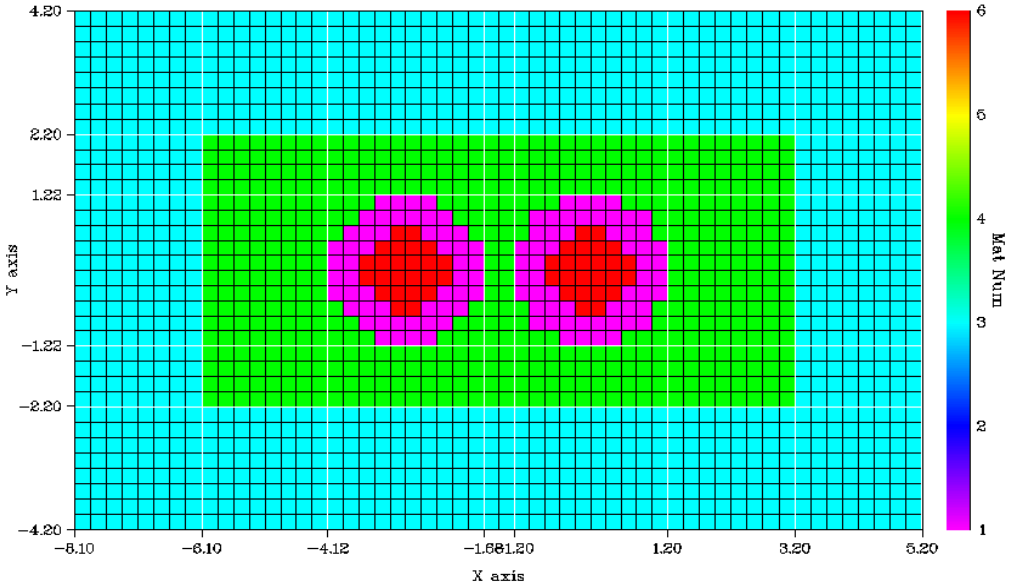

Fig. 5.9. Dual ^{10}B-lined tubes with the same radii (1.27 cm) for a ^{10}B density thickness of 1.00 mg cm^{-2} (1.84 cm radius required for 0.28 mg cm^{-2}).

[21] Forward Group 1 (fast) is Adjoint Group 47 and vice versa.

5.7 Design 6 - Single ^{10}B-Loaded Poly-Vinyl Toluene (PVT) Cylinder

The same ^{10}B that was utilized in the previously discussed designs can also be incorporated into PVT to provide for gamma and neutron measurements with a single scintillation detector [8 – 9, 14]. An upper concentration bound of 5% by weight provides for excellent neutron sensitivity, while minimizing light quenching caused by the black color of the boron. The PVT material is also an excellent moderator due to the large number of hydrogen atoms and greater density than its gas counterparts. This means that a small PVT detector can provide the equivalent sensitivity of much larger gas-filled tubes. In fact, although the PVT cylinder used in Design 6 has the same diameter as the ^{3}He tube used for measurements, it is only 4.5 cm in height, compared with 19.6 cm for the gas tube.

From a computational perspective, the PVT does, however, require some model modifications related to neutron scattering. All the other plug-in detectors previously discussed used some form of gas at densities roughly a thousand times less than PVT. The addition of hydrogen-containing compounds at higher density ensures far more scattering events in the detector than is the case with gases. This means that the simplified S_8 / P_2 approach used in the other designs is inadequate for this case. Convergence of < 1E-03 was impossible for a 1-inch diameter PVT cylinder inserted into the Figure 5.1 design space, even by reducing the universal mesh size to ~0.1 cm as shown on Figure 5.10. Therefore, in addition to reducing the mesh size for this model,

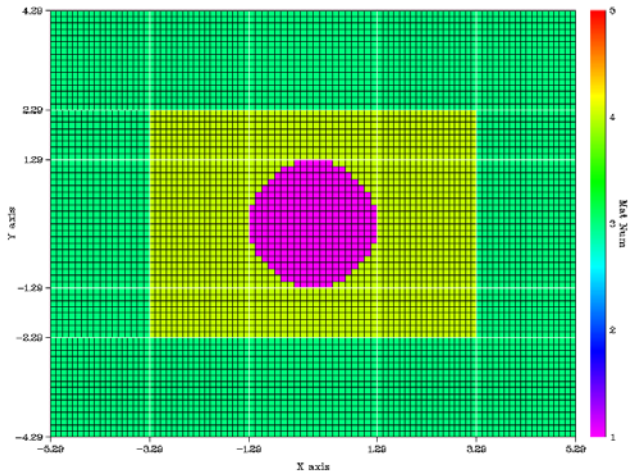

Fig. 5.10. Single 1.27 cm radius PVT cylinder (1.78 cm radius may be necessary to account for efficiency losses).

the Legendre order was increased to P_3, which provided excellent convergence (< 2E-04) for all neutron energy groups.

The use of currently-available PVT also presents challenges associated with the collection of the scintillation light output. The first of these issues is referred to as pulse-shape discrimination (PSD) and presents issues because the ^{10}B-loaded PVT is very sensitive to both photons and neutrons. Whereas the previously mentioned detectors were relatively insensitive to photon radiation and their associated electrical pulses could easily be discriminated using a simple SCA technique, PVT is more sensitive to particles with a lower-magnitude linear energy transfer (LET) such as electrons. Therefore, any attempt to use PVT for the singular characterization of neutron or photon fields must incorporate a suitable PSD method within the overall system. Plastic scintillators have typically exhibited PSD capabilities that inferior to that of liquid scintillators [8 – 9, 14];

however, new crystalline plastics are currently being developed that exhibit PSD characteristics that rival liquid scintillator materials and that will essentially eliminate this limitation [15 – 18].

In addition to the PSD challenges, organic scintillators such as PVT can also suffer from the loss of a portion of the scintillation output signal because of the disparity of the refractive indices at the junction between the PVT and surrounding materials. When the light photons exit the plastic, some of the light is reflected, depending on the polarization and angle of incidence of the photons. The critical angle of incidence that determines whether the photons are scattered or absorbed is described by Brewster's Law [14]. This law states that the photons will not be reflected if their angle of incidence, as measured from the centerline is greater than or equal to the Brewster's Angle (θ_B) defined by

$$\theta_B = \tan^{-1}\left(\frac{n_2}{n_1}\right), \tag{5.8}$$

where n_1 refer to the refractive index of the transmitting material (i.e. PVT here) and n_2 is the refractive index of the material opposite the junction (i.e. polyethylene here).

The PVT used in the model for this section is identical to EJ-256[22] or BC-454[23] with 5% ^{10}B by weight. This particular material has a refractive index n_1 = 1.58 [8] with a 425 nm wavelength of maximum emission. Meanwhile, the index for the surrounding

[22] Eljen Technologies, 1300 W. Broadway, Sweetwater, TX 79556, (325) 235-4276.
[23] Saint-Gobain Crystals, 17900 Great Lakes Parkway, Hiram, OH 44234, (440) 834-5600.

polyethylene is n_2 = 1.512 and, substituting these values into Eq. 5.2 yields a Brewster's Angle of only 43.74º [19]. Light photons scattered at angles greater than this will be lost because they will not be reflected back into the PVT matrix and received through the optical coupling and into the photomultiplier tube. Therefore, in most cases, users will have the PVT covered with a TiO_2-based white paint with n_2 = 2.731 or a vermillion-colored paint with n_2 = 3.14, which yields Brewster Angles of 60.90º - 63.14º and greatly enhances the detection efficiency compared with the bare case.

Since MCNP5 does not allow the user to account for efficiency losses associated with the scintillation light output or edge effects in the PVT, this particular design will likely need a larger PVT diameter of up to 1.78 cm in order to account these and other efficiency loss mechanisms, which could reach 24%. As was the case with the ^{10}B-lined tubes, each particular system design will require testing in order to identify the exact plug-in dimensions. The material data and cross sections used for the PENTRAN calculations are shown in Tables 5.10 and 5.11.

Table 5.11. ^{10}B-loaded PVT material data (5% ^{10}B – Design 6).

Number	Material	Density (g cm^{-3})	Volume (cm^3)
1	PVT	1.03E+00	22.80
3	Air Source	1.20E-03	295.68
4	Polyethylene	9.40E-01	112.81

Table 5.12. ^{10}B-loaded PVT absorption cross sections derived from the BUGLE-96 library.[24]

Group	Σ_a (cm^{-1})	Group	Σ_a (cm^{-1})	Group	Σ_a (cm^{-1})	Group	Σ_a(cm^{-1})
1	3.11E-03	13	2.01E-04	25	7.26E-04	37	1.21E-02
2	4.07E-03	14	2.11E-04	26	9.79E-04	38	1.98E-02
3	4.81E-03	15	2.75E-04	27	1.21E-03	39	2.89E-02
4	8.10E-03	16	3.16E-04	28	1.50E-03	40	4.50E-02
5	4.08E-03	17	1.84E-04	29	1.79E-03	41	7.95E-02
6	2.79E-04	18	1.27E-04	30	1.99E-03	42	1.30E-01
7	2.17E-04	19	1.50E-04	31	2.13E-03	43	2.02E-01
8	2.56E-04	20	1.85E-04	32	2.23E-03	44	3.12E-01
9	2.26E-04	21	2.53E-04	33	2.52E-03	45	4.55E-01
10	2.52E-04	22	3.83E-04	34	3.36E-03	46	8.66E-01
11	2.18E-04	23	4.81E-04	35	4.91E-03	47	2.00E+00
12	1.97E-04	24	5.47E-04	36	7.30E-03		

[24] Forward Group 1 (fast) is Adjoint Group 47 and vice versa.

5.8 References

1. Ghita, G., Comprehensive Modeling of Special Nuclear Materials Detection Using 3-D Deterministic and Monte Carlo Methods. University of Florida Dissertations, 2008.

2. Chadwick, M., et al., ENDF/B-VII.0: Next Generation Evaluated Nuclear Data Library for Nuclear Science and Technology. Nuclear Data Sheets, Vol. 107, Issue 12, pp. 2931 – 3060, Dec., 2006.

3. Ghita, G., Sjoden, G., Baciak, J., Walker, S., and Cornelison, S., An Equivalent Neutron Source for Weapons-Grade Plutonium Derived from a Spectrum-Shifted PuBe Source. Proceedings of SPIE 2008, Defense and Security Symposium, 6945, Orlando, FL, March, 2008.

4. Ghita, G., Sjoden, G., and Baciak, J., Computational and Experimental Validation of a WGPu Neutron Leakage Source Using a Shielded PuBe (α,n) Neutron Source. Nuclear Technology, Vol. 168, 310, 2009.

5. Koperny, S. and Kowalski, T., Performance of Proportional Counters Under High Count Rate, High Gas Gain, and at High Working Gas Pressure. Nuclear Physics B, 197, pp. 370 – 373, 2009.

6. Baaliouamer, M., Belaragueb, C., and Mazed, D., Gas Gain Measurement in Helium-Isobutane Mixtures Filled Proportional Counters. Nuclear Instruments and Methods in Physics Research A, 382, pp. 490 – 494, 1996.

7. Mazed, D., Experimental Gas Amplification Study in Boron-Lined Proportional Counters for Neutron Detection, Radiation Measurements, 42, pp. 245 – 250, 2007.

8. Knoll, G., Radiation Detection and Measurement, 4th ed. John Wiley & Sons, Inc., New York, 2010.

9. Tsoulfanidis, N. and Landsberger, S., Measurement and Detection of Radiation, 3rd ed., CRC Press, Boca Raton, FL, 2011.

10. Evans, R., The Atomic Nucleus, Krieger Publishing, Co., Malabar, FL, 1985.

11. Attix, F., Introduction to Radiological Physics and Radiation Dosimetry, John Wiley & Sons, Inc., New York, 1986.

12. McKinney, K., Anderson, T., and Johnson, N., Optimization of Coating in Boron-10 Lined Proportional Counters, IEEE Transactions on Nuclear Science, Vol. 60, No. 2, April 2013.

13. Lintereur, A., Siciliano, E., and Kouzes, R., Boron-10 Lined Proportional Counter Model Validation, Pacific Northwest National Laboratory (PNNL), PNNL Report-21501, June 2012.

14. Birks, J., The Theory and Practice of Scintillation Counting, Pergamon Press, Oxford, 1964.

15. Lawrence Livermore National Laboratory (LLNL), U.S. Patent Publication No. 2010/0256923, Compounds for Neutron Radiation Detectors and Systems Thereof (IL11668). LLNL, Livermore, CA, 2010.

16. Lawrence Livermore National Laboratory (LLNL), U.S. Patent Publication No. 2010/0252741, Solution-Grown Crystals for Neutron Radiation Detectors and Methods of Solution Growth (IL11950). LLNL, Livermore, CA, 2010.

17. Hull, G., Zaitseva, N., Cherepy, N., Newby, J., Stoeffl, W., and Payne,S., New Organic Crystals for Pulse Shape Discrimination, IEEE Transactions on Nuclear Science, Vol. 56, No. 3, June 2009.

18. Zaitseva, N., Newby, J., Hamel, S., Carman, L.,Faust, M., Lordi, V., Cherepy, N., Stoeffl, W., and Payne, S., Neutron Detection with Single Crystal Organic Scintillators, Proceedings of SPIE, Vol. 7449, pp. 744911-1 – 744911-10, 2009.

19. Refractive Index Database, located at www.filmetrics.com/refractive-index-database , Filmetrics, Inc., San Diego, CA 92121, accessed from April – May, 2013.

CHAPTER 6
EXPERIMENTAL CONDITIONS

This chapter provides a description of the conditions that existed during the measurement period. General information is provided about the area where the measurements were conducted along with a description of the radioactive source used to produce the detector responses.

6.1 Test Facility Description

6.1.1 General Area

The measurements for the gas-filled detectors were conducted in a secure room associated with the Florida Institute of Nuclear Detection and Security (FINDS). FINDS was program that had been mandated by the State of Florida in 2004 to engage in the design and testing of detection systems for homeland security applications. This greater portion of the room was empty with the exception of a large *CONEX* (Container Express) that had been placed here for use in various cargo monitoring experiments.

There were also two internal rooms within the FINDS research area that housed computer equipment and a CT scanner associated with the medical physics program as shown in Figure 6.1. The discrimination setting for each neutron detector system was evaluated with and without exposure to a ^{137}Cs source because of the presence of the CT device. This precaution was taken to ensure that photons emanating from the scanner

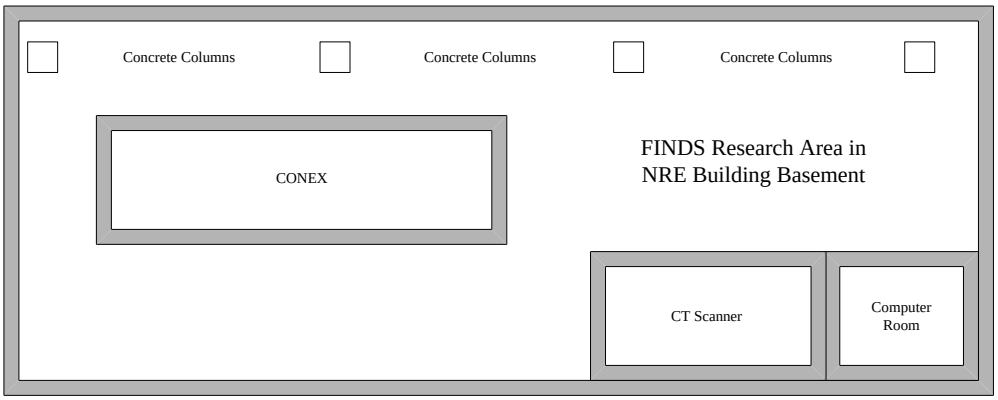

Fig. 6.1. Overhead view of the FINDS research area.

would not produce enough coincidence pulses in the detector tubes to cause an elevation in the neutron count rate, which could possibly skew the counting results and render the computational modeling comparisons invalid.

The overall dimensions of the room were 60 feet x 30 feet x 20 feet (length x width x height). There were four separate concrete columns that support the roof inside this research area; however, only one of the columns was in close enough proximity to potentially reflect neutrons back into the detectors.

6.1.2 CONEX Container

The CONEX is multi-purpose container used for safe and secure storage and shipping of materials along a global intermodal route that can include road, rail, or seagoing vessels. CONEX containers come in various sizes according to the application and they can range from 8 – 56 feet in width, 8 – 9.5 feet in height, and lengths of > 10

feet. Since these containers are routinely used to bring foreign goods into the U.S., the use of a CONEX was a natural choice.

The particular container used in this research effort had dimensions of 20 feet (length), 8 feet (width), and 8 feet (height), and the walls, floor, and ceiling of the container consisted of 14 gauge (1/16 or 0.0625 inches) galvanized steel. An example of this type of container is given in Figure 6.2, while an internal view of the actual CONEX used in this research is provided in Figure 6.3. The latter figure also shows the placement of the radioactive source within the container itself. A more thorough discussion of the source and its configuration will be covered in the subsequent section of this chapter. For orientation purposes, the detector and the concrete columns were located beyond the wall on the left side of Figure 6.3.

Fig. 6.2. CONEX example.

Fig. 6.3. Interior view of the CONEX container (reflected conditions).

All portions of the CONEX were at least six feet away from any other wall inside the basement with the exception of a single concrete column. An expanded view of the research area around the CONEX is provided as Figure 6.4 and clearly shows this column, which was offset from the center of the southern CONEX wall by a few feet. Ordinarily, the detectors and source would have been repositioned; to prevent any potential scatter from the column from reaching the detectors; however, because of some additional testing that was taking place in the room, no other arrangements were available. Therefore, an MCNP5 evaluation was conducted to verify that the column did not produce an albedo effect that needed to be incorporated into the computational models as discussed in Chapter 5. During the equipment set up, a number of measurements were also taken to determine the scattering effect of the column and the results showed that there was a negligible effect (<<1%). The measurement results,

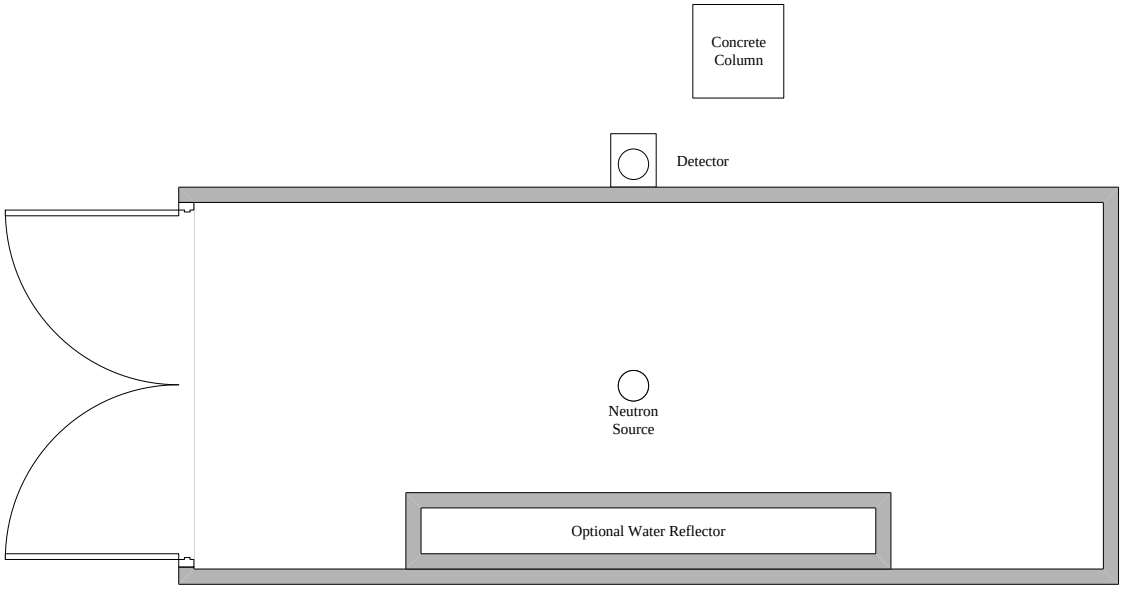

Fig. 6.4. Expanded view of the floor plan surrounding the CONEX.

coupled with the fact that any scatters would be uniformly seen by all the detectors, meant that this column did not need to be incorporated into the computational models.

6.2 Neutron Emissions

6.2.1 Source Construction

The neutron emitter used in these experiments was a plutonium-beryllium (^{239}PuBe) source that was manufactured by Mound Laboratories in June, 1971. PuBe is a very popular neutron source because of the long half-life of ^{239}Pu (~24000 years) which lends stability to the neutron emissions and the reduced photon background compared to other mixtures such as radium-beryllium (RaBe), americium-beryllium, and polonium-

beryllium (PoBe). Neutrons are produced in the PuBe according to the following reaction

$$ {}^{4}_{2}He \; + \; {}^{9}_{4}B \rightarrow ({}^{13}_{6}C)^{*} \rightarrow + \; {}^{12}_{6}C + \; {}^{1}_{0}n + \; 5.71 \, MeV \, , \tag{6.1} $$

which, due to variances in the excitation energy of the compound nucleus, yields a complex neutron energy spectrum with an average energy of 4.61 MeV.

Beryllium is an effective target in neutron sources because the binding energy of the last neutron is only 1.66 MeV and, since it is a light element, its nucleus presents a relatively small coulomb repulsion to an incident alpha particle, which makes the interaction more likely. To ensure the best neutron yield, it is important to achieve a homogenous mixture of the alpha-emitter and the beryllium within the active source material. PuBe sources of this type have a typical yield of ~10^{7} $n\ s^{-1}\ Ci^{-1}$ (Curie) of ^{239}Pu and generally contain up to 1 *Ci* or ~16 g of ^{239}Pu. Sources of this type are doubly-encapsulated to ensure the actinide is adequately sealed/protected and that expansion of the source due to the buildup of ^{4}He from the alpha decay does not result in a capsule breach. Tantalum has very similar thermal and mechanical properties to ^{239}Pu; therefore, this metal is almost always used as the inner capsule liner, and with a stainless steel outer layer as seen in Figure 6.5.

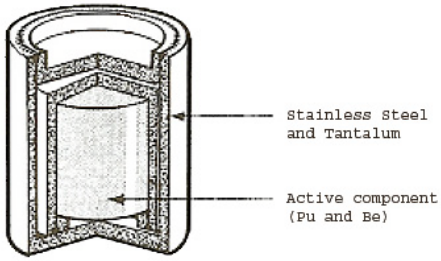

Fig. 6.5. PuBe source configuration [1]

According to the shipping documents provided by Mound Laboratories, this PuBe source had a capsule density of 4.35 g cm^{-3}, with 7.86 g of beryllium and 15.02 g of ^{239}Pu (0.94 *Ci*). The manufacturer's documents also specified the cylindrical dimensions of the outer container as 2.59 cm (diameter) and 3.68 cm (height). The stated emission rate was listed as 1.93×10^6 *n* s^{-1}, which produced a dose rate of 100 *mrem* h^{-1} at 88.9 cm. This particular source was extensively studied by Ghita et al [1, 3 – 4] using both Monte Carlo and deterministic transport techniques. The calculated neutron leakage accounting for sub-critical multiplication and age of the Pu resulted in an average emission rate of $(1.925 \pm 0.0001) \times 10^6$ *n* s^{-1}, which is within round-off of the manufacturer's stated emission rate [1]. The BUGLE-96 neutron energy bins used in this research were previously provided in Table 4.2 and the probability of emission associated with these bins was given in Table 5.1. The information listed in those two tables formed the basis for the source term for both the PENTRAN and MCNP5 models.

6.2.2. Moderator Materials

The neutron source was measured in both a bare and reflected condition inside the CONEX container. The reflected case used containers of bottled water, 3-feet thick, that were placed on the north side of the source (away from the detector) as shown in Figure 5.3. This water was removed for the bare source exposures and the only other moderating material consisted of polyethylene that encased the detectors. Although counting information was gathered for the bare and reflected conditions, only the bare case was used for direct comparison with the computational models because the arrangement and openings between the water bottles produced variations that would skew the comparisons to the computational models.

6.2.3 Shielded Container

One of the main objectives of any special nuclear material (SNM) detection system is to identify plutonium in cargo that is passing through a border crossing or into a port of entry (POE). The testing of such systems have been hampered over the years by a lack of (α, n) sources and/or plutonium metal due to security issues or the availability of another suitable source such as ^{252}Cf because of radioactive decay or supply limitations. Ghita et al. was able to overcome these technical issues through the use of a high-purity nickel scatter shield that can shift and alter a PuBe neutron spectrum to match that of subcritical multiplication in Pu metal, with average emission energy of only 2.11 MeV [3].

An example of the shielded spectrum from this research is shown in Figure 6.6 and demonstrates the excellent spectral response provided by the nickel shielding. The nickel geometry consisted of a right-cylinder with a diameter of 15.6 cm and a total height of 14.6 cm. Since a casting of pure nickel would have been very expensive, the shield was formed by stacking flat cylindrical pieces of nickel and using clamps to ensure good contact between individual pieces. The inner portions of the nickel plates had a 3 cm hole drilled through them to allow for the placement of the PuBe source. This configuration resulted in a total of 6.3 cm of nickel between the source wall and the exterior surface of the shield.

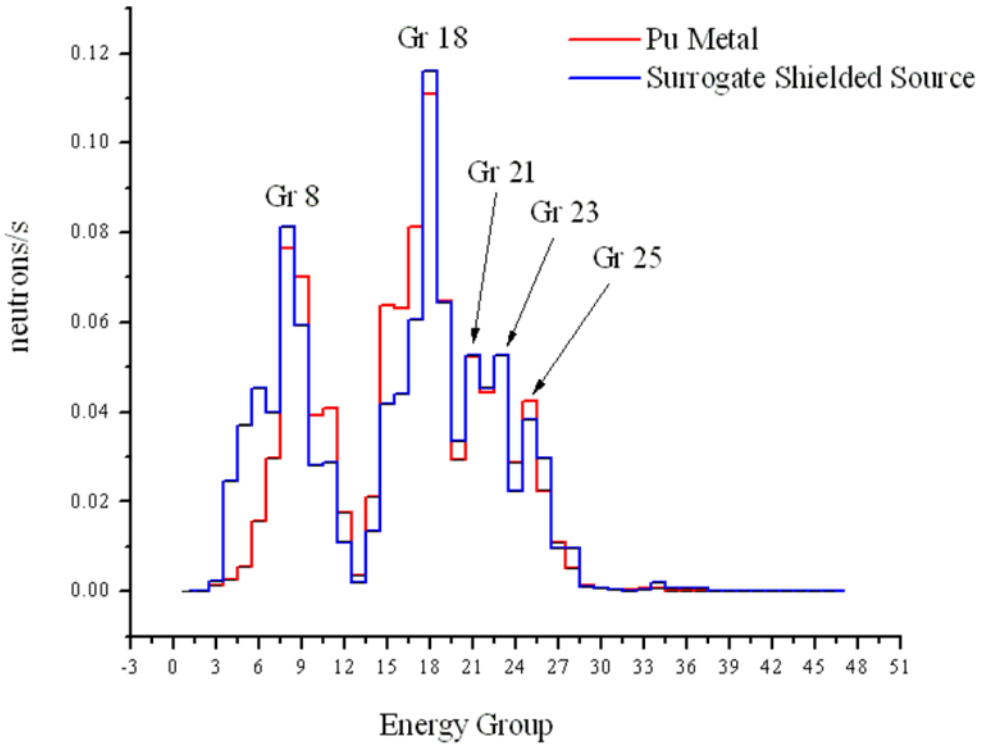

Fig. 6.6. Forward neutron leakage spectra from Pu metal and shielded PuBe [3].

The source was placed into the shield as shown in Figure 6.7 and the resulting cylinder had 5.3 cm of nickel beneath the PuBe and 4.8 cm above it. The nickel plates were clamped as shown in Figure 6.8 to match the laboratory conditions to the computational models as closely as possible [1, 3 – 4]. The nickel-shielded PuBe source was used for all the detector measurements and was also incorporated into the associated computational models to ensure a direct comparison could be made between all results.

Fig. 6.7. Placement of the PuBe source into the nickel shield.

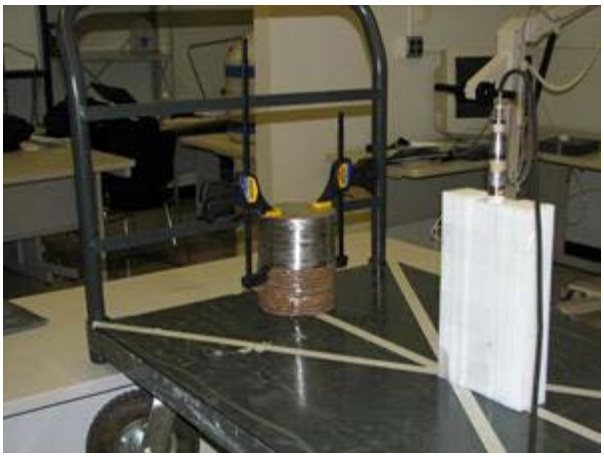

Fig. 6.8. PuBe source in its nickel shield.

6.3 References

1. Ghita, G., Sjoden, G., and Baciak, J., Computational and Experimental Validation of a WGPu Neutron Leakage Source Using a Shielded PuBe (α,n) Neutron Source, Nuclear Technology, Vol. 168, 310, 2009.

2. Chadwick, M., et al., ENDF/B-VII.0: Next Generation Evaluated Nuclear Data Library for Nuclear Science and Technology. Nuclear Data Sheets, Vol. 107, Issue 12, pp. 2931 – 3060, Dec., 2006.

3. Ghita, G., Comprehensive Modeling of Special Nuclear Materials Detection Using 3-D Deterministic and Monte Carlo Methods. University of Florida Dissertations, 2008.

4. Ghita, G., Sjoden, G., Baciak, J., Walker, S., and Cornelison, S., An Equivalent Neutron Source for Weapons-Grade Plutonium Derived from a Spectrum-Shifted PuBe Source. Proceedings of SPIE 2008, Defense and Security Symposium, 6945, Orlando, FL, March, 2008.

CHAPTER 7
NEUTRON DETECTOR SETUP AND MEASUREMENTS

The correlation between the laboratory measurements taken with the ^{3}He and BF_3 detectors and their associated computational models discussed in Chapter 5 provided the fidelity by which the modeling techniques could be extrapolated to other materials, such as the PVT and ^{10}B-loaded PVT. The procedures for preparing and using both gas-filled detection systems were identical, therefore, these issues will be discussed in a single section and noting any differences.

7.1 Laboratory Equipment and Operational Setup

7.1.1 Laboratory Equipment

Prior to monitoring for neutrons, the appropriate individual components had to be gathered and assembled into a functioning system that would meet the needs of the research. The components and their associated arrangement are shown in Figure 7.1. These items were were arranged into a nuclear instrument module (NIM) bin as shown in Figure 7.2. The system components were almost exclusively manufactured by ORTEC[25] with the exception of a Canberra[26] Model 2006 pre-amplifier. The other system components consisted of a Model 556 high-voltage supply, Model 410 linear amplifier,

[25] ORTEC, 801 South Illinois Avenue, Oak Ridge, TN 37831
[26] Canberra Industries, 800 Research Parkway, Meriden, CT 06450

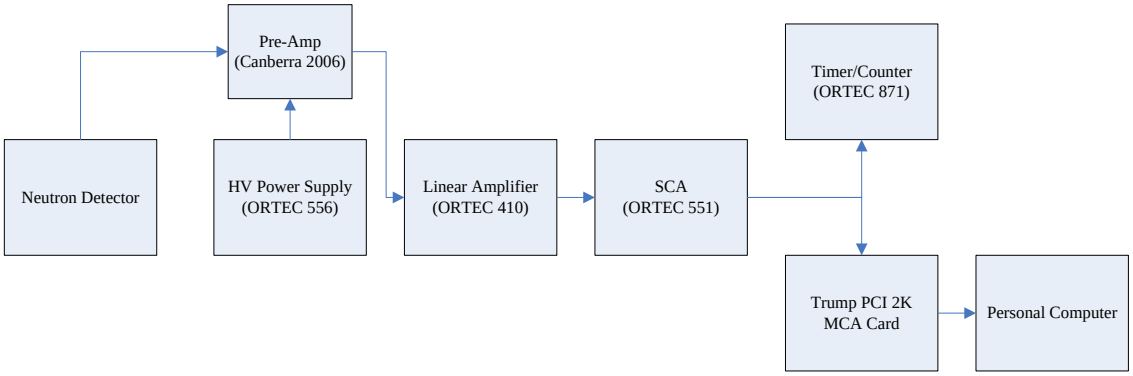

Fig. 7.1. ^{3}He system setup.

Fig. 7.2. NIM components for the ^{3}He and BF_3 systems.

and a Model 551 single-channel analyzer (SCA). Bipolar output pulses (seen in Figure 7.3) from the linear amplifier were fed to the SCA using a 2 μs shaping time. The SCA output was directed to either a Model 871 timer/counter or a Trump PCI 2K multi-channel analyzer (MCA) card, depending on whether the system counting parameters or the output pulse shape or spectra were being evaluated. The information from the Trump

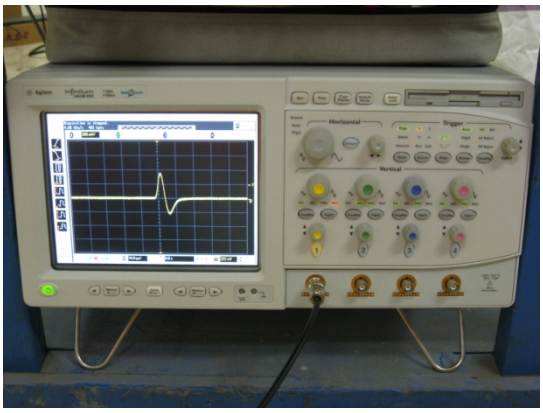

Fig. 7.3. Bipolar output pulse from the linear amplifier.

PCI card was processed through a personal computer and the ORTEC Maestro software to display the differential pulse height spectra.

The ^{3}He neutron detector was a Model 252 manufactured by LND, Inc. and was pressurized to 4 atm (3040 torr). The detector had an overall length of 11.20 inches with an effective length of 8.0 inches and an active volume of 89.01 cm^{3}. The BF_3 detector was a Model G-10-8 manufactured by the N. Wood Counter Laboratory, Inc. and with an internal pressure of 0.96 atm (730 torr), which will be rounded to 1 atm for the remainder of this document. The BF_3 gas was enriched with 96% ^{10}B to increase the neutron absorption in the detector. The tube itself had an overall length of 10 inches and, like the LND-252, an effective length of 8.0 inches with an active volume of 89.01 cm^{3}. The two tubes are shown side-by-side in Figure 7.4.

Fig. 7.4. Neutron tubes used in the study.

7.1.2 Operational Setup

Prior to establishing the initial system parameters, an ORTEC Model 480 pulser and an Infinium[27] Model S4832B oscilloscope (Figure 6.3) were used in conjunction to verify the electrical connections were sound and to ensure the electronic components were trouble free. Prior to using the system, the oscilloscope was also used together with a 1 *Ci* PuBe source and a 10 μCi ^{137}Cs source to determine an appropriate setting for the linear amplifier gain and the lower limit of detection (LLD) for the SCA. A coarse gain of 30 (0 fine gain) and an LLD of 200 milli-Volts (mV) or 20 pulse height units (PHU) on these units ensured that only single neutron events would be registered by the detection system by taking advantage of the large *Q*-value of the neutron interactions as compared with photon interactions. These settings worked well and were applied to both detector types.

[27] Agilent Technologies, Inc., 5301 Stevens Creek Blvd., Santa Clara, CA 95051

The final operational step that had to be completed before using the system was to determine the optimal operating voltage for the tubes by systematically increasing the HVPS voltage until a stable plateau was achieved. This action was necessary to ensure that minor fluctuations in the building voltage did not adversely impact the counting results of the experiment. The HVPS was energized at 100 V and allowed to stabilize for five minutes prior to beginning the process. During this interval, the bare PuBe source was removed from its container and positioned one foot away from the neutron tube centerline (see Figure 7.5). After the stabilization period was over, a one-minute count was entered into the timer/counter to stop the counting process and display the final count information. A series of these one-minute counts was taken with both tubes using incremental voltage increases in steps of 100 V. The incremental counts were continued to a maximum voltage of 2000 V for ^{3}He or 2300 V for BF_3.

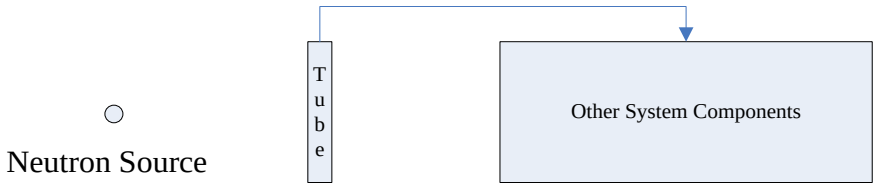

Fig. 7.5. Source-to-detector arrangement used for the operational tests.

The gathered data were plotted and evaluated to establish the optimal operating voltage for each probe. Prior to using each probe, the correct voltage was input to the HVPS and the system was allowed to stabilize for at least five minutes to preclude recording errant pulses. Once this stabilization period was over, the system was essentially ready for use; however, since one of the goals of this research is to establish a methodology for

evaluating ^{3}He candidate replacements, it was vital to gain an understanding about the system response in the presence of a mixed field of photon and neutron radiation.

The system response was evaluated according to the important features associated with the differential pulse height spectra of the two gases. The important features being considered were the overall spectral appearance and the expression of peaks associated with the decay directly to the ground state or subsequent decay from the first excited state of the nucleus. By comparing the baseline spectra to those associated with a mixed-field component, a judgment could be rendered about the ability of the detector to discriminate against photons. The baseline information was obtained through a five-minute count of the bare PuBe source at a distance of 3 feet. A second five-minute count was subsequently performed after the 10 μCi ^{137}Cs source was taped directly onto the cylindrical wall of the tube. The data from both tests were exported from the Maestro software into Microsoft Excel for plotting.

7.2 Measurements of the Shielded PuBe Source

After the completion of the operational checks, the PuBe source was inserted into the shielded container of nickel as discussed in Chapter 6. Once the source was prepared, measurements were taken with both a reflected and bare source condition as was also previously described in Chapter 6. A series of two-minute counts were completed with each source configuration and with varying amounts of a polyethylene moderator between the source and detector. The polyethylene thicknesses were increased in increments of 0.5 cm from a bare condition and up to a maximum of 6 cm. The *bare*

moderator configuration wasn't totally bare as the name implies, but consisted of a specially-machined rectangular parallel piped which maintained the majority of the front hemisphere (toward the source) of the detector open as seen in Figs. 7.6 and 7.7. This particular moderator had a height of 21 cm, a width of 4.54 cm (toward the source), and a width of 6 cm on the axis perpendicular to the tube shown in Figure 7.6. Ghita determined that 2 cm of the polyethylene should be maintained behind the detector to maintain the spectral quality of the neutron source, while maximizing the performance of gas-filled detectors, therefore, this constant amount was maintained on the rear-side of the detector (away from the source) during each measurement [1].

The standard parallel piped used for all other measurements was originally cut to the same overall dimensions of the *bare* unit by the author as part of his assistance to Ghita [2 – 3]; however, the detector opening was drilled through the centerline of the polyethylene block as shown in Figure 7.8. This machining left only 1 cm of polyethylene on both sides of the detector, so an additional 1.0 cm of polyethylene was added to the front and rear of the base unit to achieve the optimal amount. Figure 7.8 shows the addition to the rear of the detector and the identical thickness was added to the front of the detector as well. The final piped was firmly secured against the side of the CONEX by using a test assembly that clamped onto the outside of the polyethylene.

Fig. 7.6. ^{3}He detector inserted into the bare polyethylene parallelepiped (from an unrelated experiment).

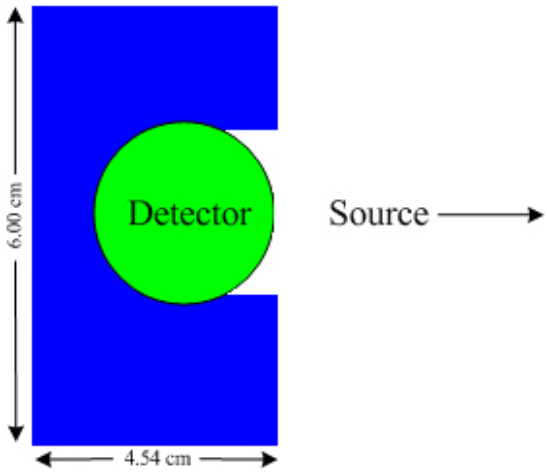

Fig. 7.7. Bare polyethylene parallelepiped configuration.

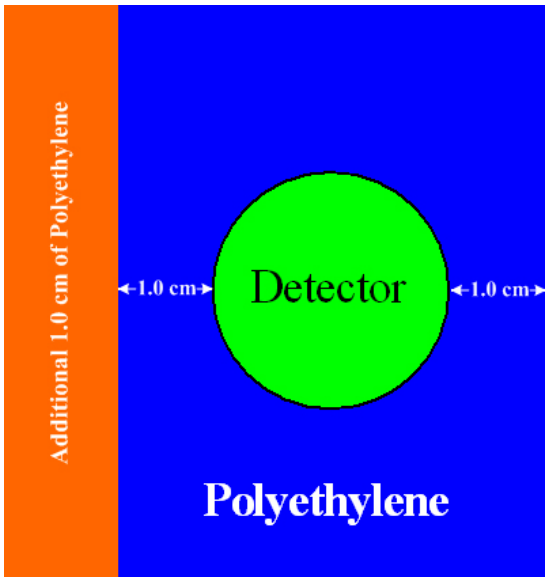

Fig. 7.8. Standard polyethylene parallelepiped configuration.

Figure 7.9 shows how the tube and moderator assembly were secured during the experiments. The polyethylene was marked to ensure the detectors were always attached to the stand at the correct height of 30.6 cm above the floor, which aligned the tube centerline with the neutron source. The tubes themselves fit snugly within the center of the polyethylene, so that no restraint was necessary to hold them in place. As the experiment progressed, additional polyethylene slabs were attached to the base unit to achieve the desired thickness for each individual measurement. The extra slabs were secured with duct tape to the front face of the polyethylene (toward the CONEX container).

The source measurements detailed in this section provided the standard by which the computational methods were judged. The successful comparison of these models to

Fig. 7.9. Moderated detector assembly positioned against the CONEX container.

actual measurements meant that the computational approach could be trusted to assess the usefulness of designs for serving as plug-in replacements for the baseline ^{3}He detector. The results of all the various research tasks, including the neutron measurements, are provided in the following chapter. The measurement data will be presented immediately following some general statements because of their importance to the research.

7.3 References

1. Ghita, G., Sjoden, G., Baciak, J., Walker, S., and Cornelison, S., An Equivalent Neutron Source for Weapons Grade Plutonium Derived from a Spectrum-Shifted PuBe Source. Proceedings of SPIE 2008, Defense and Security Symposium, 6945, Orlando, FL, March 16-21, 2008.

2. Ghita, G., Sjoden, G., and Baciak, J., Computational and Experimental Validation of a WGPu Neutron Leakage Source Using a Shielded PuBe Neutron Source, Nuclear Technology, Vol. 168, 310, 2009.

3. Ghita, G., Comprehensive Modeling of Special Nuclear Materials Detection Using 3-D Deterministic and Monte Carlo Methods. University of Florida Ph.D. Dissertations, 2008.

CHAPTER 8
RESULTS AND DISCUSSION

The previous four chapters have provided the necessary detail about the computational modeling and neutron measurements employed for developing equivalent spectrum plug-in designs for a baseline 4-atm ^{3}He detector. Although no specific results were presented in Chapter 4, the activities connected to the remaining chapters all produced results that require elaboration. These details will be covered in this chapter; however, before doing so, a brief review of how we arrived at this point is in order.

Chapter 5 detailed the computational modeling activities along with the designs that were produced from the application of the transport codes described in Chapter 4. The experimental testing facility profile was the focus of Chapter 6, and the information presented defined the overall facility configuration, moderating materials, and the nickel-filtered PuBe source used for the neutron measurements. The information in Chapter 7 specifically pertained to the neutron detection systems used for the laboratory measurements and described the individual system components for each and their operational setup. The discussion also covered the protocols that yielded the neutron measurements of the nickel-filtered PuBe source. Since the neutron measurements were conducted prior to any other effort associated with this research, we will begin this chapter with a presentation of the measurement results and progress according to the order events in each associated chapter.

8.1 Operational Setup

8.1.1 ^{3}He Detection System

The data for the high-voltage determination was tabulated in Table 8.1 and plotted in Figure 8.1 to help select the optimal tube operating voltage. Since only one data point was taken at each voltage, the error term is quoted at 1.96 times the standard deviation (95% confidence) of the count. The beginning of the proportional plateau can be seen at 1500 V, and the plateau continues to 1800 V, after which the count rate increases substantially. An optimal operating voltage of 1700 V was selected for the ^{3}He tube, which was directly in the mid-range of the plateau. It is worth noting the slightly positive slope of the voltage plateau. This outcome, which was also expected, stemmed from slight increases in the detector efficiency, which occurs even in the proportional region of the gas amplification curve.

Table 8.1. High-voltage determination in ^{3}He.[28]

Voltage	Neutron Counts	Uncertainty (1.96σ)
1100	0	0
1200	0	0
1300	40	12.4
1400	926	59.6
1500	1406	73.5
1600	1611	78.7
1700	1645	79.5
1800	1721	80.8
1900	1960	86.8
2000	2628	100.5

[28] ^{3}He data obtained from laboratory measurements.

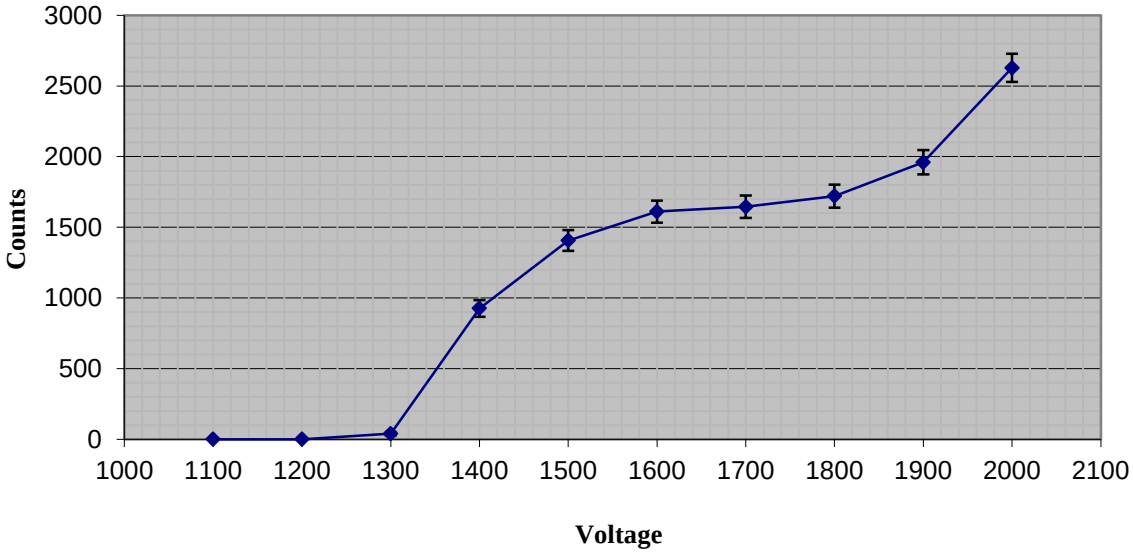

Fig. 8.1. ^{3}He voltage curve at 95% confidence.

The ^{3}He response for a five-minute count of the unshielded PuBe source was extracted from the Trump PCI card and plotted in Figure 8.2. Wall effects can be seen beginning with Channel 38, and continue to approximately channel 100 for this particular tube. The wide spectrum of neutron energies from the PuBe also produced a wide continuum of energies in the spectrum resulting from a partial energy transfer to the ^{3}He as seen in Channels 110 – 187. The operational constraints of the facility where the measurements were being taken precluded a long count time for the source. The restricted counting time prevented all the features of the idealized differential pulse-height spectrum (*dN/dE*) seen in Figure 8.3 from being manifested.

In particular, the epithermal peak, which results from thermal neutron interactions in the gas, cannot be readily distinguished from the overall recoil proton distribution; however, the maximum energy of the recoil distribution can be seen at channel 187 and

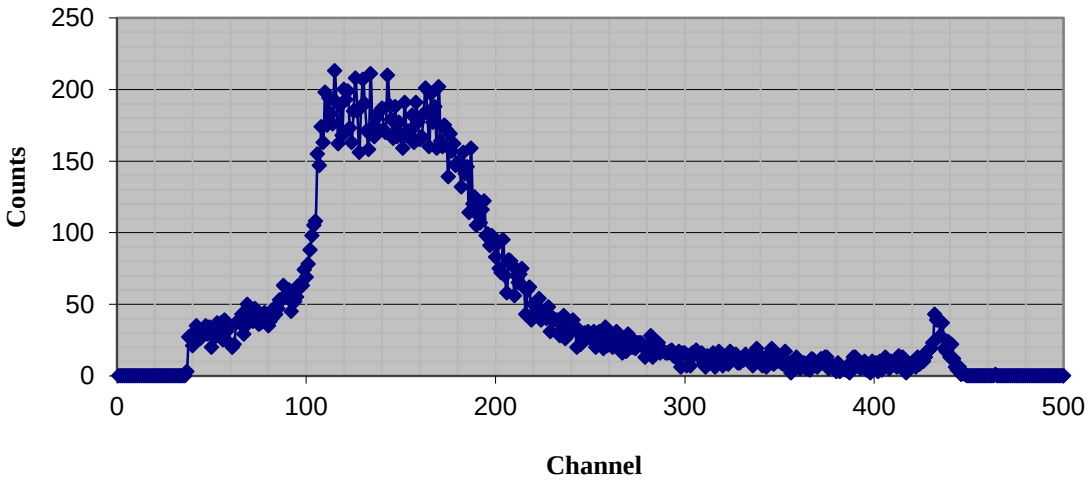

Fig. 8.2. Source response in the ^{3}He tube operating at 1700 V (PuBe only).

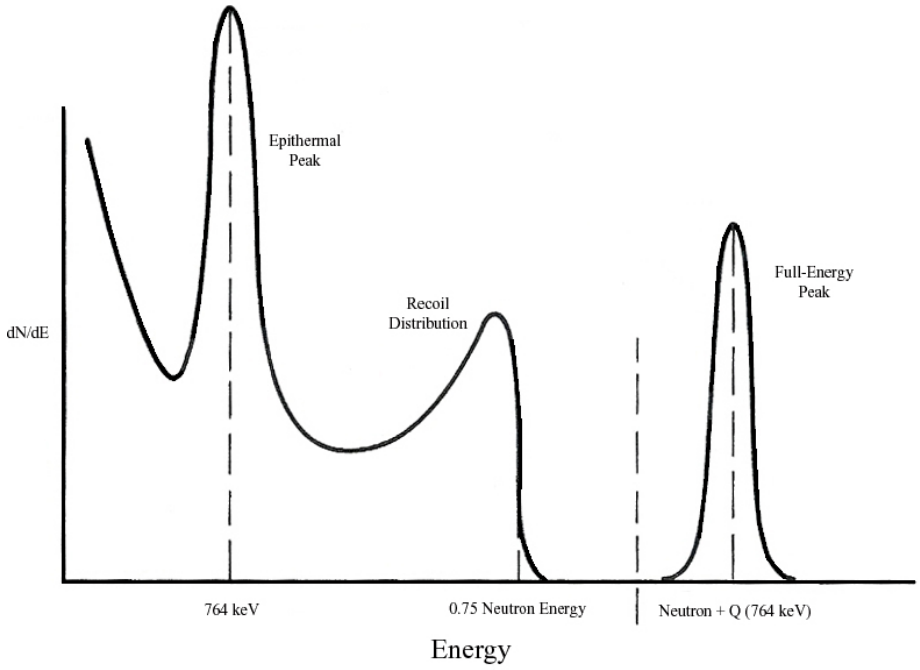

Fig. 8.3. Idealized ^{3}He response from a mono-energetic fast neutron source [1].

the peak centroid of the full-energy deposition is clearly displayed at channel 432. There is a 25 channel range (415 – 440) about the peak centroid, which was produced by the energy distribution of the source neutrons emitted by the PuBe source.

The maximum energy of the recoil proton distribution can be found through the use of Eq. 3.68, which resulted from an elastic neutron scatter at π radians or 180 degrees in the center-of-mass system. Using this relation, the scattered neutron energy can be determined by

$$E' = E\left(\frac{M-1}{M+1}\right)^2 = 0.25E\,, \tag{8.1}$$

for the non-relativistic case in ^{3}He (M = 3), and the energy imparted to the recoil proton is

$$E_p = E - 0.25\,E = 0.75E\,, \tag{8.2}$$

which is prominently displayed in the idealized spectrum of Figure 8.3.

Although the initial settings for the linear amplifier were selected to prevent signals from noise and/or photons from being amplified and recorded as neutron events, the potential effect of photon radiation on the neutron counts was also evaluated to ensure that this was indeed the case due to a CT scanner that was housed on the other side of the CONEX container laboratory as shown in Chapter 6. Figure 8.4 shows the results of another 5-minute count of the same PuBe source, but with the 10 μCi ^{137}Cs source affixed directly to the tube. A direct comparison to Figure 8.2 confirms that photons did not produce any noticeable effects on the neutron count tally, spectrum appearance, or associated channel numbers. This conclusion, which was expected, helped to confirm the

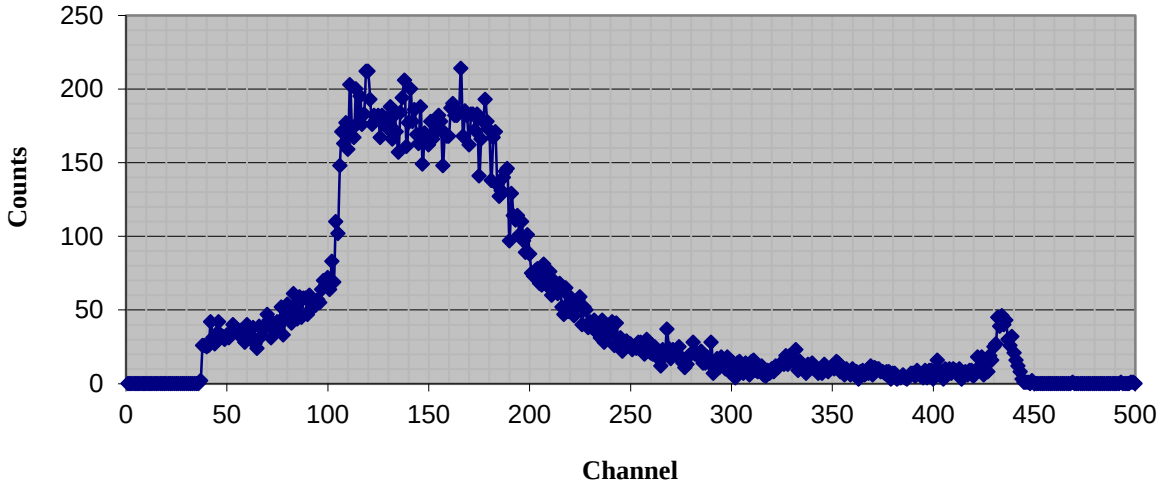

Fig. 8.4. Source response in the ^{3}He tube for a mixed radiation field (PuBe and ^{137}Cs).

appropriateness of the electronic settings while demonstrating that, although ^{3}He has a relatively small *Q*-value compared with other neutron detector gases such as BF_3, it is still quite capable of discriminating between neutron and photon events.

The photon cross section plot in Figure 8.5 demonstrates why this is so [2]. It can be readily seen that for a gas such as ^{3}He, with a density on the order of 10^{-4} g cm^{-3} and a thickness of only a few centimeters, he energy deposition for any photon will be at least five orders of magnitude lower than the smaller *Q*-value of ^{3}He. This information demonstrates why, in the absence of a very large photon function, a coincidence pulse large enough to be mistaken for a neutron event will not result. In the majority of non-proliferation monitoring situations, large photon functions will not be present, thus ^{3}He doesn't present any true impediments.

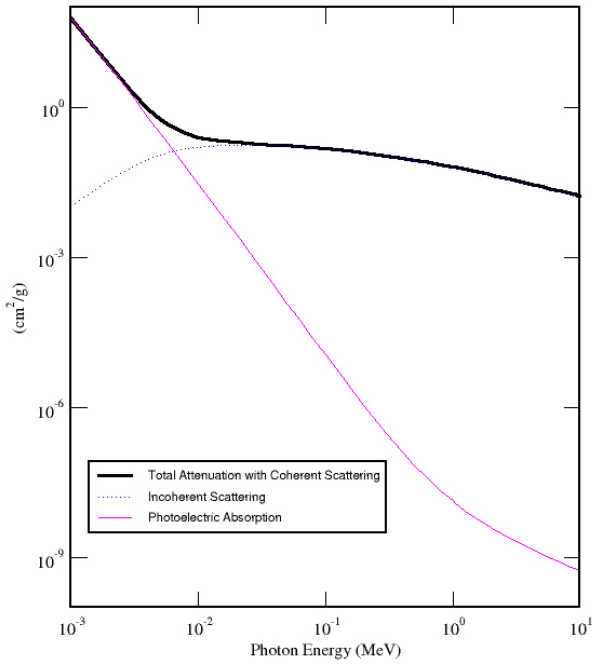

Fig. 8.5. ^{3}He photon cross section at 4 atm (1 keV to 10 MeV) [2].

8.1.2 BF_3 Detection System

The data for the high-voltage determination was tabulated in Table 8.2 and plotted in Figure 8.6 to help select the optimal tube operating voltage. The beginning of the proportional plateau can be seen at 1600 V, and the plateau continued to about 2100 V, after which time the count rate increased substantially. An optimal operating voltage of 1800 V was chosen for this particular BF_3 tube, which was in the middle of the proportional plateau. This plateau region also exhibited a slightly positive slope, which was discussed in the previous section.

Table 8.2. High-voltage determination in BF_3.[29]

Voltage	Neutron Counts	Uncertainty (1.96σ)
1300	0	0
1400	83	17.9
1500	185	26.7
1600	230	29.7
1700	248	30.9
1800	241	30.4
1900	241	30.4
2000	258	31.5
2100	283	33.0
2200	369	37.7
2300	496	43.7

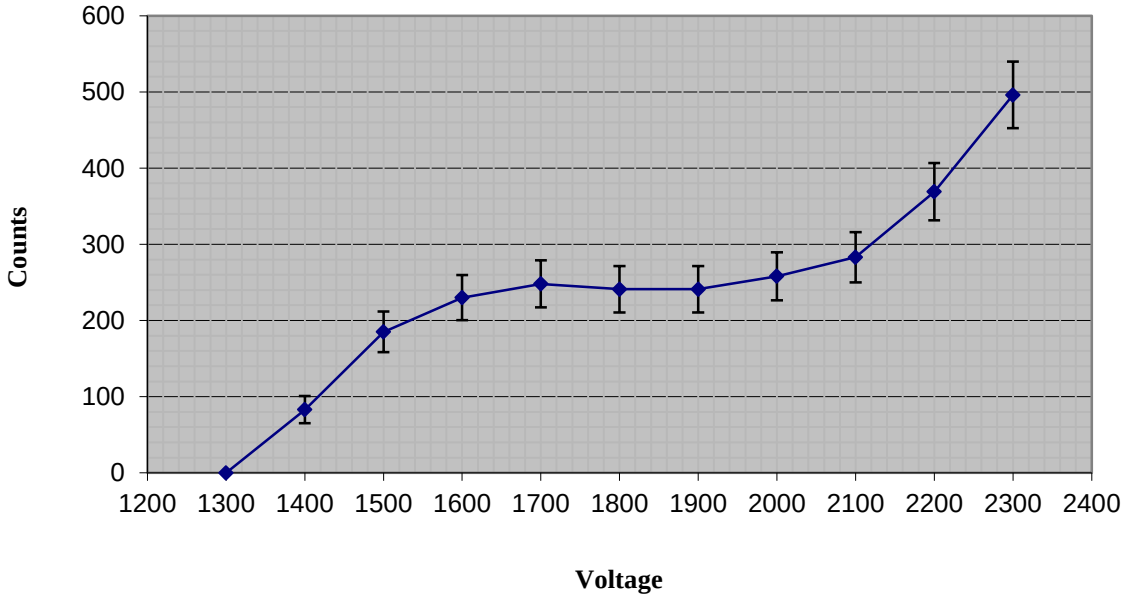

Fig. 8.6. BF_3 voltage curve at 95% confidence.

It is particularly interesting to compare the magnitude of the voltage plateaus for the two gases. By comparing Figs. 8.1 and 8.6, it can be seen that the ^{3}He plateau is only

[29] BF_3 data obtained from laboratory measurements.

about 60% of the length for that of BF_3. This phenomenon resulted from a combination of wall effects and a lower *Q*-value in the ^{3}He gas. There is considerably more separation between the energy of a *Q*-value deposition in ^{10}B and the reaction product energies; however, the relatively small *Q*-value of the ^{3}He reaction means that the triton and proton energies are more closely spaced with the full-energy peak at 764 keV. As the level of amplification increases, this smaller separation lead to a reduced voltage range over which an acceptable proportional plateau was observed in ^{3}He [1]. The larger plateau width of the BF_3 provided more stability during the experiment because voltage changes that would have had serious repercussions for the ^{3}He tube would not have caused a departure from the proportional region in this gas.

Once the operating voltages were determined, the HVPS was set to the new value of 1850 V and a fifteen-minute count of the PuBe source was taken to help account for the lower detection efficiency of the BF_3 gas. The response data from this count are plotted in Figure 8.7 and demonstrates a striking difference from the ^{3}He response curve. Wall effects for the BF_3 tube can also be seen beginning with channel 38, but they continue to channel 300 as compared to channel 100 for ^{3}He. This phenomenon resulted from three main reasons: 1) the larger *Q*-value of the BF_3 reactions compared with ^{3}He; 2) the absence of a fast neutron interaction mechanism in the BF_3 gas; and, 3) a low elastic scattering cross section in the heavier BF_3 gas compared with the (*n, p*) reaction in ^{3}He, which varies from one to three orders of magnitude in the neutron energy range of 1000 eV – 0.01 eV [3].

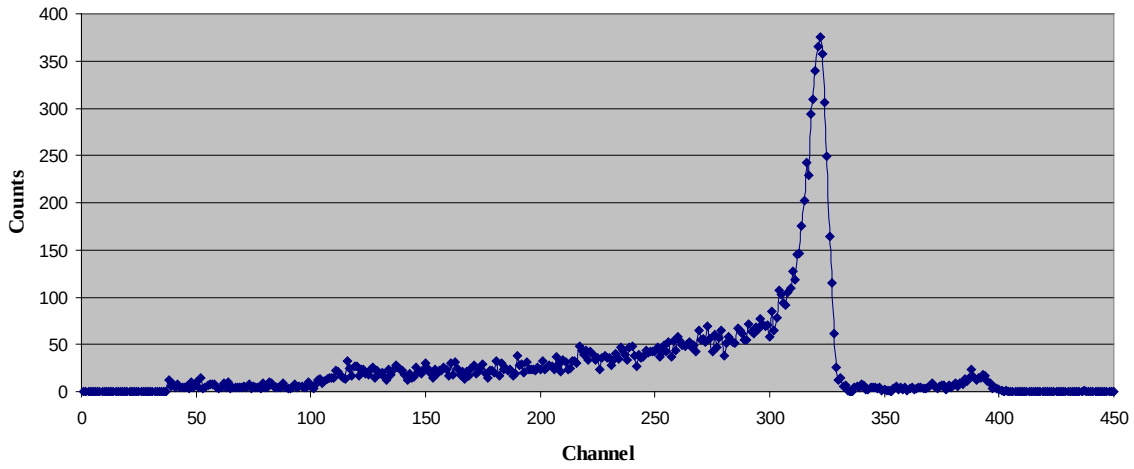

Fig. 8.7 Source response in the BF_3 tube operating at 1800 V (PuBe only).

The larger magnitude BF_3 peak at Channel 322 resulted from the excited state of ^{7}Li (Q = 2.310 MeV), while the smaller, but more energetic peak at Channel 387 (Q = 2.792 MeV) occurred due to the ground state reaction. Once again, there was some variance about the peak centroid of both peaks due to the energy distribution of the PuBe neutron emissions. The count result for both energy peaks agrees exactly with the branching ratios of the Q-value reactions (94% excited state / 6% ground state).

The initial settings for the linear amplifier were evaluated for BF_3 in the same manner as for ^{3}He, because, although BF_3 has a larger Q-value for neutron absorption, it also has a larger effective atomic number (Z_{eff}), which can be calculated by Eq. 3.3.

$$Z_{eff} = \sum_{i=1}^{N} w_i Z_i = (0.159 \times 5) + (0.841 \times 9) = 8.364\,. \qquad (8.3)$$

The larger Z_{eff} means that BF_3 will respond more readily to photon radiation because the main photon cross section components (photoelectric effect, Compton scattering, and pair production) are all dependent on this quantity as seen in Eqs. 3.2, 3.5, and 3.21 and as depicted in Figure 8.8 [4].

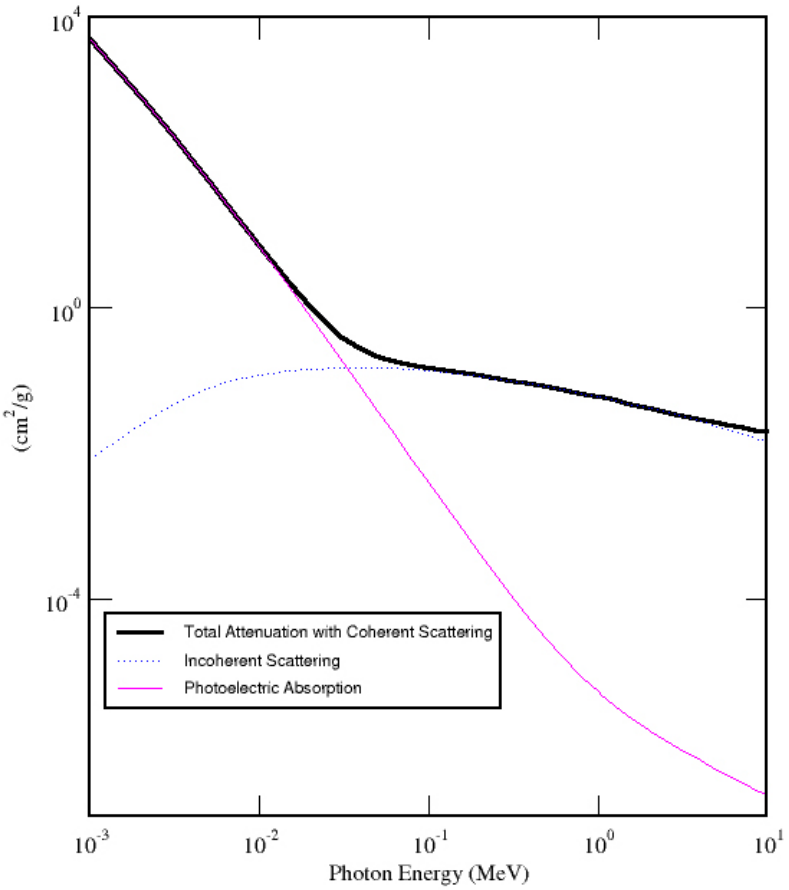

Fig. 8.8. BF_3 photon cross section at 1 atm (1 keV to 10 MeV) [2].

By comparison of tabular data used to produce these two figures [2], the BF_3 photoelectric cross section is about 100 times greater than that of ^{3}He; however, this larger value still produces an insignificant energy deposition in the gas for the same reasons discussed in Section 2.2.1.1 for ^{3}He. The slight increase in the energy deposition

is also mitigated by the larger *Q*-value of the neutron reaction in BF_3. The fact that photon energy deposition is negligible in BF_3 is borne out by the comparison of Figure 8.9, which includes the effects of the photon contributions from the 10 μCi ^{137}Cs source discussed in the prior section. As was the case with ^{3}He, a comparison of Figs. 8.7 and 8.9 confirms that the photons did not produce any noticeable effect on the neutron count, the spectrum appearance, or any associated channel values. The satisfactory results of this test further confirmed that the electronic settings of linear amplifier and single-channel analyzer (SCA) were appropriate for this particular gas and would effectively discriminate photon events.

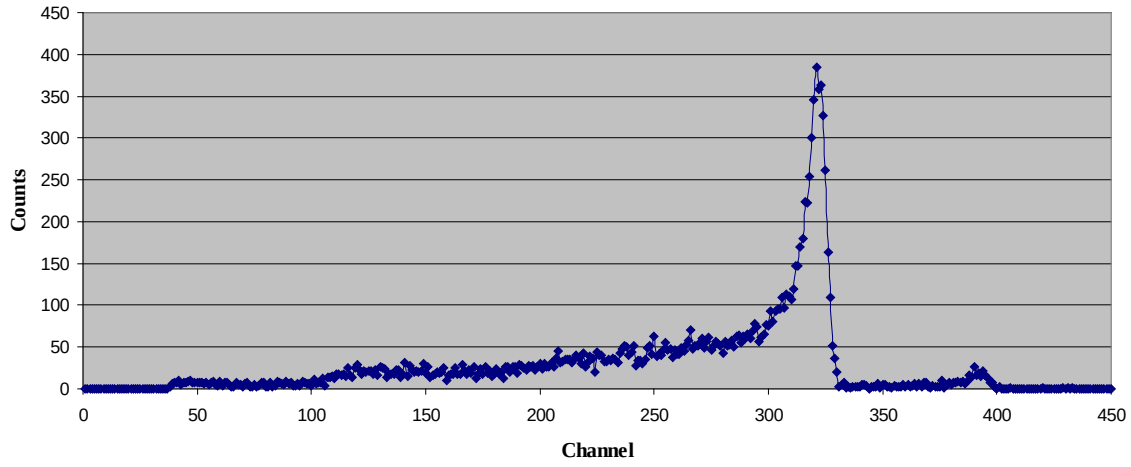

Fig. 8.9. Source response in the BF_3 tube for a mixed radiation field (PuBe and ^{137}Cs).

8.2 Baseline ^{3}He Computational Model

The adjoint PENTRAN file for a 1-inch diameter ^{3}He tube at 4 atm pressure and 10 cm length was initially executed to provide the baseline result. Afterwards, the

forward PENTRAN and MCNP5 cases were executed and their results tabulated for comparison to the adjoint case. The results for the baseline detector are shown in Table 8.3 and demonstrate excellent agreement between the three different transport models with the largest bias being only 1.585%. The difference between the non-adjoint cases is referred to as the bias and was calculated by the relation:

$$Bias = \frac{(R - R_{adj})}{R_{adj}} \times 100\,, \tag{8.4}$$

where R_{adj} is the adjoint reaction rate and R is the reaction rate for either the forward PENTRAN or the MCNP5 case. The bias calculation was carried out in this fashion so that a positive or negative value would indicate whether the reaction rate was less than or greater than the adjoint rate and at the calculated percentage that is specified.

Table 8.3. Reaction rates for ^{3}He baseline.

Method	Rate (s^{-1})	Bias (%)	Uncertainty (1.96σ)
PENTRAN Adjoint	2.650	---	--
PENTRAN Forward	2.674	0.906	--
MCNP5 Forward	2.608	-1.585	0.005

For the baseline detector and model comparisons to this baseline, a forward neutron source of 1000 $n\ s^{-1}$ was uniformly inserted around the detector assembly as discussed in Section 5.1. The overall source volume was 607.01 cm^3, which means that each discretized cell contained a 1.65 $n\ cm^{-3}\ s^{-1}$ volumetric neutron source and, since the

overall reaction rates for the designs were within a range of 2.6 *cts* s^{-1} - 2.7 *cts* s^{-1} this means that the overall absolute efficiency of the baseline detector on the front face of the assembly was ~0.3% for this emission scenario. The baseline case was also executed for a flat source consisting of equal source emission probabilities of 2.50E-02 rather than the true source probabilities given Table 6.2. This run was completed as a second check to demonstrate that the models were not specifically tailored to the shielded PuBe spectrum alone and the results varied between 6.312 *cts* s^{-1} – 6.360 *cts* s^{-1}, which is a range of only 0.75%.

The aluminum tubes that usually form the pressurized container for neutron detectors was not included in any of the deterministic or MCNP5 models, since the typically thin wall thickness has been shown to alter results by no more than a few percent or less [5]. However, to verify this assertion, an MCNP5 simulation was conducted that compared the reaction rate of a bare ^{3}He gas volume with the same gas contained within the tube walls of the baseline LND-252 detector (1.78 mm thickness). The resultant reaction rate was smaller by only 0.4%, which justified the simplification.

The adjoint PENTRAN calculation was completed in 94.78 minutes on four processors, while the forward executed in only 64.83 minutes on the same number of processors. These times were typical of all the PENTRAN executions. The MCNP5 input file executed in 253.89 minutes on four processors, with a total of 1.60E8 particles started to an average error of 0.05%. The excellent agreement achieved between the PENTRAN and MCNP5 reaction rate results demonstrated that the 47-group BUGLE-96

library performed in a consistent and favorable manner when compared with the MCNP5 calculations that used the continuous-energy Evaluated Nuclear Data File/B-VII [6].

Function profiles can be produced by the DISLIN library implemented in the PENMSHXP utility. The profiles are created using data from the respective function files that are tabulated by the PENDATA utility following post-processing of PENTRAN output files. Although profiles can be produced for all 47 BUGLE-96 energy groups, only those for the Adjoint Groups 1, 29, and 47 are provided in Figs. 8.10 – 8.12 below, along with a 3-D plot of the detector geometry. These groups were selected in order to display and highlight the behavior of the adjoint function for thermal, midrange, and fast neutron energies. It is important to remember that in this work, the adjoint function is synonymous with detector efficiency as demonstrated in Chapter 4, and by viewing the fluctuations in this function, one can ascertain regions of a detector system that produce the majority of detection events for a particular neutron energy group (i.e. the detection "sweet spots") in the geometry as a function of energy group.

For example, in Figure 8.10, it can be seen that the highest region of importance (efficiency) for *thermal* neutrons is within the detector itself (~7.4E-01) and that the thermal neutrons in the region surrounding the detector assembly are far less important (~4.2E-03). This makes physical sense, because thermal neutrons emitted outside the detector assembly are less likely to penetrate the polyethylene and then react within the ^{3}He gas. As the neutron energy increases, Figs. 8.11 and 8.12 demonstrate that the adjoint function for neutrons emitted in this same region decreases to ~7.0E-03 and

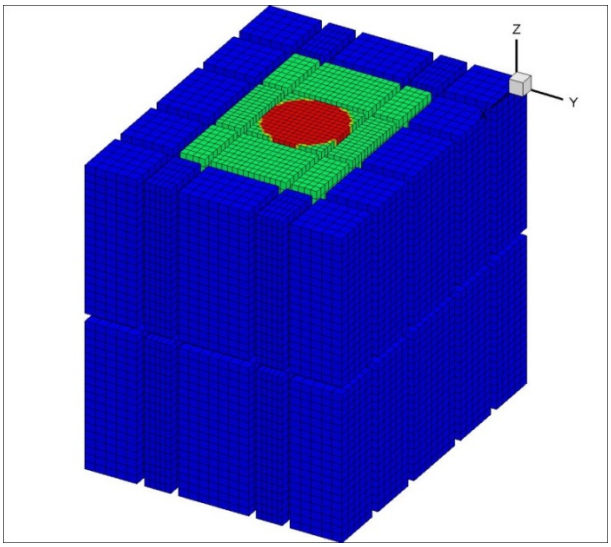

(a)

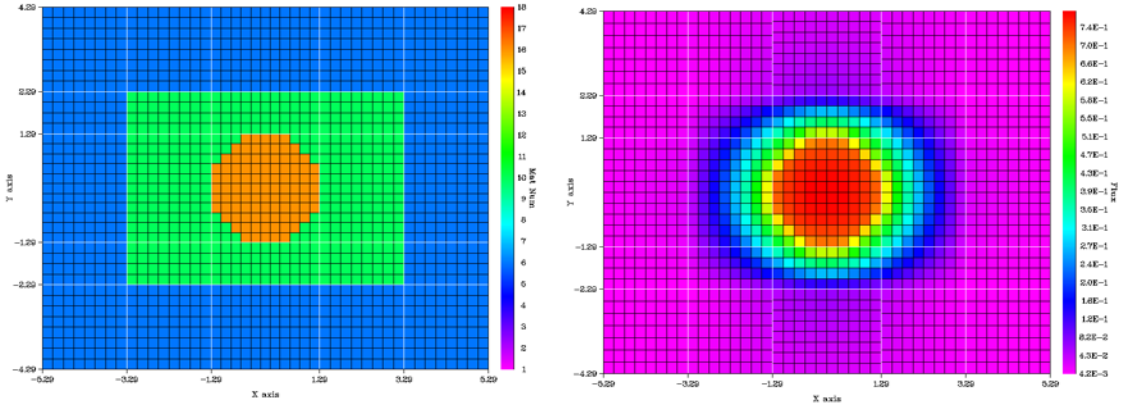

(b) **(c)**

Fig. 8.10. A 3-D view of the baseline ^{3}He detector model (a), an *XY* slice of the model (b) and the corresponding Adjoint Group 1 (thermal) flux profile (c).

finally to ~4.2E-04, which is a reduction of more than a factor 1700 over the entire neutron energy range. Note that in Fig. 8.10 (b), the course meshes of air (blue) adjacent to polyethylene (green) on the right-side of the figure are those that would be considered *toward the source* in a normal detection application.

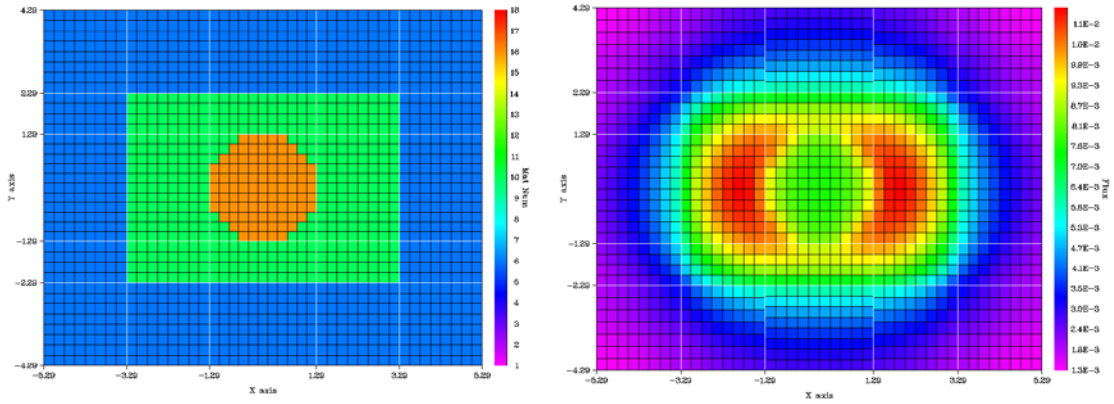

(a) **(b)**

Fig. 8.11. An *XY* slice of the baseline ^{3}He detector model (a) and the corresponding Adjoint Group 29 (1 MeV) flux profile (b).

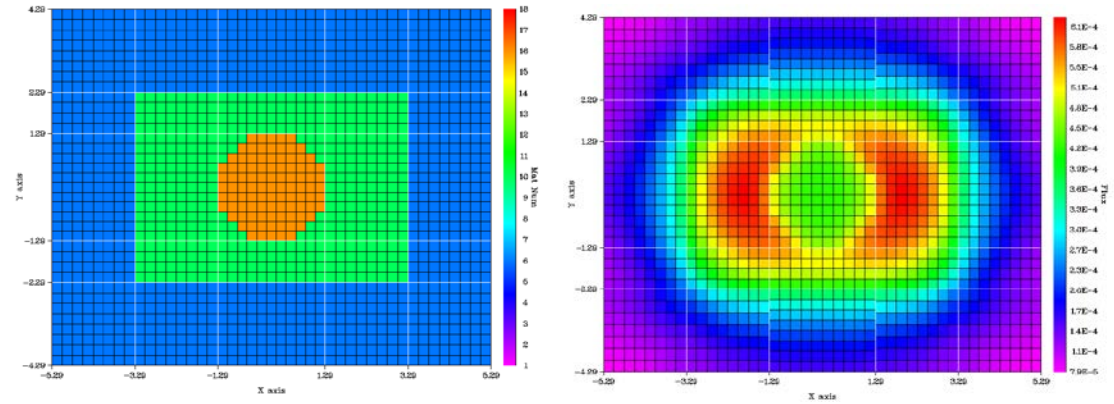

(a) **(b)**

Fig. 8.12. An *XY* slice of the baseline ^{3}He detector model (a) and the corresponding Adjoint Group 47 (17.3 MeV) flux profile (b).

These adjoint function profiles demonstrate the need for some degree of moderation on the part of the higher-energy neutrons before they will appreciably interact within the gas volume. The neutrons in Adjoint Group 29 (1 MeV) require less moderation than Adjoint Group 47 (17.3 MeV), since they are almost two orders of

magnitude lower in energy. This is indicated by the adjoint efficiency difference that is slightly more than two orders of magnitude higher for Adjoint Group 29. The lower efficiencies that exist on the top and bottom of the detector in Figs. 8.10 – 8.12 are due to the thinner polyethylene sidewalls (1 cm) as compared with the 2 cm walls to the immediate right and left of the detector. If the models had a constant 2 cm of polyethylene surrounding the detector, the area of increased efficiency would extend around the entire tube.

Finally, a plot of the adjoint function as a function of neutron energy across all course meshes is given in Figure 8.13 and the adjoint reaction rate as a function of the adjoint energy group in the forward course meshes (toward the source) is given in Figure 8.14. These figures form the basis by which the various detector designs will be judged in the subsequent sections. The maximum for Figure 8.13 and its counterparts for the various detector designs that will be discussed occur in either Adjoint Groups 5 or 6, which represents energies from 5.04 – 10.78 eV, although Figure 8.14 demonstrates that, in general, the groups with higher efficiencies contribute little to nothing toward the reaction rate. In fact, the only general adjoint groups contributing for all the detector designs discussed herein are Adjoint Groups 20 – 41 (6.74E-02 MeV – 7.41 MeV).

The behavior at the lower energies occurs because the neutrons need to possess some threshold energy to adequately penetrate the moderator. The higher-energy neutrons, in contrast, reach a point where they do not experience scatter appreciable enough to produce any detector counts. In models that have been well characterized, the

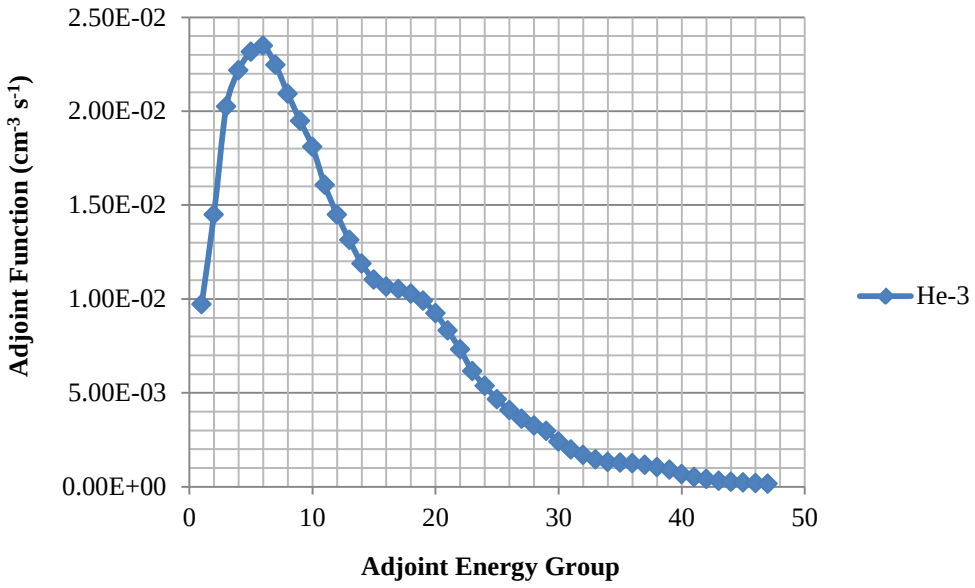

Fig. 8.13. Adjoint function per unit source density in the forward air-filled course meshes adjacent to the polyethylene (toward a source) for the ^{3}He baseline detector with a 1-inch diameter, 10 cm active length, operating at 4 atm pressure.

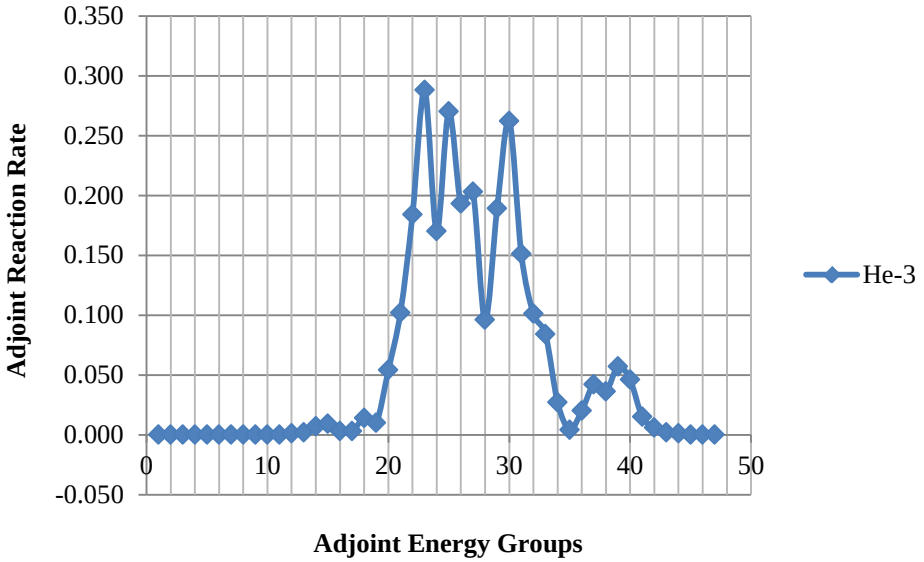

Fig. 8.14. Adjoint reaction rate across all air-filled course meshes for the ^{3}He baseline detector exposed to a nickel-filtered PuBe source.

neutron energy groups that are non-contributors could be removed from the source term, thus saving valuable computational time and speeding the deterministic calculations; however, these energies were included and tracked for all models associated with this research.

Before proceeding, it is important to mention that features absent from the adjoint function plots are possibly as important as those that are readily observable. For example, none of the plots display large gradient behavior along boundaries that would be indicative of mesh sizes that are too dissimilar. Poor meshing choices will also typically manifest themselves in an inability to achieve convergence of the solution to a reasonable level (e.g. infinity norms < 1E-03). Another feature that is not present on the plots is ray effects, as discussed in Chapter 4. If ray effects were present, they would appear as fingers or a *star-like pattern* with oscillatory adjoint function values emanating from the center of the plot along the individual ordinates as shown in Figure 8.15. The inadequate convergence in the model execution can even produce unusual asymmetry in the adjoint function solution for the mid-range energies as seen in Figure 8.15(b).

The absence of these effects in Figs. 8.10 – 8.12 confirms that the combination of S_8 (80 ordinates in 3-D on the unit sphere) and P_2 scattering moments adequately handled the source and material characteristics associated with the baseline ^{3}He tube. This combination was used for evaluating all the research model designs except for Design 6, which required a higher scattering moment (P_3) due to the presence of a hydrogenous solid with a much higher density than gases used in the alternate designs.

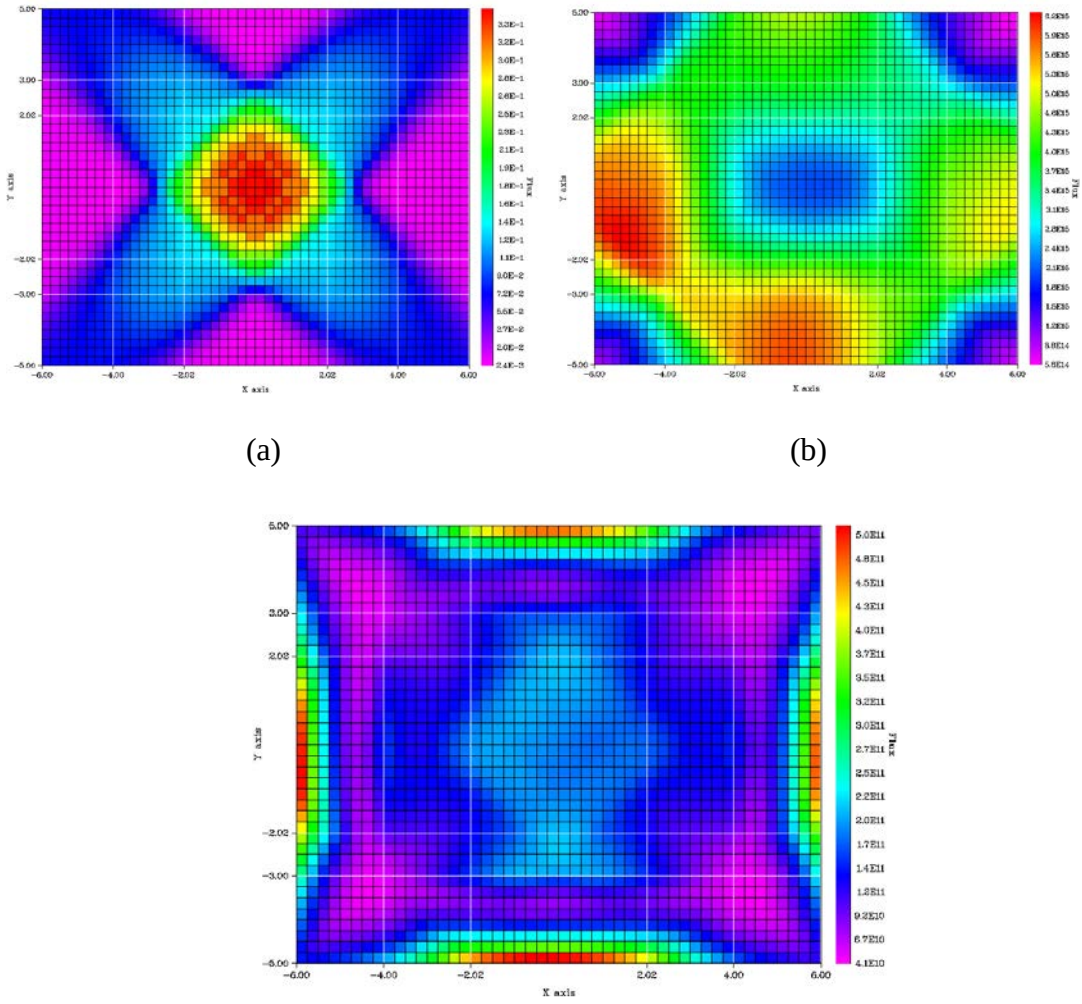

(a) (b)

(c)

Fig. 8.15. An *XY* slice of Design 1 (large BF_3 tube) demonstrating ray effects produced by source neutrons from a nickel-filtered PuBe source in the adjoint model. The ray effects resulted from an inadequate quadrature (S_N=2) and scattering moment (P_N=1) and are displayed for (a) Adjoint Group 1 (thermal), (b) Adjoint Group 29 (1 MeV), and (c) Adjoint Group 47 (17.3 MeV).

8.3 Neutron Measurements of the PuBe Source

The measurements of emissions from the shielded PuBe source were conducted as discussed in Section 7.2. The original intention was to monitor the source solely in an

unreflected condition (no water behind the source) in order to limit unknown variables and to ensure the best possible comparison to the computational models. During this same time period, however, a separate detection system was being tested in the same CONEX which required that cases of bottled water be emplaced behind the PuBe source to produce scatter as seen in Figure 8.16. To wait for the unrelated test to be completed would have introduced a significant period of inactivity; therefore, it was finally decided to make measurements in the reflected case simply to serve as another qualitative verification for our neutron detection measurements (^{3}He and BF_3).

Fig. 8.16. Shielded PuBe source in the reflected condition.

In an unreflected case, source neutrons emitted in a solid angle pointed away from the detector would escape the CONEX container with a high probability; however, having the water in place should produce an increase in the detector counts due to

scattering backwards toward the detectors. Three data points were obtained for each of the source configurations and with varying amounts of polyethylene inserted between the detectors and the PuBe source. Note that each tube also had a constant amount (2 cm) of moderator behind it for each measurement, as discussed in Chapter 7. The average number of counts was calculated for each of these data points with both detectors and the measurement uncertainty was calculated at the 95% confidence level (1.96σ). The results for each individual detector are given in the subsequent two sub-sections.

8.3.1 ^{3}He Results

The ^{3}He measurement data produced by the unreflected and reflected source conditions are given in Tables 8.4 and 8.5. The reflected counts were indeed greater than the unreflected case by an average of 9% as expected. The total number of counts rose gradually with an increasing moderator thickness up to a maximum at 2 cm for the unreflected case; however, the maximum for the reflected case occurred at only a 1.5 cm thickness, although the 2 cm moderator produced an almost equivalent count. The slight difference between the two source conditions was caused by the slight shift in the neutron energy spectrum resulting from neutron scatter from behind the source. The degraded energies of the scattered neutrons made them more susceptible to moderation in the polyethylene and they stopped prematurely or scattered more readily when compared with the unreflected condition. The ratio of the reflected to the unreflected counts and count differential for the lower neutron energies in Table 8.5 substantiates this finding. Based on the information from Table 8.4, a 2-cm moderator was used between the source

and detector for the computational models and the comparative detector measurements used to verify the fidelity of the computational approach used in the subsequent sections.

Table 8.4. ^{3}He counting results for a shielded PuBe source in the unreflected condition.

Polyethylene (cm)	Neutron Counts	Uncertainty (1.96σ)
Bare	14600	112
0.5	15525	137
1.0	15862	82
1.5	16149	191
2.0	16184	119
2.5	15727	203
3.0	15394	118
3.5	14749	146
4.0	14467	225
4.5	13781	251
5.0	13303	247
5.5	12376	194
6.0	12180	231

Table 8.5. ^{3}He counting results for a reflected (R) source with a comparison to the unreflected (U) condition.

Polyethylene (cm)	Neutron Counts	Uncertainty (1.96σ)	Δ Counts (R-U)	Ratio (R/U)
Bare	17236	54	2636	1.18
0.5	17316	60	1791	1.12
1.0	17395	68	1532	1.10
1.5	17430	116	1281	1.08
2.0	17416	117	1232	1.08
2.5	17271	171	1544	1.10
3.0	16812	252	1418	1.09
3.5	15990	259	1241	1.08
4.0	15397	146	930	1.06
4.5	14670	151	889	1.06
5.0	14002	246	699	1.05
5.5	13325	208	949	1.08
6.0	12604	142	425	1.03

8.3.2 BF_3 Results

The BF_3 measurement data associated with the unreflected and reflected source conditions are provided in Tables 8.6 and 8.7. The resulting tally for this particular detector was less than the ^{3}He detector by an average factor of 5.10 for the two source conditions. Ratios of up to four have been reported in literature [7]; however, the outcome of the previously-reported measurements resulted from smaller tubes that were exposed to spontaneous fission neutrons from a ^{252}Cf source, which is quite different from the filtered PuBe spectrum used in this research. Therefore the differences reported herein are considered valid and quite acceptable.

Table 8.6. BF_3 results of a shielded PuBe source in the unreflected condition.

Polyethylene (cm)	Neutron Counts	Uncertainty (1.96σ)
Bare	2098	44
0.5	2818	69
1.0	2966	159
1.5	3042	119
2.0	3169	189
2.5	3126	194
3.0	3080	180
3.5	3052	128
4.0	2916	177
4.5	2713	169
5.0	2661	94
5.5	2577	268
6.0	2391	174

The BF_3 tube exhibited the same overall behavior as the ^{3}He tube regarding the varying moderator thickness. The 2-cm forward moderator also produced the greatest number of counts for the unreflected source, and there was also a shift in the amount of

Table 8.7. BF_3 counting results for a reflected (R) source with a comparison to the unreflected (U) condition.

Polyethylene (cm)	Neutron Counts	Uncertainty (1.96σ)	Δ Counts (R-U)	Ratio (R/U)
Bare	2649	128	551	1.26
0.5	3139	148	321	1.11
1.0	3307	71	341	1.11
1.5	3425	207	350	1.11
2.0	3367	109	265	1.08
2.5	3426	65	300	1.10
3.0	3220	225	140	1.05
3.5	3168	61	116	1.04
4.0	3045	140	125	1.04
4.5	2919	127	206	1.08
5.0	2804	213	143	1.05
5.5	2734	130	157	1.06
6.0	2574	212	183	1.08

moderator that produced the greatest number of counts for reflected case. Unlike the ^3He case, however, the shift in the reflected case was toward more moderation (see Table 8.7) and not less as was seen in Table 8.5. This behavior was expected because of the overall tendency witnessed in the computational results for the BF_3 designs versus the ^3He baseline (see Figs. 8.21, 8.26, and 8.31). In all of these comparisons, the BF_3 presented a negative bias at the lower neutron energies, which could be compensated by slightly more moderator.

The data from Tables 8.4 – 8.7 were also used to demonstrate that the ratio of the ^3He / BF_3 reaction rates varies little over the entire range of moderator thicknesses and source conditions that existed during the counting experiments. This information is presented in Table 8.8.

Table 8.8. ^{3}He / BF_3 reaction rate ratios as a function of moderator thickness and source condition.

Polyethylene (cm)	Reflected	Unreflected
Bare	6.51	6.96
0.5	5.52	5.51
1.0	5.26	5.35
1.5	5.14	5.31
2.0	5.07	5.11
2.5	5.04	5.03
3.0	5.22	5.00
3.5	5.05	4.83
4.0	5.06	4.95
4.5	5.03	5.08
5.0	4.99	5.00
5.5	4.87	4.80
6.0	4.90	5.09

8.4 Computational Modeling Results Associated with the PuBe Measurements

It is a relatively easy undertaking to build a computational model for a radiation detector and then execute the model through some transport code to yield a result. However, one must always ask what the computational result means and whether it reflects the reality of the detection environment. Some sort of comfort can be taken if the model produces a result that compares favorably with a standard transport code such as MCNP5 and its derivatives. However, the ultimate judgment for computational results is the degree to which it matches actual physical measurements. Computational measurements should always be validated by measurements to the greatest extent possible. Adherence to this policy will prevent a myopic dependence on purely computational results that may have no basis in reality.

A great deal of time and effort went into building and computationally testing the plug-in models provided in Section 8.5; however, if they could not accurately reflect reality, then they would prove to be of limited value. Therefore, a detailed comparison was completed to determine how well the new designs compared to actual measurements taken of the unreflected nickel-filtered PuBe source using the baseline ^{3}He detector system. The MCNP5 models utilized the actual nickel-filtered PuBe source spectrum detailed in Chapters 5 and 7, while the PENTRAN models used the surrogate source box as described in Chapter 7 to reduce the computational expense by allowing eliminating a meter of air space. The results of the comparisons are given in Tables 8.9 and 8.10.

Table 8.9. Comparison of the ^{3}He measured reaction rate (neutron counts) recorded over a 2-minute interval for a nickel-filtered PuBe source and computational calculations of the same source with PENTRAN and the 47-group BUGLE-96 broad-group cross sections [8] and MCNP5 with the continuous-energy ENDF/B-VII cross sections [6].

Method	Counts	Uncertainty (1.96σ)	Fractional Bias
^{3}He Measurement	16184	119	--
PENTRAN Adjoint	15780	--	-0.025
PENTRAN Forward	16120	--	-0.004
MCNP5 Forward	15582	31	-0.037

Table 8.10. Comparison of the BF_3 measured reaction rate (neutron counts) recorded over a 2-minute interval for a nickel-filtered PuBe source and computational calculations of the same source with PENTRAN and the 47-group BUGLE-96 broad-group cross sections [8] and MCNP5 with the continuous-energy ENDF/B-VII cross sections [6].

Method	Counts	Uncertainty (1.96σ)	Fractional Bias
BF_3 Measurement	3169	109	--
PENTRAN Adjoint	3183	--	0.004
PENTRAN Forward	3218	--	0.015
MCNP5 Forward	3273	14	0.033

It should be noted once again that MCNP5 is not capable of accounting for detection system losses produced by electrical noise, inefficient counting, and/or pulse pileup that tend to produce negative modeling biases in exact representations of detection scenarios. The positive biases associated with the BF_3 results are well within the propagated error associated with the source box determination, cross section values, and model parameters and should not be taken to imply that all potential loss mechanisms have been accounted for in the model. Regardless, the strong agreement that exists between the adjoint/forward deterministic and Monte Carlo transport computations and the laboratory measurement data firmly establishes the validity of the applied computational approach, and the validity of the plug-in alternative designs for the baseline ^{3}He detector.

8.5 Plug-In Replacement Designs for the Baseline ^{3}He Tube

Now that we have high confidence that the transport methods undertaken give results consistent with laboratory tests, each of the replacement designs will be evaluated in a manner similar to that of the baseline ^{3}He detector. The reaction rates for the three different models will be presented in tables along with adjoint function plots for energy groups 1, 29, and 47 as before. In other words, a forward PENTRAN reaction rate calculated for a BF_3 design will be compared to the forward PENTRAN reaction rate for the ^{3}He baseline detector provided in Table 8.3 and not to the baseline adjoint or MCNP5 results. This will eliminate confusion and ensure an appropriate evaluation is made.

8.5.1 Detector Equivalency

The focus of this research has been to *identify detector designs that match the neutron spectral response and the reaction rate of a 1-inch diameter ^{3}He tube operating at 4 atm*, such that the newer designs could serve as a direct *plug-in replacement* for the ^{3}He detector. Consequently, a discussion regarding what exactly constitutes this match is in order to ensure completeness on the part of this dissertation.

Since the adjoint function as treated in this work is synonymous with detector efficiency, the general expectation is that detectors having the same spectral response and overall reaction rate should have the same efficiency (adjoint function) for all neutron energy groups; however, this is not necessarily the case. Eq. 4.21 demonstrated that if the discretization of space, energy, and angle is properly handled, then the exact calculation of the adjoint-based reaction rate could be reduced to an approximate summation term and coupled to the discretized calculation of the adjoint function by

$$R_{adj} \approx \sum_{\substack{\Delta V_i \in V_d \\ g=1,G}} \phi^{\dagger}_{d\,g,i}\; q_{g,i}\, \Delta V_i \,, \tag{8.5}$$

where these terms have all been previously defined. If a detector design is to serve adequately as a plug-in replacement, its computed reaction rate must always be equal within some acceptable user tolerance. This does not, however, always mean that the unit-less adjoint function term in Eq. 8.5 will be equivalent for the alternative detectors

and the baseline detector across the entire neutron energy spectrum, although that is a notable design goal.

In fact, the only time the adjoint functions for two distinct detectors will be a match is if both detectors are activated by an identical source density ($n\ cm^{-3}\ s^{-1}$) and overall geometry footprint. Because none of the detector assemblies could possibly have the same dimensions as the ^{3}He design, the approach that was taken here was to maintain a consistent design approach (see Chapter 5) wherein all the detector models contained the same degree of moderation, scatter, and other physics treatments in the detector for the transport simulations. This means that the air volumes for all the models, which function as the *adjoint detectors* in the adjoint sense, are not equivalent and, therefore, have different source densities while preserving the total number of source particles in a given response model. This poses no issue at all from the standpoint of the reaction rate calculations; however, it does preclude a direct model-to-model adjoint function comparison.

In order to make side-by-side comparisons of the adjoint functions for the various designs against the baseline ^{3}He design, each adjoint response must be normalized to their respective source densities. This approach ensures the adjoint functions are being evaluated for a constant number of source particles across all designs. A revised baseline ^{3}He model was created using a similar air volume as Design 5, which has the greatest volumetric air difference of all the plug-in designs. This model was executed to ensure that the normalized source density equivalent to Design 5 would produce the same

adjoint response and this was the case. Although it was not possible to get every portion of the model into the same configuration as Design 5 (due to different detector dimensions), the adjoint function differed by < 10% for all adjoint groups. Table 8.11 is provided below to refresh the memory of the reader regarding the important aspects of the plug-in designs and to preclude the need to refer back to Chapter 5 where these features were originally discussed.

Table 8.11. Summary of the plug-in designs from Chapter 5.

Design	Sensitive Material	Number of Detectors	Length / Cylinder Radius (cm)	Pressure (atm)
1	BF_3	1	10.00 / 2.00	2
2	^{10}B lining	1	10.00 / 1.90	10 (^4He)
3	^{10}B lining	2	10.00 / 1.27 (both tubes)	10 (^4He)
4	BF_3	2	10.00 / 2.05 (rear) & 1.27 (forward)	1
5	BF_3	2	10.00 / 2.20 (both tubes)	1
6	PVT with ^{10}B	1	4.50 / 1.27	---

Notwithstanding the previous discussion, the parameter that most effectively demonstrates whether a detector design is a suitable plug-in replacement for another detector is the relationship between the reaction rates as a function of the neutron energy group for a prescribed number of source particles. If these rates match reasonably well, then the adjoint function will be an acceptable group-by-group efficiency match for the baseline unit. This type of comparison will also be made in the next section, demonstrating how well the various proposed designs perform.

The foregoing discussions also emphasize the close attention that must be paid to the selection of the source term and cell volumes when calculating reaction rates based on discrete ordinates code results. These codes generate very large quantities of information and, even after post-processing the files, the user must typically write some sort of computer program to gather, tabulate, and calculate desired quantities of interest such as reaction rates. When writing this type of program, one must be careful to not get confused regarding what constitutes the source and detector in the forward and adjoint senses; otherwise, the resulting reaction rates will be erroneous. Two separate reaction rate programs (forward and adjoint) were written during this research effort to extract the necessary data from the PENTRAN output files for the reaction rate calculations. Both of these codes are provided in Appendices F and G for the forward and adjoint cases respectively.

8.5.2 ^{3}He-Equivalent Tube Designs Based on BF_3 Gas

The plug-in designs exhibit similar behavior compared with each other and ^{3}He in some circumstances. The first of these similarities is that only the Adjoint Groups 20 – 41 account for the reaction rate, according to the discussion from the previous section. One other similarity of the gas tube designs is the tendency for the reaction rate to gradually increase from a minimum around Adjoint Group 20 (6.74E-02 MeV), to around Adjoint Group 25 (4.98E-01 MeV) due to a gradual increase in the ^{10}B (n, α) cross section versus that of ^{3}He (n, p).

There is also a general tendency for positive biases to occur from Adjoint Group 29 (1.00 MeV) to Adjoint Group 41 (6.07 MeV) due to a rapid increase in the ^{10}B cross section. In fact, this cross section exceeds that of ^{3}He (*n, p*) above neutron energies of about 4 MeV. The disparity is tempered somewhat, however, because elastic scattering with the nucleus becomes the predominant ^{3}He reaction for neutrons beyond 150 keV.

Deviations from the general tendencies mentioned above will be elaborated upon; however, adherence to these behaviors will not be mentioned further. Adhering to this convention will ensure the results discussions are thorough and concise.

8.5.2.1 Design 1 – Large Single BF_3 Tube Operating at 2 Atmospheres

The reaction rate results for Design 1 are provided in Table 8.12 and display excellent agreement with that of the ^{3}He baseline case. Adjoint function profiles for Design 1 are provided in Figs. 8.17 – 8.19 for comparison to the baseline case. All these figures contain an *XY* slice of the detector to allow a more complete evaluation of the flux profiles and Figure 8.17 also includes a 3-D view of the model. These figures demonstrate that this design exhibits the same overall behavior as the baseline detector. They also exhibit smaller magnitude adjoint functions that were expected based on prior discussions, including the smaller efficiency along the detector sidewalls (top and bottom) where there is less polyethylene.

Table 8.12. Reaction rates results for Design 1 (BF_3 tube at 2 atm).

Method	Rate (s^{-1})	Uncertainty (1.96σ)	Bias (%)
PENTRAN Adjoint	2.644	--	-0.226
PENTRAN Forward	2.648	--	-0.972
MCNP5 Forward	2.587	0.004	-0.805

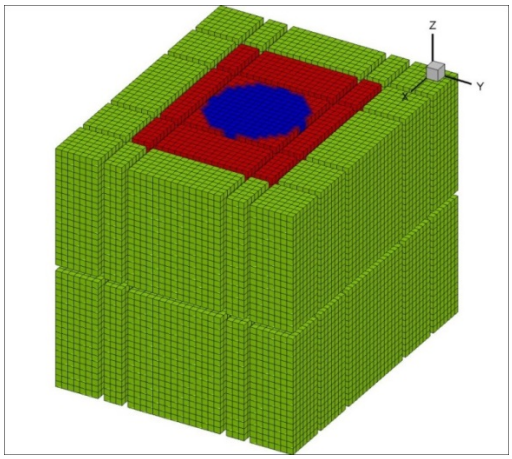

(a)

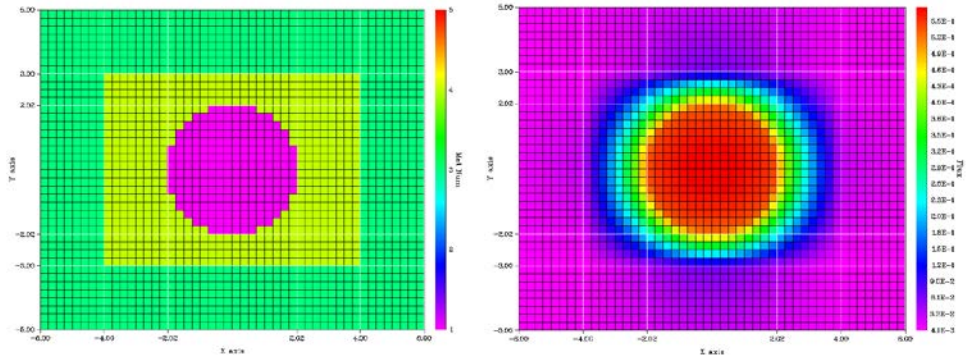

(b) **(c)**

Fig. 8.17. A 3-D view of the Design 1 detector model (BF_3 tube at 2 atm) (a), an *XY* slice of the model (b) and the corresponding Adjoint Group 1 (thermal) flux profile (c).

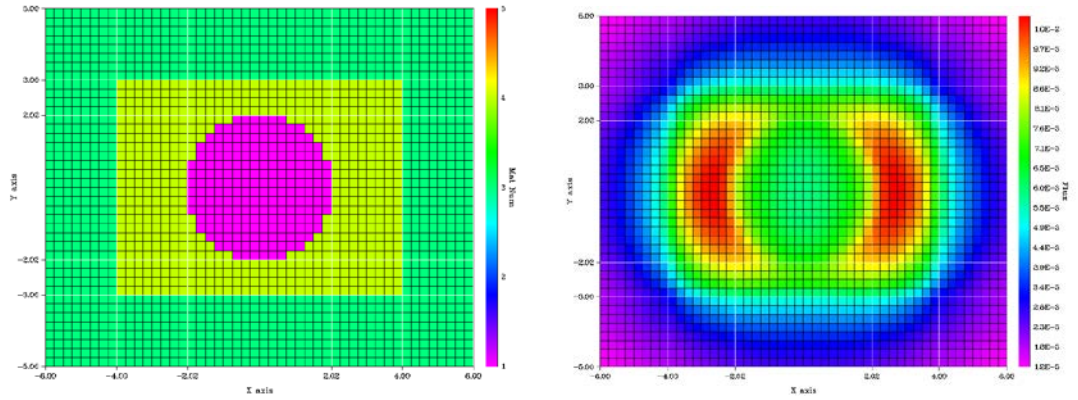

(a) **(b)**

Fig. 8.18. An *XY* slice of the Design 1 detector model (BF_3 tube at 2 atm) (a) and the corresponding Adjoint Group 29 (1 MeV) flux profile (b).

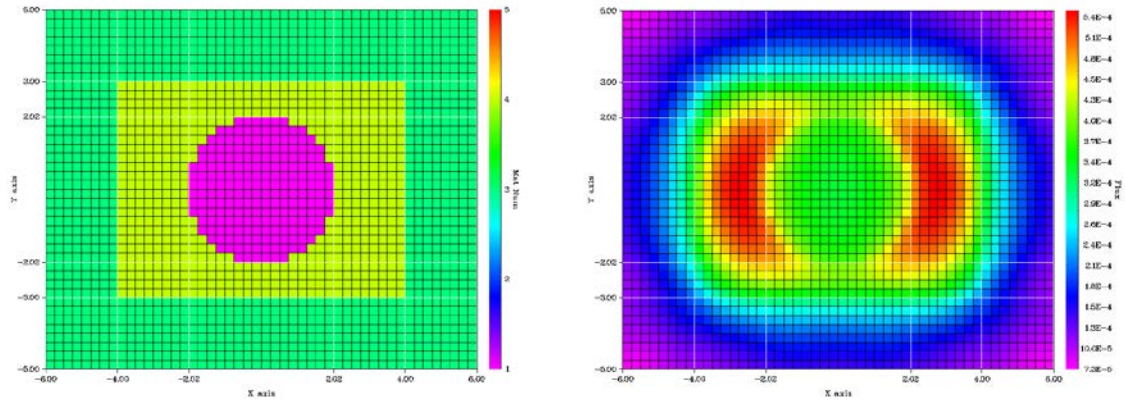

(a) **(b)**

Fig. 8.19. An *XY* slice of the Design 1 detector model (BF_3 tube at 2 atm) (a) and the corresponding Adjoint Group 47 (17.3 MeV) flux profile (b).

The *XY* slice of the entire region of detector material inside the tube in Figure 8.17 also displays the same efficiency behavior as did the ^{3}He tube, with an orderly decrease as particles are moved farther from the detector. The second outer ring around the detector shown in green in this figure appears to be about twice as thick as the same

region in the ^{3}He tube and this is likely due to the larger tube dimension as well because the larger detector presents a bigger target for any scattered neutrons. There are also regions of slightly greater efficiency at the top and bottom of the detector assembly, which occur due to the smaller degree of moderation on the sidewalls, which allows slower neutrons to more easily penetrate into the detector.

The overall adjoint function behavior in Figs. 8.18 and 8.19 is essentially the same as that of the ^{3}He baseline, with the exception of a larger region of smaller importance at the top and bottom of the figures. These features are associated with the larger tube dimensions as well, because there is less moderator material in this area when compared with that of the ^{3}He tube. This means there is a smaller probability for neutrons of higher energy to scatter in the moderator here and then be absorbed in the detector.

Figs. 8.20 and 8.21 show the adjoint function per unit source density and the reaction rate per neutron energy group for Design 1. The excellent behavior displayed in these figures proves that this design would serve well as a replacement for the for the baseline ^{3}He tube. The reaction rate plot, in particular, is very telling, because all but two of the reaction rates across the entire breadth of neutron energies are within 5% of the ^{3}He rate and the largest bias of only 6.7% occurs at Adjoint Group 41 (6.07 MeV). Note that a positive bias means that the reaction rate for a particular design is greater than the rate for ^{3}He at that same neutron energy, and the converse is true for negative biases.

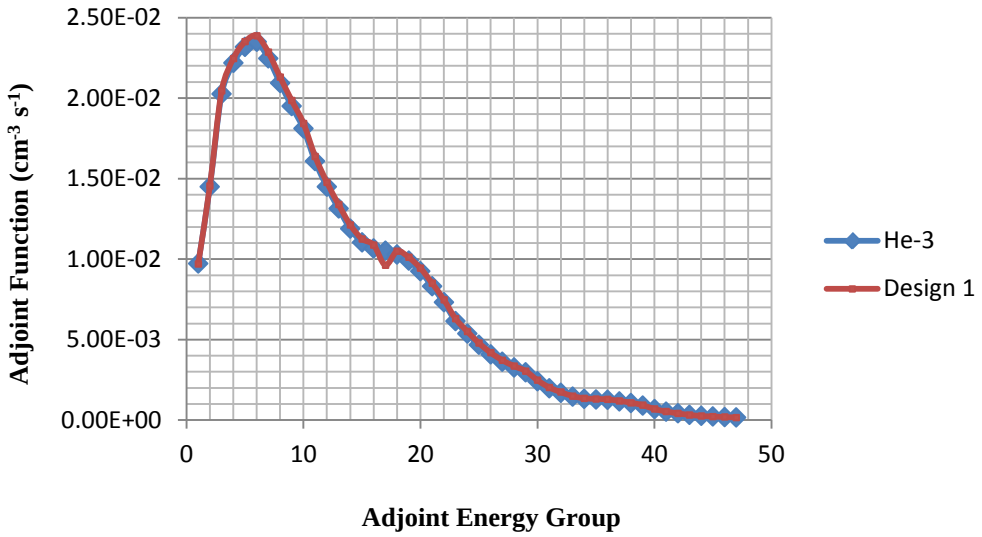

Fig. 8.20. Design 1 (BF_3 tube at 2 atm) adjoint function per unit source density in the forward air-filled course meshes adjacent to the polyethylene (toward a source) and in comparison with ^{3}He.

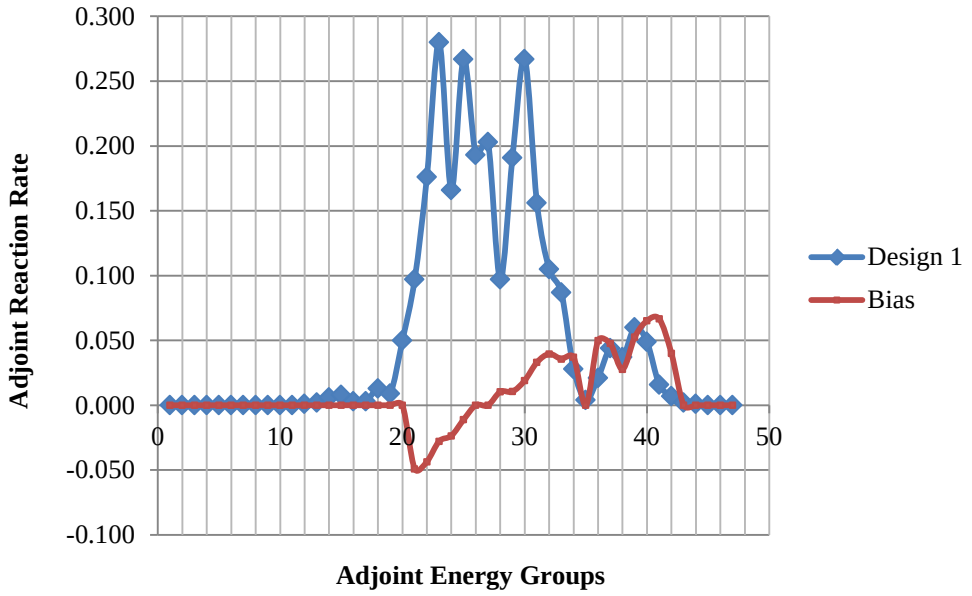

Fig. 8.21. Design 1 (BF_3 tube at 2 atm) adjoint reaction rate across all air-filled course meshes and the fractional bias with ^{3}He.

The negative bias dip at Adjoint Group 21 (1.11E-01 MeV) will be seen in all of the designs using BF_3 gas and is associated with a neutron energy region where the ^{3}He

(*n*, *p*) cross section follows an orderly decrease, while the ^{10}B cross section becomes slightly erratic (see Figure 3.12).

8.5.2.2 Design 4 – Two Dissimilar BF_3 Tubes Operating at 1 Atmosphere

The reaction rate results for Design 4 are detailed in Table 8.13 and display excellent agreement with that of the ^{3}He baseline case. Adjoint function profiles associated with this design are provided in Figs. 8.22 – 8.24 with an *XY* slice of the detector alongside each to ease the profile comparisons. Figure 8.22 also includes the addition of a 3-D view of the model to give the reader an overall sense of the assembly. There are a number of interesting features that appear in each figure which results from the twin-tube design and each of these features bears some additional discussion

Table 8.13. Reaction rates for Design 4 (dissimilar BF_3 tubes at 1 atm).

Method	**Rate (s^{-1})**	**Uncertainty (1.96σ)**	**Bias (%)**
PENTRAN Adjoint	2.603	--	-1.774
PENTRAN Forward	2.608	--	-2.468
MCNP5 Forward	2.561	0.004	-1.802

In considering Figure 8.22, one will notice that the adjoint function is about 10% higher within the rear tube due to a larger volume that increases the probability of interactions within the gas. There is also a larger degree of moderation surrounding the

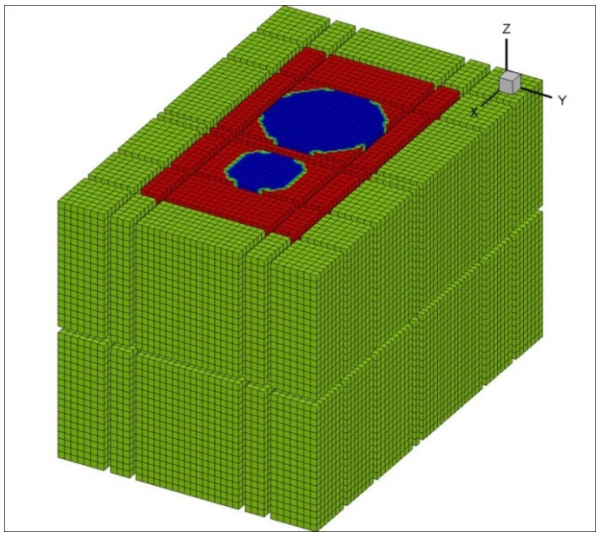

(a)

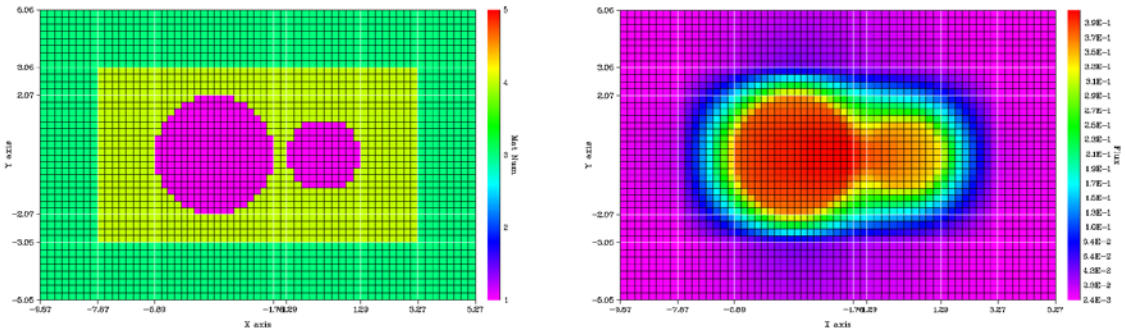

(b) **(c)**

Fig. 8.22. A 3-D view of the Design 4 detector model (dissimilar BF_3 tubes at 1 atm) (a), an *XY* slice of the model (b) and the corresponding Adjoint Group 1 (thermal) flux profile (c).

forward tube, which produces a region of lower efficiency around the edges when compared with the rear tube. This occurred because the lower-energy neutrons have farther to penetrate in the polyethylene to react with the forward tube. And unlike other regions of the polyethylene, the area between the two tubes retains a rather large efficiency because the material is sandwiched between two regions of neutron detector material.

Some additional interesting features are evident in Figs. 8.23 and 8.24 with increasing neutron energy. In these plots, the larger rear tube that was featured so prominently in the previous thermal-energy region seems to have almost disappeared in the shadow of the smaller forward tube. The same phenomena that produced a smaller thermal efficiency for the forward tube, here creates efficiencies that are 45% and 34% greater respectively and for a much smaller tube! These plots suggest that dissimilar tube

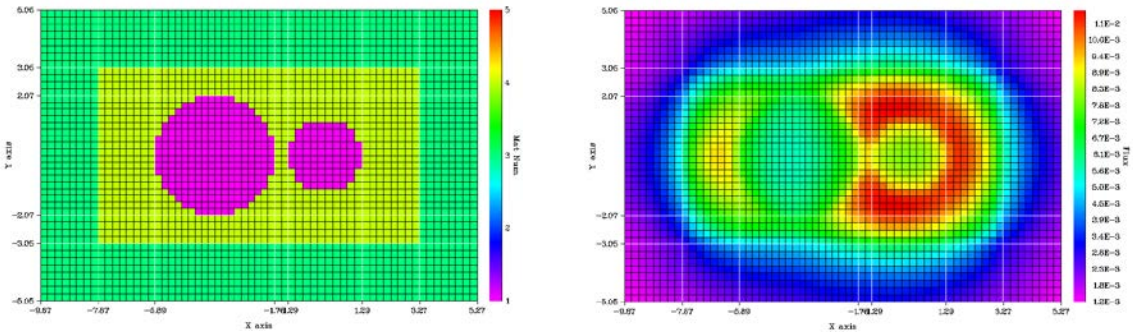

(a) **(b)**

Fig. 8.23. An *XY* slice of the Design 4 detector model (dissimilar BF_3 tubes at 1 atm) (a) and the corresponding Adjoint Group 29 (1 MeV) flux profile (b).

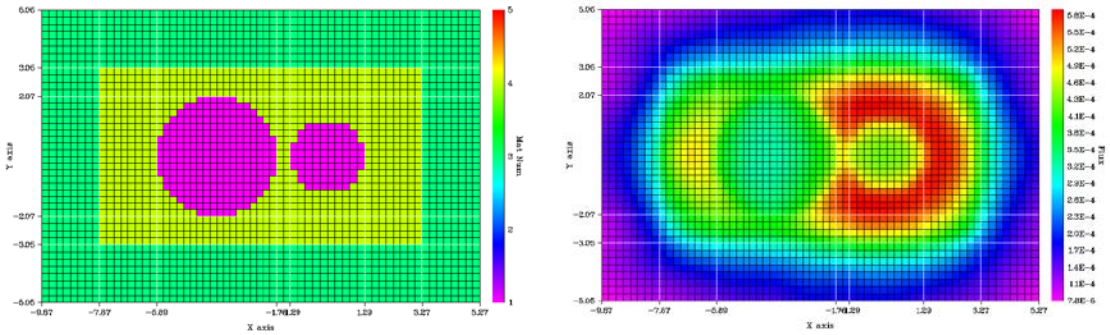

(a) **(b)**

Fig. 8.24. An *XY* slice of the Design 4 detector model (dissimilar BF_3 tubes at 1 atm) (a) and the corresponding Adjoint Group 47 (17.3 MeV) flux profile (b).

designs may hold some promise for developing detectors that have a relatively flat energy response across a wide range of neutron energies.

Figure 8.25 displays the comparison between the adjoint functions per unit source density for Design 4 and the ^{3}He baseline detector. The reaction rate per adjoint group in Design 4 is shown in Figure 8.26 and proves that this design is also a very good overall

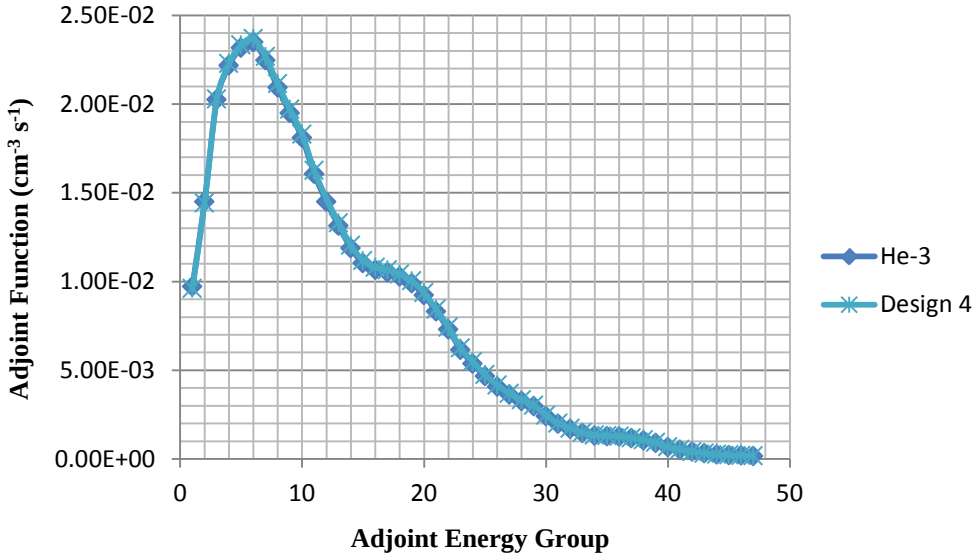

Fig. 8.25. Design 4 (dissimilar BF_3 tubes at 1 atm) adjoint function per unit source density in the forward air-filled course meshes adjacent to the polyethylene (toward a source) and in comparison with ^{3}He.

replacement for the baseline ^{3}He tube. The large disparity between the tube sizes produced biases that were slightly more pronounced, with 10 of the 47 adjoint groups having biases > 5%; however, only four of these biases were > 10% and the maximum difference was 13.3%, which is quite acceptable in the realm of neutron detection. The more exaggerated negative bias dip at Adjoint Group 21 (1.11E-01 MeV) when

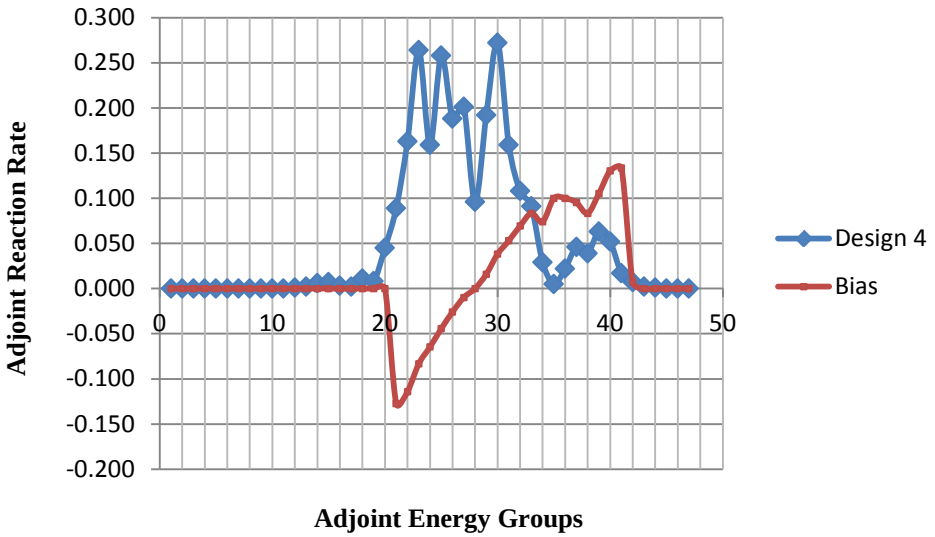

Fig. 8.26. Design 4 (dissimilar BF_3 tubes at 1 atm) adjoint reaction rate across all air-filled course meshes and the fractional bias with ^3He.

with Design 1 is due to the extra polyethylene surrounding the forward detector that prevents some of these neutrons from being detected. Conversely, the bias increase in the region of Adjoint Groups 36 – 40 (2.47 – 4.97 MeV) is most likely due to the larger dimension of the rear tube that presents a larger target to neutrons scattered in the polyethylene. The detector did, however, exhibit the same behavior regarding the energy groups contributing to the reaction rate (20 – 42).

8.5.2.3 Design 5 – Two Identical BF_3 Tubes Operating at 1 Atmosphere

The reaction rate results for Design 5, shown in Table 8.14, also exhibit excellent agreement with the ^3He baseline case. The adjoint function profiles associated with this specific design are provided in Figs. 8.27 – 8.29 and reveal essentially the same behavior as the baseline detector, but with a mirrored image because of the two-tube design and

Table 8.14. Reaction rates for Design 5 (identical BF_3 tubes at 1 atm).

Method	Rate (s^{-1})	Uncertainty (1.96σ)	Bias (%)
PENTRAN Adjoint	2.574	--	-2.868
PENTRAN Forward	2.590	--	-3.141
MCNP5 Forward	2.498	0.004	-4.218

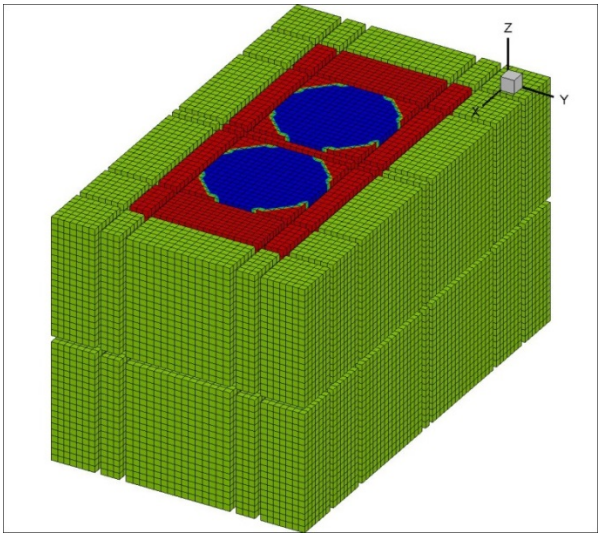

(a)

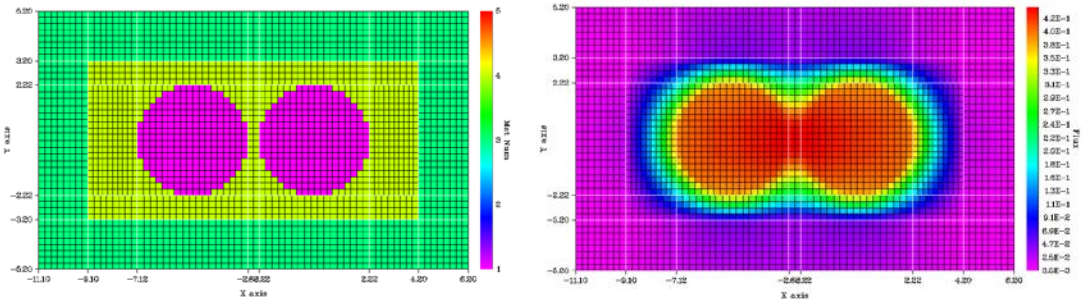

(b) **(c)**

Fig. 8.27. A 3-D view of the Design 5 detector model (identical BF_3 tubes at 1 atm) (a), an *XY* slice of the Design 5 detector model (b) and the corresponding Adjoint Group 1 (thermal) flux profile (c).

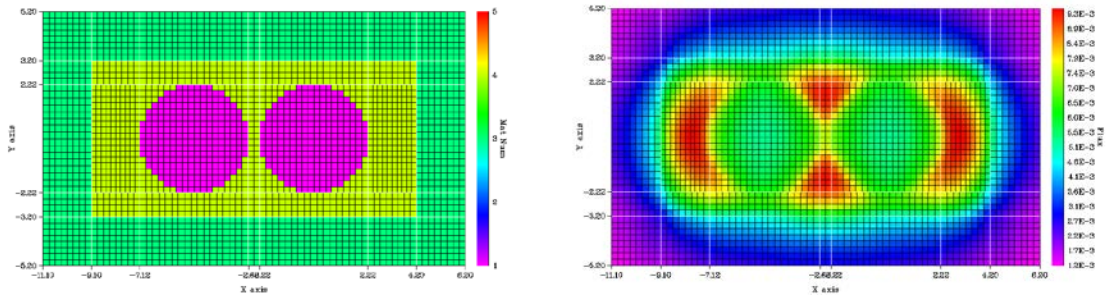

(a) **(b)**

Fig. 8.28. An *XY* slice of the Design 5 detector model (identical BF_3 tubes at 1 atm) (a) and the corresponding Adjoint Group 29 (1 MeV) flux profile (b).

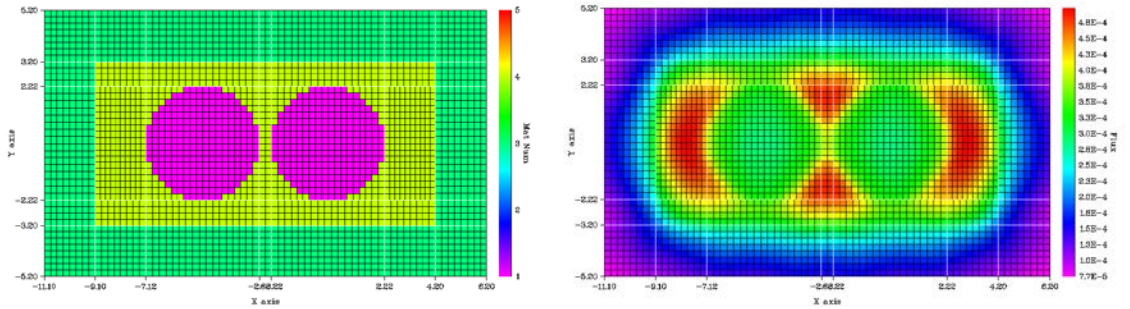

(a) **(b)**

Fig. 8.29. An *XY* slice of the Design 5 detector model (identical BF_3 tubes at 1 atm) (a) and the corresponding Adjoint Group 47 (17.3 MeV) flux profile (b).

the increased efficiency in the region between the tubes, which was also evident in the Design 4 plots.

Figs. 8.30 and 8.31 give the adjoint function per unit source density and the reaction rate comparisons with ^{3}He. The overall behavior of all these figures is very similar to Design 1, which was expected because of the large tube diameters that are part of this design.

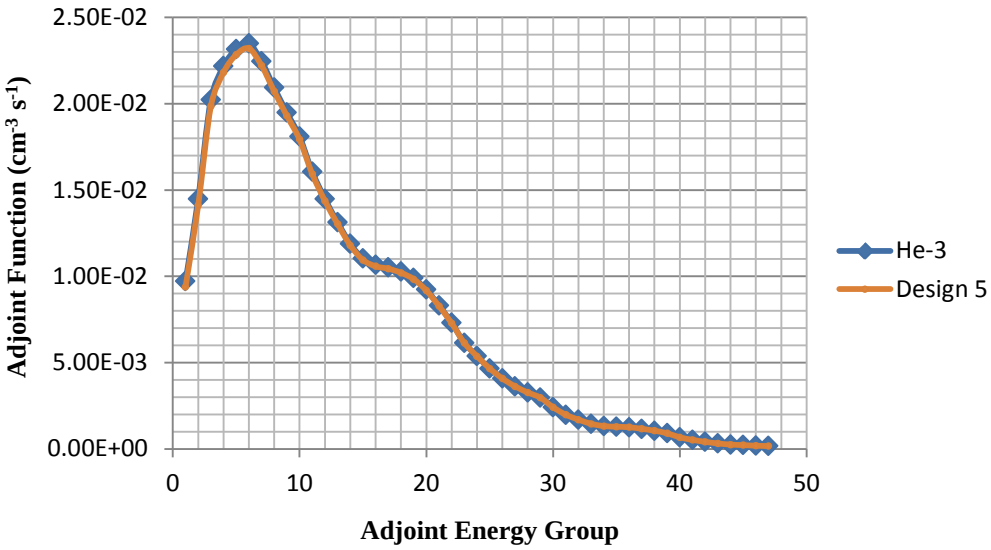

Fig. 8.30. Design 5 (identical BF_3 tubes at 1 atm) adjoint function per unit source density in the forward air-filled course meshes adjacent to the polyethylene (toward a source) and in comparison with ^{3}He.

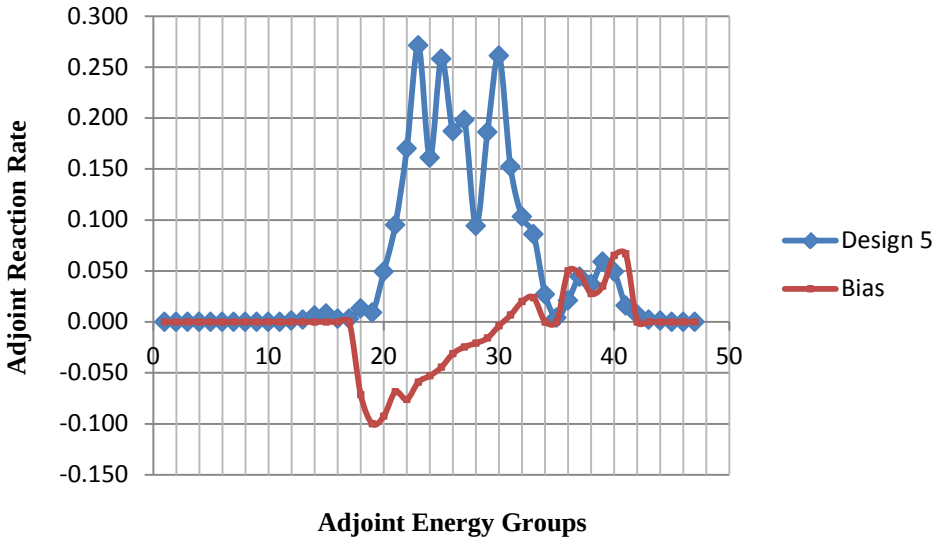

Fig. 8.31. Design 5 (identical BF_3 tubes at 1 atm) adjoint reaction rate across all air-filled course meshes and the fractional bias with ^{3}He.

8.5.3 ^{3}He-Equivalent Tube Designs Based on a ^{10}B-Lining

From a discrete ordinates perspective, materials with a vanishingly small thickness such as the ^{10}B lining used in the two subsequent designs present a problem from a mesh standpoint. Not only is the overall material thickness very small, but the corresponding mesh size will of necessity become even smaller. All of the gas tube designs in this research used a maximum mesh size of 0.25 cm in all directions and at least two meshes were desired for each coarse mesh in all directions. This constraint would have resulted in fine mesh sizes for the ^{10}B lining that were on the order of 5E-05 cm, which is too small to produce accurate deterministic results; therefore, to ensure adequate material coverage in the ^{10}B, the material density and thickness was adjusted in accordance with Eq. 5.1 to provide the desired model parameters.

8.5.3.1 Design 2 – Large ^{10}B-Lined Tube with ^{4}He Operating at 10 Atmospheres

Table 8.15 displays the reaction rate results for Design 2 that demonstrates excellent agreement with the ^{3}He baseline detector. The validity of Eq. 5.1 was also successfully established by altering the MCNP5 model associated with this design. The only changes to the model included reducing the ^{10}B thickness to 4.27E-04 cm and increasing the boron density to 2.34 g cm^{-3} in accordance with Eq. 5.1. The revised MCNP5 model yielded a neutron count rate of 2.524 $c\ s^{-1}$ that is only 0.5% different from the result in Table 8.15 and, therefore, validates the material balance approach that was implemented in order to increase the coarse mesh size in the accompanying PENTRAN

models. However, some cautionary comments concerning neutron counting must be mentioned about this specific type of detector design before moving onto a presentation of the profiles and plots connected with Design 2.

Table 8.15. Reaction rates for Design 2 (^{10}B-lined tube at 10 atm).

Method	Rate (s^{-1})	Uncertainty (1.96σ)	Bias (%)
PENTRAN Adjoint	2.595	--	-2.075
PENTRAN Forward	2.599	--	-2.805
MCNP5 Forward	2.511	0.005	-3.719

Chapter 2 detailed the pulse-height discrimination technique and demonstrated why this simple technique can be very effectively applied to gas detectors. The specific pulse-height spectrum of a ^{10}B-lined tube design was also detailed in Section 2.2.2.3 of that same chapter and discussed the fact that only one of the two reaction products (alpha or recoil ^{7}Li) produced in neutron absorption could be collected per event. Radiation transport codes such as PENTRAN and MCNP5 can provide information related to reactions that occur within a particular material; however, they cannot account for information lost due to inefficient charge collection associated with the detector electronics. Therefore, the dimensions and reaction rates associated with Design 2 are applicable only to the extent that the pulse-height discriminator setting has been properly established by the user.

If a single-channel method is chosen, the threshold must not preclude the counting of pulses produced by the 0.84 MeV ^{7}Li recoil product or if a window method is

employed, the thresholds must allow for tallying pulses from the 1.47 MeV alpha particles as well. The discriminator must obviously be properly chosen for the gas tubes as well; however, since both reaction products are emitted into the sensitive volume for these, there is much more room for error associated with the lower threshold setting.

Adjoint function profiles for this design are given in Figs. 8.32 – 8.34 with *XY* slices of the mode alongside each profile to aid in analyzing the profiles. Figure 8.32 also includes the addition of a 3-D model view to help the reader gain an overall sense of the design. Figs. 8.32 and 8.33 exhibit much the same overall behavior as the previously-discussed designs; however, there is one unique feature associated with Figure 8.32 that bares some discussion. The inner portions of all the gas tube designs discussed to this point have exhibited an overall constant efficiency throughout their volume and this is because the proportional gas functioned as both a charge carrier and the actual detection mechanism. Chapter 5 discussed the weaknesses of BF_3 as a proportional gas and also mentioned that one advantage of using a ^{10}B-lined tube was that a proportional gas with better qualities could be used as the charge carrier. Both ^{10}B-lined tubes detailed in this section accordingly use ^{4}He at 10 atm pressure for this purpose.

While ^{4}He has similar moderation properties ^{3}He, the gas itself serves no function for the actual neutron detection itself. Therefore, the inner volume of these detectors will not reveal the uniform nature of the adjoint function at thermal neutron energies as have all the other designs evaluated to this point. This feature is readily apparent in Figure 8.32 where there is an adjoint function difference of approximately 11% between the ^{4}He

and the ^{10}B lining. One might expect that the efficiency disparity would be greater, since ^{4}He does not detect neutrons; however, thermal neutrons that are placed inside the ^{4}He have a high probability of nonetheless being detected and this contributes to the relatively small function difference. Once we progress beyond the thermal-energy case, there really are no discernible differences between the adjoint functions in Figs. 8.33 and 8.34 and those associated with the other single-tube designs.

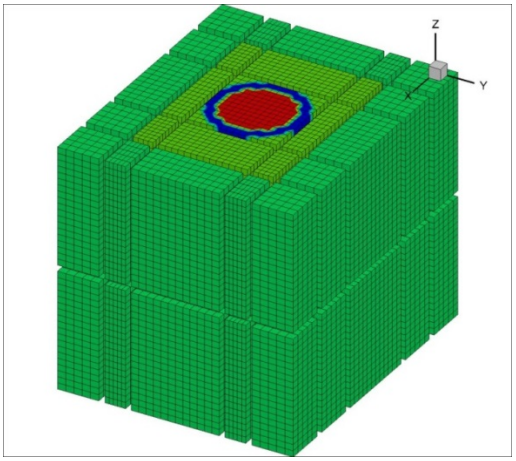

(a)

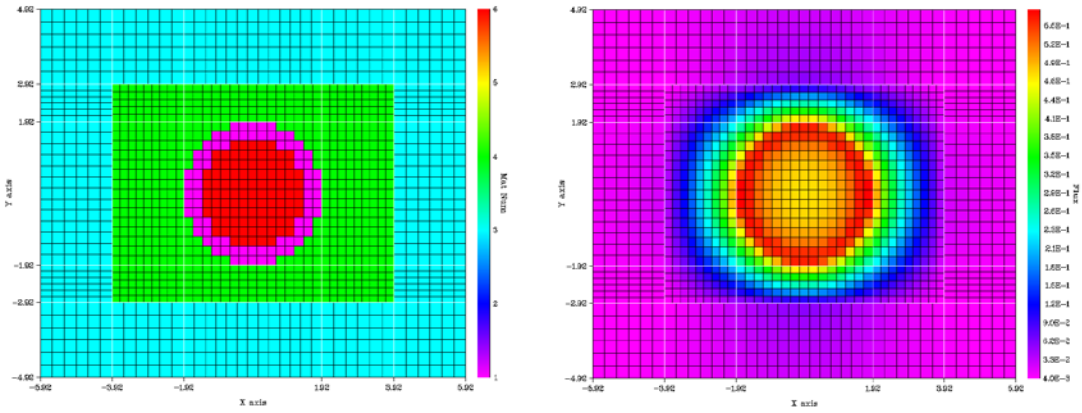

(b) **(c)**

Fig. 8.32. A 3-D view of the Design 2 detector model (^{10}B-lined tube at 10 atm) (a), an *XY* slice of the model (b) and the corresponding Adjoint Group 1 (thermal) flux profile (c).

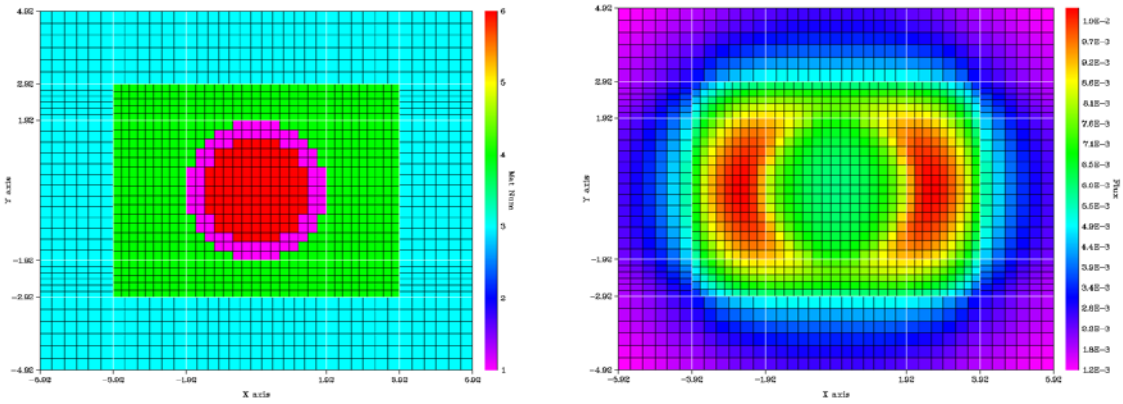

(a) **(b)**

Fig. 8.33. An *XY* slice of the Design 2 detector model (^{10}B-lined tube at 10 atm) (a) and the corresponding Adjoint Group 29 (1 MeV) flux profile (b).

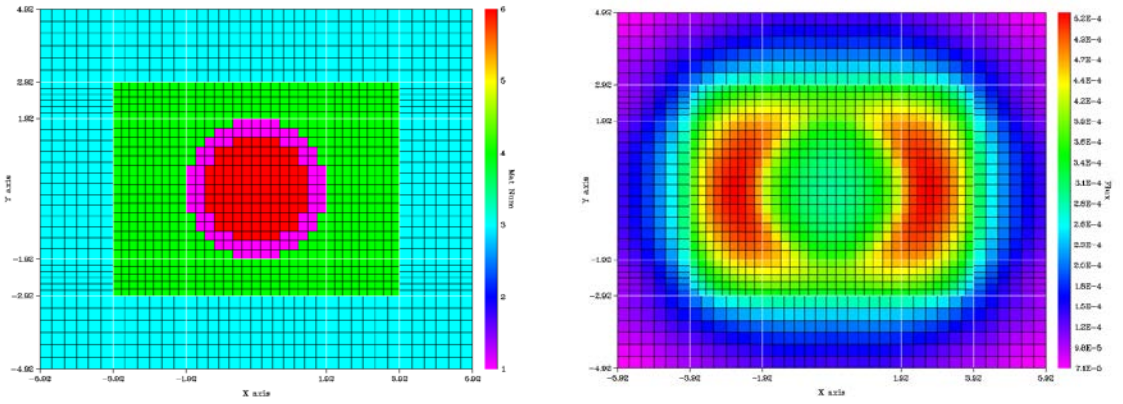

(a) **(b)**

Fig. 8.34. An *XY* slice of the Design 2 detector model (^{10}B-lined tube at 10 atm) (a) and the corresponding Adjoint Group 47 (17.3 MeV) flux profile (b).

Plots of the adjoint function per unit source density and the reaction rate for Design 2 are given in Figs. 8.35 and 8.36. The close comparison of these figures with the baseline case reveals that this design approximates the behavior of ^{3}He very closely. In particular, only three of the adjoint group biases as a function of adjoint energy group shown in Figure 8.36 exceed 5%.

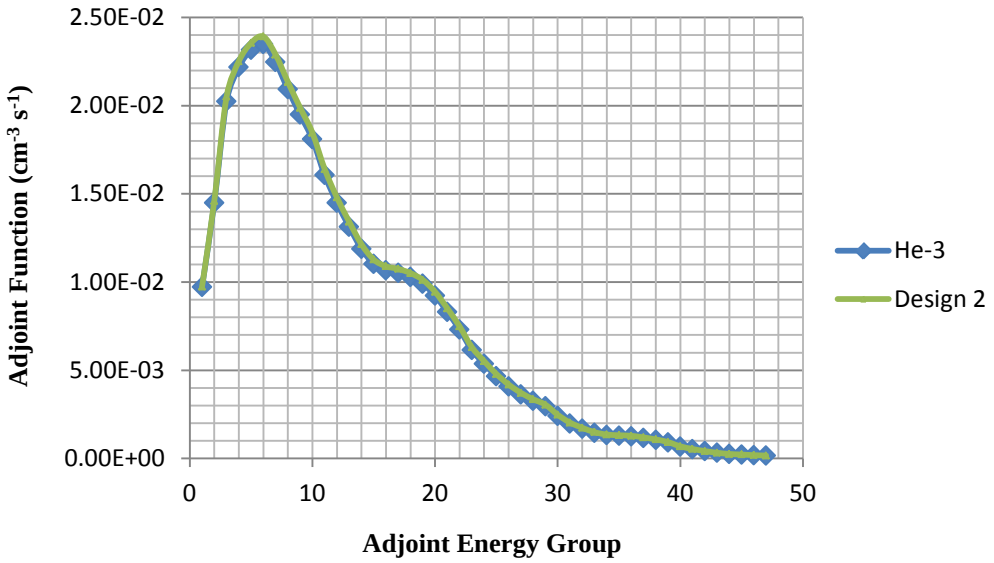

Fig. 8.35. Design 2 (^{10}B-lined tube at 10 atm) adjoint function per unit source density in the forward air-filled course meshes adjacent to the polyethylene (toward a source) and in comparison with ^{3}He.

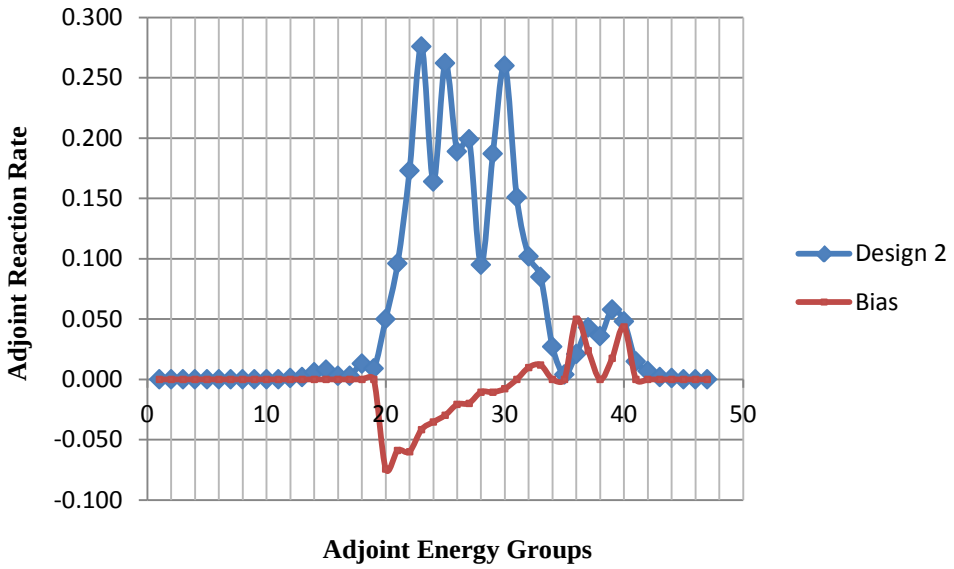

Fig. 8.36. Design 2 (^{10}B-lined tube at 10 atm) adjoint reaction rate across all air-filled course meshes and the fractional bias with ^{3}He.

8.5.3.2 Design 3 – Twin ^{10}B-Lined Tubes with ^{4}He Operating at 10 Atmospheres

Reaction rate results for Design 3 are given in Table 8.16 and prove that this design also approximates the performance of the baseline ^{3}He detector very well. However, since this design also utilizes ^{10}B-lined tubes, the same cautionary discussion associated with Design 2 also applies here. Figs. 8.37 – 8.39 display the adjoint function profiles for this design with the *XY* detector slices that have been included in each of the other designs. The 3-D view of the model has also been included in Figure 8.37 as well. These graphics are very similar to those of the dual-tube designs that have been previously discussed. However, since the sensitive volume for the neutron detection is concentrated on the periphery of the embedded tubes, there are a few interesting items of note that should be discussed.

Table 8.16. Reaction rates for Design 3 (identical ^{10}B-lined tubes at 10 atm).

Method	Rate (s^{-1})	Uncertainty (1.96σ)	Bias (%)
PENTRAN Adjoint	2.738	--	3.321
PENTRAN Forward	2.754	--	2.992
MCNP5 Forward	2.625	0.004	0.652

The interface region between the twin tubes in Figure 8.37 exhibits an increased efficiency as has been the case with the other multi-tube designs; however, because of the concentration of ^{10}B toward the outside of the tubes, there is a factor of 20 increase in efficiency for Adjoint Group 29 compared with Design 4 and more than a 25%

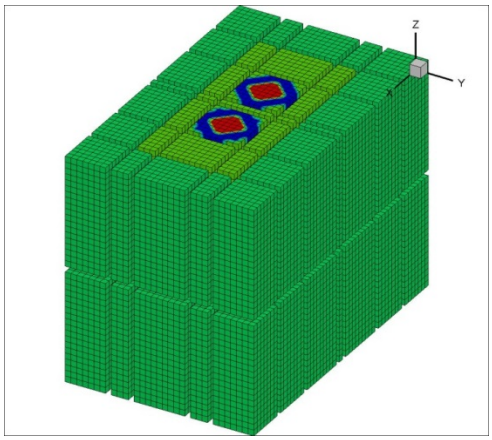

(a)

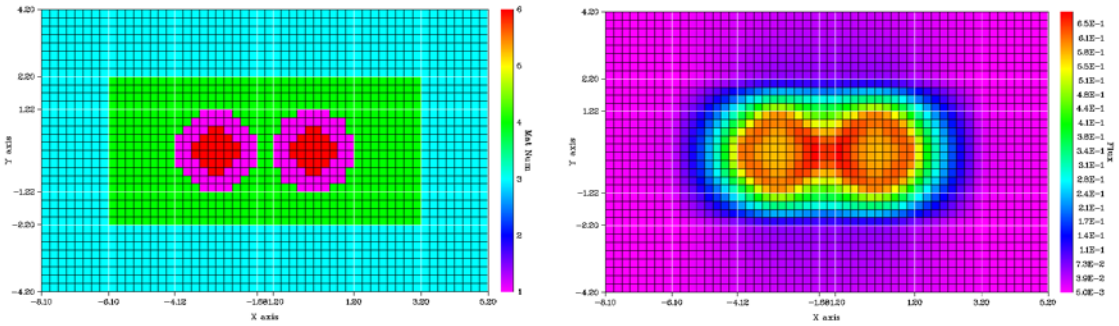

(b) **(c)**

Fig. 8.37. A 3-D view of the Design 3 detector model (identical ^{10}B-lined tubes at 10 atm) (a), an *XY* slice of the model (b) and the corresponding Adjoint Group 1 (thermal) flux profile (c).

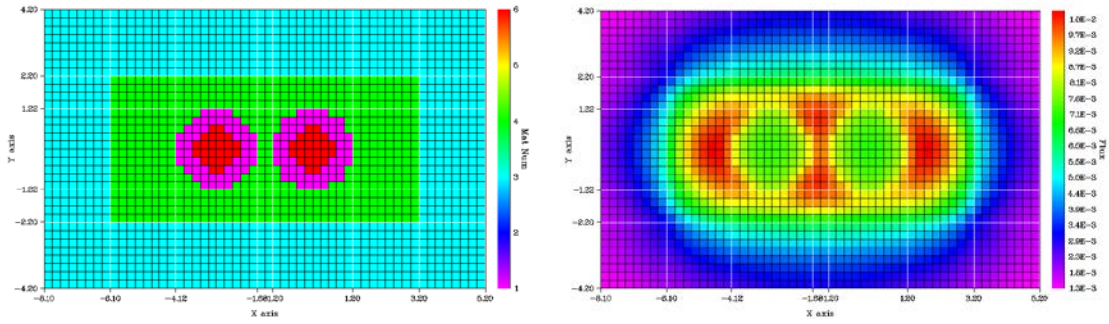

(a) **(b)**

Fig. 8.38. An *XY* slice of the Design 3 detector model (identical ^{10}B-lined tubes at 10 atm) (a) and the corresponding Adjoint Group 29 (1 MeV) flux profile (b).

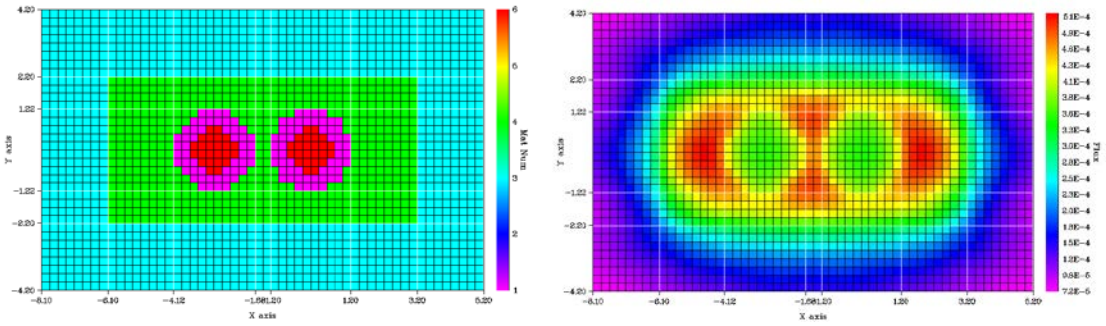

(a) **(b)**

Fig. 8.39. An *XY* slice of the Design 3 detector model (identical ^{10}B-lined tubes at 10 atm) (a) and the corresponding Adjoint Group 47 (17.3 MeV) flux profile (b).

improvement in Adjoint Group 47. There is also a reduction in efficiency of about 11% between this region and the outer edges of both tubes to the left and right. This increase is due solely to the higher concentration of ^{10}B that is in close proximity to the interface region.

Another interesting feature to note is the region of higher efficiency surrounding the tubes in Figs. 8.38 and 8.39. The appearance of these regions is very similar to that of Figs. 8.11 and 8.12 associated with ^{3}He and this is due to the concentration of the ^{10}B along the periphery along with the same tube diameters. Apart from these two observations, all other features exhibit behavior similar to that of similar designs. Similar sentiment applies to the plot of the adjoint function per unit source density in Figure 8.40; however, the adjoint reaction rate bias in Figure 8.41 displays an interesting feature not seen in any other designs evaluated to this point.

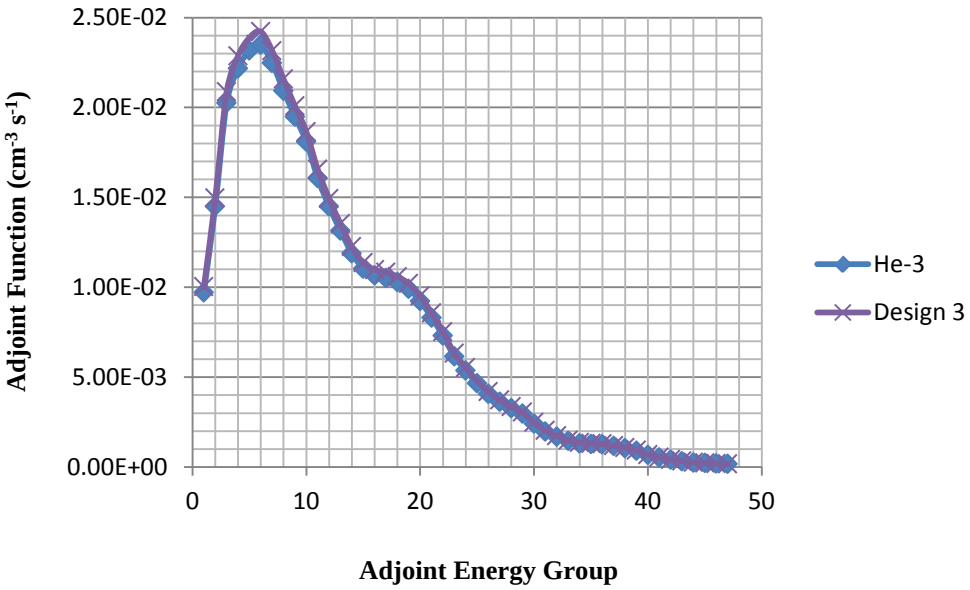

Fig. 8.40. Design 3 (identical ^{10}B-lined tubes at 10 atm) adjoint function per unit source density in the forward air-filled course meshes adjacent to the polyethylene (toward a source) and in comparison with ^{3}He.

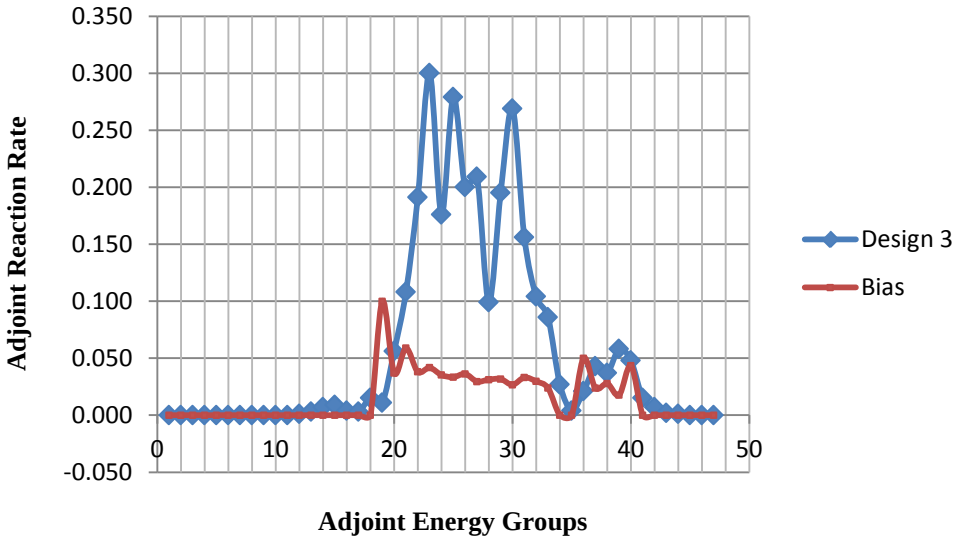

Fig. 8.41. Design 3 (identical ^{10}B-lined tubes at 10 atm) adjoint reaction rate across all air-filled course meshes and the fractional bias with ^{3}He.

The unique aspect that should be noted is the absence of a negative bias across the entire range of neutron energy. This feature also results from an accumulation of ^{10}B in

the interface region between the two detectors; however, only two responses have a bias greater than 5% and, oddly enough, these occur in the region of Adjoint Group 21, which typically has produced the largest negative bias for several of the other detectors. The likely cause for the increased efficiency at these energies is the higher concentration of the ^{10}B near the sidewalls of the detector (top and bottom), which allows many of these lower-energy neutrons to be detected because of the smaller moderator thickness in this region. As a result of the positive bias behavior, the dual-tube ^{10}B-lined design represents the most conservative case from the perspective of criticality safety monitoring.

8.5.4 ^{3}He-Equivalent Tube Design Based on a ^{10}B-Loaded PVT – Design 6

The combination of a large hydrogen content at higher density (compared to the gases) produced an inability to converge the PVT model to an infinity norm < 2E-03 with the S_8 and P_2 parameters used within the other models. Reducing the overall coarse mesh thicknesses by half to approximately 0.12 cm and using the former PENTRAN parameters also failed to produce convergence below 1E-03; therefore, a higher scattering moment (P_3) was selected for the execution of the PENTRAN ^{10}B-loaded PVT model. The higher scattering moment was necessary for neutron scattering physics and produced a convergence of < 5E-04.

The reaction rate produced by Design 6 during the computational modeling is shown in Table 8.17. As with the other designs, this particular one also matched the overall response of ^{3}He quite well; however, this particular design is less than half the size of the other detectors (4.5 cm height), which means that it is more efficient by a

factor of about 2.2 compared with the baseline detector on a volumetric basis. The plots of the adjoint function profiles are also given in Figs. 8.42 – 8.44 along with the XY detector slices and the 3-D model view as was done for the other designs. Design 6 displays the same overall thermal appearance as the other single detector designs; however, there are two unique features related to Figs. 8.43 and 8.44 that require some discussion.

Table 8.17. Reaction rates for Design 6 (^{10}B-loaded PVT).

Method	Rate (s^{-1})	Uncertainty (1.96σ)	Bias (%)
PENTRAN Adjoint	2.668	--	0.679
PENTRAN Forward	2.699	--	0.935
MCNP5 Forward	2.610	0.004	0.077

Unlike all the other detectors in this study, including ^{3}He, the PVT response for the midrange neutrons in Figure 8.43 demonstrates a good efficiency that covers the entire detector region and extends outwardly into the polyethylene on all sides in an ellipsoidal fashion, which is also unique among the different designs. The efficiency in this entire region is approximately 50% greater than the highest ^{3}He efficiency at this neutron energy, which results from the plastic content of the PVT and its higher overall density. Had the detector been equally moderated on all sides (2 cm), the appearance of the higher-efficiency region would most likely be more spherical in nature.

The other unusual feature related to the PVT energy response is associated with the higher neutron energies beginning with Adjoint Group 43 (8.61 MeV). The plot

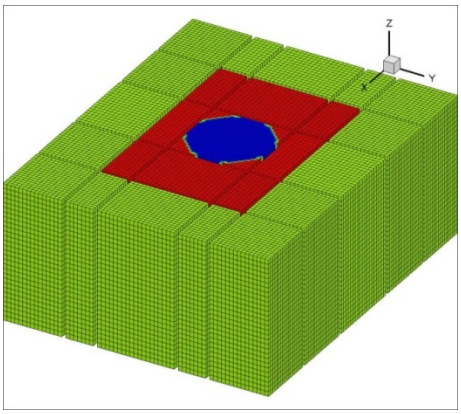

(a)

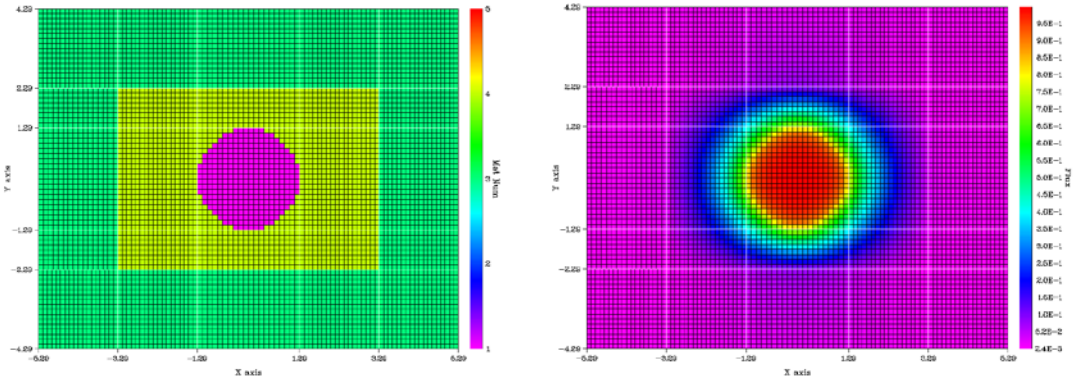

(b) **(c)**

Fig. 8.42. A 3-D view of the Design 6 detector model (^{10}B-loaded PVT) (a), an *XY* slice of the Design 6 model (b) and corresponding Adjoint Group 1 (thermal) flux profile (c).

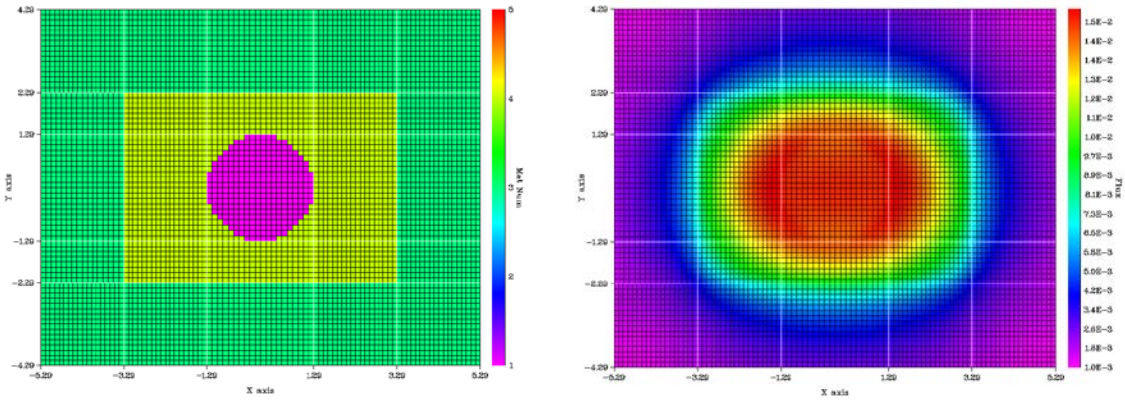

(a) **(b)**

Fig. 8.43. An *XY* slice of the Design 6 detector model (^{10}B-loaded PVT) (a) and the corresponding Adjoint Group 29 (1 MeV) flux profile (b).

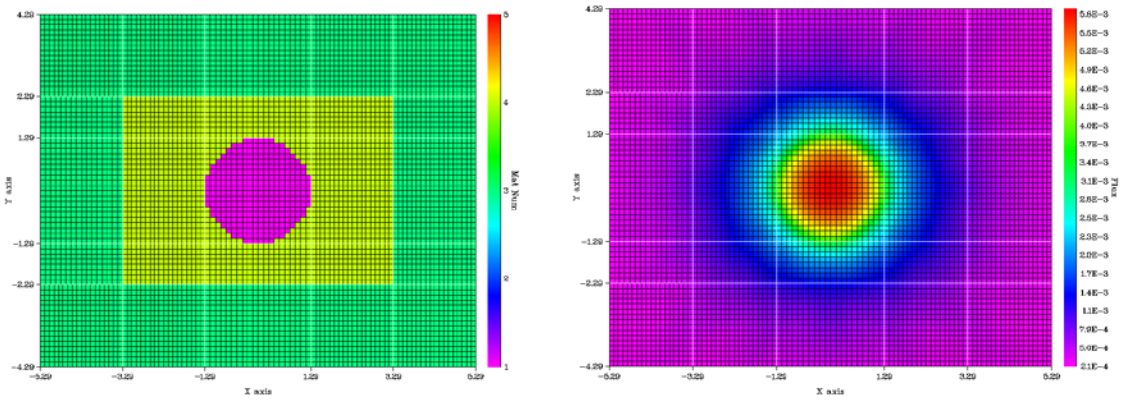

(a) **(b)**

Fig. 8.44. An *XY* slice of the Design 6 detector model (^{10}B-loaded PVT) (a) and the corresponding Adjoint Group 47 (17.3 MeV) flux profile (b).

shown in Figure 8.44 is obviously for a much higher energy (17.3 MeV); however, its characteristics capture the essence of the function plot for Adjoint Group 43 and will be used for discussion purposes. The nature of the gradient used in the DISLIN module in the PENMSHXP software gives the appearance that the PVT is efficient only within the detector region itself; however, by comparing the adjoint function profiles closely, one will notice that, with the exception of the corners of the plot, every coarse mesh possesses a greater adjoint function (efficiency) than the greatest function regions of the ^{3}He plot for this neutron energy. Some of this behavior is once again due to the higher density of the PVT, but other aspects that lead to the improved performance are a good concentration of ^{10}B within the PVT matrix and the moderation properties of the PVT.

The comparison of the adjoint function per unit source density for the PVT and ^{3}He baseline is given in Figure 8.45 and the reaction rate comparison with ^{3}He is given in Figure 8.46. While Figure 8.45 delivers a similar appearance compared with the

other detectors, the reaction rate plot stands in stark contrast to any other detector in this study. The adjoint reaction rate in Design 6 specifically appears to be an almost mirror reflection of plots for the other detectors. Instead of a negative bias in the Adjoint Group 20 region, there is 10% positive bias; after which the reaction rate gradually decreases until Adjoint Group 34 (2.35 MeV). The overall response is excellent, with only 5 of 47 groups having > 5% bias.

The opposite behavior exhibited by the PVT in Figure 8.46, results from the PVT components having a higher density. Even in the more highly efficient ^{3}He gas, thermal neutrons can still leak out of the detector and escape counting; however, with the PVT, the increased density and scattering properties of the plastic excel at keeping those same

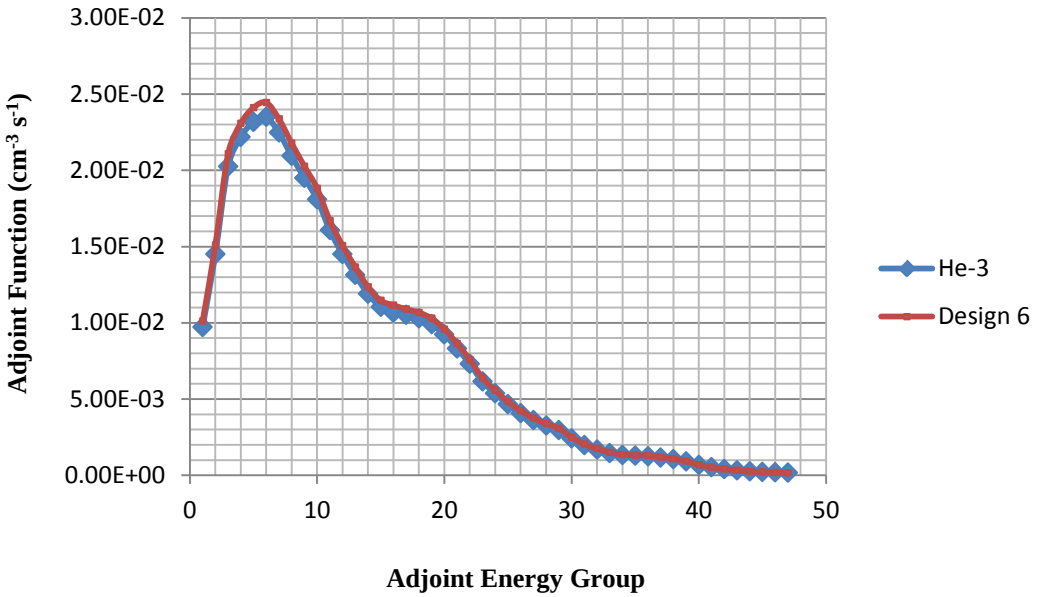

Fig. 8.45. Design 6 (^{10}B-loaded PVT) adjoint function per unit source density in the forward air-filled course meshes adjacent to the polyethylene (toward a source) and in comparison with ^{3}He.

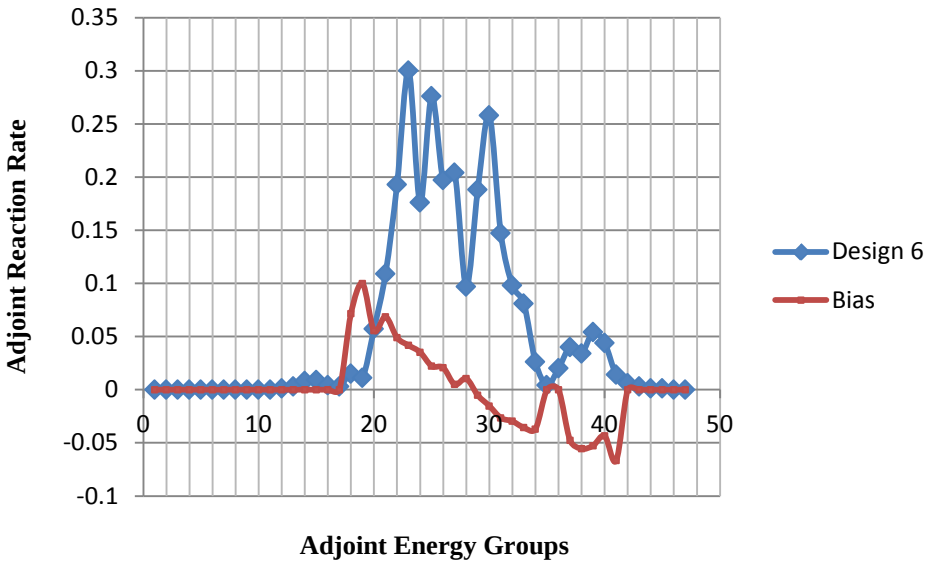

Fig. 8.46. Design 6 (^{10}B-loaded PVT) adjoint reaction rate across all air-filled course meshes and the fractional bias with ^{3}He.

neutrons within the confines of the detector, where they are more efficiently captured in the ^{10}B.

Conversely, the PVT can also act as an inhibitor to detection at the higher neutron energies, because the scattering properties that more efficiently contained thermal neutrons within the PVT, can adversely affect the higher-energy response by producing scattering from the detector at rates exceeding the absorption events. In addition to hydrogen, the PVT also contains a good deal of carbon. At 10 MeV, both of these elements have scattering cross sections that are at least double that of the ^{10}B (n, α) reaction and at 1 MeV, the disparity is much greater. Therefore, unlike the thermal energy case, the cross section behavior of the PVT constituents produces a net-negative effect at the higher neutron energies. This overall behavior still favors the ^{10}B-loaded PVT, however, because the emission rate of neutron emitters at the higher energies is far

less than those of lower energies. For example, the emission rate for a 4.97 MeV neutron in the source term of the computational models used in this research compared with that of a 1 MeV neutron is approximately 2000 times less likely.

8.6 Summary of the Results

The overall objective of this dissertation effort was to investigate the use of deterministic adjoint transport methods toward developing at least one plug-in replacement for our 4 atm baseline ^{3}He tube. A secondary objective of the research was to accomplish the former using commercial off-the-shelf materials in order to preclude the availability issues that continue to plague the ^{3}He economy. It can be unequivocally stated that both these goals were achieved, while delivering a total of six plug-in designs that match the overall spectral performance of 4 atm moderated ^{3}He.

The excellent agreement demonstrated between the computational calculations and the neutron measurements in Section 8.4 validated the use of radiation transport simulations for designing the plug-in detectors. Based upon the ability of these simulations to represent the reality of an actual neutron monitoring environment, it can be confidently stated that the designs discussed in Section 8.5 can all serve as valid plug-in detectors for a 1-inch diameter ^{3}He detector operating at 4 atmospheres pressure and with an active length of 10 cm.

Furthermore, the results of this research demonstrate that the techniques developed here can be applied toward the testing of new detector materials and/or designs to determine their suitability as spectrally-equivalent alternatives to ^{3}He. The data also prove that these methods can be effectively utilized for radiation detector design in general by taking advantage of the important insights that can be gained through an adjoint transport evaluation.

However, having said this, the reader should not assume that this design process was trivial. The MCNP5 code was utilized to greatly reduce the amount of guesswork related to the initial design choices; however, a minimum of 15 – 20 PENTRAN simulations were still necessary to establish the correct dimensions associated with each equivalent design. The design process can also be extended by the choice of quadrature, scattering order, and the spatial coarse mesh dimensions necessary for convergence.

The decision to use an in-line arrangement for the dual tube designs was motivated by the extra *vertical* space that is generally available between a detector and the assembly housing as was previously mentioned. In these cases, the in-line design would allow for the insertion of a second detector directly behind the existing unit without causing a configuration control challenge.

8.7 References

1. Knoll, G., Radiation Detection and Measurement, 4th ed., John Wiley & Sons, Inc., New York, 2009.

2. Walker, S., Photon Cross Section Evaluation, data retrieved from XCOM: Photon Cross Sections Database, available at www.nist.gov/pml/data/xcom/index.cfm , accessed during 2012 – 2013.

3. Walker, S., ENDF/B-VII Evaluation, data retrieved from the ENDF database, available at www.nndc.bnl.gov, accessed during 2012 – 2013.

4. Evans, R., The Atomic Nucleus, Krieger Publishing, Co., Malabar, FL, 1985.

5. Sjoden, G., Deterministic Adjoint Transport Applications for He-3 Neutron Detector Design. Annals of Nuclear Energy, 29, pp. 1055 – 1071, 2002.

6. Chadwick, M., et al., ENDF/B-VII.0: Next Generation Evaluated Nuclear Data Library for Nuclear Science and Technology. Nuclear Data Sheets, Vol. 107, Issue 12, pp. 2931 – 3060, Dec., 2006.

7. Kouzes, R., Ely, J., Lintereur, A., Siciliano, E., and Woodring, M., BF_3 Neutron Detector Tests, PNNL Technical Report-19050. PNNL, Richland, WA, 2009.

8. White, J., Ingersoll, D., Slater, C., and Roussin, R., BUGLE-96: A Revised Multi-Group Cross Section Library for LWR Applications Based on ENDF/B-VI Release 3. ORNL, DLC-185, 1996.

CHAPTER 9
CONCLUSIONS AND RECOMMENDATIONS

9.1 Conclusions

This dissertation describes a specific computational methodology for designing spectrally-matched plug-in replacements for a baseline ^{3}He detector (1-inch diameter and 10 cm length) operating at 4 atm pressure. The application of computational adjoint transport methods toward this end has never been attempted in literature, and represents a large step forward in radiation detector development because of the unique insights that can be gained through this type of assessment. In particular, the adjoint technique provides a comprehensive picture of the detector environment, allowing a designer to choose appropriate materials and to position them accordingly to optimize detector performance. The technique also allows the designer to evaluate potential combinations of detector materials that take advantage of the strengths of each by evaluating the potential reaction rate performance across a wide range of neutron energies.

The motivation for this research stemmed from the tremendous shortage of ^{3}He gas that presented technical challenges for numerous non-proliferation applications; however, an important issue that has been lost in the scientific clamor is the effect on domestic and international non-proliferation policy. Obligations associated with curtailing terrorist activities by non-state actors that stemmed from positions such as those found in U.N. Security Council Resolution 1530 have been severely hampered by

the lack of ^{3}He gas, because many of the nuclear-related goals were directly tied to detection programs. Specifically, the unavailability of the ^{3}He gas inhibited the ability of the various member states to develop effective prevention measures related to the proliferation of nuclear weapons and/or radiological devices because so much focus had been placed on a singular technology. For this reason, only off-the-shelf products that are readily available to replace ^{3}He were chosen for testing in this research.

Although the primary focus of the research was on developing plug-in replacements for a specific ^{3}He neutron detector design, the computational adjoint method demonstrated herein can be directly applied toward any radiation detector design associated with neutrons and/or photons. A combination of forward transport methods and physical measurements firmly established the validity of the methods and, therefore, the designs that resulted from them. The excellent agreement between the PENTRAN adjoint and forward deterministic calculations and MCNP5 also attested that the broad-energy multi-group BUGLE-96 cross section library produces results that are in agreement with the current continuous-energy ENDF/B-VII cross section library.

The successful conclusion of the research yielded six different novel designs that can serve as direct plug-and-play alternatives for a baseline ^{3}He detector. This achievement, which has never been demonstrated, allows for the use of existing and readily-available detector materials in place of ^{3}He for applications such as portal monitoring, material control and accountability (MC&A), fissile material assessments, and other non-proliferation efforts that have been established on the basis of a ^{3}He

detector response. The capability of these proven and less-expensive detectors should not only have a positive technological impact on non-proliferation programs, but also on policy-based application, because it is highly probable that these alternatives will find a wider application solely because of their affordability.

The equivalent designs consisted of both larger individual tubes containing BF_3 gas or a ^{10}B lining and smaller dual tube designs using the same materials. Each design demonstrated its equivalency to the baseline detector by matching the adjoint function (importance or efficiency) and reaction rate across 47 neutron energy groups ranging from 0.1 eV to 17.3 MeV. The final analysis of each design yielded valuable information about the adjoint function (importance or efficiency) behavior and the reaction rate as a function of neutron energy. The analysis also revealed that the only adjoint neutron energy groups that typically contribute to the detector reaction rate are Adjoint Groups 20- 41, which represent the neutron energy range of 6.74E-02 – 7.41 MeV. This information, which has never been published in literature, allows for the elimination of source neutrons outside this particular energy range, which can accelerate deterministic calculations and lower their overall computational expense without adversely affecting the outcome of a calculation.

The knowledge gained about the reaction rate performance also hints about possible designs that exploit a combination of multiple detector types that do not rely on a single material or detection mechanism in order to produce a relatively flat neutron energy response. For example, the PVT testing demonstrated that this particular design

excelled at detection of neutrons at lower energies, whereas the other ^{10}B-based designs all performed better at higher neutron energies. This behavior immediately suggests that the best overall ^{3}He replacement detector should consist of a combination of PVT/BF_3 (Designs 1 and 6) or a PVT/^{10}B-lining (Designs 2 and 6) in order to enhance the overall reaction rate response as a function of neutron energy. The combination designs could potentially be able to estimate quantities like the equivalent dose far better than any detector currently on the market due to a more horizontal energy response. If a singular material approach is preferable, then the dual ^{10}B-lined tube design (Design 3) should be considered, especially in the area of criticality safety, since the detector bias for this particular design had a consistently small positive bias.

It should be noted that the plug-in designs that were identified in the research results were determined by the adjoint deterministic method on the basis of their individual reaction rate and spectral response; therefore, one cannot simply add detector biases for two separate designs together in order to specify a plug-in design on the basis of composite materials. Rather, the materials would need to be incorporated into a new combinatorial design and processed in the same manner as that specified in Figure 5.3 to accurately determine the associated dimensions.

9.2 Recommendations

The materials chosen for this study all utilized ^{10}B in some form, be it a gas or a solid. The choice of these materials and the ^{10}B reaction was prudent because the

materials have been in use for decades, they are readily available today, and the cross section exhibits characteristics similar to ^{3}He across a wide neutron energy range. One future extension of this research might be to focus on detector materials whose cross section behavior is atypical of ^{3}He and then insert combinations of various moderators and/or materials to alter their associated adjoint function and reaction rate to match the ^{3}He response.

Another extension could be to develop replacement designs for existing systems being operated in support of special nuclear material assessment programs or another non-proliferation application. One example is well counters used for ^{239}Pu analyses associated with spent fuel or other reprocessing. Facilities with these counters are all being adversely affected by the ^{3}He shortage because any available gas stock is generally consumed by the Department of Homeland Security (DHS) or the National Nuclear Security Administration (NNSA) before anyone else is aware of its availability. The spectrally-matched ^{3}He alternatives developed herein can be directly substituted for existing detectors in these applications would meet with a welcome audience. Subsequently, Georgia Tech has filed a provisional patent on this technology as a result of this work.

One final area that can be investigated is the application of these techniques to neutron detector design in general. There are very few applied examples of the adjoint transport method a detector design in the literature, once one migrates from the educational community. This technique is far superior to a singular forward approach

using MCNP because information is gained about the entire phase space and not just a singular point or region. The additional information that is provided by the adjoint method should be able to drastically improve the ways in which neutron detectors are designed and constructed. This approach should also yield detectors that are smaller, more adaptable, and that are more efficient than currently available units.

Finally, now that it has been absolutely proven that alternative detectors can serve as plug-in replacements for ^{3}He tubes in even the most challenging of spectral applications, the nuclear industry should be able to break free from the restraints that this shortage has shackled us with. Furthermore, we must be willing to accept the chief lesson that this shortage emphasized, which is that we should never again fall into the trap of "*placing all our eggs into one detection basket*," so to speak. Once we are able, as an industry, to apply the hard lessons we've learned from this lengthy hardship, we will be able to break free from a singular focus on *replacement efforts* and instead, become empowered to move beyond ^{3}He's capability whenever possible.

APPENDIX A
DERIVATION OF COMPTON WAVELENGTH (EQ. 3.6)

The Compton scattering process is depicted in Figure A.1 where an incoming photon of energy (E) is scattered through an angle (θ_s), producing a Compton electron of kinetic energy (T) scattered through angle (θ_c) and where each angle is

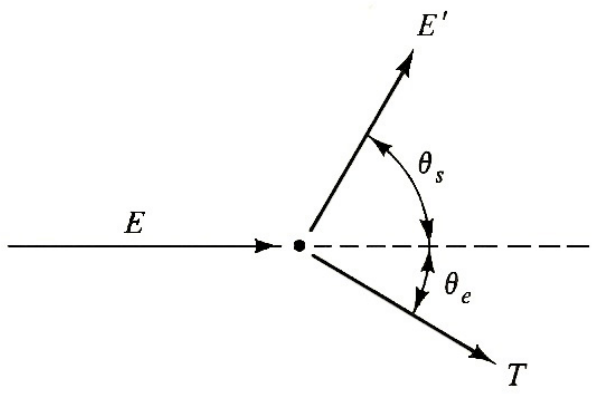

Fig. A.1. Diagram Illustrating a Compton Scattering Event.

measured relative to the original direction of the incident photon. Considering the case where an incoming photon strikes an electron at rest, the conservation of energy dictates that initial and final energy states of the photon and electron are given by

$$E_\gamma + E_e = E_\gamma^{'} + E_e^{'}\,, \tag{A.1}$$

where $E_\gamma = h\upsilon$, $E_\gamma{}' = h\upsilon'$. From the relativistic energy-momentum relationship, the energy of the electron at rest (E_e) is

$$E_e = \frac{m_e c^2}{\sqrt{1 - \left(\frac{v}{c}\right)^2}} = m_e c^2 \,. \tag{A.2}$$

However, for the case of the recoil electron, the total energy term must now include a consideration of kinetic energy, since the particle has been accelerated by the momentum transfer from the photon. The momentum transfer can be included in the equation for energy by first squaring the full version of Eq. A.2

$$E_e{}'^2 = (mc^2)^2 = \frac{m_e^2 c^4}{1 - \left(\frac{v}{c}\right)^2} \,. \tag{A.3}$$

Next, rearrange the terms to get

$$m^2 c^4 \left(1 - \left(\frac{v}{c}\right)^2\right) = m_e^2 c^4 \,. \tag{A.4}$$

Now, expand the left-side of A.4

$$m^2 c^4 - m^2 c^2 v^2 = m_e^2 c^4 \tag{A.5}$$

and rearrange A.5 to obtain

$$m^2c^4 = m_e^2c^4 + m^2c^2v^2 \ . \tag{A.6}$$

The left-side of A.5 may now be reinserted to get

$$E_e^{'2} = m_e^2c^4 + m^2c^2v^2 \ . \tag{A.7}$$

Solving for the energy term yields

$$E_e^{'} = \sqrt{m_e^2c^4 + m^2c^2v^2} \ . \tag{A.8}$$

Using the fact that momentum (p) = mc (rest mass) or mv (kinetic), A.5 can also be written as

$$E_e^{'} = \sqrt{(m_ec^2)^2 + p^2c^2} \ . \tag{A.9}$$

Substituting A.5 into A.1 gives

$$h\upsilon + m_ec^2 = h\upsilon^{'} + \sqrt{(m_ec^2)^2 + p^2c^2} \ , \tag{A.10}$$

where the photon energy terms have been changed to quantum relations. By moving $h\upsilon'$ to the left-hand side of A.10 and squaring both sides of the equation, one gets

$$(h\upsilon + m_e c^2 - h\upsilon')^2 = (m_e c^2)^2 + p^2 c^2 , \tag{A.11}$$

Moving the rest-mass term to the left-hand side gives

$$p^2 c^2 = (h\upsilon + m_e c^2 - h\upsilon')^2 - (m_e c^2)^2 . \tag{A.12}$$

Since A.12 is in terms of momentum, we now shift our focus to the evaluation of this quantity. Since the electron is initially at rest, the conservation of momentum relation is

$$P_\gamma + 0 = P_\gamma' + P_e' , \tag{A.13}$$

Solving for the momentum of the recoil electron yields

$$P_e' = P_\gamma' - P_\gamma . \tag{A.14}$$

By making use of the scalar product rule, we can write

$$P_e'^2 = P_e' \cdot P_e' = \left(P_\gamma' - P_\gamma\right) \cdot \left(P_\gamma' - P_\gamma\right) \tag{A.15}$$

$$= P_{\gamma}^{'2} + P_{\gamma}^{2} - 2P_{\gamma}^{'}P_{\gamma}\cos\theta\,.$$

Multiplying both sides of A.13 by c^2 yields

$$P_{e}^{'2}c^2 = P_{\gamma}^{'2}c^2 + P_{\gamma}^{2}c^2 - 2c^2P_{\gamma}^{'}P_{\gamma}\cos\theta, \tag{A.16}$$

Using the relation $pc = h\upsilon$ for photons, A.13 can be rewritten as

$$P_{e}^{'2}c^2 = h\upsilon^{'2} + h\upsilon^2 - 2h\upsilon^{'}h\upsilon\cos\theta. \tag{A.17}$$

A.17 can now be equated to Eq. A.12 to obtain

$$(h\upsilon + m_e c^2 - h\upsilon^{'})^2 - (m_e c^2)^2 = h\upsilon^{'2} + h\upsilon^2 - 2h\upsilon^{'}h\upsilon\cos\theta. \tag{A.18}$$

Solving A.18 algebraically provides the following relation

$$2h\upsilon m_e c^2 + 2h\upsilon^{'}m_e c^2 = 2h^2h\upsilon h\upsilon^{'}(1-\cos\theta), \tag{A.19}$$

Dividing both sides of A.19 by $2h\upsilon\upsilon^{'}m_e c$ supplies us with

$$\frac{c}{\upsilon'} - \frac{c}{\upsilon} = \frac{h}{m_e c}(1 - \cos\theta). \tag{A.20}$$

Substituting the relations $c = \upsilon\,\lambda = \upsilon'\lambda'$ into A.20 provides the final outcome

$$\lambda' - \lambda = \frac{h}{m_e c}(1 - \cos\theta). \tag{A.21}$$

APPENDIX B
DERIVATION OF ENERGY TRANSFER AND SCATTER PROBABILITY TERMS (EQUATIONS 3.62 – 3.64)

Derivation of Equation 3.62

The velocity term in Eq. 3.60 provides a motivation for developing the energy relationships. We first begin by squaring Eq. 3.60 to get

$$(\boldsymbol{v}_l')^2 = (\boldsymbol{v}_c')^2 + (\boldsymbol{V}_{CM})^2 + 2\boldsymbol{v}_c'\boldsymbol{V}_{CM}\cos\theta\,. \tag{B.1}$$

Using the fact that *cos* $(\pi - \theta_c)$ = - cos θ_c and rearranging terms gives

$$2\boldsymbol{v}_c'\boldsymbol{V}_{CM}\cos(\pi-\theta) = (\boldsymbol{v}_c')^2 + (\boldsymbol{V}_{CM})^2 - (\boldsymbol{v}_l')^2\,. \tag{B.2}$$

Now, leaving the cosine term on the left-hand side of B.2

$$\cos(\pi-\theta) = \frac{(\boldsymbol{v}_c')^2 + (\boldsymbol{V}_{CM})^2 - (\boldsymbol{v}_l')^2}{2\boldsymbol{v}_c'\boldsymbol{V}_{CM}}\,. \tag{B.3}$$

Next, we substitute the following terms into B.3 which were taken from Eqs. 3.39, 3.40, 3.41, 3.52, and 3.53

$$\boldsymbol{V}_{CM} = \frac{m\boldsymbol{v}_l}{m+M}, \tag{B.4}$$

$$\boldsymbol{v}_c = \boldsymbol{v}_l - \boldsymbol{V}_{CM} = \frac{M\boldsymbol{v}_l}{m+M}, \tag{B.5}$$

$$\boldsymbol{V}_c = -\boldsymbol{V}_{CM} = -\frac{m\boldsymbol{v}_l}{m+M}\ , \tag{B.6}$$

$$mv_c = MV_C\ , \tag{B.7}$$

$$mv_c' = MV_C'\ , \tag{B.8}$$

And substituting B.4 – B.8 into B.3 yields

$$\cos(\pi-\theta) = \frac{\left(\frac{M}{m+M}\right)^2 \boldsymbol{v}_l^2 + \left(\frac{m}{m+M}\right)^2 \boldsymbol{v}_l^2 - (v_l')^2}{2\left(\frac{M}{m+M}\right)\left(\frac{m}{m+M}\right)v_l^2}. \tag{B.9}$$

Reducing B.9 gives the following relationship

$$\cos(\pi - \theta) = \frac{\left(\frac{v_l}{m+M}\right)^2 (M^2 + m^2) - (v_l')^2}{2mM\left(\frac{v_l}{m+M}\right)^2}. \tag{B.10}$$

Reduce B.10 and separate the right-hand side of the equation

$$\cos(\pi - \theta) = \frac{(M^2 + m^2)}{2mM} - \frac{(v_l')^2}{2mM\left(\frac{v_l}{m+M}\right)^2}. \tag{B.11}$$

Move the velocity terms to the left-hand side of the equation and change the cosine term

$$\frac{(v_l')^2}{2mM\left(\frac{v_l}{m+M}\right)^2} = \frac{(M^2 + m^2)}{2mM} - \cos\theta. \tag{B.12}$$

Reduce the left-hand side of B.12 to velocity terms only

$$\frac{{v_l'}^2}{{v_l}^2} = \frac{M^2 + m^2 + (2\mathrm{mM})\cos\theta}{(m+M)^2}. \tag{B.13}$$

Multiply the left-hand side of B.13 by one to achieve energy terms

$$\frac{\frac{1}{2}mv_l'^{\,2}}{\frac{1}{2}mv_l{}^2} = \frac{E'}{E} = \frac{M^2 + m^2 + (2\mathrm{mM})\cos\theta}{(m+M)^2}. \tag{B.14}$$

Substitute the values $A = M$, $m = 1$ into B.14

$$\frac{E'}{E} = \frac{A^2 + 1 + 2\mathrm{A}\cos\theta}{(A+1)^2}. \tag{B.15}$$

The approach now will be to essentially complete the square twice for the right-hand side of B.15. First begin by multiplying the right-hand side by a value of 2/2

$$\frac{E'}{E} = \frac{2A^2 + 2 + 4\mathrm{A}\cos\theta}{2(A+1)^2}. \tag{B.16}$$

Now add zero to the right-hand side of B.16

$$\frac{E'}{E} = \frac{2A^2 + 2 + (A^2 - A^2 + 2\mathrm{A} + 2\mathrm{A} + 1 - 1)\cos\theta}{2(A+1)^2}. \tag{B.17}$$

Gather the appropriate terms in B.17 (first square is completed)

$$\frac{E'}{E} = \frac{2A^2 + 2 + [(A^2 + 2A + 1) - (A^2 - 2A + 1)]\cos\theta}{2(A+1)^2}. \quad \text{(B.18)}$$

Now, begin the final square completion by working on the first portion of the numerator in B.18

$$\frac{E'}{E} = \frac{A^2 + A^2 + 2A - 2A + 1 + 1 + [(A^2 + 2A + 1) - (A^2 - 2A + 1)]\cos\theta}{2(A+1)^2}. \quad \text{(B.19)}$$

Gather the appropriate terms and reduce B.19

$$\frac{E^{'}}{E} = \frac{(A^2 + 2A + 1) + (A^2 + 2A - 1) + [(A^2 + 2A + 1) - (A^2 - 2A + 1)]\cos\theta}{2(A+1)^2}, \quad \text{(B.20)}$$

$$\frac{E^{'}}{E} = \frac{(A^2 + 2A + 1)(1 + \cos\theta) + (A^2 + 2A - 1)(1 - \cos\theta)}{2(A+1)^2}, \quad \text{(B.21)}$$

$$\frac{E'}{E} = \frac{(A+1)^2(1 + \cos\theta) + (A-1)^2(1 - \cos\theta)}{2(A+1)^2}, \quad \text{(B.22)}$$

Now factor the $(A+1)^2$ term from the numerator and denominator and reduce the terms

$$\frac{E'}{E} = \frac{(1+\cos\theta) + \left(\frac{A-1}{A+1}\right)^2 (1-\cos\theta)}{2} \tag{B.23}$$

$$\frac{E'}{E} = \frac{1 + \left(\frac{A-1}{A+1}\right)^2 + \left[\cos\theta - \left(\frac{A-1}{A+1}\right)^2 \cos\theta\right]}{2}. \tag{B.24}$$

Substitute Eq. 3.65 into B.24 and reduce the terms to reach arrive at Eq. 3.62

$$\frac{E'}{E} = \frac{1 + \alpha + [\cos\theta - \alpha\cos\theta]}{2}.$$

or

$$\frac{E'}{E} = \frac{(1+\alpha) + (1-\alpha)\cos\theta}{2}. \tag{B.25}$$

Derivation of Equation 3.63

We begin by noting that the scattering angles and, therefore, the angular distributions of particles emerging from the laboratory and center-of-mass systems are different. However, the total number of neutrons appearing in a given differential solid angle must be the same in each system. We can see this one-to-one relationship displayed in Figure 3.6, which showed that

$$\sin\vartheta \propto \sin\theta \,. \tag{B.26}$$

Since we are interested in developing an equation that expresses the probability of scattering from an incident energy (E) and into a final energy (E'), our expression must involve the use of the microscopic cross section (σ), because this quantity is defined as the measure of the probability of interaction between a particle (neutron in this case) and a target nucleus. The term can also be viewed as the effective cross sectional area presented by each target nuclei to an incident neutron beam.

Because of the one-to-one relationship discussed above, we can write

$$\sigma(\vartheta)\sin\vartheta\, d\vartheta = \sigma(\theta)\sin\theta\, d\theta \,. \tag{B.27}$$

Now, since quantities are calculated in the center-of-mass system, we want to focus our efforts on developing the right-hand side of Eq. B.27 which relates to this frame of reference.

The probability of a neutron scattering into a given differential energy is

$$P(E \rightarrow E')dE' \,, \tag{B.28}$$

And, since we know there is a one-to-one relationship between the final neutron energy and its scattering angle, we can further express B.28 using the laws of probability as

$$P(E \rightarrow E')dE' = P(scatter\ into\ \theta)\ P(differential\ solid\ angle)\ . \tag{B.29}$$

The first term is related to the probability of scattering into a certain angle (θ) in relation to all other possible angles or probabilities; therefore, this term is simply

$$P(\theta) = \frac{\sigma_{CM}(\theta)}{\sigma_s}\ . \tag{B.30}$$

and the probability of scattering within a given differential solid angle ($d\Omega$) is just

$$2\pi \sin\theta\ d\theta\ , \tag{B.31}$$

since there is no dependence on φ. So therefore, Eq. B.28 can be expressed as

$$P(E \rightarrow E')dE' = -\left(\frac{\sigma_{CM}(\theta)}{\sigma_s}\right) 2\pi \sin\theta\ d\theta\ , \tag{B.32}$$

where the minus sign appears because of the relationship between E' and θ . E' decreases with increasing θ and a positive value of $d\theta$ necessarily implies a negative value of dE'.

Now, expand the left-hand side of Eq. B.25 (previous section) by moving E to the right-hand side and taking the derivative of both sides to get

$$dE' = \frac{-E(1-\alpha)\sin\theta\, d\theta}{2}. \tag{B.33}$$

Now substitute B.33 into B.32 and solve for $P(E \rightarrow E')$ to get

$$P(E \rightarrow E') = \begin{cases} \dfrac{4\pi\, \sigma_{CM}(\theta)}{E\sigma_s(1-\alpha)} & \text{for } \alpha E \leq E' \leq E \\ o, & \text{otherwise} \end{cases}. \tag{B.34}$$

The remaining unknown scattering terms can be resolved by noting that, for neutrons of E < 10 MeV in low-Z materials, scatter in the center-of-mass system is isotropic, which means it is equally probable in all directions. Therefore, the probability of an interaction scattering into angle θ is

$$P(\theta) = \sigma_{CM}(\theta) = \frac{\sigma_s}{4\pi}, \tag{B.35}$$

which is known as *S*-wave scatter. When we substitute this result into B.34, we arrive at Eq. 3.63

$$P(E \rightarrow E') = \begin{cases} \dfrac{1}{E(1-\alpha)} & \text{for } \alpha E \leq E' \leq E \\ o, & \text{otherwise} \end{cases} . \tag{B.36}$$

It should be noted that the *S*-Wave (zeroeth moment) scatter assumption will not hold for neutron interactions with higher-Z materials and it will be necessary to correct for this anisotropy by developing higher scattering moments. These conditions will be discussed in Chapter 4 and developed in Appendix C.

APPENDIX C
LEGENDRE POLYNOMIALS AND SCATTERING MOMENTS

C.1 Developing the Legendre Polynomials

Legendre's Equation is a very important one in Nuclear Engineering, because its solution is used to describe the scattering relation of neutrons in deterministic radiation transport codes. The equation has the following form:

$$(1 - x^2)y" \; - \; 2xy' \; + \; p(p+1)y \, . \tag{C.1}$$

where the coefficient *p* is real and analytic. We now guess a power series solution of the form

$$y = \sum_{j=0}^{\infty} a_j x^j \; = \; a_0 + \; a_1 x + \; a_2 x^2 + \; \cdots \; , \tag{C.2}$$

and then calculate the first derivative as

$$y' = \sum_{j=1}^{\infty} j a_j x^{j-1} \; = \; a_1 + \; 2a_2 x + \; 3a_3 x^2 + \; \cdots \; , \tag{C.3}$$

and finally, the second derivative is

$$y'' = \sum_{j=2}^{\infty} j(j-1)a_j x^{j-2} \;=\; 2a_2 + \; 3 \cdot 2 \cdot a_3 x + \; \cdots \; . \qquad \text{(C.4)}$$

Now, we substitute Eqs. C.2 – C.4 into C.1

$$\sum_{j=2}^{\infty} j(j-1)a_j x^{j-2} \; - \sum_{j=2}^{\infty} j(j-1)a_j x^{j} \; - \sum_{j=1}^{\infty} 2ja_j x^{j}$$

$$+ \; p(p+1) \sum_{j=2}^{\infty} a_j x^{j} \;\; = \;\; 0 \, . \qquad \text{(C.5)}$$

The index of summation is now adjusted to contain terms of x^j rather than x^{j-2} and we collect terms to reach

$$\sum_{j=2}^{\infty} (j+2)(j+1)a_{j+2} x^{j} \; - \sum_{j=2}^{\infty} j(j-1)a_j x^{j} \; - \sum_{j=2}^{\infty} 2ja_j x^{j}$$

$$+ \; p(p+1) \sum_{j=2}^{\infty} a_j x^{j}$$

$$= \; -2a_2 - 6a_3 + 2a_1 x - p(p+1)a_0 - p(p+1)a_1 x \; . \qquad \text{(C.6)}$$

We can now collect terms and reduce C.6 to

$$\sum_{j=2}^{\infty}[\,(j+2)(j+1)a_{j+2} - j(j-1)a_j - 2ja_j + p(p+1)a_j$$

$$- p(p+1)a_1x\,]\,x^j$$

$$= -2a_2 - 6a_3 + 2a_1x - p(p+1)a_0 - p(p+1)a_1x\ . \qquad \text{(C.7)}$$

Now because a power series can only be identically zero if all the coefficients equal zero as well, we can equate the right side of Eq. C.7 to zero and solve for the recursion relationships by

$$-2a_2 - p(p+1)a_0 = 0\,. \qquad \text{(C.8)}$$

And

$$-6a_3 + 2a_1 - p(p+1)a_0 = 0\,. \qquad \text{(C.9)}$$

The recursion relations are then

$$a_2 = -\frac{p(p+1)}{1\cdot 2}\cdot a_0\ , \qquad \text{(C.10)}$$

$$a_3 = -\frac{(p-1)(p+2)}{2\cdot 3}\cdot a_1\,, \qquad \text{(C.11)}$$

and finally

$$a_{j+2} = -\frac{(p-j)(p+j+1)}{(j+2)(j+1)} \cdot a_j \quad for\ j = 2, 3, .. \tag{C.12}$$

We notice that the coefficients a_0 and a_1 are not specified, so we set $a_0 = y_1$ and $a_1 = y_2$. Using C.10 – C.12, we can solve for the remaining coefficients of the series as shown below.

$$a_2 = -\frac{p(p+1)}{2} \cdot y_1 \ , \tag{C.13}$$

$$a_3 = -\frac{(p-1)(p+2)}{2 \cdot 3} \cdot y_2 \ , \tag{C.14}$$

$$a_4 = -\frac{(p-2)(p+3)}{3 \cdot 4} \cdot a_2 = \frac{p(p-2)(p+1)(p+3)}{4!} \cdot y_1 \ , \tag{C.15}$$

$$a_5 = -\frac{(p-3)(p+4)}{4 \cdot 5} \cdot a_3$$

$$= \frac{(p-1)(p-3)(p+2)(p+4)}{5!} \cdot y_2 \ , \tag{C.16}$$

Inserting the coefficients into Eq. C.2 yields the general solution for the Legendre equation

$$y = y_1\left[1 - \frac{p(p+1)}{2!}x^2 + \frac{p(p-2)(p+1)(p+3)}{4!}\,x^4 - \,+\cdots\right]$$

$$+\,y_2\left[x - \frac{(p-1)(p+2)}{3!}x^3\right.$$

$$\left.+\,\frac{p(p-2)(p+1)(p+3)}{5!}\,x^5 + -\ldots\right]. \qquad \text{(C.17)}$$

In the special cases when y_1 is a positive even integer, the first bracket terminates as a polynomial. And, in the special case when y_2 is a positive odd integer, the second bracket also terminates as a polynomial. These polynomials are referred to as Legendre polynomials and they form the basis for scattering moments in the LBE solution. It can be seen from Eq. C.17 that the first few Legendre polynomials are

$$P_0 = 1\ , P_1 = x\ , P_2 = (1 - 3x^2), P_3 = \left(x - \frac{5}{3}x^3\right), \ldots. \qquad \text{(C.18)}$$

C.2 Developing the Scattering Moments

Legendre polynomials are convenient for adjusting isotropic (*S*-wave) scatter for the anisotropy conditions associated with neutron interactions with higher-*Z* materials. There are a few motivations for using such an approach. First of all, Legendre polynomials are orthogonal on the interval [-1, 1], which corresponds to the range of the cosine function that is used for neutron scattering. The second reason is that the scattering moments are easily calculated because of the orthogonal properties of the

Legendre polynomials on this same interval. This is not true in the case of a power series expansion, which is another advantage.

To demonstrate how these moments are calculated, we begin by considering an expansion of the scattering cross section by

$$\sigma_s(\mu) = \sum_0^\infty \gamma\, \sigma_{sl}\, P_l(\mu)\,, \tag{C.19}$$

where γ is a normalization constant, σ_{sl} is the l^{th} scattering moment of $\sigma_s\,(\mu)$ and $P_l\,(\mu)$ is the Legendre polynomial. Multiply both sides of C.19 by $P_m\,(\mu)$ and integrate to solve for $\sigma_s\,(\mu)$ by

$$\int_{-1}^{1} \sigma_s(\mu)\, P_m(\mu) = \int_{-1}^{1} \sum_0^\infty (\gamma\, \sigma_{sl})\, P_l(\mu)\, P_m(\mu)\,, \tag{C.20}$$

Keeping in mind the following important property of Legendre polynomials:

$$\frac{\delta_{lm}}{2l+1} = \int_{-1}^{1} \sum_0^\infty P_l(\mu)\, P_m(\mu)\,, \tag{C.21}$$

where δ_{lm} is zero in all cases except when $l = m$, when it attains the value of 1. This is very important, because all other terms will not survive and the calculation proceeds

quickly. Since C.21 is non-zero in a singular case, the summation can be eliminated, and C.20 becomes

$$\int_{-1}^{1} \sigma_s(\mu)\, P_l(\mu) = \frac{\gamma\, \sigma_{sl}}{2l+1}\ , \tag{C.22}$$

where m was replaced by *l* due to equivalence. Now, we rearrange terms to solve for the scattering moment

$$\gamma\, \sigma_{sl} = (2l+1) \int_{-1}^{1} \sigma_s(\mu)\, P_l(\mu)\ . \tag{C.23}$$

And, by letting $\gamma = 2l + 1$, the l^{th} scattering moment of σ_s (μ) is

$$\sigma_{sl} = \int_{-1}^{1} \sigma_s(\mu)\, P_l(\mu)\ . \tag{C.24}$$

By substituting all known terms into C.19, we get

$$\sigma_s(\mu) = \sum_{0}^{\infty} (2l+1)\sigma_{sl}\, P_l(\mu)\,. \tag{C.25}$$

The original goal of this exercise was to adjust the isotropic (*S*-wave) scattering term (σ_s /4π) for anisotropic conditions when necessary. Therefore, we can immediate write our final result of

$$\sigma_s(\mu_0) = \sum_0^\infty \frac{(2l+1)}{4\pi}\sigma_{sl}\, P_l(\mu)\,, \tag{C.26}$$

where, σ_{sl} is defined by C.24. It can easily be verified that in the P_0 case, C.26 reduces to the isotropic scattering moment for one group in 1-D. The scattering term can be expanded to the 3-D case by using a truncated set of spherical harmonics with the following relationships

$$\hat{\Omega} \to \langle\theta,\phi\rangle\,, \left(\hat{\Omega}'\cdot\hat{\Omega}\right) \to (\mu_0), \mu = (\cos\theta), and\ \mu' = (\cos\theta') \tag{C.27}$$

$$\sigma_{s\,g'\to g}(\vec{r},\mu_0) = \sum_0^L (2l+1)\sigma_{s\,g'\to g,l}\,(\vec{r})P_l(\mu_0)\,, \tag{C.28}$$

$$\sigma_{s\,g'\to g,l}(\vec{r}) = \int_{-1}^{1} \frac{d\mu_0}{2}\sigma_{s\,g'\to g}\,(\vec{r},\mu_0)P_l(\mu_0)\,, \tag{C.29}$$

$$\mu_0 \;=\; \mu\mu' \;+ (1-\mu^2)^{0.5}\left(1-\mu'^2\right)^{0.5}\cos(\phi-\phi')\,. \tag{C.27}$$

The Legendre polynomial in C.25 and C.26 is expressed using the Legendre Addition Formula as

$$P_l(\mu_0) = \frac{1}{2l+1} \sum_{k=-l}^{l} Y_{l,k}^*(\theta', \phi')\, Y_{l,k}(\theta, \phi), \tag{C.28}$$

where the spherical harmonic terms on the right-side of C.28 are defined by Legendre polynomials and an exponential term by the following two expressions

$$Y_{l,k}(\theta, \phi) = \sqrt{(2l+1)\frac{(l-k)!}{(l+k)!}}\; P_l^k(\mu) exp(ik\phi) \;\; and \tag{C.29}$$

$$Y_{l,-k}(\theta, \phi) = \; (-1) Y_{l,k}^*(\theta, \phi)\,. \tag{C.30}$$

Now, by inserting C.29 and C.30 into C.28, $P_l(\mu_0)$ can be expressed as:

$$P_l(\mu_0) = P_l(\mu) P_l(\mu') + 2 \sum_{k=1}^{l} \frac{(l-k)!}{(l+k)!}\; P_l^k(\mu) P_l^k(\mu') \cos\big(k(\phi - \phi')\big)\;, \tag{C.30}$$

and by trigonometric identity,

$$\cos\big(k(\phi-\phi')\big) = \cos(k\phi)\cos(k\phi') + \sin(k\phi)\sin(k\phi')\,. \tag{C.31}$$

Eqs. C.30 and C.31 are folded into Eq. 4.3 to arrive at the Legendre expanded multi-group form of the LBE in 3-D Cartesian geometry shown in Eq. 4.4. And, finally, the other two variables in the streaming term (η and ξ) are also expressed as direction cosines on the unit sphere expressed in terms of the polar angle (θ) and azimuthal angle (ϕ) as:

$$\eta = \sqrt{1-\mu^2}\cos\phi \quad and \tag{C.32}$$

$$\xi = \sqrt{1-\mu^2}\sin\phi\,. \tag{C.33}$$

Incorporating C.32 and C.33 into the streaming term in Eq. 4.4, provides the final 3-D non-multiplying discrete ordinates form of Eq. 4.1 in Cartesian coordinates as given in Eq. 4.9.

APPENDIX D
COARSE CELL / DIFFERENCING MAPPING TABLE ASSOCIATED WITH PENTRAN OUTPUT FILES FOR A 50-COARSE MESH PROBLEM

Crs Cell	Global i	j	k	Difference Method/Metric	Dom Mtl	In Bdy	Out Bdy	Rgt Bdy	Lft Bdy	Bot Bdy	Top Bdy	X Fin	Y Fin	Z Fin	Mesh Cells
1	1	1	1	2DTW 5.8E-01	3	-1	2	-3	6	-5	26	8	8	20	1280
2	2	1	1	2DTW 6.1E-01	3	1	3	-3	7	-5	27	8	8	20	1280
3	3	1	1	3EDI 1.0E+00	3	2	4	-3	8	-5	28	16	8	20	2560
4	4	1	1	2DTW 6.1E-01	3	3	5	-3	9	-5	29	8	8	20	1280
5	5	1	1	2DTW 5.8E-01	3	4	-2	-3	10	-5	30	8	8	20	1280
6	1	2	1	2DTW 5.9E-01	3	-1	7	1	11	-5	31	8	4	20	640
7	2	2	1	2DTW 5.9E-01	4	6	8	2	12	-5	32	8	4	20	640
8	3	2	1	3EDI 2.2E+00	4	7	9	3	13	-5	33	16	4	20	1280
9	4	2	1	2DTW 5.9E-01	4	8	10	4	14	-5	34	8	4	20	640
10	5	2	1	2DTW 5.9E-01	3	9	-2	5	15	-5	35	8	4	20	640
11	1	3	1	3EDI 1.0E+00	3	-1	12	6	16	-5	36	8	16	20	2560
12	2	3	1	3EDI 2.2E+00	4	11	13	7	17	-5	37	8	16	20	2560
13	3	3	1	3EDI 2.2E+00	1	12	14	8	18	-5	38	16	16	20	5120
14	4	3	1	3EDI 2.2E+00	4	13	15	9	19	-5	39	8	16	20	2560
15	5	3	1	3EDI 1.0E+00	3	14	-2	10	20	-5	40	8	16	20	2560
16	1	4	1	2DTW 5.9E-01	3	-1	17	11	21	-5	41	8	4	20	640
17	2	4	1	2DTW 5.9E-01	4	16	18	12	22	-5	42	8	4	20	640
18	3	4	1	3EDI 2.2E+00	4	17	19	13	23	-5	43	16	4	20	1280
19	4	4	1	2DTW 5.9E-01	4	18	20	14	24	-5	44	8	4	20	640
20	5	4	1	2DTW 5.9E-01	3	19	-2	15	25	-5	45	8	4	20	640
21	1	5	1	2DTW 5.8E-01	3	-1	22	16	-4	-5	46	8	8	20	1280
22	2	5	1	2DTW 6.1E-01	3	21	23	17	-4	-5	47	8	8	20	1280
23	3	5	1	3EDI 1.0E+00	3	22	24	18	-4	-5	48	16	8	20	2560
24	4	5	1	2DTW 6.1E-01	3	23	25	19	-4	-5	49	8	8	20	1280
25	5	5	1	2DTW 5.8E-01	3	24	-2	20	-4	-5	50	8	8	20	1280
.															
.															
.															
50	5	5	2	2DTW 5.8E-01	3	49	-2	45	-4	25	-6	8	8	20	1280
Total #Equations 6.1440E+06											XYZ mesh total				76800

APPENDIX E – BASIC MONTE CARLO PROCEDURE

E.1 Principles

The random numbers that are so critical to the Monte Carlo method are generated by a computer using some form of random number generator (*RNG*). In actuality, *RNGs* produce numbers that are only pseudo-random and this is actually desirable, because the production of truly random numbers is impractical and undesirable. Instead, pseudo-random numbers are desired because they can be reproduced from the same seed (stating point) and their statistical properties can be evaluated to ensure the *RNG* is acceptable.

The basic Monte Carlo procedure begins with a description of the basic physical process that can be simulated using a stochastic (random) process. In a stochastic process, we cannot say with certainty exactly what will occur at each individual point; instead, we simply seek to characterize the process by estimating the average behavior of a large number of elements. The events (outcomes) of physical processes can be either discrete or continuous, but for the purposes of this section, discussion is limited to continuous random variables, because of its applicability to particle emissions from radioactive materials and to problems of radiation transport. The overall description of a random variable is encompassed by two important functions that will be discussed in further detail: the probability density function (*PDF*) and the cumulative density function (*CDF*).

The *PDF* or *p(x)dx* is defined as the probability that some random variable (*x*) will assume a value in the range of *x* and *x* + *dx*. The *PDF* is further constrained by requiring that the probability of obtaining some value x on the interval $a \leq x \leq b$ is equal to 1. The correlation to the random number ξ now begins by establishing the following relationships

$$p(x)dx = q(\xi)d\xi \tag{E.1}$$

$$q(\xi) = 1 \quad for\ 0 \leq \xi \leq 1\,, \tag{E.2}$$

$$p(x) = \frac{d\xi(x)}{dx}\,, and \tag{E.3}$$

$$p(x) = \frac{\tilde{f}(x)}{\int_a^b \tilde{f}(x)dx} = \frac{1}{b-a}\,. \tag{E.4}$$

The *CDF* or *P(x)* is defined as the probability that the random variable will not exceed *x* as shown in the following expression

$$P(x) = \int_a^x p(x)\,dx = \frac{x-a}{b-a}, \tag{E.5}$$

and furthermore,

$$P(x) = \int_a^x p(x)\,dx = \xi\,, \tag{E.6}$$

which follows from direct integration of Eq. E.1. Now, by inverting Eq. E.6, we can finally translate our random number to the continuous random variable (x) by

$$x = P(x)^{-1}(\xi)\,. \tag{E.7}$$

This basic procedure is applied to each event in a stochastic process (e.g. scatter energy deposition, etc.) to arrive at the final outcome of the problem.

A simple example will be considered to demonstrate exactly how the Monte Carlo process is applied toward problems of radiation transport. In this example, mono-energetic (1-group), mono-directional neutrons will be injected directly into a one-dimensional (1-D) homogeneous slab consisting of a singular elemental composition. Furthermore, the only interaction mechanisms that will be allowed are absorption and elastic scattering, with the final goal of determining how many neutrons exit the slab. Techniques associated with the handling of more elaborate models will be briefly discussed, although the details of these calculations will be left as an exercise to the reader.

E.2 Path Length Determination

Since the neutrons are being inserted directly into the slab (i.e. velocity vector is normal to the slab), the first step is to determine the distance the neutron travels prior to interacting. We begin by considering the process by which neutrons penetrate or are transported through the slab. In order to do this, we need to consider the probability that a neutron travels a distance (x) without an interaction (collision) and then experiences a collision within the next small differential distance (dx). The relation or *PDF* describing this stochastic event is

$$p(x)dx = e^{-\Sigma_t x}(\Sigma_t dx)\,, \tag{E.8}$$

where the terms on the right-hand side of the equation have been grouped to denote their relation to the description above. Now that the *PDF* has been formulated, we can immediately solve for the *CDF* by writing

$$P(x) = \int_a^x \Sigma_t e^{-\Sigma_t x} dx\,. \tag{E.9}$$

The solution to this integral was provided in Section 3.2.5 and we will now equate result to the first random number, ξ_1, by

$$\xi_1 = 1 - e^{-\Sigma_t x} . \tag{E.10}$$

We can now solve this equation to attain the desired relationship for *x* as

$$x = -\frac{1}{\Sigma_t}\ln(1 - \xi_1) . \tag{E.11}$$

Eq. E.10 can be used as is; however, the calculation of the term within the parenthesis produces an unnecessary inefficiency. The relation can be streamlined by remembering that, since ξ is randomly distributed on the interval [0, 1], then $1 - \xi_1$ must also be randomly distributed on this same interval. Eq. E.11 can therefore be replaced by the simpler relation

$$x = -\frac{1}{\Sigma_t}\ln(\xi_1) , \tag{E.12}$$

which can be reasonably employed to determine the neutron path length within a code. However, in the case of a multi-region shield (several layers) or a shield that is relatively thick in comparison to the mean-free path (*MFP*) of the neutron, one final adjustment can be made to reduce Eq. E.12 to its most efficient form of

$$x\Sigma_t = -\ln(\xi_1) = b , \tag{E.13}$$

where the term *b* represents the number MFPs represented by the shield thickness. Once the path length is calculated, it will first be compared to the thickness of the shield. If the length exceeds this distance, the neutron is considered to have escaped and is tallied accordingly; otherwise, the neutron is computationally moved to the new location in the shield and the remaining processes move forward.

E.3 Interaction Types

Now that interaction location has been determined, an additional random number is used to determine the interaction type. In our simplified model, there are only two interaction options; however, the selection of the interaction types is still determined in the same general manner through the relation

$$P_n = \sum_{i=1}^{N} p_i \quad for\ n = 1, N\ , \tag{E.14}$$

where the p_i terms describe the cumulative interaction probability of the i^{th} element in a particular material. To illustrate how the interaction mechanism is chosen, we will consider the case where our homogeneous shield material consists of a fictitious material exhibiting the absorption and elastic scattering cross sections shown in Table E-1.

Table E-1. Fictitious Material Characteristics.

Interaction Type	$\Sigma_{a,s}$ **(cm^{-1})**	p_i **($\Sigma_{a,s}$ / Σ_t)**	P_i
Absorption (a)	0.300	0.333	0.333
Elastic Scatter (s)	0.600	0.667	1.000
Total	0.900	1.000	

Since the shield in our example consists of a single element, we obtain a second random number (ξ_2) and make the following comparison to determine which of our two interactions will occur. If, however, the shield composition was non-singular, we would first need to determine

$$\xi_2 = \leq P_1 \begin{cases} neutron\ is\ absorbed \\ otherwise, neutron\ is\ scattered \end{cases}. \quad \text{(E.15)}$$

which element was involved in the interaction using ξ_2 and then we would evaluate the interaction type using a third random number, ξ_3. The actual method for selecting the element and interaction is conducted using the same method (Eq. E.15); however, when choosing the element type, the p_i terms shown in the third column of Table E-1 must be replaced by the fractional weight percent (w_i / w_{total}) for each element that is part of the shield.

E.4 Neutron Scattering Angle and Energy

Since our model consisted of a 1-D shield, we won't need to concern ourselves with the evaluation of the neutron scattering angle; however, the method for doing so will be briefly discussed in order to provide an adequate coverage of the Monte Carlo method. There are different ways of treating the problem of scattering; however, the most straightforward method deals with the consideration of the azimuthal angle (ϕ) (2-D or 3-D models) and a further consideration of the polar angle (θ) for 3-D models. Although there is no convention between mathematicians and scientists on the use of ϕ for the azimuthal angle or θ for the polar angle, this has become standard in nuclear engineering as depicted in Figure E.1. The convention in radiation transport has also been to sample ϕ uniformly in the range $0 \leq \phi \leq 2\pi$ and θ from $0 \leq \theta \leq \pi$ and using the polar angle to develop the proper PDF for elastic scattering. Therefore, Eq. 4.31 can be directly used for ϕ, while θ requires a more elaborate evaluation.

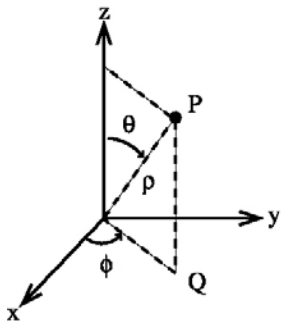

Fig. E.1 Schematic of the Neutron Scattering Angles.

Since we are sampling ϕ uniformly, Eq. E.4 yields the following result

$$p(x) = \frac{\tilde{f}(\phi)}{\int_0^{2\pi} \tilde{f}(\phi) d\phi} = \frac{1}{2\pi} \,, \tag{E.16}$$

and Eq. E.6 yields

$$P(x) = \int_0^{\phi} \left(\frac{1}{2\pi}\right) d\phi = \frac{\phi}{2\pi} = \xi_3 \,, \tag{E.17}$$

or

$$\phi = 2\pi\xi_3 \,. \tag{E.18}$$

Eq. E.18 above is not only important for locating the scattered neutron within the slab, but the result for ξ_3 can be inserted directly into Eq. 3.63 to determine the energy of the scattered neutron as well.

In order to develop the *PDF* expression for selecting θ, one must begin by considering the differential scattering cross section that is defined as

$$\Sigma_s\left(\hat{\Omega} \rightarrow \hat{\Omega}'\right) d\Omega' \,, \tag{E.19}$$

which represents the probability per unit path length that a particle moving in direction Ω will be scattered into a solid angle $d\Omega'$ about Ω'. The left-hand side of Eq. E.19 above describes the projection of omega onto omega prime, which is referred to as the dot product in physics and is calculated as

$$\boldsymbol{A} \cdot \boldsymbol{B} = |\boldsymbol{A}||\boldsymbol{B}| \cos\theta \,, \tag{E.20}$$

where *A* and *B* are vectors and their dot product is equivalent to the absolute value of the individual vectors times the cosine of the angle between them. In nuclear engineering terminology, the term μ is generally used to describe the magnitude of the unit vector in the *z* direction as seen in Figure E.1 and, since we're using the cosine of the polar angle (θ) is generally given the following definition

$$\mu_0 = \cos\theta \,, \tag{E.21}$$

where μ_0 denotes the initial angle of the neutron with respect to the *z* axis before the scattering event. By using this new angle term along with the knowledge that the differential scattering cross section is only dependent on ϕ, we can now rewrite Eq. E.19 in terms of μ and ϕ as

$$\Sigma_s\left(\hat{\Omega} \rightarrow \hat{\Omega}'\right) d\Omega' = \Sigma_s(\mu_0) d\mu' d\phi', \tag{E.22}$$

The term $\Sigma_s\ (\mu_0)$ can be expanded into separate scalar and probability components in exactly the same manner as was discussed for the differential energy scattering cross section in section 3.2.1.2 and shown in Eq. 3.33. The new terms describe the scattering probability per unit path length and probability per steradian according to the following relation

$$\Sigma_s(\mu_0) = \Sigma_s\, p'(\mu_0)\,. \tag{E.23}$$

Therefore, we may now write the expanded form of Eq. E.23 as

$$\Sigma_s(\mu_0)d\mu' d\phi' = \Sigma_s\, p'(\mu_0)d\mu' d\phi', \tag{E.24}$$

and if we now align the *z*-axis with the direction of μ_0, we can replace the μ' terms and the relation becomes

$$\Sigma_s(\mu_0)d\mu_0 d\phi' = \Sigma_s\, p'(\mu_0)d\mu_0 d\phi', \tag{E.25}$$

now integrate the equation above over all ϕ angles to remove the azimuthal component and solve for the differential probability term by

$$p(\mu_0)d\mu_0 = \frac{\int_0^{2\phi} \Sigma_s(\mu_0)d\mu_0\, d\phi'}{\Sigma_s}, \tag{E.26}$$

where $p(\mu_0)$ is determined by

$$p(\mu_0)d\mu_0 = \int_0^{2\phi} p'(\mu_0)\, d\phi'\,. \tag{E.27}$$

The result of this effort is the following relation

$$p(\mu_0)d\mu_0 = \frac{2\pi\,\Sigma_s(\mu_0)d\mu_0}{\Sigma_s}, \tag{E.28}$$

which is the *PDF* form of the scattering term we're seeking. We now solve for the *CDF* term we need and set it equal to our next random number by

$$P(\mu_0) = \int_{-1}^{\mu_0} \frac{2\pi\,\Sigma_s(\mu_0)d\mu_0}{\Sigma_s} = \xi_4\,. \tag{E.29}$$

Recall from the scattering discussions of Chapter 3 that neutron scattering is isotropic in the center-of-mass system for reactor engineering applications (i.e. $E_n \leq 10$ MeV) and, in this case,

$$\Sigma_s(\mu_0) = \frac{\Sigma_s}{4\pi}. \tag{E.30}$$

By substituting this term into Eq. E.29 and simplifying the expression, we reach the conclusion that

$$\frac{\mu_0 + 1}{2} = \xi_4\,, \tag{E.31}$$

or

$$\mu_0 = 2\xi_4 - 1\,, \tag{E.32}$$

which is the new scattering angle. Finally, the new direction cosine is calculated using

$$\mu' = \mu\mu_0 + \sqrt{1-\mu^2}\sqrt{1-\mu_0^2}\,\cos\phi_0\ , \tag{E.33}$$

where μ is the previous μ' and ϕ_0 is determined by evaluating the angular probability for ϕ in the Cartesian coordinate system

$$P(\phi_0) = \frac{\phi_0}{2\pi} = \xi_5\,, \tag{E.34}$$

or,

$$\phi_0 = 2\pi\xi_5\,. \tag{E.35}$$

At this point, the process reverts back to Eq. E.10 and continues in a loop until the particle track is terminated by escape (streaming), capture, etc.

APPENDIX F
AREACT COMPUTER CODE FOR CALCULATING ADJOINT REACTION RATES

```
!
!     Adjoint Reaction Rate Calculator
!
!       by CRITCEL Group
!
!     Version 1.5g
!
!     This code is used to process the aflux files from adjoint PENTRAN
!     runs to calculate reaction rates and various other quantities.
!
!-----------------------------------------------------------------------
!
      PROGRAM AREACT
!
      IMPLICIT REAL (A-H,O-Z)
      IMPLICIT INTEGER (I-N)
!
!     MAIN PROGRAM
!
!/////////////////
!
      CALL IHEADR
      CALL INSIFT
!
      STOP
!
      END
!
!-----------------------------------------------------------------------
!
!     SUB IHEADR
!
!     PURPOSE OF IHEADR ROUTINE:
!     -To print header when program is initiated
!
      SUBROUTINE IHEADR
!
      WRITE(*,'(A2///) ')'                                              '
      WRITE(*,'(2X,A46)')' Adjoint Reaction Rate Evaluation Program     '
      WRITE(*,'(A2)')'                                                  '
      WRITE(*,'(2X,A48)')'       Version 1.5  SINGLE PRECISION          '
      WRITE(*,'(2X,A48)')'               CRiTCEL Group                  '
      WRITE(*,*) '                                                      '
      WRITE(*,'(2X,A48)')'                DEC  2012                     '
      WRITE(*,'(A2)')'                                                  '
!
      END
!
!-----------------------------------------------------------------------
```

```
!
!     SUB INSIFT
!
!     PURPOSE OF INSIFT ROUTINE:
!     -To read and process data
!
      SUBROUTINE INSIFT
!
      IMPLICIT REAL (A-H,O-Z)
      IMPLICIT INTEGER (I-N)
!
      REAL, DIMENSION(150) :: tstnum, grpegy, srcspc, qsrc
      REAL, DIMENSION(1500) :: dx,dy,dz,vol,rr
      INTEGER, DIMENSION(1500) :: icm
      CHARACTER(10) :: matname
      CHARACTER(64) :: datfnam, outfnam, dxdydzf, srcspecf, aflxlgf
      CHARACTER(80) :: dummy
      INTEGER :: ngroups
      LOGICAL  exists, opend
!
!     Information location in aflux (.flx) files :
!
!     Note: Adjoint files give results in reverse group order,
!     Group 1 adjoint is the adjoint result for FORWARD group 47
!
!     Total number of ASCII Columns  in data files
      ntdat=7
!
!     Coarse mesh data Column Index
      icmidx=2
!
!     Target Material # Column Index
      itargm=3
!
!     x data Column Index
      ixcol=4
!
!     y data Column Index
      jycol=5
!
!     z data Column Index
      kzcol=6
!
!     Scalar Adjoint data Column Index
      iaflux=7
!
!     Total Isotropic Sn Source #/s over a volume(cc)
!     comment: source is isotropic in 24960 meshes
!
      totsrc = 1000
      srcvolcc = 720.72
!
!-----------------------------------------------------------------------
!
!     Files Needed:
!
!        source spectrum forr response
!        dxdydz.out for Coarse mesh data -> Volume
```

```
!        flx.Log to list group data files in a listing
!        group files named in flx.Log
!
!     Input information:
!
c     WRITE(*,'(A40)')' Input Source Material # to sum reactions for: '
c      READ(*,*) nmat
      nmat=3
!
c     WRITE(*,'(A22)')' Input Source Material Name: '
c      READ(*,*) matname
      matname='Air-source'
!
!     Generalized support for arbitrary number of groups
c     WRITE(*,'(A24)')' Input Number of Groups: '
c      READ(*,*) ngroups
      ngroups=47
!
!     Prompt for number of coarse meshes (technically this is in dxdydz)
c     WRITE(*,'(A31)')' Input Total Number of Coarse Meshes: '
c      READ(*,*) ntgcm
      ntgcm=50
!
!
!     Arbitrary Energy Group Selection
!     Read and Echo our energy to the screen for reference
!
!     ENERGY.FWD ***File format, starting from top line:
!       BUGLE96.grp 67 Group n-gamma (use Upper Energy Group Bins in MeV)
!       #neut_grps  FissNeutTemp(t,e,f)
!         47             t
!       Grp#  Upper_MeV
!        1    17.332
!        2    14.191
!        ...
!
!     Note this is loaded in Reverse order to match reverse order of
!     adjoint results (g47 is input and reported as g1 adjoint, etc)!
!
      WRITE(*,*) ' '
      WRITE(*,*) 'Opening Forward Energy Groups File:'
      WRITE(*,*) ' '
      OPEN(17, FILE='energy.fwd', ACCESS='SEQUENTIAL')
        DO i=1,4
          READ(17,*) dummy
        END DO
        DO jg = ngroups, 1, -1
          READ(17,*) igrpno, grpegy(jg)
          WRITE(*,*) 'Group (', jg,'): ', grpegy(jg),' MeV'
        END DO
      CLOSE(17)
      WRITE(*,*)
!
!     Initialize problem: responses, etc
!
      respons=0
      rr=0
      afavgmx=0.0
```

```
      eavgmx=0.0
      igrp=0
!
!     Read dxdydz file and compute volume
!
!     Note: This dxdydz term is the volume of the forward source term!
!     When EOF is reached, control transfers to statement 150
!        and continues from there.
!     DXDYDZ.OUT starting from top line:
!     Coarse Cell     dx        dy        dz
!         1        0.333     0.333     0.250
!         ...
!
      WRITE(*,*) ' '
      WRITE(*,*) 'Reading Mesh Volume File:'
      WRITE(*,*) ' '
      dxdydzf='dxdydz.out'
      OPEN (3, FILE=dxdydzf, ACCESS='SEQUENTIAL')
        i=0
        READ (3,'(A)') dummy
        WRITE(*,'(A80)') dummy
100     i=i+1
        READ (3,*,END=150) icm(i), dx(i), dy(i), dz(i)
        WRITE(*,'(I5,3(2X,F8.3))') icm(i), dx(i), dy(i), dz(i)
        vol(i)=dx(i)*dy(i)*dz(i)
        GOTO 100
150     i=i-1
        IF(i.NE.ntgcm)THEN
          WRITE(*,*)'ERROR: Cell count i ',i,' mismatch ntgcm ', ntgcm
          STOP
        END IF
        WRITE(*,*)' Read ',i,' Cell Dimensions '
        WRITE(*,*) ' '
      CLOSE(3)
!
!     Read source spectrum and normalize spc data from device 1
!       Note this is loaded in Reverse order to match reverse order of
!       adjoint results (g47 is input and reported as g1 adjoint, etc)!
!
      WRITE(*,*) ' '
      WRITE(*,*) 'Opening Forward Source File:'
      WRITE(*,*) ' '
      srcspecf = 'design1.spc'
      OPEN (1, FILE = srcspecf, ACCESS = 'SEQUENTIAL')
        srcspc = 0.0
        srcsum = 0.0
        DO jg = ngroups, 1, -1
          READ (1,*) srcspc(jg)
          srcsum = srcsum + srcspc(jg)
        END DO
      CLOSE(1)
!
!     Construct isotropic volumetric source
!     Arrays qsrc and srcspc
!
      WRITE(*,*) ' '
      WRITE(*,*) 'Setting Isotropic Source density:'
      WRITE(*,*) ' '
```

```
      DO jg=1, ngroups
        qsrc(jg) = (srcspc(jg)/srcsum) * totsrc/srcvolcc
        WRITE(*,*)'G ',jg,' (MeV):',grpegy(jg),
     &    ' qsrc=',qsrc(jg),' #/s/cc'
      END DO
      WRITE(*,*) ' '
!
!     Read aflux logfile listing from device 2
!
      WRITE(*,*) ' '
      WRITE(*,*) 'Opening Adjoint Data Log Filelist: '
      WRITE(*,*) ' '
      aflxlgf = 'flx.Log'
      OPEN (2, FILE = aflxlgf, ACCESS='SEQUENTIAL')
        READ (2,'(A)') dummy
        WRITE(*,'(A80)') dummy
!
!     ------BEGIN GROUP DEPENDENT SEQUENCE------
!
200   CONTINUE
!
!     Increment group counter, reset material counter, target matl volume
!       igrp was previously set to 0.
!       Initialize afluxmax and mean free path
!
      igrp=igrp+1
!
!     Read Group Response Cross Section from 1
!
      IF (igrp .LE. ngroups) THEN
        imatcnt=0
        voltarg=0.0
        afluxmax=0
        WRITE(*,*)'Group Counter = ', igrp,' Out of ',ngroups,
     & ' groups.'
        rr(igrp)=0.00
      ELSE
        igrp=igrp-1
      END IF
!
!     Get aflux datafile assignment data from 2
!
250     CONTINUE
        READ (2,*,END=400) datfnam
!
!       Open aflux datafile and read vectors of aflux data
!
!       The aflux files are opened below and the read statement dumps
!        the header information to dummy.  The write statement lists
!        the name of the aflux file and the read statement at 350
!        begins to pull out the necessary data.
!
          OPEN (10, FILE = datfnam, ACCESS='SEQUENTIAL')
           READ (10,'(A)') dummy
           WRITE(*,'(A18,A40)')' Read data from : ', datfnam
300        CONTINUE
           READ (10,*,END=350) (tstnum(iety), iety=1,ntdat)
!
```

```
!         The read statements above read information from columns
!         1 to n of the aflux file datfnam
!         When the EOF is reached, control goes to line 350.
!
!          If target material compute response from that cell
!
           IF (INT(tstnum(itargm)).EQ.nmat) THEN
             imatcnt=imatcnt+1
             itstcm=INT(tstnum(icmidx))
             voltarg = voltarg + vol(itstcm)
             afluxmaxold = afluxmax
             afluxmax=MAX(afluxmax, tstnum(iaflux))
!
!            Compute group rxn rate and total rxn respons
!
             rr(igrp) = rr(igrp) +
     &           (tstnum(iaflux)*qsrc(igrp)*vol(itstcm))
             respons = respons +
     &           (tstnum(iaflux)*qsrc(igrp)*vol(itstcm))
           END IF
         GOTO 300
350     CONTINUE
        CLOSE(10)
!
!       Finished a group...  wrap up responses:
!
1200    FORMAT(A7,I6,1X,A7,I3,1X,A17,F10.2,A4)
        WRITE(*,1200) ' Found ',imatcnt,' matl# ',nmat,
     &  ' meshes covering ', voltarg,' cm3'
!
        WRITE(*,'(A5,I3,A1,1PE10.3,A5,A15,1PE13.6,A10,
     &    0PF6.2,A1,0PF6.2,A1,0PF6.2,A2,1PE13.6)')
     &   ' Grp ',igrp,' ',grpegy(igrp),' MeV ',' abs  #/s : ',
     &    rr(igrp)
        WRITE(*,*)' '
!
!       Compute Response-Weighted max aflux, and energy
!
        afavgmx=afavgmx + (afluxmax*rr(igrp))
        eavgmx=eavgmx + (grpegy(igrp)*rr(igrp))
!
!       If any left, do more groups
!
        IF(igrp .EQ. ngroups) THEN
          GOTO 400
        END IF
      GOTO 200
!
400   CONTINUE
!
!     Report avg Results
!
      afavgmx = afavgmx/respons
      eavgmx = eavgmx/respons
!
      WRITE(* ,*)' '
      WRITE(* ,*)'-----------------------------------------------------'
      WRITE(* ,*)'  READ Data from the Following Files : '
```

```
      WRITE(* ,'(A31,A30)')'          dxdydz mesh data...  ',dxdydzf
      WRITE(* ,'(A31,A30)')'              Source data...  ',srcspecf
      WRITE(* ,'(A31,A30)')'Adjoint data filename list...  ',aflxlgf
      WRITE(* ,'(A40)') '       forward energy list... energy.fwd'
      WRITE(* ,*)'-------------------------------------------------'
!
      WRITE(* ,*) '  -- Summary for ',matname,' --'
      WRITE(* ,*) ' Tot Src: ', totsrc,' #/s'
      WRITE(* ,1000)' Total Neutron Response from ', ngroups,
     & ' Groups: ',  respons,' cts/s '
1000  FORMAT(' ',A28,I3,A9,1PE13.6,A7)
      WRITE( *,*) ' Response/source: ', (respons/totsrc)
      WRITE( *,*) ' Avg g Resp-Weighted aflux ',afavgmx ,' imp '
      WRITE(* ,*) ' Avg g Resp-Weighted energy ',eavgmx ,' MeV '
      WRITE(* ,*) ' '
      WRITE(* ,*)' --- End of Data for ',matname,' ---'
      WRITE(* ,*) ' '
!
      CLOSE(2)
      CLOSE(11)
!
      STOP
!
      END
```

Energy.Fwd filed called from within AREACT

```
BUGLE96.grp 67 Group n-gamma (use Upper Energy Group Bins in MeV)
#neut_grps  FissNeutTemp(t,e,f)
  47              t
Grp#  Upper_MeV
 1    1.7332E+01
 2    1.4191E+01
 3    1.2214E+01
 4    1.0000E+01
 5    8.6071E+00
 6    7.4082E+00
 7    6.0653E+00
 8    4.9659E+00
 9    3.6788E+00
 10   3.0119E+00
 11   2.7253E+00
 12   2.4660E+00
 13   2.3653E+00
 14   2.3457E+00
 15   2.2313E+00
 16   1.9205E+00
 17   1.6530E+00
 18   1.3534E+00
 19   1.0026E+00
 20   8.2085E-01
 21   7.4274E-01
```

22	6.0810E-01
23	4.9787E-01
24	3.6883E-01
25	2.9721E-01
26	1.8316E-01
27	1.1109E-01
28	6.7379E-02
29	4.0868E-02
30	3.1828E-02
31	2.6058E-02
32	2.4176E-02
33	2.1875E-02
34	1.5034E-02
35	7.1017E-03
36	3.3546E-03
37	1.5846E-03
38	4.5400E-04
39	2.1445E-04
40	1.0130E-04
41	3.7266E-05
42	1.0677E-05
43	5.0435E-06
44	1.8554E-06
45	8.7643E-07
46	4.1399E-07
47	1.0000E-07

APPENDIX G
REACT COMPUTER CODE FOR CALCULATING FORWARD REACTION RATES

```
!
!     Forward Reaction Rate Calculator
!
!       by G. Sjoden/Scottie Walker
!
!     Additional contributions from:
!     Michael Chin (May 2012)
!     Matthew Molinar (May 2012)

!     Version 1.5g
!
!     This code is used to process the flux files from fwd PENTRAN
!     runs to calculate reaction rates and various other quantities.
!
!-----------------------------------------------------------------------
!
      PROGRAM REACT
!
      IMPLICIT REAL (A-H,O-Z)
      IMPLICIT INTEGER (I-N)
!
!     MAIN PROGRAM
!
!/////////////////
!
      CALL IHEADR
      CALL INSIFT
!
      STOP
!
      END
!
!-----------------------------------------------------------------------
!
!     SUB IHEADR
!
!     PURPOSE OF IHEADR ROUTINE:
!     -To print header when program is initiated
!
!     NOTES:
!     -None
!
!     AUTHOR (date):
!     S. W. Walker/G. Sjoden (January 2012)
!
!     WITH CONTRIBUTIONS FROM:
!     M. Chin (May 2012)
!     M. Molinar (May 2012)
!
      SUBROUTINE IHEADR
```

```
!
      WRITE(*,'(A2///) ')'                                                '
      WRITE(*,'(2X,A46)')' Forward Reaction Rate Evaluation Program    '
      WRITE(*,'(A2)')'                                                    '
      WRITE(*,'(2X,A48)')'       Version 1.5  SINGLE PRECISION         '
      WRITE(*,'(A2)')'                                                    '
      WRITE(*,'(2X,A48)')'       Scottie W. Walker / G. Sjoden         '
      WRITE(*,'(2X,A48)')'            Michael R. Chin                  '
      WRITE(*,'(2X,A48)')'            Matthew P. Molinar               '
      WRITE(*,*) '                                                        '
      WRITE(*,'(2X,A48)')'                DEC  2012                    '
      WRITE(*,'(A2)')'                                                    '
!
      END
!
!     ****************************************************************
!     SUB INSIFT
!     ****************************************************************
!
!     PURPOSE OF INSIFT ROUTINE:
!     -To read and process data
!
      SUBROUTINE INSIFT
!
      IMPLICIT REAL (A-H,O-Z)
      IMPLICIT INTEGER (I-N)
!
      REAL, DIMENSION(150) :: tstnum, grpegy
      REAL, DIMENSION(1500) :: dx,dy,dz,vol,rr
      INTEGER, DIMENSION(1500) :: icm
      CHARACTER(10) :: matname
      CHARACTER(64) :: datfnam, outfnam, dxdydzf, rrxsecf, flxlogf
      CHARACTER(80) :: dummy
      CHARACTER(80) :: xsname
      INTEGER :: ingrp
      LOGICAL  exists, opend
!
!     ****************************************************************
!     Information location in flux (.flx) files :
!     ****************************************************************
!
!     Total number of ASCII Columns  in data files
      ntdat=7
!
!     Coarse mesh data Column Index
      icmidx=2
!
!     Target Material # Column Index
      itargm=3
!
!     x data Column Index
      ixcol=4
!
!     y data Column Index
      jycol=5
!
!     z data Column Index
      kzcol=6
```

```
!
!     Flux data Column Index
      iflux=7
!
!     Total Sn Source #/s
      totsrc = 1000
!
!     Material to Sum Rxns
!
!     ****************************************************************
!     Files Needed:
!     ****************************************************************
!        response xsecs for response xsec
!        dxdydz.out for Coarse mesh data -> Volume
!        flx.Log to list group data files in a listing
!        group files named in flx.Log
!
!     ****************************************************************
!     Input information:
!     ****************************************************************
!     Each of the read (*,*) statements require an input
!
c     WRITE(*,'(A40)')' Input Material # to sum reactions for: '
c      READ(*,*) nmat
      nmat=1
!
c     WRITE(*,'(A22)')' Input Material Name: '
c      READ(*,*) matname
      matname='Large Tube-BF3 at 2 atm'
!
!     Generalized support for arbitrary number of groups
c     WRITE(*,'(A24)')' Input Number of Groups: '
c      READ(*,*) ingrp
      ingrp=47
!
!     Prompt for number of coarse meshes (technically this is in dxdydz)
c     WRITE(*,'(A31)')' Input Number of Coarse Meshes: '
c      READ(*,*) ntgcm
      ntgcm=50
!
!     Generalized support for different cross section files - MC
c     WRITE(*,'(A35)')' Input Cross Section Filename (.xs): '
c      READ(*,*) xsname
      xsname='bf32x.xs'
!
!     Arbitrary Energy Group Selection
!     Read and Echo our energy to the screen for reference
!
!     ENERGY.FWD ***File format, starting from top line:
!       BUGLE96.grp 67 Group n-gamma (use Upper Energy Group Bins in MeV)
!       #neut_grps  FissNeutTemp(t,e,f)
!         47             t
!       Grp#  Upper_MeV
!        1    17.332
!        2    14.191
!        ...
!
      OPEN(17, FILE='energy.fwd', ACCESS='SEQUENTIAL')
```

```
        DO i=1,4
          READ(17,*) dummy
        END DO
        DO jg = 1, ingrp
          READ(17,*) igrpno, grpegy(jg)
          WRITE(*,*) 'Group (', jg,'): ', grpegy(jg),' MeV'
        END DO
      CLOSE(17)
      WRITE(*,*)
!
!     ******************************************************************
!     Initialize problem: averages, fluxsums, responses, group count
!     ******************************************************************
!
      respons=0
      rr=0
!
      favgmx=0.0
      eavgmx=0.0
      igrpcnt=0
!
!     ******************************************************************
!     Read dxdydz file and compute volume
!     ******************************************************************
!
!     Note: This dxdydz term is the volume of the forward source term!
!     When EOF is reached, control transfers to statement 150
!        and continues from there.
!     DXDYDZ.OUT starting from top line:
!     Coarse Cell     dx        dy        dz
!         1        0.333     0.333     0.250
!         ...
!
      dxdydzf='dxdydz.out'
      OPEN (3, FILE=dxdydzf, ACCESS='SEQUENTIAL')
        i=0
        READ (3,'(A)') dummy
        WRITE(*,'(A80)') dummy
100     i=i+1
        READ (3,*,END=150) icm(i), dx(i), dy(i), dz(i)
        WRITE(*,'(I5,3(2X,F8.3))') icm(i), dx(i), dy(i), dz(i)
        vol(i)=dx(i)*dy(i)*dz(i)
        GOTO 100
150     i=i-1
        IF(i.NE.ntgcm)THEN
          WRITE(*,*)'ERROR: Cell count i ',i,' mismatch ntgcm ', ntgcm
          STOP
        END IF
        WRITE(*,*)' Read ',i,' Cell Dimensions '
        WRITE(*,*) ' '
      CLOSE(3)
!
!     ----------------------------------------------------------------
!
!     Read Response Cross section file header from device 1 and
!        the flx.log header from device 2.
!
!        The two read statements read and write the data of the first
```

```
!        two lines in the cross section file to the variable dummy
!        (not needed).  The data actually begins on the 3rd line.
!
!        The first line of the flx.log is a header and the single
!        read/write statement puts that information into dummy.
!
!        Both of these files remain open until the very end of the
!        program.
!     ------------------------------------------------------------------
!
!     ******************************************************************
!     Read cross section input file and flx.Log file
!     ******************************************************************
!
!     Read rr xs data from device 1
!
      rrxsecf = 'bf32x.xs'
      OPEN (1, FILE = rrxsecf, ACCESS = 'SEQUENTIAL')
!       read header on xs file
        READ (1,'(A)') dummy
        WRITE(*,'(A80)') dummy
        READ (1,'(A)') dummy
        WRITE(*,'(A80)') dummy
!
!     Read flux datafile listing from device 2
!
      flxlogf = 'flx.Log'
      OPEN (2, FILE = flxlogf, ACCESS='SEQUENTIAL')
        READ (2,'(A)') dummy
        WRITE(*,'(A80)') dummy
!
!     ******************************************************************
!     Open output file
!     ******************************************************************
!
c     itest=INDEX(matname,' ')-1
c     IF(itest.LE.10) THEN
c       outfnam=matname(1:itest)//'-frx.out'
c     ELSE
c       outfnam=matname(1:10)//'-frx.out'
c     END IF
c
c     OPEN (11, FILE=outfnam, ACCESS='SEQUENTIAL')
c     WRITE(* ,*)'  ',outfnam
!
      WRITE(* ,*)' '
      WRITE(* ,*)'-----------------------------------------------------'
      WRITE(* ,*)'  READ Data from the Following Files : '
      WRITE(* ,'(A31,A30)')'          dxdydz mesh data...  ',dxdydzf
      WRITE(* ,'(A31,A30)')'                  xs data...  ',rrxsecf
      WRITE(* ,'(A31,A30)')'    flux log filename list...  ',flxlogf
      WRITE(* ,'(A40)') '       forward energy list... energy.fwd'
      WRITE(* ,*)'-----------------------------------------------------'
!
!
!     ******************************************************************
!               ------BEGIN GROUP DEPENDENT SEQUENCE------
!     ******************************************************************
```

```
!
200   CONTINUE
!
!     Increment group counter, reset material counter, target matl volume
!        igrpcnt was previously set to 0.
!       Initialize fluxmax and mean free path
!
      igrpcnt=igrpcnt+1
!
!     Read Group Response Cross Section from 1
!
      IF (igrpcnt .LE. ingrp) THEN
        imatcnt=0
        voltarg=0.0
        fluxmax=0
        rmfpa=0.0
        WRITE(*,*)' Group Counter = ', igrpcnt,' Out of ',ingrp,
     & ' groups.'
        READ (1,*) sigabs
        IF(sigabs.GT.1E-10)THEN
          rmfpa = 1.0/sigabs
        ELSE
          rmfpa = 0.0
        END IF
        WRITE(*,*) ' siga = ',sigabs, ' 1/cm,    mfp= ',rmfpa,' cm'
        rr(igrpcnt)=0.00
      ELSE
        igrpcnt=igrpcnt-1
      END IF
!
!     Get flux datafile assignment data from 2
!
250     CONTINUE
        READ (2,*,END=400) datfnam
!
!       Open flux datafile and read vectors of flux data
!
!       The flux files are opened below and the read statement dumps
!        the header information to dummy.  The write statement lists
!        the name of the flux file and the read statement at 350
!        begins to pull out the necessary data.
!
         OPEN (10, FILE = datfnam, ACCESS='SEQUENTIAL')
          READ (10,'(A)') dummy
          WRITE(*,'(A18,A40)')' Read data from : ', datfnam
300       CONTINUE
          READ (10,*,END=350) (tstnum(iety), iety=1,ntdat)
!
!         The read statements above read information from columns
!         1 to n of the flux file datfnam
!         When the EOF is reached, control goes to line 350.
!
!          If target material compute response from that cell
!
          IF (INT(tstnum(itargm)).EQ.nmat) THEN
            imatcnt=imatcnt+1
            itstcm=INT(tstnum(icmidx))
            voltarg = voltarg + vol(itstcm)
```

```
              fluxmaxold = fluxmax
              fluxmax=MAX(fluxmax, tstnum(iflux))
!
!             Compute group rxn rate and total rxn respons
!
              rr(igrpcnt) = rr(igrpcnt) +
     &             (tstnum(iflux) * sigabs * vol(itstcm))
              respons = respons +
     &             (tstnum(iflux) * sigabs * vol(itstcm))
            END IF
           GOTO 300
350       CONTINUE
          CLOSE(10)
!
!         Finished a group...  wrap up responses:
!
1200      FORMAT(A7,I6,1X,A7,I3,1X,A17,F10.2,A4)
          WRITE(*,1200) ' Found ',imatcnt,' matl# ',nmat,
     &    ' meshes covering ', voltarg,' cm3'
!
          WRITE(*,'(A5,I3,A1,1PE10.3,A5,A15,1PE13.6,A10,
     &      0PF6.2,A1,0PF6.2,A1,0PF6.2,A2,1PE13.6)')
     &     ' Grp ',igrpcnt,' ',grpegy(igrpcnt),' MeV ',' abs  #/s : ',
     &      rr(igrpcnt)
          WRITE(*,*)' '
!
!         Compute Response-Weighted max flux, and energy
!
          favgmx=favgmx + (fluxmax*rr(igrpcnt))
          eavgmx=eavgmx + (grpegy(igrpcnt)*rr(igrpcnt))
!
!         If any left, do more groups
!
          IF(igrpcnt .EQ. ingrp) THEN
            GOTO 400
          END IF
        GOTO 200
!
400     CONTINUE
!
!       Report avg Results
!
        favgmx = favgmx/respons
        eavgmx = eavgmx/respons
!
1000    FORMAT(' ',A28,I3,A9,1PE13.6,A7)
!
        WRITE(* ,*) '  -- Summary for ',matname,' --'
        WRITE(* ,*) ' Tot Src: ', totsrc,' #/s'
        WRITE(* ,1000)' Total Neutron Response from ', ingrp,
     &  ' Groups: ',  respons,' cts/s '
        WRITE( *,*) ' Response/source: ',
     &    (respons/totsrc)
        WRITE( *,*) ' Response/source/cm3: ',
     &    (respons/totsrc/voltarg)
        WRITE( *,*) ' Avg g Resp-Weighted flux ',favgmx ,' n/cm2/s '
        WRITE(* ,*) ' Avg g Resp-Weighted energy ',eavgmx ,' MeV '
        WRITE(* ,*) ' '
```

```
      WRITE(* ,*)' --- End of Data for ',matname,' ---'
      WRITE(* ,*) ' '
!
      CLOSE(2)
      CLOSE(1)
      CLOSE(11)
!
      STOP
!
      END
```

The energy.fwd file called within REACT is the same as that attached to Appendix F.

VITA

Scottie Wayne Walker was born in 1962 in Warm Springs, GA. He graduated from Manchester High School in Manchester, GA in 1980 and enlisted in the United States Navy, where he spent nine years in the Naval Reactors Program. During his naval career, he served as a staff instructor at the Knolls Atomic Power Laboratory (S3G reactor), Engineering Watch Supervisor onboard the USS Mariano G. Vallejo (SSBN-658G), and Radiological Controls Shift Supervisor for the submarine tender USS Holland (AS-32).

Scottie accepted a position with the Waste Isolation Pilot Plant (WIPP) in Carlsbad, NM after completing his naval service and remained there until 1993. He completed his Bachelor of Science in Radiation Protection through Thomas Edison State College in Trenton, NJ during this period and afterwards accepted a contractor position at Sandia National Laboratories (SNL) in Albuquerque, NM. Scottie was later awarded a DOE Fellowship for his graduate studies at Texas A&M University and he accepted a staff position with SNL upon graduating with his Master of Science degree in Health Physics.

While at SNL, Scottie was certified by the American Board of Health Physics (ABHP) and served in several different capacities. He began his doctoral work in nuclear engineering at the University of Florida in 2006, but transferred with his research group to the Georgia Institute of Technology in 2010 following the termination of that program.

He is married to Kay Diahn Bell-Walker and resides in Albuquerque, NM where he remains employed as a Principal Member of the Technical Staff with SNL.